Atom Interferometry at Geodetic Observatories

Precision Gravity Measurements with Quantum and Classical Sensors

zur Erlangung des akademischen Grades
doctor rerum naturalium
(Dr. rer. nat.)
im Fach Physik

eingereicht an der
Mathematisch-Naturwissenschaftlichen Fakultät
Humboldt-Universität zu Berlin

von
Dipl.-Phys. Christian Freier

Präsidentin der Humboldt-Universität zu Berlin:
Prof. Dr.-Ing. Dr. Sabine Kunst

Dekan der Mathematisch-Naturwissenschaftlichen Fakultät:
Prof. Dr. Elmar Kulke

Gutachter:
1. Prof. Achim Peters, Ph.D.
2. Prof. John Close, Ph.D.
3. Prof. Dr. Thomas Elsässer

Tag der mündlichen Prüfung: 14.02.2017

Abstract

Atom interferometers have become a widely used and flexible tool for a range of applications in fundamental and applied physics, such as inertial sensing and the measurement of physical constants. The gravimetric atom interferometer (GAIN) is a transportable setup which was specifically designed to perform high-precision gravity measurements at sites of interest for geodesy or geophysics. It is based on a ^{87}Rb atomic fountain, stimulated Raman transitions and a three-pulse Mach-Zehnder atom interferometry sequence.

The presented work is concerned with the optimization and application of GAIN as a transportable gravimeter in order to perform gravity measurements beyond the state-of-the-art. An absolute accuracy of $29\,\mathrm{nm/s^2}$, long-term stability of $0.4\,\mathrm{nm/s^2}$ and short-term noise level as low as $82\,\mathrm{nm/s^2}/\sqrt{\mathrm{Hz}}$ was achieved. The obtained long-term stability and accuracy values are, to the knowledge of the author, the best published performance of any transportable atom interferometer to date and represent a significant advancement in the field of gravimetry.

A comprehensive analysis of the systematic error budget was performed to improve the accuracy and stability of the measured gravity value. Several setup improvements were implemented to this end, including Coriolis force and alignment control systems, an improved vibration isolator with post-correction and magnetic shielding which reduces spurious coupling due to stray fields. Measurement campaigns were conducted in Berlin and at geodetic observatories in Wettzell, Germany, and Onsala, Sweden, in order to compare GAIN to other state-of-the-art absolute and relative gravimeters.

The direct comparison of GAIN to other absolute and relative gravimeters shows the general advantage of atom interferometers due to their unique combination of absolute accuracy, stability and robust architecture enabling continuous measurements. This was demonstrated during the presented campaigns by the improvement of the scale factor calibration of two superconducting gravimeters by a factor 2 to 5 using GAIN data.

Deutsche Zusammenfassung

Atominterferometrie hat sich zu einem weit verbreiteten und flexiblen Werkzeug für eine Reihe von Anwendungen in der fundamentalen und angewandten Physik entwickelt, wie z.B. der Messung von physikalischen Konstanten oder Inertialkräften. Das gravimetrische Atominterferometer (GAIN) ist ein transportables Atominterferometer welches spezifisch für hochpräzise Schweremessungen in der Geodäsie und Geophysik entwickelt wurde. Er basiert auf einer ^{87}Rb Atomfontäne, stimulierten Ramanübergängen und einer 3-Puls Mach-Zehnder Interferometriesequenz.

Die vorliegende Arbeit beschäftigt sich mit der Optimierung und Anwendung von GAIN als transportables Gravimeter für Absolutschweremessungen an geodätischen Observatorien welche über den aktuellen Stand der Technik hinaus gehen. Dabei wurden eine Absolutgenauigkiet von $29\,\mathrm{nm/s^2}$, eine Langzeitstabilität von $0.4\,\mathrm{nm/s^2}$ sowie eine Sensitivität von $82\,\mathrm{nm/s^2}/\sqrt{\mathrm{Hz}}$ erreicht. Die gemessene Genauigkeit und Langzeitstabilität stellen, nach dem Wissen des Authors, die bis heute besten publizierten Werte für ein transportablen Atominterferometer dar und repräsentieren einen bedeutenden Fortschritt im Bereich der Gravimetrie.

Um dies zu erreichen wurden umfangreiche Verbesserungen am Gerät umgesetzt und eine ausführliche Analyse der systematischen Messabweichungen durchgeführt. Unter anderem wurden ein System zur Kompensation von Corioliskräften und Ausrichtungsfehlern, ein verbessertes Schwingungsisolationssystem zur nachträglichen Korrektur von Umgebungsvibrationen und eine magnetische Abschirmung instrumenteller Streufelder implementiert. Darüber hinaus wurden insgesamt vier Messkampagnen in Berlin, sowie an den geodätischen Observatorien in Wettzell, Deutschland und Onsala, Schweden durchgeführt, um GAIN mit anderen hochmodernen Absolut- und Relativgravimetern zu vergleichen.

Der direkte Vergleich zwischen GAIN und anderen Gravimetern stellt den prinzipbedingten Vorteil der Atominterferometrie durch die Kombination aus Absolutgenauigkeit, Stabilität und Langzeitbetrieb klar hervor. Dies wurde in der Arbeit durch die um einen Faktor 2-5 verbesserte Kalibrierung des Skalenfaktor von zwei supraleitenden Gravimetern demonstriert.

Contents

Chapter 1

Introduction

The gravitational acceleration on the surface of Earth has occupied the minds of people for millennia. One of the first modern scientific descriptions of the laws of gravity was written by Isaac Newton in *Philosophiae Naturalis Principia Mathematica* in 1687. It describes the mutual force F_{12} between two point masses m_1 and m_2 with a distance r relative to each other.

$$F_{12} = G\frac{m_1 m_2}{r^2} \tag{1.1}$$

Several remarkable features of the gravitational force can be extracted from Newton's law of universal gravitation. The first is the inverse-square law that gravity shares with the electromagnetic force and which leads to interactions with a much longer range than the ones due to the strong and weak forces. Due to size of the gravitational constant

$$G = 6.674{\times}10^{-11}\,\mathrm{Nm^2/kg^2}$$

gravity can secondly be quite weak in comparison to the other fundamental forces. This can be illustrated by the fact that, e.g., the gravitational force between an electron an a proton is about 10^{39} times smaller than the corresponding Coulomb force. Due to its small size and because no theory exists that links gravity to other forces of nature, G is to this day the fundamental constant with the largest uncertainty of its numerical value [1]. Nevertheless gravity is the force which dominates the shape of the universe on an astronomical and cosmological scale due to the fact that the gravitational "charge", or heavy mass, is always positive and therefore aggregates. Third, the remarkable coincidence between gravitational mass m from equation 1.1 and the inertial mass in Newton's second law of motion $F = m{\cdot}a$, which quantifies a body's resistance to changing its state of motion. This is called the weak equivalence principle (WEP) and leads directly to the universality of free fall (UFF) which was established by Galileo and Newton as an experimental fact in the 17th century. UFF combined with local Lorentz invariance (LLI) and local position invariance (LPI) constitutes Einstein's equivalence principle (EEP) which is the foundation of general relativity and one of the corner stones of modern physics.

These properties and principles are a matter of ongoing research [2, 3] for which atom interferometers are uniquely suited. So far, however, no deviation from the expected results have been found and general relativity, with Newton's law as non-relativistic approximation, has prevailed. As the latter is sufficient to describe the presented experiment and the resulting data, it will be used throughout the rest of this work. When a relativistic correction was considered or found to be significant, this will be pointed out explicitly.

In addition to testing the laws of physics, gravity measurements are also conducted to gain insight into the details of Earth‘s gravitational field. Numerous temporal and spatial changes of the local gravitational acceleration g exist and can be measured with gravimeters to, e.g., draw conclusions on the figure of Earth or geophysical processes underneath the surface. Most of these variations are significantly smaller than 10^{-6} g and, for some applications, difficult to measure with current, classical gravimeters.

This thesis is primarily concerned with terrestrial gravity measurements and with the development and application of a new type of gravimeter using atom interferometry at geodetic observatories. The rest of this chapter will briefly summarize the working principle of a simple atom interferometer and mention the development and applications of this research field. Afterwards, some details about Earth's gravity field with its spatial and temporal variations will be given and the properties of other types of gravimeters will be discussed briefly. This will be important in order to understand the gravimetric data presented and the relevance of current and future applications.

1.1 Atom Interferometry

The first atom interferometers were demonstrated in 1991 and 1992 by four different research groups in the United States and Germany around the same time . The first two groups used mechanical, micro-fabricated slits or gratings [4, 5], whereas the other groups employed the light grating [6, 7] of a laser pulse to induce interference fringes in the detected signals. The experiment described in [7] and shortly after in [8] showed the first measurements of the gravitational acceleration with atom interferometry. It is based on stimulated two-photon Raman transitions [9] and its basic working principle is still the basis for the atomic gravimeter used during this work. The essential mechanism will therefore be explained here briefly, in addition to the proper theoretical description presented in chapter 2.

Atoms in an ultra-high vacuum (UHV) chamber are first laser-cooled in a magneto-optical trap (MOT) and subsequent optical molasses to micro-Kelvin temperatures [10] where their wave-like properties start to appear. After releasing the atoms by either simply dropping or launching them upwards using moving molasses, the atomic matter-waves are split, reflected and recombined during a so-called $\frac{\pi}{2}$-π-$\frac{\pi}{2}$ Raman pulse sequence as shown in figure 1.1, where the central pulse is twice as long as the other two pulses. During this time both interferometer arms are in opposite internal states and separated vertically due to the photon recoil collected during the state transition. The atomic state population after the last pulse then depends on the phase difference $\Delta\Phi$ accumulated between the upper and lower interferometer paths, resulting in the appearance of interference fringes. For atoms initially in the ground state, the probability of an atom being in the excited state after the last pulse is given by

$$P_e = \frac{1}{2}\left(1 - \cos\Delta\Phi\right) \tag{1.2}$$

The dominating phase shift in this configuration is caused by the atom-light interaction during which the local laser light phase is imprinted on the atomic wave function whenever a state transition occurs. When entering the phase at the space-time points A-D as indicated in figure 1.1 and using parabolic atomic trajectories, the phase shift becomes

$$\Delta\Phi = \left(\phi^A_{\text{eff}} - \phi^B_{\text{eff}} + \phi^C_{\text{eff}}\right) - \phi^D_{\text{eff}} = k_{\text{eff}} g T^2 \tag{1.3}$$

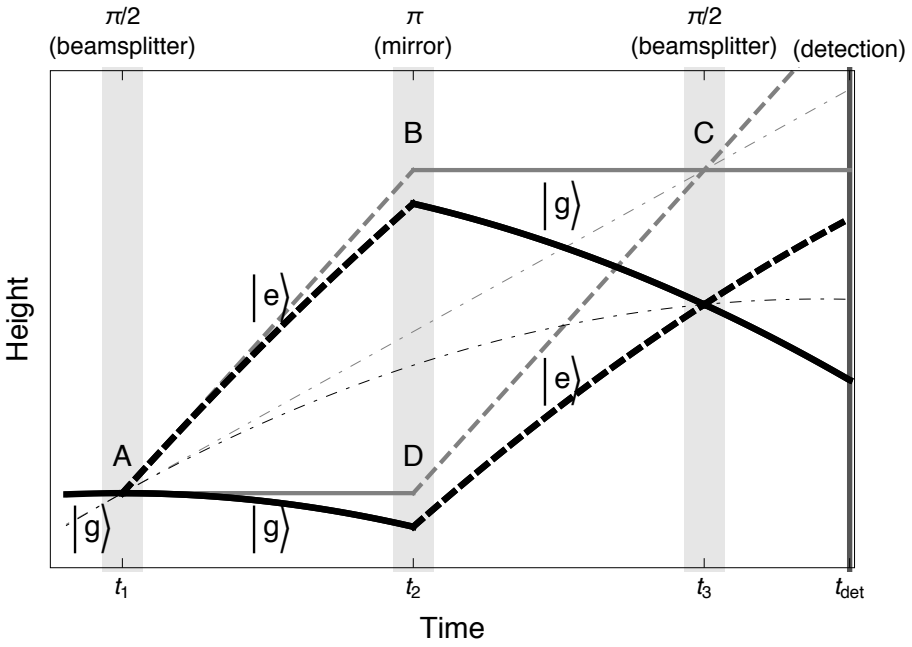

Figure 1.1: Space-Time diagram of a Mach-Zehnder atom interferometer with(black) and without(gray) gravity and vertical gravity gradient. Atomic wave-packets are split, reflected and recombined by a $\frac{\pi}{2} - \pi - \frac{\pi}{2}$ light pulse sequence separated by a time T. When stimulated Raman transitions are used, the phase shift between both interferometer arms is encoded in the output state population as stated in equation 1.2.

where k_{eff} is the length of effective wave vector of the Raman pulses and T the spacing between pulses. g denotes the local gravitational or any other acceleration along $\boldsymbol{k}_{\text{eff}}$. Note that this interpretation of the experiment is analogous to a classical g measurement with a free-falling test mass whose vertical position is recorded at three discrete points in time. The "storage" of the z-coordinate in this case effectively takes place in the phase of the atomic wave-function. This picture is very similar to the working principle of "classical" falling corner-cube gravimeter (FCCG) which measure g by determining the free-fall trajectory of a macroscopic test mass and will be detailed in chapter 1.3.2.

After the first demonstrations by Kasevich and Chu [9], the performance of atom interferometers improved quickly and became comparable to other state-of-the-art absolute gravimeters with short-term sensitivities below $10^{-8}\,\text{g}/\sqrt{\text{Hz}}$ and absolute accuracies of a few $10^{-9}\,\text{g}$ [11, 12]. The first atom interferometers, however, were complex, laboratory based setups unsuitable for use as transportable sensor. The development of mobile instruments with similar performance is ongoing, and similar performances have recently been demonstrated during mobile gravity comparisons [13, 14].

1.1.1 Applications of Atom Interferometry

Atom interferometry is a versatile technique in atomic physics which, by changing the geometry of the interferometer, has been adapted for many different applications beyond acceleration sensing. This involves the measurement of other inertial forces such as rotations [6, 15, 16, 17], differential accelerations [18, 19] and even acceleration in combination

with magnetic field sensing [20]. The extreme sensitivity to inertial forces can also be employed for the measurement of physical constants such as G [21, 22] or $\hbar/m$ [23]. Using differential atom interferometry, schemes for testing the inverse square law [24] and general relativity [25] have been proposed. Multi-species atom interferometers have further tested EEP through the UFF [26]. A comparison of an atomic gravimeter and an FG5 absolute gravimeter (AG) presented in [11] was in fact the first UFF test between quantum- and macroscopic particles with a relative uncertainty of a few times 10^{-9} [27]. This is still about four order of magnitude below the bound set by other methods [28] but may be improved in the future by advanced atom interferometers [29]. Gravitational wave detectors based on atom interferometry have also been proposed on earth and in space[30, 31], widening the scope of this technique to the fields of astronomy and astrophysics. Finally, even tests of dark energy due to so-called chameleon fields using atom interferometry have been proposed [32, 33].

This list, although far from complete, shows the scope of atom interferometry today in basic and applied physics, and the generality and flexibility of this method. Geodesy and other Earth sciences provide another wide field of applications which will be detailed in the following chapters. This work realizes the potential of atom interferometry in this field by performing high-precision absolute gravity measurements beyond the state-of-the-art at geodetic observatories and comparing them directly to other types of gravimeters. In order to compare the measured signals it is necessary to understand the gravity variations on the surface of Earth. The next chapter will therefore give a brief overview over this field.

1.2 Surface Gravity on Earth

To get an understanding of the sources and shape of the expected gravity variations found on Earth, this chapter will briefly discuss the models and results describing the gravitational potential and field. Note that this discussion can only be a short overview. A complete description can be found in geodesy textbooks and review articles [34, 35]. A summary of the most relevant gravity effects is shown in table 1.1.

Earth's gravity field is the subject of geodesy which is defined according to Helmert [36], as *"... the science of the measurement and mapping of the Earth's surface."*. Since the surface of Earth is, to a large extent, shaped by gravitation, this definition includes the determination of the Earth's figure and its external gravity field $\boldsymbol{g}(\boldsymbol{r})$. Its features are in the following roughly divided into spatial, global and regional gravity effects on one hand and time-dependent effects on the other hand. The former will be described here first. After covering the basic definitions, temporal gravity changes are discussed in the following chapters.

In order to simplify the mathematical description we write the conservative gravity field $\boldsymbol{g}$ it in terms of its scalar potential W so that $\boldsymbol{g} = -g\boldsymbol{n} = \nabla W$ with the upwards pointing unit vector $\boldsymbol{n}$. By convention, the centrifugal acceleration due to Earth's rotation is already incorporated into the potential, yielding [34]

$$W(\boldsymbol{r}) = V(\boldsymbol{r}) + Z(p) = G\int_{\text{Earth}} \frac{\rho(\boldsymbol{r'})}{|\boldsymbol{r}-\boldsymbol{r'}|} d^3r' + \frac{\Omega_E^2}{2}p^2 \tag{1.4}$$

where V denotes the gravitational potential of Earth without rotation defined by its density distribution ρ. Z gives the centrifugal potential depending on the distance from the

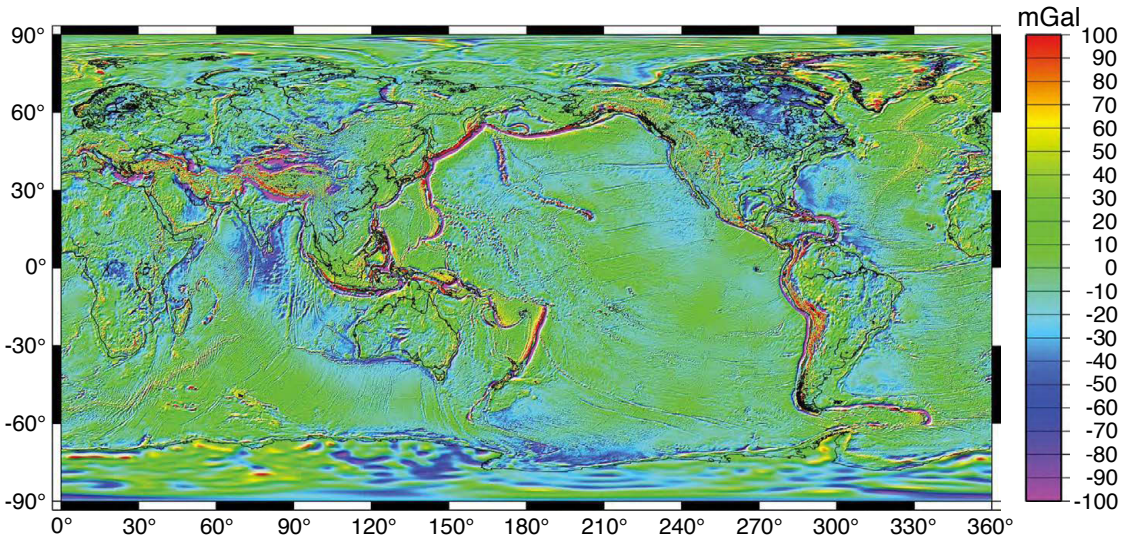

Figure 1.2: Free-air gravity anomalies Δg derived from the EGM08[37] model, combining the satellite ITG-GRACE03s [38] gravitational model with terrestrial, altimetry-derived and airborne gravity data $\left(1\,\mathrm{mGal} = 10^{-6}\,\mathrm{g}\right)$. Figure from [39]

rotation axis $p = R\cos(\bar{\theta})$, where $\bar{\theta}$ is the geographical latitude and R is the radius of Earth. The first term gives as a first, crude, approximation for a spherical Earth, with $GM = 398.6{\times}10^{12}\,\mathrm{m^3/s^2}$ and $R = 6371\,\mathrm{km}$ a potential $V = 6.26{\times}10^{7}\,\mathrm{m^2/s^2}$ and gravitational acceleration $9.82\,\mathrm{m/s^2}$ on Earth's surface. The rotation superimposes the additional centrifugal acceleration $\Omega_E^2 p \leq 0.03\,\mathrm{m/s^2}$. This causes the flattening of Earth, giving it its ellipsoidal shape and a gravity value of around $9.78\,\mathrm{m/s^2}$ at the equator and $9.83\,\mathrm{m/s^2}$ at the poles. Note that, throughout this work, relative quantities or SI units were used for g whenever possible. When citing existing literature, however, the older but still widely used Gal is sometimes used: $1\,\mathrm{Gal} = 10^{-2}\,\mathrm{m/s^2} \approx 10^{-3}\,\mathrm{g}$.

Local features and anomalies of Earth's gravity field are contained in the geoid which was introduced in 1828 by C.F. Gauss [34] as the *"equipotential surface of the Earth's gravity field coinciding with the mean sea level of the oceans"*, or $W(\boldsymbol{r}) = W_0$. If the density distribution ρ inside the earth was fully known, the gravity potential and the geoid W_0 could be calculate with equation 1.4. Unfortunately, accurate density measurements are only available for the upper layers of Earth [34]. Gravity observation therefore have to be used to construct a model which is usually expressed as a spherical harmonic expansion [34]. Figure 1.2 shows a global model of Earth's gravitational field compiled from a multitude of gravity observations. The free-air anomalies Δg denote the difference between the measured surface gravity value g_P and the calculated value at normal height[1] H^N above the ellipsoid, so that

$$g_P = \tilde{g}_0 + \gamma \cdot H^N + \Delta g \tag{1.5}$$

where $\tilde{g}_0$ is the calculated normal gravity value on the ellipsoid surface [34]. The vertical free-air gravity gradient $\gamma := \partial_r g$ can for this purpose be approximated by a mean value of $\gamma \approxeq -3086\,\mathrm{nms^{-2}/m}$. Note that the geoid height itself is related to the shown gravity

[1] More specifically, H^N gives the height above the ellipsoid with normal potential equal to the surface potential at point P (telluroid). See also [34], chapter 6.

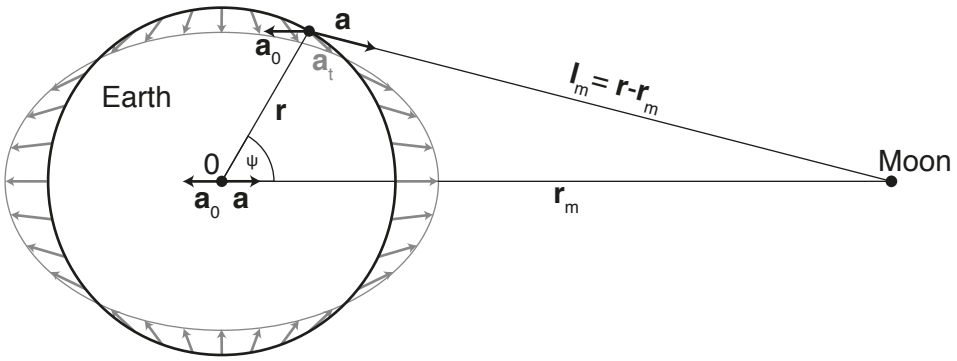

Figure 1.3: Basic tidal acceleration $\boldsymbol{a}_t$ of the moon according to equation 1.6, shown as gray arrows. A bulge forms on the front- and back-facing sides causing semi-diurnal gravity variations. The gray elliptic surface indicates the vertical shift of a level surface by the tidal potential V_t.

anomalies and derived from the same model [37]. Figure 1.2 shows many regional and local anomalies with a magnitude of 10^{-6}–10^{-4} g. Geographic features such as mountains, ocean as well as tectonic or other geophysical influences such as ocean trenches and plate tectonics are clearly visible.

The shown model is complete to spherical harmonic coefficients to degree and order 2159. The satellite data only contributes to degree 360 while the higher frequency components are only possible by combining this with terrestrial gravity data.

1.2.1 Tidal Gravity Variations

In addition to the more or less static local, regional and global structure described above, the gravitational field at a fixed location is also time-dependent. Although much smaller at a maximum size of around 10^{-7} g, temporal gravity effects are actually more relevant for this work which is concerned with gravity observations conducted over several days or weeks at one given measurement site. The largest effect is given by the gravitation of sun and moon, the other planets in the solar system contribute on a much smaller scale. These lunisolar accelerations result in the basic tidal effect on earth which will be summarized below for the two-body problem Earth-Moon. Consider a non-rotating geocentric coordinate system in which all points experience the same orbital acceleration $\boldsymbol{a}_0$ due to the movement around the barycenter of the Earth-Moon system. At Earth's center of mass, $\boldsymbol{a}_0$ and the gravitational force $\boldsymbol{a}$ cancel out whereas all other points on Earth are subject to tidal forces $\boldsymbol{a}_t$. When applying Newton's law of gravitation as illustrated in figure 1.3, one obtains:

$$\boldsymbol{a}_t = \boldsymbol{a} - \boldsymbol{a}_0 = \frac{GM_m}{l_m^2}\frac{\boldsymbol{l}_m}{l_m} - \frac{GM_m}{r_m^2}\frac{\boldsymbol{r}_m}{r_m} \tag{1.6}$$

where r_m is the distance between both center of masses and $l_m := |\boldsymbol{r} - \boldsymbol{r}_m|$ is the local distance to the moon. These tidal forces deform Earth's gravity field which, in a coordinate system fixed to its surface, cause the diurnal and semi-diurnal tidal gravity variations. In order to simplify the calculations it is again useful to transition from the tidal acceleration

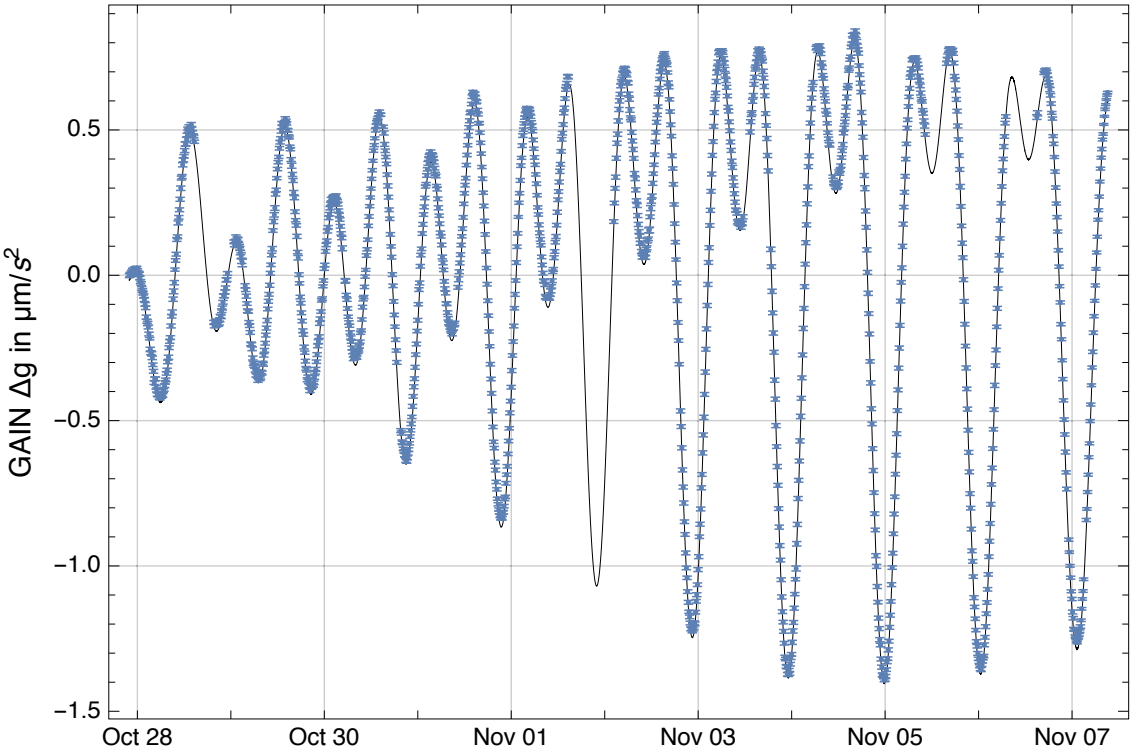

Figure 1.4: Continuous gravity registration of the atomic gravimeter GAIN over a period of several days during the comparison campaign in Wettzell, Bavaria, demonstrating the effect of tidal gravity changes. Each data point represents the mean-value for 10 min of data.

to its potential $\boldsymbol{a}_t =: \nabla V_t = \nabla(V - V_0)$. Using this and equation 1.6, the tidal acceleration and potential caused by sun, moon and the other planets in the solar system could be calculated from their respective positions which are given by the ephemerides. It is more practical, however, to use tidal potential catalogs based on a rapidly converging spherical harmonic expansion [40]. They represent the tidal potential by a series of harmonic functions which are denoted as partial tides or tidal wave components [34] and consist of frequency, amplitude and phase factor for each component. Examples for popular tide potential catalogs are Tamura[41] and HW95 [42]. As they treat Earth as a rigid body, the amplitude and phase of each partial tide is constant in time and depends on the latitude and height. This basic tidal effect is the largest contribution to temporal gravity changes at around $1\,\mu\mathrm{m/s^2}$ or $10^{-7}\,\mathrm{g}$, and the deformation V_t/g of the level surface indicated in figure 1.3 is on the order of 30–40 cm in Germany. In order to give an example of the resulting shape of the signals which will be presented later on in this work, figure 1.4 shows an excerpt of a dataset measured at the geodetic observatory in Wettzell, Germany in 2013.

Earth Tides and Ocean Loading

The above description regards Earth as a solid, rigid body. In reality, however, it responds to the tidal acceleration with significant elastic deformations called *Earth body tides*. The

total potential change ΔV at the surface of Earth therefore consists of the direct perturbation V_t superimposed with a potential change due to the tidal induced mass shift and the potential change caused by the vertical shift of the surface [34]. The latter two contributions can be described empirically using gravimetric amplitude and phase factors δ_i, $\Delta\varphi_i$ for each partial tide i. The measured gravity variations including these effects are then given by the observation equation [34]

$$g_{\mathrm{el}}(t) = \sum_i \delta_i A_i^{\mathrm{theo}} \cos\left(\omega_i t + \varphi_i^{\mathrm{theo}} + \Delta\varphi_i\right) \tag{1.7}$$

$$\delta_i := A_i^{\mathrm{obs}}/A_i^{\mathrm{theo}} \qquad \Delta\varphi_i := \varphi_i^{\mathrm{obs}} - \varphi_i^{\mathrm{theo}} \tag{1.8}$$

$$\tag{1.9}$$

where $g_{\mathrm{el}}(t)$ is the observed change at a given point on the surface of Earth including the elastic response and ω_i, A_i^{theo}, $\varphi_i^{\mathrm{theo}}$ denote the calculated values for the respective partial tide from e.g. a tidal potential catalog. To first order, Earth tides can be described using the theoretically derived Love numbers [43] resulting in an amplitude factor of $\delta = 1.16$. Note that measured gravity changes which include the elastic response are therefore about 16 % larger than the modeled tides on the rigid Earth. Because the resonance frequency of the elastic Earth is far below the dominating semi-diurnal and diurnal partial tides, the associated phase shift vanishes in this case.

Similar to Earth tides, shifting water and atmospheric masses and the associated height changes due to loading effects perturb the tidal gravity potential and are referred to as *tidal loading*. Contrary to the elastic response of Earth, however, the oscillation periods of ocean tides depend strongly on the topography of the sea floor and the coastline. The phase factors associated with ocean loading therefore vary significantly from zero and are strongly position dependent. The amplitude of the ocean loading also depends strongly on the distance to the coastline and can reach the same magnitude as Earth tides. Atmospheric loading effects due to the solar heating and associated pressure oscillations also have a tidal component which is, however, one order of magnitude smaller than Earth tides and ocean loading [34].

Detailed synthetic models of both earth tide and ocean loading have previously been published and combined in order to calculate worldwide synthetic tide models [44, 45, 46] which provide accurate gravimetric reductions on the 10^{-9} g level except for locally disturbed coastal and polar regions. Alternatively, models which are restricted to a certain measurement site can be derived from continuous gravity observations over periods longer than the respective partial tide period. Depending on the stability of the instrument and length of the dataset, up to 40 partial tides can be resolved this way with current superconducting gravimeters [34]. Further advantages and limitations of this approach are related to the instrumental properties of currently used gravimeters and will be discussed in detail in chapter 1.3.

All tidal models used throughout this work are presented in Appendix B and include tidal and ocean loading in terms of amplitude and phase factors. The denoted frequency range of each wave group contains a number of partial tides. Gravity predictions were derived from the model using the program Tsoft [47] which uses the tidal potential catalog by Tamura containing 1200 partial tides [41].

1.2.2 Atmospheric Pressure Variations

The local gravity value is strongly correlated with air-pressure due to the direct attraction of the air and the atmospheric loading similar to the effects described in the previous chapter. Their combined effect can be estimated and removed from gravity time-series reasonably well using the simple reduction [48]

$$\Delta g_{\mathrm{atm}} = a_p \left(p(t) - p_0\right) \tag{1.10}$$

where $a_p \approx 3\,\mathrm{nm/s^2/hPa}$ [49, 50] is the pressure admittance factor which can vary slightly between measurement sites, $p(t)$ is the local time-variable air pressure and p_0 is the height dependent base pressure according to the barometric formula B.1. Equation 1.10 only accounts for about 95 % of the total atmospheric effect. More sophisticated models [51, 52] are available which calculate the direct attraction using a 3D density distribution of the atmosphere over a larger area around the measurement sites from weather models. For the purpose of this work, however, the simple reduction formula 1.10 proved sufficient.

1.2.3 Polar Motion

Earth's rotational vector $\boldsymbol{\Omega}_E$ is subject to periodic and irregular changes which are monitored with high precision through space geodesy methods such as VLBI. The horizontal movement of the pole coordintates leads to variations in the centrifugal acceleration $\boldsymbol{z}$. The associated gravity effect can be calculated using the formula [53]

$$\Delta g_{\mathrm{pol}} = -\delta \cdot \Omega_E^2 R \sin 2\theta \left(x_{\mathrm{pol}} \cos\lambda - y_{\mathrm{pol}} \sin\lambda\right) \tag{1.11}$$

with the geographical latitude $\bar{\theta}$ and longitude λ of the measurement position and the approximate amplitude factor δ introduced in chapter 1.2.1 accounting for Earth's elasticity. $(x_{\mathrm{pol}}, y_{\mathrm{pol}})$ are daily pole coordinates with respect to the IERS reference pole [54]. Predicted values are available for analysis during a measurement campaign and final values with a high accuracy for post-processing. The magnitude of Δg_{pol} is usually smaller than $10^{-8}\,\mathrm{g}$ and can, due to the high accuracy of the Earth orientation parameters, be reduced to less than $10^{-10}\,\mathrm{g}$ [34]. During this work an existing implementation of equation 1.11 in the program Tsoft was used.

1.2.4 Hydrology

After applying an accurate tidal model which includes loading effects and accounting for atmospheric pressure and polar motion corrections, the residual gravity signal at most measurement sites has a magnitude in the low $10^{-9}\,\mathrm{g}$ range. The remaining part is usually caused by non-tidal environmental mass redistributions such as changes in the local water table due to precipitation and other climate effects. The associated effect is dominated by direct attraction and could in principle be approximated to first order by using a similar method chosen for air pressure correction [53]. This method is, however, restricted to regions with homogeneous sediment layers and handicapped by missing data on the local or regional hydrology. It therefore constitutes one of the least well modeled signals in terrestrial gravity monitoring [55] with a magnitude of 10^{-10}–$10^{-9}\,\mathrm{g}$ over days and up to $10^{-8}\,\mathrm{g}$ for longer data sets during seasonal changes which can be ascribed to total water storage dynamics. This is an important application of superconducting gravimeters as mentioned in chapter 1.3.3.

Effect description	Magnitude		Timescale
Geographical			
Global Scale	10^{-3}	g	
Regional Scale	10^{-4}–10^{-6}	g	constant
Free-air gravity gradient	-3×10^{-7}	g/m	
Tidal			
Direct Lunisolar Gravitation	10^{-7}	g	
Earth Tides	10^{-8}	g	6 h - years
Ocean Loading	10^{-8}	g	
Atmospheric Loading	10^{-9}	g	
Environmental			
Atmospheric Pressure	-3×10^{-10}	g/hPa	hours - days
Water Table / Hydrology	10^{-8}–10^{-10}	g	days - seasonal
Astronomical & Geophysical			
Polar Motion	$\leq 10^{-8}$	g	weeks - secular
Glacial Isostatic Adjustment	10^{-9}	g/year	secular
Tectonic Plate Movement	10^{-9}	g/year	
Volcanology	10^{-10}–10^{-7}	g	secular, sudden events
Earthquakes, Seismic Modes	10^{-10}–10^{-9}	g	

Table 1.1: Overview of temporal and geographical gravity changes on the surface of Earth. ($1\,\mu\text{Gal} = 10\,\text{nm/s}^2 \approx 10^{-9}\,\text{g}$). Refer to [34, 35] for a more detailed description.

1.3 Terrestrial Gravimetry

Today, no single type of gravimeter can fulfill the requirements for all applications and the different instruments often have to be used in combination to obtain the required gravity data. This is a direct consequence of the technological limitations of their respective measurement principles which will be discussed below. Atom interferometers such as the gravimetric atom interferometer (GAIN) presented here show the potential to alleviate this situation and combine the advantages of the different gravimeter types into a single instrument. This will reduce both the effort needed in acquiring this data and improve its quality due to reduced instrumental uncertainties.

This chapter attempts to give an overview of the working principles as well as the advantages and drawbacks of the current, classical types of gravimeters. Based on these properties their various applications in geodesy and related fields will then be highlighted in chapter 1.3.3 in order to identify the areas where atomic gravimeters can benefit current and future applications most.

Two different sorts of instrument have been developed for generating gravity data, relative and absolute gravimeters. The former only record differences between gravity values during continuous registrations or transport and need to be calibrated against a known gravimetric standard in order to relate their output to physical gravity signals. Absolute gravimeters (AGs), on the other hand, obtain the full value of g by referencing the free fall acceleration of a test mass to a time and length standard. Within the accuracy limits of those underlying standards no calibration is necessary which, in principle, makes this

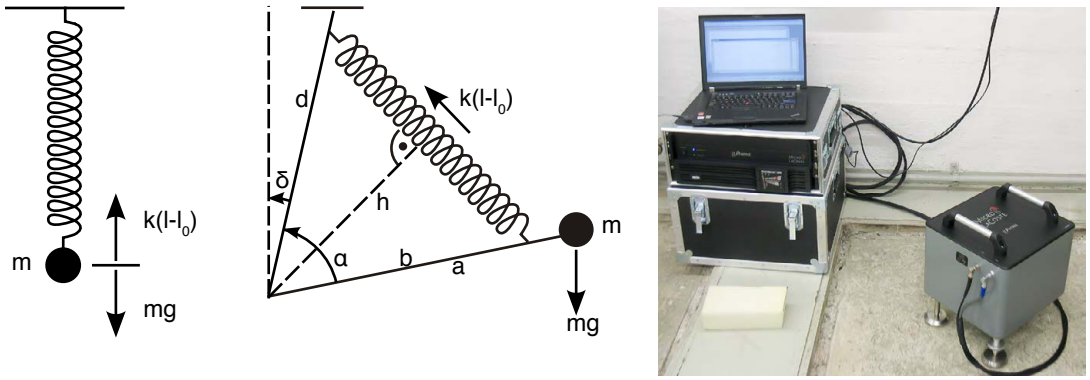

Figure 1.5: Operating principle of vertical spring (left) and general lever spring balance gravimeter (middle), from [56]. Microg-LaCoste gPhone (right) in operation with electronics and sensor head (bottom right). Image courtesy of M. Schilling, IfE Hannover.

type of instrument more attractive for many applications. Practically, however, the technical limitations of current state-of-the-art instruments require both types of instruments to cover the whole spectrum of applications in Earth sciences. In order to put the gravity comparisons between GAIN and other state-of-the-art gravimeters into context it is therefore relevant to understand their instrumental differences.

1.3.1 Relative Gravimeters

Within this section, again two main categories exist: spring-type and superconducting gravimeters. Both are based on measuring the gravitational force on a vertically suspended oscillatory system and will be described here briefly. Refer to [34, 35] for more details.

Spring Gravimeters

Spring gravimeters are based on a test mass m, suspended against gravity with a very stable mechanical spring of initial length l_0 as shown in figure 1.5. For the simple vertical spring system, changes in g can then be measured simply by monitoring the length of the spring which is governed by Hooke's law, yielding

$$g = \frac{k}{m}\left(l - l_0\right) \tag{1.12}$$

where k is the spring constant. The mechanical sensitivity $\partial_g l = m/k = \omega_0^{-2}$ is problematically low for vertical spring gravimeters, requiring a mass position readout precision of typically less than 1 nm for a gravity change of 10^{-8} g for realistic resonance frequencies [53]. Nevertheless this principle is successfully employed in Scintrex gravimeters due to its robustness and compact size.

In order to improve the intrinsic sensitivity and relax the readout system requirements, LaCoste-Romberg (LCR) type lever spring balance systems [57] were developed. The equilibrium condition for the torques as shown on the right side of figure 1.5 reads

$$mg\sin\left(\alpha+\delta\right) = k\left(l-l_0\right)h = k\left(l-l_0\right)b\frac{b}{l}\sin\alpha \tag{1.13}$$

The associated sensitivity in this configuration is given by

$$\frac{d\alpha}{dg} = \frac{\sin(\alpha+\delta)\sin\alpha}{g\sin\delta} \tag{1.14}$$

which becomes large for small δ and $\alpha \approx 90\,°$. The sensitivity improvement compared to a vertical spring is about three orders of magnitude which results in only µm level readout precision requirements. Examples for LCR instruments are the ZLS Burris or the Microg-LaCoste gPhone gravimeter, see also [58]. The gPhone which is depicted in figure 1.5 was also present for the first gravity comparison campaign shown in chapter 5. In order to reduce the influence of thermal expansion and other systematic effects, the spring-mass system of all modern spring gravimeters is housed in a hermetically sealed casing with temperature- and pressure stabilization as well as magnetic shielding. In order to suppress non-linearities of the mechanical system and extend the dynamic range of the instrument, electronic feedback systems keep the mass at the zero position during gravity changes by applying an additional feedback force. The output signal in this closed-loop configuration is then given by the amplitude of the feedback error signal. The long-term stability of the spring, which is usually made from NiFe alloys LCR or fused silica (Scintrex), is a critical parameter for these instruments. Despite considerable optimization efforts, drifts of several 10^{-8} g/day remain and have to be removed in post-processing on a best-effort basis which severely limits the range of applications.

In order to relate the output signal to physical gravity changes, a calibration function for these instruments is usually determined through relative measurements on calibration lines, controlled environments with significant gravity differences that were previously characterized using absolute gravimeters.

Superconducting Gravimeters

In order to overcome the drift limitations of spring gravimeters, superconducting gravimeter (SCG) were developed [60]. Their basic idea is to replace the mechanical spring with a permanent current through a superconducting coil pair. The test mass is facilitated by a superconducting sphere levitating in the associated magnetic field, with its position monitored by a capacitive bridge as depicted in figure 1.6. The current difference between the upper and lower field coils is carefully tuned in order to create a field gradient which results in a shallow potential and large vertical sphere displacements during gravity changes. An additional feedback coil applies a correcting force to zero the sphere position within the loop bandwidth. Due to the superconducting, cryogenic system without ohmic resistance, the drift rate of these systems can be as low as 10^{-11} g/day when operating continuously over several years at a fixed measurement site. The noise level is lower than any other type of instrument's and can reach down to only a few $\mathrm{nm/s^2}/\sqrt{\mathrm{Hz}}$. In addition to previous observatory instruments, portable SCG have recently become available [61]. Due to the more complex setup and the fact that gravity comparison between sites may be subject to significant flux jumps, the predominant use of SCGs lies in stationary, long term gravity observations.

Just like any relative gravimeter, the calibration factors of SCGs need to be determined with respect to a known gravity difference. For SCG this is usually done through simultaneous absolute gravimeter measurements by exploiting the tidal gravity signal. This method, however, is limited to a calibration error of around 10^{-3} due to measurement

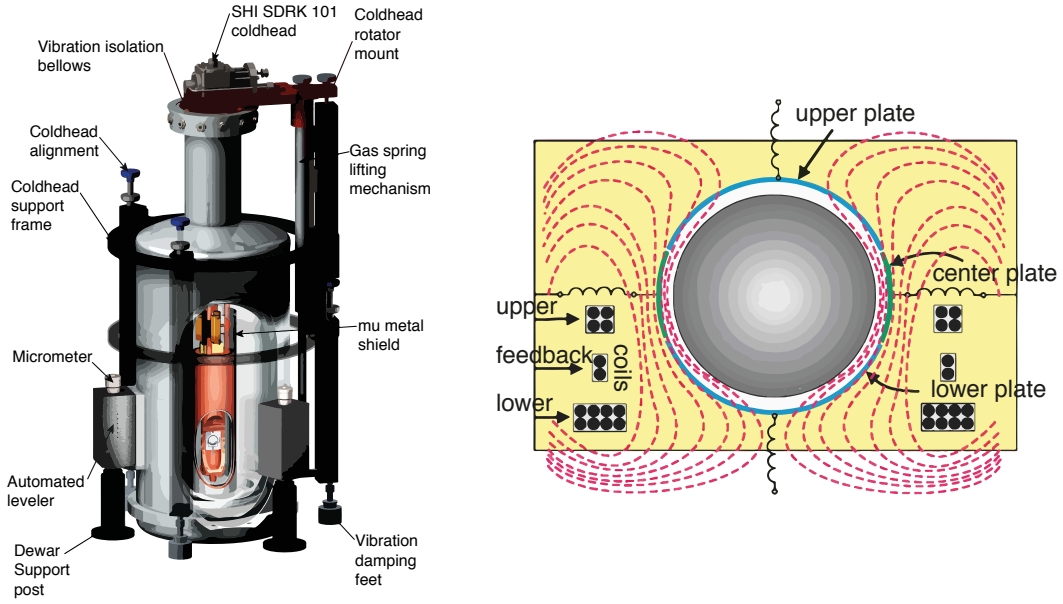

Figure 1.6: **Left:** Superconducting gravimeter cut-view through the dewar system. **Right:** Detailed view of the sensor head with superconducting sphere and magnetic field coils and capacitive position readout [59]. Figures courtesy of GWR instruments.

noise of current falling corner-cube gravimeters. During this work, the scale factor of the superconducting gravimeters at the geodetic observatories in Wettzell and Onsala have been improved by almost a full order of magnitude by exploiting the improved short- and long-term stability of the presented atomic gravimeter. See chapter 5.5.1 for a detailed description of the performed scale factor calibration.

1.3.2 Absolute Gravimeters

Atomic gravimeters such as gravimetric atom interferometer (GAIN) presented in this thesis have shown a number of advantages for absolute gravimetry, as indicated below. Their working principle was already described in chapter 1.1 and the current state of development and future applications will be discussed in chapter 1.3.3.

Historically, however, the first commonly used AGs were classic pendulums which reached a respectable accuracy of 2.5×10^{-7} g in portable setup in the 1930s [62]. The development of lasers and frequency standards in the 1960s enabled the development of the first free-fall AGs [63] which, in form of the FG5 instrument [64], have become the worldwide standard for absolute gravimeters with an accuracy of a few times 10^{-9} g.

Since the accuracy of absolute gravimeters is a prerequisite for the fidelity and usefulness of todays gravity networks, the equivalence of different types of instruments and even specimen of the same instrument is controlled on a regular basis during international comparison campaigns [65, 13].

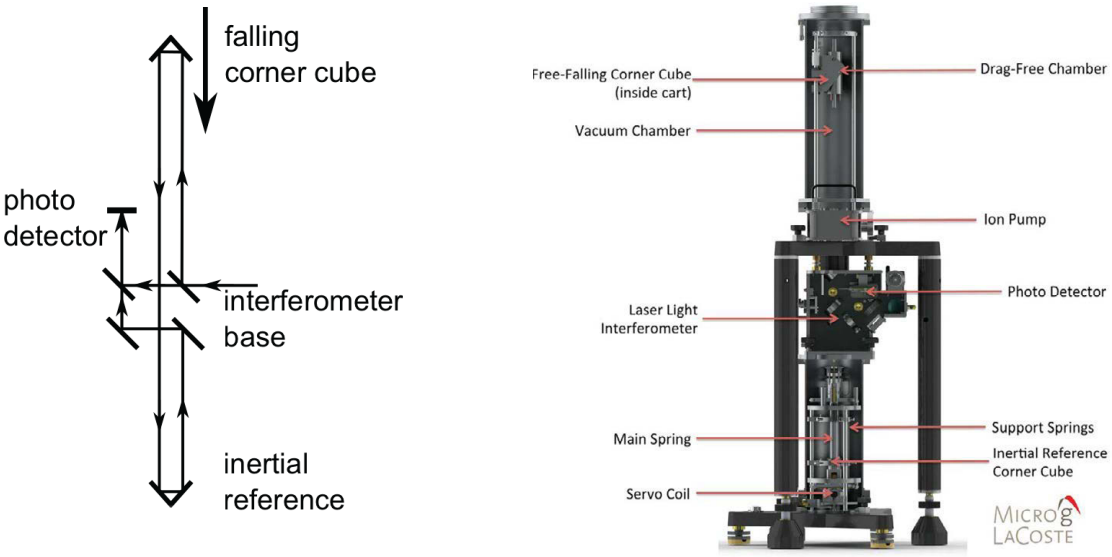

Figure 1.7: **Left:** Mach-Zehnder interferometer beam path of falling corner-cube gravimeters, from [56]. **Right:** FG5 with main functional elements: dropping chamber (top), interferometer housing (middle) and superspring (bottom). Courtesy of Microg-LaCoste.

Falling Corner-Cube Gravimeters

The most commonly used absolute gravimeters today are FCCGs based on measuring the free-fall trajectory of a retro-reflecting corner cube using an optical interferometer. Although alternative developments exist [35], the Microg-LaCoste FG5 and its field version A10 are by far the most common type of FCCG. Since only the FG5X-220 was involved in the gravity comparisons conducted during this work, the following description will be based on this instrument.

In order to reduce atmospheric drag the free fall takes places in a vacuum chamber. An elaborate elevator system facilitates the dropping and raising of test mass at a repetition rate of around 0.1 Hz[2]. The elevator cage also removes residual drag due to background gas by co-propagating in front of the corner-cube without mechanical contact. The free-fall distance is 30 cm for the FG5X instrument [66] and slightly smaller for more compact and for older instruments. The laser light is provided by wave-length stabilized HeNe laser and guided to the interferometer unit through an optical fiber. The optical beam path is shown in figure 1.7 and enables a precise relative distance measurement between the falling corner cube and the inertial reference. In order to reduce measurement noise caused by environmental vibrations, the reference is mechanically decoupled from the environment using an active, low frequency vibration isolation system coined superspring [67, 68].

The resulting interferometer fringes are converted to an electric signal by a photo-diode. The standard analysis method involves timing of the zero-crossings of the fringes using an electronic counter referenced to a Rubidium frequency standard with an accuracy of better than 5×10^{-10} which results in a maximum measurement error of 10^{-9} g [69]. Local gravity g can then be calculated using the free fall trajectory of the test mass while accounting

[2]Faster operation is possible but not always beneficial for a number of reasons discussed in chapter 1.3.3

for the vertical gravity gradient γ

$$z(t) = -\frac{g_0}{2}t^2 + v_0 t - z_0 + \gamma t^2 \left(-\frac{1}{24} g_0 t^2 + \frac{1}{6} v_0 t + \frac{1}{2} z_0 \right) + O(\gamma^2) \tag{1.15}$$

where $g_0 := g(z = 0)$ and z_0, v_0 are the initial position and velocity of the test mass. The specified performance of the state-of-the-art FG5X instrument under optimal conditions is given by $150\,\mathrm{nm/s^2/\sqrt{Hz}}$ and an absolute accuracy of $20\,\mathrm{nm/s^2}$. During international comparisons, the results of different instruments are consistent within 20–$50\,\mathrm{nm/s^2}$ [65, 13].

Typical operation during an FG5 gravity measurement involves performing around 100 dropping experiments per hour with an interval of 10 s between drops for around 8-10 hours during a period of low micro-seismic vibrations in order to minimize measurement noise [69]. For the rest of the time the device rests in order to minimize mechanical wear and tear. This is repeated around 3-4 times, potentially while repeating the set-up procedure with different device orientations in order to prevent set-up dependent systematics [14, 70].

1.3.3 Applications of Current and Future Gravimeters

This subchapter summarizes the typical use cases of the above mentioned types of gravimeters which are closely connected to their technical strengths and limitations. The resulting picture is then used to motivate the use of atomic gravimeters in geodesy and geophysics. Starting from their current state of development, this constitutes the main idea behind this thesis which will be summarized.

FG5 or other FCCG absolute gravimeters are most often used for gravity point measurements which, e.g., implement reference sites as part of gravity networks. When repeated periodically, FG5 measurement have also been used to investigate secular geophysical processes such as post-glacial rebound [71]. Relative gravimeters are unsuitable for this purpose as the small amplitude and rate of change would make it almost impossible to distinguish the desired gravity signal from instrumental drift. The mechanical wear and tear and the comparatively large measurement noise of FCCG, on the other hand, make them unsuitable for continuous operation over extended periods of time.

Relative spring gravimeters are, due to their portability and cost effectiveness, often employed to lay out local gravity networks for geophysical monitoring or to increase the density of absolute gravity networks. They are furthermore used to support absolute gravity measurements through the determination of vertical and horizontal gradients. Additionally, long-term gravity registrations over several weeks or months for, e.g. tide model characterizations can be carried out using LCR spring gravimeters. Here the instrumental drift unfortunately prevents the study of slow gravity changes in the $10^{-9}\,\mathrm{g}$ range due to water table fluctuations or other environmental mass redistributions. Superconducting gravimeters have in the past been used for long-term gravity observations over years or even decades [35] in permanent installations. Their small and very linear drift enables investigations of hydrological and geophysical gravity signal in the $10^{-10}\,\mathrm{g}$ range not possible with spring-type instruments. More recently a portable SCG instrument has been developed [61, 72] with similar performance, extending the reach for these instruments beyond geodetic observatories. This instrument has, for instance, been used successfully to monitor local water storage variations under field conditions [73]. Despite the vast

improvement compared to spring gravimeters, SCG data are still subject to instrumental drift of several 10^{-9} g over a number of years which is large enough to mask secular signals of geophysical origin such as plate tectonics of post-glacial rebound. Comparison campaigns involving FCCG are therefore required on a regular basis for drift determination which introduces uncertainties in the 10^{-9} g level due to error in the FG5 point measurements [35] and significantly increases the cost and effort needed for drift-free continuous gravity data. Atomic gravimeters, on the other hand, enable long-term absolute gravity monitoring with a stability in or below the 10^{-9} g range as shown in this work. This would be highly beneficial for a these and related applications in geodesy, geophysics and hydrology.

Another practical consideration is the range of available measurement sites. FG5 absolute gravimeters are only employed on a solid concrete foundation in order reduce self-induced vibration due to the moving test-mass. They also exhibit increased measurement noise in the presence of elevated micro-seismic vibrations caused by, e.g., stormy and windy weather conditions or human activity. Both factors strongly restrict the availability of measurement sites for absolute gravimetry. Atom interferometers have shown the potential to relax these restrictions of currently used absolute and relative gravimeters. As they do not rely on moving parts and operate with a high repetition rate, they offer the prospect of continuous absolute measurements with high long- and short-term stability in the 10^{-9} g or better while being less sensitive to environmental noise.

Most of the atomic gravimeters developed to date, however, were realized as large, stationary, experimental setups unsuitable for field use [27, 12] and the development of compact, portable and robust field instruments is still in progress today [14, 74]. Although the first commercial atomic gravimeters have recently become available [75, 76, 77], their adaption in geodesy and specific other earth sciences is still in its infancy and their exact performance not yet fully known.

The underlying goal of the presented work is therefore to make a state-of-the-art atomic gravimeter available for geodetic applications and exploit the potential of this new class of sensors under realistic conditions during measurement campaigns at several geodetic sites. This was demonstrated specifically by conducting state-of-the-art absolute gravity measurements outside of the laboratory at geodetic observatories in Wettzell, Germany and Onsala, Sweden with the Gravimetric atom interferometer (GAIN) at Humboldt Universität zu Berlin (HUB). A comparison to other state-of-the-art absolute and relative gravimeters was carried out during each campaign in order to distinguish instrumental effects from real gravity changes and demonstrate the benefits of this new kind of sensor for the above-mentioned applications. Before conducting these measurements the performance, mobility and robustness of the atom interferometer setup was improved and verified during test measurements in Berlin.

1.4 Thesis Structure

After reviewing the objective framework, chapter 2 will review the theoretical description of the atom interferometer. The following chapters 3 and 4 describe the experimental setup and the measurement sequence which was used for the gravity comparison campaigns. Special emphasis here is put on the parts to which the author contributed most during the work on the setup, namely the vibration isolation and Coriolis compensation setup,

RF frequency control system and improvements on the atomic source. Chapter 5 includes a detailed analysis of the gravity data obtained during all four gravity campaigns with a quantitative comparison to the other gravimeters types. This includes the achieved GAIN measurement noise, long-term stability and the absolute accuracy. Chapter 6 gives a detailed account of the systematic effects and error budget that were investigated during this work. The conclusion explores the implications of the presented results. An outlook on current and future benefits of atom interferometry for the field of gravimetry both in geodetic observatories and other environments will be derived.

Chapter 2

Theory

In order to realize gravimetric measurements with the desired accuracy, the gravity induced atom interferometer phase $\Delta\Phi$ needs to be known, including higher-order corrections. This derivation summarizes the important results in a self-contained manner and refers to the extensive existing literature on light-pulse atom interferometers where appropriate.

First, the atom-light interaction during stimulated, two-photon Raman transition is introduced which causes the dominating phase contribution. The complete interferometer phase will then be derived using the path integral method including higher order corrections due to gravity gradients. Finally, the sensitivity function of Mach-Zehnder atom interferometers is used to derive the effect of finite-length Raman pulses and Raman phase noise.

2.1 Stimulated Raman Transitions

The interferometer sequence described later in this chapter infers transitions between two internal atomic states, $|g\rangle$ and $|e\rangle$, which have to be stable enough to neglect spontaneous decay within the time scale of the experiment. One good candidate are the hyperfine states of Alkali metals such as Rubidium with transition frequencies in the radio frequency (RF) range. As will become clear later, the sensitivity of the interferometer phase to inertial forces scales linearly with the Doppler shift $\Delta\omega = \mathbf{k} \cdot \mathbf{v}$ of the transition frequency, where $\mathbf{k}$ is the light's wave vector and $\mathbf{v}$ the atomic velocity . In order to increase the sensitivity it is beneficial to make $\mathbf{k}$ larger by not driving the RF transition directly, but employing two-photon Raman transitions via an intermediate state $|i\rangle$ using counter-propagation beams as depicted in figure 2.1. This results in a Doppler sensitivity of $\Delta\omega = \mathbf{k}_{\text{eff}} \cdot \mathbf{v}$, with the effective wave vector

$$\mathbf{k}_{\text{eff}} := \mathbf{k_1} - \mathbf{k_2} = (|\mathbf{k_1}| + |\mathbf{k_2}|)\,\mathbf{e_k}$$

For ^{87}Rb, Doppler sensitive Raman transitions via the D2 line lead to $k_{\text{eff}} \approxeq 1.61{\times}10^7\,\text{m}^{-1}$ compared to $k_{\text{RF}} \approx 143\,\text{m}^{-1}$ when driving the transition directly using a 6.8 GHz microwave, a gain of five orders of magnitude. The description of the atom-light interaction giving here follows a treatment from [78] and briefly outlines intermediate and main results of the calculation.

Both the internal state of a three-level system and the external momentum of the atomic wave-packet need to be considered. The latter can be conveniently describe as a

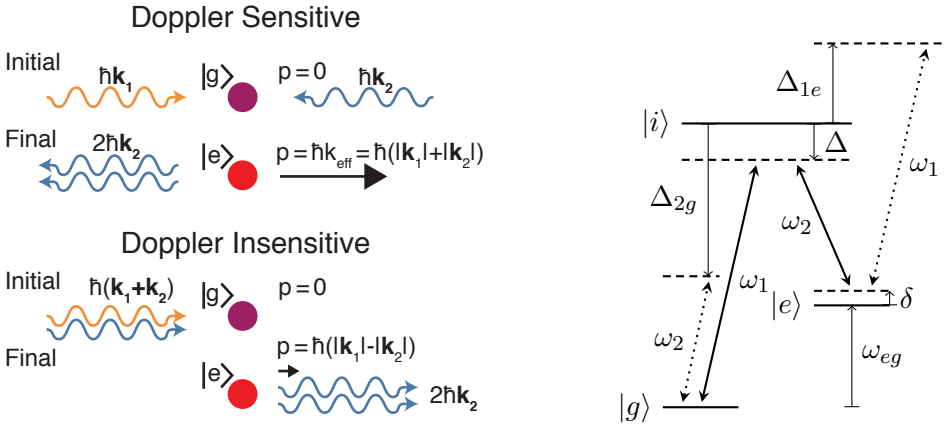

Figure 2.1: **Left:** Stimulated Raman transitions and momentum recoil for Doppler sensitive (counter-propagating) and insensitive (co-propagating) beam configurations. **Right:** Three-level system and Raman driving fields $\omega_{1/2}$ with one- and two-photon detunings Δ and δ. The dotted off-resonant transitions cause additional AC-stark offsets.

sum of momentum plane-wave states $|\mathbf{p}\rangle$ and the internal atomic states $|g\rangle, |e\rangle, |i\rangle$ and be written as the tensor product of two Hilbert spaces

$$\begin{aligned} |g, \mathbf{p}_g\rangle &= |g\rangle \otimes |\mathbf{p}_g\rangle \\ |e, \mathbf{p}_e\rangle &= |e\rangle \otimes |\mathbf{p}_e\rangle \\ |i, \mathbf{p}_i\rangle &= |i\rangle \otimes |\mathbf{p}_i\rangle \end{aligned}$$

The Hamiltonian for this problem is given by [78]:

$$\hat{H} = \underbrace{\frac{\hat{\mathbf{p}}^2}{2m} + \hbar\omega_g |g\rangle\langle g| + \hbar\omega_e |e\rangle\langle e| + \hbar\omega_i |i\rangle\langle i|}_{=:\hat{\mathrm{H}}_0} - \underbrace{\mathbf{d}\cdot\mathbf{E}}_{=:\hat{\mathrm{H}}_{\mathrm{int}}}$$

with the internal states as depicted in the level diagram in figure 2.1. The electric dipole interaction term $\hat{H}_{\mathrm{int}}$ couples to the two optical driving fields:

$$\mathbf{E} = \mathbf{E}_1 \cos(\underbrace{\mathbf{k}_1\cdot\mathbf{x} - \omega_1 t + \phi_{\mathrm{L1}}}_{=:\phi_1}) + \mathbf{E}_2 \cos(\underbrace{\mathbf{k}_2\cdot\mathbf{x} - \omega_2 t + \phi_{\mathrm{L2}}}_{=:\phi_2})$$

In order to simplify the calculation of the time evolution, it is beneficial to move to the interaction picture where the time evolution due to $\hat{H}_0$ is factored out. The state and Schrödinger equation in this picture read [79]:

$$\begin{aligned} |\Psi_I(t)\rangle &= e^{i\hat{H}_0 t/\hbar} |\Psi(t)\rangle \\ i\hbar\tfrac{\partial}{\partial t} |\Psi_I(t)\rangle &= e^{i\hat{H}_0 t/\hbar} \hat{H}_{\mathrm{int}} e^{-i\hat{H}_0 t/\hbar} |\Psi_I(t)\rangle \end{aligned} \tag{2.1}$$

Assuming an initial state $|g, \mathbf{p}\rangle$ without loss of generality, the atomic state form a closed momentum family and can be written in the given basis as:

$$\begin{aligned} |\Psi_I(t)\rangle = c_g(t)\,|g, \mathbf{p}\rangle + c_e(t)\,|e, \mathbf{p} + \hbar\mathbf{k}_{\mathrm{eff}}\rangle + \\ c_{i1}(t)\,|i, \mathbf{p} + \hbar\mathbf{k_1}\rangle + c_{i2}(t)\,|i, \mathbf{p} + \hbar\mathbf{k_2}\rangle + c_{i3}(t)\,|i, \mathbf{p} + \hbar(\mathbf{k}_{\mathrm{eff}} + \mathbf{k_2})\rangle \end{aligned} \tag{2.2}$$

Inserting state 2.2 into the Schrödinger equation 2.1 results in an equation system for the slowly varying coefficients $c_{ij}(t)$. This can be simplified through the rotating wave approximation (RWA) which removes rapidly oscillating terms and by employing the closure relation with respect to the momentum states:

$$e^{\pm i\mathbf{k}_1 x} = \int \mathrm{d}^3\mathbf{p}\; e^{\pm i\mathbf{k}_1 x} \left|\mathbf{p}\right\rangle \left\langle\mathbf{p}\right| = \int \mathrm{d}^3\mathbf{p} \left|\mathbf{p} \pm \hbar\mathbf{k_1}\right\rangle \left\langle\mathbf{p}\right| \tag{2.3}$$

The excited state coefficients $c_{ij}(t)$ can now be adiabatically eliminated from the system under the assumption that the one-photon detuning Δ is much larger than the Rabi-frequencies $\Omega_{jk} = -\left\langle i\right| \mathbf{d}\cdot\mathbf{E_k} \left|j\right\rangle/\hbar$. See for example [80] for a more detailed description of this step. This yields an effective two-level system governed a Hamiltonian with the following form in the spinor representation of $(|e, \mathbf{p}+\hbar\mathbf{k}_{\mathrm{eff}}\rangle, |g, \mathbf{p}\rangle)$

$$H = \hbar \begin{pmatrix} \Omega_e^{AC} & (\Omega_{\mathrm{eff}}/2)\, e^{-i(\delta_{12}t+\phi_{\mathrm{eff}})} \\ (\Omega_{\mathrm{eff}}/2)\, e^{-i(\delta_{12}t+\phi_{\mathrm{eff}})} & \Omega_g^{AC} \end{pmatrix} \tag{2.4}$$

with symbol definitions again as depicted in figure 2.1 and defined as

$$\Omega_e^{AC} := \frac{|\Omega_{e2}|}{4\Delta} \qquad \Omega_g^{AC} := \frac{|\Omega_{g1}|}{4\Delta} \qquad \Omega_{jk} := -\frac{\left\langle i\right| \mathbf{d}\cdot\mathbf{E_k} \left|j\right\rangle}{\hbar} \tag{2.5}$$

$$\delta_{12} := (\omega_1 - \omega_2) - \left(\omega_{eg} + \frac{\mathbf{p}\cdot\mathbf{k}_{\mathrm{eff}}}{m} + \frac{\hbar|\mathbf{k}_{\mathrm{eff}}|^2}{2m}\right) \tag{2.6}$$

$$\Omega_{\mathrm{eff}} := \frac{\Omega_{e1}^*\Omega_{g2}}{2\Delta} \qquad \phi_{\mathrm{eff}} := \phi_2 - \phi_1 \tag{2.7}$$

with the resonant Rabi frequency Ω_{jk}, AC-Stark shifts $\Omega_{e/g}^{AC}$, two-photon detuning δ_{12}, effective two-photon Rabi-frequency Ω_{eff} and phase ϕ_{eff}. Note that additional terms in $\Omega_{e/g}^{AC}$ that were caused by the off-resonant dotted transitions in figure 2.1 were neglected here for simplicity. The atoms thus perform Rabi oscillations [81] between the states $|e, \mathbf{p}+\hbar\mathbf{k}_{\mathrm{eff}}\rangle$ and $|g, \mathbf{p}\rangle$ with the effective resonant Rabi frequency Ω_{eff}. The time evolution of the coefficients c_g, c_e under this Hamiltonian is given by [78, 23]

$$c_{e,\mathbf{p}+\hbar\mathbf{k}_{\mathrm{eff}}}(t_0+\tau) = \tag{2.8}$$

$$e^{-i\varphi_{\mathrm{AC}}} e^{-i\delta_{12}\tau/2} \cdot \left[c_{e,\mathbf{p}+\hbar\mathbf{k}_{\mathrm{eff}}}(t_0)\cdot\Theta_0^* + c_{g,\mathbf{p}}(t_0) e^{-i(\delta_{12}t_0+\phi_{\mathrm{eff}})}\left(-i\frac{\Omega_{\mathrm{eff}}}{\Omega_r}\sin\frac{\Omega_r\tau}{2}\right)\right] \tag{2.9}$$

$$c_{g,\mathbf{p}}(t_0+\tau) = \tag{2.10}$$

$$e^{-i\varphi_{\mathrm{AC}}} e^{i\delta_{12}\tau/2} \cdot \left[c_{e,\mathbf{p}+\hbar\mathbf{k}_{\mathrm{eff}}}(t_0) e^{i(\delta_{12}t_0+\phi_{\mathrm{eff}})}\left(-i\frac{\Omega_{\mathrm{eff}}}{\Omega_r}\sin\frac{\Omega_r\tau}{2}\right) + c_{g,\mathbf{p}}(t_0)\cdot\Theta_0\right] \tag{2.11}$$

With the differential and mean AC-Stark shifts δ_{AC} and φ_{AC}, off-resonant effective Rabi-frequency Ω_r and the phase term Θ_0:

$$\delta_{\mathrm{AC}} = \Omega_e^{AC} - \Omega_g^{AC} \tag{2.12}$$

$$\varphi_{\mathrm{AC}} = \frac{\Omega_e^{AC} + \Omega_g^{AC}}{2} \tag{2.13}$$

$$\Omega_r = \sqrt{\Omega_{\mathrm{eff}}^2 + (\delta_{12} - \delta_{\mathrm{AC}})^2} \tag{2.14}$$

$$\Theta_0 = \cos\frac{\Omega_r\tau}{2} + i\frac{\delta_{\mathrm{AC}} - \delta_{12}}{\Omega_r}\sin\frac{\Omega_r\tau}{2} \tag{2.15}$$

Transition	Phase Shift
$\|g,\mathbf{p}\rangle \rightarrow \|g,\mathbf{p}\rangle$	$(-2\varphi_{\mathrm{AC}}+\delta_{12})\,\frac{\tau}{2}+\arg(\Theta_0)$
$\|g,\mathbf{p}\rangle \rightarrow \|e,\mathbf{p}+\hbar\mathbf{k}_{\mathrm{eff}}\rangle$	$(-2\varphi_{\mathrm{AC}}-\delta_{12})\,\frac{\tau}{2}-(\delta_{12}t_0+\phi_{\mathrm{eff}})-\frac{\pi}{2}$
$\|e,\mathbf{p}+\hbar\mathbf{k}_{\mathrm{eff}}\rangle \rightarrow \|e,\mathbf{p}+\hbar\mathbf{k}_{\mathrm{eff}}\rangle$	$(-2\varphi_{\mathrm{AC}}-\delta_{12})\,\frac{\tau}{2}-\arg(\Theta_0)$
$\|e,\mathbf{p}+\hbar\mathbf{k}_{\mathrm{eff}}\rangle \rightarrow \|g,\mathbf{p}\rangle$	$(-2\varphi_{\mathrm{AC}}+\delta_{12})\,\frac{\tau}{2}+(\delta_{12}t_0+\phi_{\mathrm{eff}})-\frac{\pi}{2}$

Table 2.1: Raman transition phase contributions. The effective light phase ϕ_{eff} is added(subtracted) during each (de)excitation of the atom. Mean/diff. AC-Stark shifts also enter through φ_{AC} and $\arg(\Theta_0)$. Note that $\arg(\Theta_0)\cong 0$ near resonance $(\delta_{12}-\delta_{AC})\ll\Omega_r$.

Equations 2.8 to 2.11 can now be used to determine the phase shifts imprinted onto the atomic state during a Raman laser pulse as summarized in table 2.1. Note in particular that the local light phase ϕ_{eff} is added to the wave-function each time the atom undergoes a state transition. This will be used in chapter 2.3 to calculate the interferometer phase contribution due to the atom-light interaction.

In order to write the resulting atom's output state of after interacting with the light fields for a time τ in a more clear and concise manner, one can employ a matrix based approach inspired by ABCD matrices from classical optics. It allows to write the effect of each Raman pulse in the form of a transfer matrix M such that:

$$\begin{pmatrix} c_{e,\mathbf{p}+\hbar\mathbf{k}_{\mathrm{eff}}}(t_0+\tau) \\ c_{g,\mathbf{p}}(t_0+\tau) \end{pmatrix} = \mathbf{M}_{t_0,\tau,\phi_{\mathrm{eff}},\Omega_{\mathrm{eff}}} \cdot \begin{pmatrix} c_{e,\mathbf{p}+\hbar\mathbf{k}_{\mathrm{eff}}}(t_0) \\ c_{g,\mathbf{p}}(t_0) \end{pmatrix}$$

Where the transfer matrix $\mathbf{M}_{t_0,\tau,\phi_{\mathrm{eff}},\Omega_{\mathrm{eff}}}$ is given by equations 2.8 and 2.11. To calculate the transfer matrix for the specific pulse areas used during the $\frac{\pi}{2}-\pi-\frac{\pi}{2}$ Mach-Zehnder sequence detailed in chapter 2.2, we have $\Omega_{\mathrm{eff}}\tau=\frac{\pi}{2}$ or $\Omega_{\mathrm{eff}}\tau=\pi$, respectively. We further assume that the laser is tuned on resonance and neglect the differential and mean AC-Stark shifts so that $\delta_{12}-\delta_{\mathrm{AC}}=0$. Inserting this into equations 2.8 and 2.11 yields the transfer matrices:

$$\mathbf{M}_{\frac{\pi}{2}} = \begin{pmatrix} \frac{1}{\sqrt{2}} & -\frac{ie^{\ i\phi_{\mathrm{eff}}}}{\sqrt{2}} \\ -\frac{ie^{i\phi_{\mathrm{eff}}}}{\sqrt{2}} & \frac{1}{\sqrt{2}} \end{pmatrix} \qquad \mathbf{M}_{\pi} = \begin{pmatrix} 0 & -ie^{-i\phi_{\mathrm{eff}}} \\ -ie^{i\phi_{\mathrm{eff}}} & 0 \end{pmatrix} \tag{2.16}$$

Since the light is switched off during the periods in between the Raman pulses, the state evolution is halted and does not have to be considered resulting in $M_0=\mathbb{1}$. This is a consequence of the interaction picture chosen at the beginning of this chapter so that the state coefficients $c_{e/g}$ include only the time evolution of H_{int}.

2.2 Mach-Zehnder Atom Interferometer

The above description already allows to calculate the atomic state after the three-pulse Mach-Zehnder sequence used for the gravity measurements as introduced in chapter 1.1 and illustrated in figure 1.1. Using the transfer matrices from equation 2.16, the calculation of the interferometer output state now reduces to the evaluation of the matrix product $\mathbf{M}_{\frac{\pi}{2}}\cdot\mathbf{M}_{\pi}\cdot\mathbf{M}_{\frac{\pi}{2}}$ given by the Mach-Zehnder pulse sequence. Under the presumption that an atom is initially in the ground state, the probability for detecting it in the excited state

at the output port after the pulse sequence is given by:

$$P_e := |c_{e,\mathbf{p}+\hbar\mathbf{k}_{\text{eff}}}(2(T+\tau))|^2 = \bar{P}_e - \frac{A}{2}\cos\Delta\Phi \tag{2.17}$$

For zero detuning and precise π,$\pi/2$ pulses, the mean state population and contrast become $\bar{P}_e = \frac{1}{2}$ and $A = 1$, respectively. This recovers the simplified form of this expression given in equation 1.2. The interferometer phase $\Delta\Phi$ is given by the light phase of the Raman laser at the atomic positions ϕ^i_{eff} during the three Raman pulses. Inserting the expressions from table 2.1 yields the generalized form

$$\Delta\Phi = \phi^1_{\text{eff}} - 2\phi^2_{\text{eff}} + \phi^3_{\text{eff}} + \left(\arg(\Theta^1_0) - \arg(\Theta^3_0)\right) \tag{2.18}$$

The trailing Θ^i_0 term defined in equation 2.15 contains a secondary and often unwanted phase shifts due to different light shifts between the first and last pulse. This will be neglected here until the short theoretical description in chapter 2.2.1 and the discussion of the systematic shift in the experiment in chapter 6.4.1.

In order to express $\Delta\Phi$ through the gravitational acceleration g, the local light phases during the three pulses along the classical, free-fall parabolic atomic trajectory $z(t)$ are needed, which are given by [78]:

$$\phi^i_{\text{eff}} = -\boldsymbol{k}_{\text{eff}}\left(\frac{\boldsymbol{g}}{2}t_i^2 + \mathbf{v}_0 t_i + \mathbf{z}_0\right) + \frac{\alpha}{2}t_i^2 + \phi^i_0 \tag{2.19}$$

where $\boldsymbol{g} := -g\boldsymbol{n}$ is defined as before in chapter 1. This includes a fixed frequency chirp α which is added to the Raman laser to cancel the Doppler shift of the atoms in the free falling reference frame. The terms ϕ^i_0 denote an optional Raman laser phase offset which can be controlled at will in order to tune the output phase of the interferometer. When combining the light phases ϕ^i_{eff} during the three Raman pulses with equation 2.18 one obtains the simple gravimeter formula

$$\Delta\Phi = (\alpha - \boldsymbol{k}_{\text{eff}}\cdot\boldsymbol{g})\,T^2 + \underbrace{\left(\phi^1_0 - 2\phi^2_0 + \phi^3_0\right)}_{=:\Delta\Phi_{\text{L}}} \tag{2.20}$$

where T is the time spacing in between the Raman pulses as indicated in figure 1.1. This simple model for the gravity induced interferometer phase shift describes the experimental result surprisingly well. It also shows that the measurement sensitivity with respect to g scales linearly with k_{eff}, which concludes the argument for using stimulated Raman as opposed to direct RF transitions at the beginning of this chapter. The sensitivity also scales quadratically in T and linearly with the free-fall height or space-time area covered by the interferometer. This fact has important consequences on the design of the experimental setup described later in this work and is the main reason for the elongated interferometer region described in chapter 3.1.

2.2.1 AC-Stark / Light Shifts

The coupling of the levels $|g\rangle$ and $|e\rangle$ by the Raman transitions causes mean and differential light-shifts φ_{AC} and δ_{AC} given in equations 2.13 and 2.12. The mean shift cancels out in the total interferometer phase due to the symmetry of the sequence. This is unfortunately not the case for the differential term. This chapter will briefly summarize the theoretical

description of the differential level shift δ_{AC} on which the cancellation of this potentially important systematic effect is based. Refer to, e.g. [82, 80] or [83] for a more comprehensive description of this topic.

In order to do this accurately it is best to regard the full hyperfine structure of the atoms instead of simplified three-level system from figure 2.1. Adiabatically eliminating the excited states as in chapter 2.1 yields again an effective two-level Hamiltonian with adapted expressions for Ω_{keff}, Ω_e^{AC} and Ω_g^{AC}. We again skip this step and retrieve the final result as in [82, 80]:

$$\Omega_{\mathrm{eff}} = \sum_m \frac{\Omega^*_{m,g1}\Omega_{m,e2}}{2\,(\Delta - \Delta_m)} \quad \Omega_{m,jk} := -\langle m|\boldsymbol{d}\cdot\boldsymbol{E}_k|j\rangle\,\hbar \tag{2.21}$$

$$\Omega_g^{\mathrm{AC}} = \sum_m \frac{|\Omega_{m,g1}|^2}{4\,(\Delta - \Delta_m)} + \frac{|\Omega_{m,e2}|^2}{4\,(\Delta - \omega_{eg} - \Delta_m)} \tag{2.22}$$

$$\Omega_e^{\mathrm{AC}} = \sum_m \frac{|\Omega_{m,e2}|^2}{4\,(\Delta - \Delta_m)} + \frac{|\Omega_{m,g1}|^2}{4\,(\Delta + \omega_{eg} - \Delta_m)} \tag{2.23}$$

Combining equations 2.22, 2.23 and equation 2.12 yields, after some algebra

$$\delta_{\mathrm{AC}} = \Omega_e^{AC} - \Omega_g^{AC} =: \frac{\alpha}{4}|\Omega_1|^2 - \frac{\beta}{4}|\Omega_2|^2 \tag{2.24}$$

The ratio α/β is defined by the following equation such that δ_{AC} vanishes if

$$\frac{\alpha}{\beta} := \frac{I_2}{I_1} = \frac{\frac{1}{8(\Delta-\Delta_2+\omega_{eg})} - \frac{1}{8(\Delta-\Delta_2)} + \frac{1}{5(\Delta-\Delta_3+\omega_{eg})} + \frac{1}{120(\Delta+\omega_{eg})} - \frac{5}{24\Delta}}{\frac{1}{8(\Delta-\Delta_2-\omega_{eg})} - \frac{1}{8(\Delta-\Delta_2)} - \frac{1}{5(\Delta-\Delta_3)} + \frac{5}{24(\Delta-\omega_{eg})} - \frac{1}{120\Delta}} \tag{2.25}$$

The differential light shift can therefore be nulled for a given detuning Δ by adjusting the ratio of the single photon Rabi frequencies, which are determined simply through the light intensity of the Raman frequency components. This is the approach chosen to minimize light shifts in this experiment as detailed in chapter 6.4.1.

For other different intensity ratios δ_{AC} can be parametrized as a function of α/β and Ω_{eff} as detailed and verified experimentally in [80]. The resulting interferometer phase shift, however, dependents on additional parameters such as the temperature of the atomic cloud and Raman laser beam waist and is given explicitly in [83, 82]. Note, however, that significant uncertainties remain as these parameters are often not known well enough in the real experiment.

2.3 Path Integral Description

For high precision gravimetry on the order of 10^{-9} g, equation 2.20 still has to be corrected for vertical gravity gradients. This chapter will therefore introduce a more general approach based on Feynman path integrals [84].

The description of the atomic wave packets as a closed set of momentum plane-wave states as in equation 2.3 was valid due to the momentum conservation in a falling reference frame which, in the presence of large gravity gradients, can no longer be justified. This is illustrated by the gradient induced gravity changes of 10^{-7} g over a free fall distance of 30 cm, which is two orders of magnitude larger than the desired accuracy. For

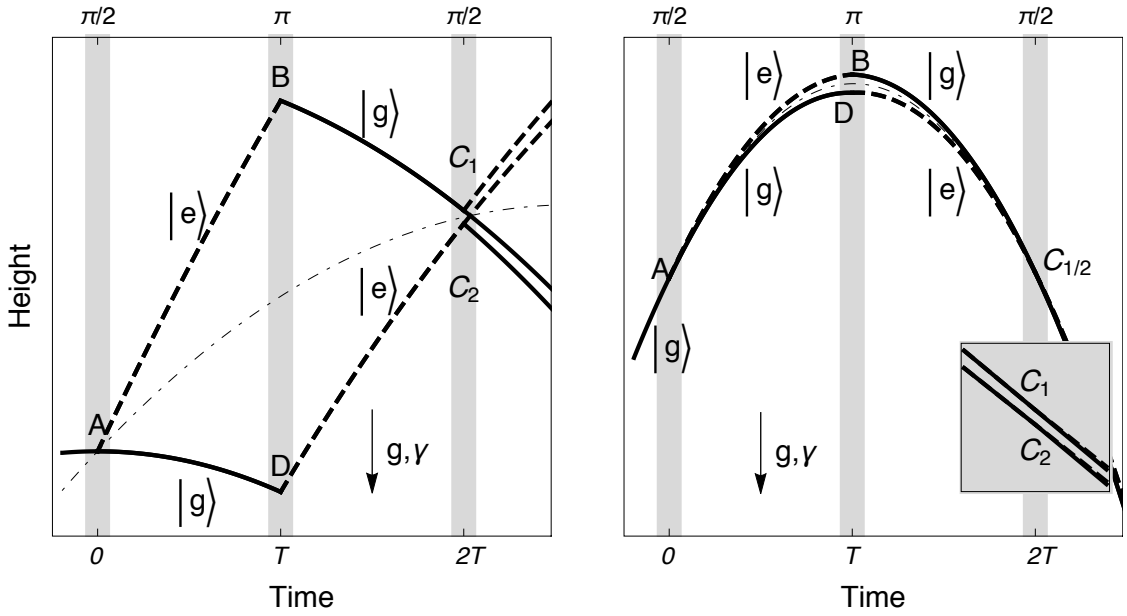

Figure 2.2: Mach-Zehnder atom interferometer under the influence of a vertical gravity gradient. **Left:** schematic representation of the path splitting C_1C_2 at the final beam splitter. **Right:** trajectories for the experimental parameters during this work. The path splitting, even though magnified tenfold here, is much smaller than the free fall distance.

the relatively simple three-pulse interferometer sequence used during this work, Feynman path integrals are one convenient method to calculate the phase accumulated along both interferometer arms. This has been successfully employed to determine the phase shift of atomic gravimeters and gyroscopes under the presence of gradients and rotations [84, 11, 85] and will be summarized here for atomic gravimeter applications.

Due to the very different nature of the atom-light interaction during the Raman pulses and the free propagation in between, the total interferometer phase is usually split into three contributions [84, 86]

$$\Phi_{\text{tot}} = \Phi_{\text{laser}} + \Phi_{\text{prop}} + \Phi_{\text{sep}} \tag{2.26}$$

where the first term Φ_{laser} denotes the phase contribution during the atom-light interaction as summarized in table 2.1 and equation 2.18. Because this part continues to dominate here we will evaluate it first and look at the two remaining terms later.

In order to retrieve the path for a particle in a gravitational field with a linear gradient γ we look at the corresponding Lagrangian

$$L(z, v) = \frac{mv^2}{2} - mg_0 z + \frac{m}{2}\gamma z^2 \tag{2.27}$$

where the coordinate axis points upwards, g_0 is the gravitational acceleration at the coordinate origin and $g_0, \gamma > 0$ are defined positive for the normal conditions on the surface of earth. The classical equation of motion can then be determined using the Euler-Lagrange

equation which results in hyperbolic trajectories

$$z(t) = \frac{g_0}{\gamma} + \left(z_0 - \frac{g_0}{\gamma}\right)\cosh\left(\sqrt{\gamma}t\right) + \frac{v_0 \sinh\left(\sqrt{\gamma}t\right)}{\sqrt{\gamma}} \tag{2.28}$$

$$\approxeq -\frac{g_0}{2}t^2 + v_0 t + z_0 + \gamma t^2\left(-\frac{1}{24}g_0 t^2 + \frac{1}{6}v_0 t + \frac{1}{2}z_0\right) \tag{2.29}$$

The values z_0, v_0 denote the atomic position and velocity during the first interferometer pulse, e.g. $z_0 = z(t_1)$. Evaluating the local light phase for the new trajectories again gives Φ_{Laser} as performed previously in equation 2.19, but now also includes the splitting of the paths ABC_1 and ADC_2. This is executed most easily using computer algebra with a piecewise path definition of the interferometer sequence, where the initial parameters of each section are defined by the final position and velocity of the previous section. It yields for upwards directed photon recoil

$$\Phi_{\text{laser}} = \left(\phi^A_{\text{eff},1} - \phi^B_{\text{eff},2} + \phi^{C_1}_{\text{eff},3}\right) - \left(\phi^D_{\text{eff},2}\right) \tag{2.30}$$

$$= \frac{4k_{\text{eff}}}{\gamma}\sinh^2\left(\frac{T\sqrt{\gamma}}{2}\right)\left[(z_0\gamma - g_0)\cosh\left(T\sqrt{\gamma}\right) + v_0\sqrt{\gamma}\sinh\left(T\gamma\right)\right] \tag{2.31}$$

$$= k_{\text{eff}}T^2\left[g_0 + \gamma\left(\frac{7}{12}g_0T^2 - v_0T - z_0\right) + O(\gamma^2)\right] \tag{2.32}$$

In the limit of vanishing recoil velocity, or infinite atomic mass, this result actually gives the complete interferometer phase Φ_{tot} and will only be corrected bellow to account for the splitting of the interferometer arms. The measured gravity value in the square brackets is in fact equivalent to measuring the position of a free falling test mass at three points and shows the similarity of this atom interferometer and a classical absolute gravimeter.

In order to obtain the complete interferometer phase including the arm splitting, we now turn our attention to the last two terms in equation 2.26. Φ_{prop} originates from the free propagation of the wave-packets along both interferometer arms and can be calculated by integrating the classical action $S_\Gamma = \int_\Gamma L\left(\mathbf{r}(t), \mathbf{v}(t)\right) dt$ along both arms shown in figure 2.2[1]. Note that in the presence of gradients, the space-time path of both arms don't generally meet at the last pulse. The last term Φ_{sep} is associated with the separation of the interferometer output ports and closes this gap. We have [84]:

$$\Phi_{\text{prop}} = \left(S_{\text{ABC}_1} - S_{\text{ADC}_2}\right)/\hbar \tag{2.33}$$

$$\Phi_{\text{sep}} = p_0 \cdot \left(z_{\text{C}_2} - z_{\text{C}_1}\right)/\hbar \tag{2.34}$$

Evaluating $\Phi_{\text{prop}} + \Phi_{\text{sep}}$ with the Lagrangian 2.27 along the exact paths from equation 2.28 and summing up with the light phase Φ_{laser} from equation 2.31 yields the total interferometer phase shift which, to first order in γ, reads

$$\Phi_{\text{tot}} = k_{\text{eff}}T^2\left[g_0 + \gamma\left(\frac{7}{12}g_0T^2 - \left(v_0 + \frac{\hbar k_{\text{eff}}}{2m}\right)T - z_0\right) + O(\gamma^2)\right] \tag{2.35}$$

This result is identical to equation 2.31 aside from the replacement $v_0 \to \bar{v}_0 := v_0 + \frac{\hbar k_{\text{eff}}}{2m}$ which represents the mean path between both interferometer arms depicted as dot-dashed

[1] This approach is formally correct only for Lagrangians up to second order in z,v [84].

lines in figure 2.2. This results in a small correction of around 5 mrad or 5×10^{-10} g for the pulse separation time $T = 0.26$ s used predominantly during this work. Note that the same result could have been achieved using a perturbative approach in which the vertical gradient is added to the Lagrangian as a perturbation such that $L = L_0 + \epsilon L_1$. The corresponding phase correction would then be given by the action integral 2.33 of L_1 along the *unperturbed* trajectory without gradient as detailed in [11, 84].

In order to assign the measured gravity value to a certain height in the laboratory reference frame, we define the measured gravity value g_{meas} valid at the effective measurement height z_{eff} defined using equation 2.35

$$g_{\text{meas}} := \frac{\Phi_{\text{tot}}}{k_{\text{eff}} T^2} = g_0 - \gamma z_{\text{eff}} \tag{2.36}$$

$$z_{\text{eff}} := -\frac{7}{12} g_0 T^2 + \bar{v}_0 T + z_0 \tag{2.37}$$

which can be used in order to transfer the measured gravity value to, e.g. floor height, if z_0,$\bar{v}_0$ are known. More general approaches have been developed to calculate the phase shift and contrast of more complex atom interferometer geometries and under more complex or more realistic conditions. Instead of evaluating the path integrals, it is possible to directly calculate the wave-packet evolution along paths using propagators and a ABCD matrix formalism detailed in [87, 88]. So-called representation free descriptions of the phase shift based on operator algebra have recently been developed and extended to cover general situations including non-inertial reference frames and arbitrary interferometer sequences [89, 90]. Neither of these approaches, however, offer a real advantage for the relatively simple case presented here and will therefore not be discussed in detail.

2.4 Sensitivity Function

In order to estimate the effect of Vibration and Raman phase noise on the total interferometer phase and to derive an expression for it that includes the finite length of the Raman pulses in a real experiment, one can use the sensitivity function introduced in [91]:

$$g(t) := \lim_{\delta\phi \to 0} \frac{\delta\Phi\left(\delta\phi, t\right)}{\delta\phi} \tag{2.38}$$

It quantifies the effect of a phase jump $\delta\phi$ at time t during and in between the three Raman pulses[2] on the total interferometer phase in equation 2.18. For the three-pulse Mach-Zehnder sequence described above and with the second pulse centered at $t = 0$, $g(t)$ is an odd function and for $t > 0$ given by

$$g(t) = \begin{cases} \sin\left(\Omega_r t\right), & 0 < t < \tau \\ 1, & \tau < t < T + \tau \\ -\sin\left(\Omega_r \left(T - t\right)\right), & T + \tau < t < T + 2\tau \\ 0, & t > T + 2\tau \end{cases} \tag{2.39}$$

where τ gives the length of the first and third pulse ($\Omega_r \tau = \pi/2$). A plot of the function is shown in figure 2.3

[2] E.g., a phase jump during the first half would affect both ϕ^2_{eff},ϕ^3_{eff} and result in a negative phase shift whereas a phase jump in the later half results in a positive overall phase shift.

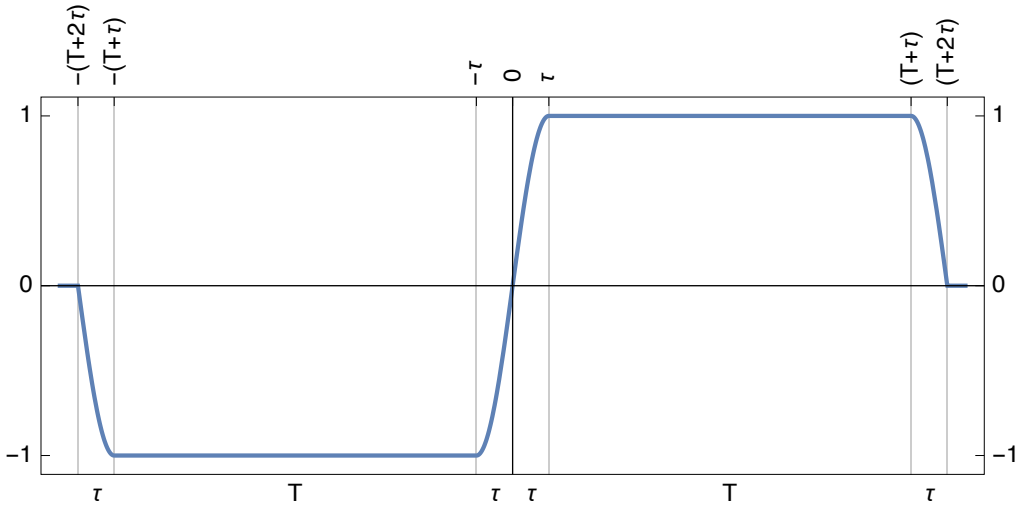

Figure 2.3: Sensitivity function $g(t)$ of a Mach-Zehnder atom interferometer sequence centered around $t = 0$ as defined in equation 2.39.

2.4.1 Finite Raman Pulse Duration

One can now deduce the total interferometer phase by integrating the Raman phase variations $\partial_t \phi$ over the entire interferometer sequence

$$\Delta\Phi = \int_{-(T+2\tau)}^{(T+2\tau)} g(t) \frac{d\phi(t)}{dt} dt \tag{2.40}$$

When combining this with the local Raman phase from equation 2.19 one obtains a corrected form of equation 2.20 that accounts for the finite length of the Raman pulses [74]

$$\Delta\Phi = (\alpha - \boldsymbol{k}_{\text{eff}} \cdot \boldsymbol{g}) (T + 2\tau) \left(T + \frac{4\tau}{\pi} \right) \tag{2.41}$$

This was confirmed experimentally using GAIN and yielded excellent agreement within the measurement resolution of better than 10^{-9} g. Note that the interferometer phase in equation 2.41 does not scale proportionally to the space-time area enclosed by the Mach-Zehnder sequence anymore, which is proportional to $(T + 2\tau)T$. See [92] for an extended formalism and detailed description of this topic.

For the practical application as atomic gravimeter, however, this is of little interest as the atom interferometer is usually operated on the central, or dark, fringe around $\Delta\Phi \approx 0$ which is insensitive to this scaling. The next chapter will therefore turn to the estimation of phase noise using the sensitivity function.

2.4.2 Raman Laser Phase Noise

The sensitivity function can also be used to estimate the effect of Raman phase noise on the interferometer phase. The transfer function from phase noise of the Raman laser to the interferometer output is derived from the sensitivity function Fourier transform $G(\omega)$

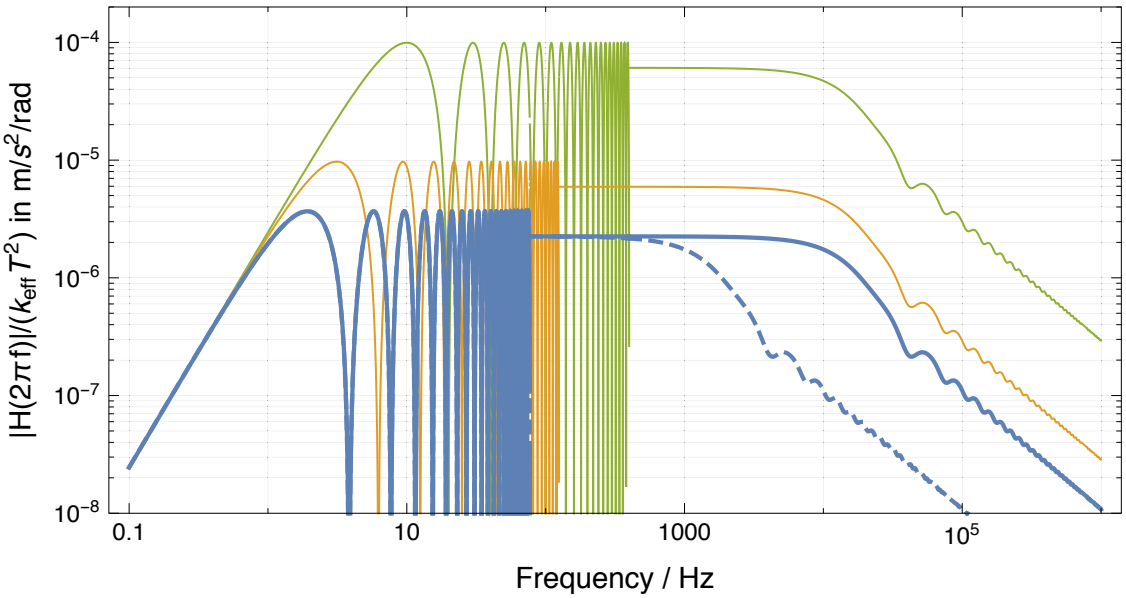

Figure 2.4: Normalized interferometer transfer function showing the influence of Raman phase noise on $\sigma^{\text{rms}}_{g,\text{Ra}}$. The GAIN setting $T = 0.26\,\text{s}$ (blue) is shown for two values $\tau = 30\,\mu\text{s}$ (solid) and $\tau = 300\,\mu\text{s}$ (dashed), yielding different low-pass corner frequencies. Yellow and green lines represent shorter pulse separations of 0.16 s and 0.05 s, respectively, which demonstrates that the relative phase noise sensitivity increases for shorter T values.

and given by [91]

$$H(\omega) = \omega G(\omega) = \frac{4i\omega\Omega_r}{\omega^2 - \Omega_r^2} \sin\left(\frac{\omega\,(T+2\tau)}{2}\right)\left[\cos\left(\frac{\omega\,(T+2\tau)}{2}\right) + \frac{\Omega_r}{\omega}\sin\left(\frac{\omega T}{2}\right)\right] \tag{2.42}$$

which is a highly oscillatory function with zeros at frequencies $f_k = k/\,(T+2\tau)$. It further shows a first order low-pass behavior due to the finite pulse length with an effective corner frequency of $f_0 = \Omega_r/(2\pi\sqrt{3})$. Assuming that the Raman phase noise is given as the power spectral density (PSD) $S_\phi(\omega)$, the resulting root-mean-square (rms) interferometer phase noise between successive measurements can be calculated by evaluating

$$(\sigma^{\text{rms}}_{\Phi})^2 = \int_0^\infty |H(\omega)|^2 S_\phi(\omega) d\omega \tag{2.43}$$

$$\left(\sigma^{\text{rms}}_{g,\text{Ra}}\right)^2 = \int_0^\infty \frac{|H(\omega)|^2}{\left(k_{\text{eff}}T^2\right)^2} S_\phi(\omega) d\omega \tag{2.44}$$

where $\sigma^{\text{rms}}_{\Phi}$ is in units of rad and $\sigma^{\text{rms}}_{g,\text{Ra}}$ in m/s^2 due to the normalization by $k_{\text{eff}}T^2$. Figure 2.4 shows the latter in order to demonstrate that the overall relevance of Raman laser phase noise for the gravity measurement decreases for larger pulse separations T.

2.4.3 Vibration Phase Noise

Vibrations of optical elements guiding the beam from the laser to the physics package are a primary concern for gravimeters and inertial sensors in general, even more than phase

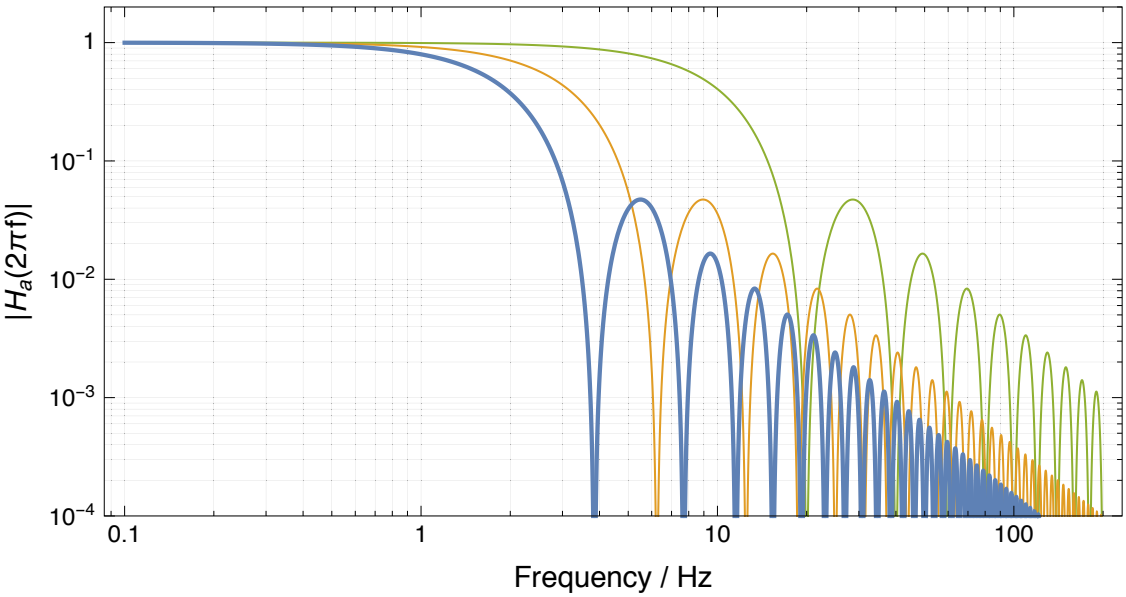

Figure 2.5: Interferometer transfer function from mirror vibrations to interferometer/gravimeter noise, showing oscillatory plus low-pass behavior. Different colors correspond to pulse spacings T of 0.26 s (blue), 0.16 s (yellow) and 0.05 s (green), respectively.

noise introduced by the Raman phase-locked loop (PLL) components,

In the setup described here, both Raman frequency components are guided to the physics package along the same beam and interact with the atoms in a retro-reflected configuration detailed in chapter 3.1.4. Only vertical displacements δz of the retro-reflection mirror therefore play a role and cause a Raman phase shift $\delta\phi = k_{\text{eff}}\,\delta z$. In order to calculate the effect of uncorrelated vibration noise of the mirror, it is again convenient to express it as a power spectral density in acceleration units $S_a(\omega)$. This corresponds to effective Raman laser phase noise PSD given by

$$S_\Phi = \frac{k_{\text{eff}}^2}{\omega^4} S_a \tag{2.45}$$

Note that, for mirror vibration frequencies where the condition $\omega \ll \Omega_r$ is usually met, equation 2.42 can be simplified to

$$H(\omega) = -4i \sin^2(\omega T/2) \tag{2.46}$$

When combining equations 2.46 and 2.45 after dividing by $k_{\text{eff}}T^2$ in order to change to acceleration units, we can write the transfer function H_a from mirror vibrations to gravimeter or acceleration noise as

$$H_a(\omega) := \frac{1}{k_{\text{eff}}T^2}\frac{k_{\text{eff}}^2}{\omega^4} H(\omega) = -\frac{4i}{(\omega T)^2}\sin^2(\omega T/2) \tag{2.47}$$

which is again an oscillatory function with zeros at frequencies $f_k = k/T$ and a low pass behavior at with a corner frequency of around $1/T$. Longer interferometer times

T therefore reduce the sensitivity to higher frequency vibrations. Note, however, that for larger T the absolute phase noise increases quadratically so that the vibration noise expressed in rad grows rapidly. Without countermeasures such as a vibration isolation system, this quickly leads to washed out interference fringes and loss of phase information. These properties of equation 2.47 were the main driving forces for the design of the active vibration isolator described in chapter 3.2.

Analogous to equation 2.44, $H_a(\omega)$ can be used to estimate the rms noise of successive interferometer measurements caused by parasitic mirror vibrations. If the spectral density of the mirror vibrations is measured by an appropriate sensor as described in chapter 3.2 it can be readily calculated with

$$\left(\sigma_{g,\mathrm{vib}}^{\mathrm{rms}}\right)^2 = \int_0^\infty |H_a(\omega)|^2 S_a(\omega) d\omega \tag{2.48}$$

Moreover, the sensitivity function 2.38 can be used directly in this case in order to derive the vibration induced phase as detailed in chapter 3.2.2.

Summary

This chapter gave a brief introduction of the atom-light interaction during stimulated Raman transitions and derived the atom interferometer phase with path integrals including all necessary corrections to measure the local gravity value with an accuracy of better than $10^{-9}\,\mathrm{g}$. Furthermore, the sensitivity function as a general tool to describe the total interferometer phase and the influence of the most important noise sources was introduced. Chapter 3 will now give a detailed account of the transportable experimental apparatus that was used for the gravity measurements presented later on in this thesis.

Chapter 3

Experimental Setup

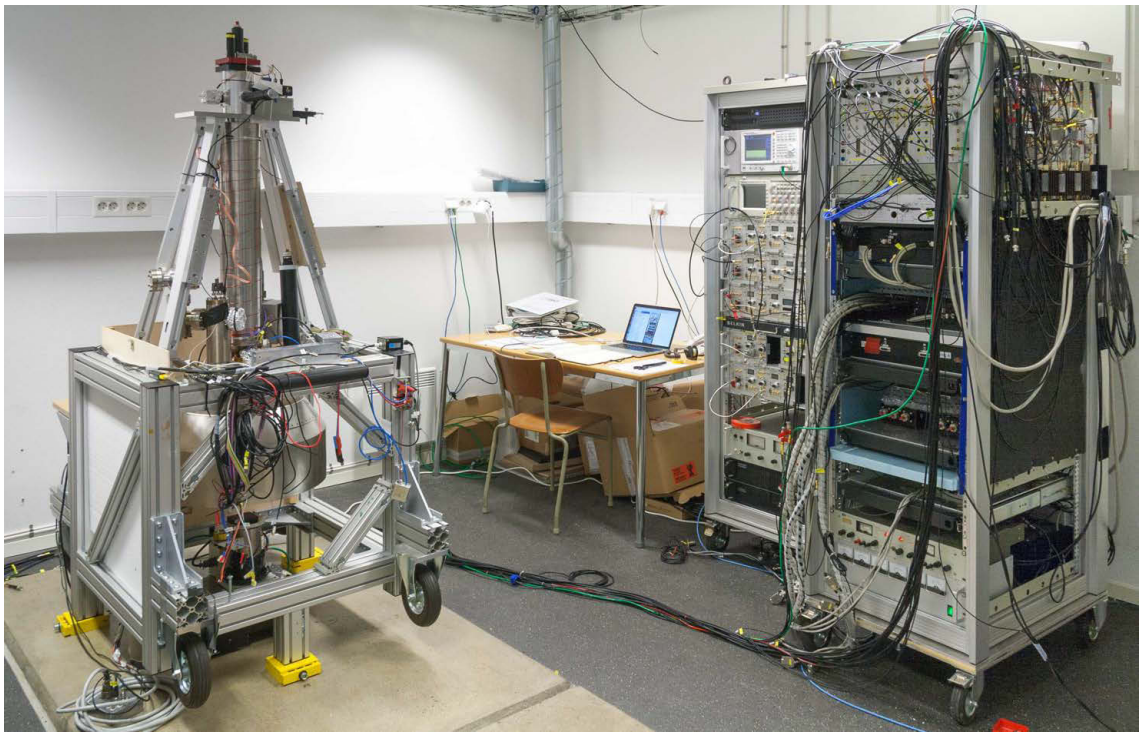

Figure 3.1: Photograph of the completed GAIN setup during the second mobile measurement campaign in Onsala, Sweden. From left to right: Physics package, electronics and control rack, laser rack.

The experimental setup used during this work is a transportable atom interferometer which was specifically designed to perform high precision gravity measurements in a mobile and robust package. It was originally conceived and built as part of a European initiative to explore future inertial atomic quantum sensors (FINAQS). In order to improve its mobility the instrument was separated into three separable units as shown in figure 3.1. Each unit has a size of less than $(1\times1\times2)\,\mathrm{m}^3$ in order fit through standard doors and can be moved around on built-in wheels by one to two people. The first unit is the

physics package containing the vacuum system were the actual gravity measurement takes place. A 19" rack containing the laser system forms the second unit which delivers all necessary optical frequencies to the physics package through optical fibers. All systems are powered and controlled from the third unit which is another 19" rack also containing two computers for sequence control and data storage, respectively. The first version of the instrument was completed and described in earlier works [82, 93, 94], and the first gravity measurements were conducted at Humboldt Universität zu Berlin in 2010. In order to reach the original goal of performing gravity measurements on remote sites beyond the state-of-the-art, several improvements of the existing hardware and additional subsystems had to be implemented as part of this work, such as a Tip/Tilt mirror or a magnetic shield around the MOT-chamber. This chapter includes a short, but comprehensive description of the overall experimental apparatus with references to previous results, as well as a detailed analysis of subsystems that were added or modified as part of this work.

3.1 Physics Package

The experimental apparatus is built around an atomic fountain with an elongated interferometry section and vertical Raman beams retro-reflected by a mirror below the vacuum system. This well-known retro-reflection architecture has the advantage that phase-noise of the Raman beams due to vibrations of all optical elements are common mode and cancel out in the gravity measurement, with the exception of the retro-reflection mirror which provides the inertial reference. The fountain chamber was designed for uncompromising gravimeter performance using a relatively long, magnetically shielded interferometer zone, but also with flexibility in mind providing a total of 42 view ports. The physics package can be divided into four functional parts as shown in figure 3.2. The first part is the elongated interferometer zone on top, the second the state selection and detection zone in the middle and third the MOT region in the bottom of the vacuum system which provides the pulsed source of laser-cooled Rubidium. Finally, the Raman retro-reflector on the vibration isolation system below the vacuum system. A schematic overview of these functional elements is depicted in figure 3.2 and each part will be reviewed in the following sub-chapters.

3.1.1 Vacuum System

The main part of the physics package is the elongated, roughly 1.15 m tall atomic fountain UHV chamber shown in figure 3.2. The UHV environment is necessary to prevent atom losses during the course of a measurement due to interactions with the background gas. Most parts of the vacuum system are milled from solid blocks of Titanium alloy due to its advantageous mechanical and vacuum properties. Its low specific conductivity furthermore enables faster decay of eddy currents than in an equivalent welded steel chamber. Conflat (CF) flanges and Indium sealed windows keep the integrated leak rate small enough to reach a base pressure of a few 10^{-10} hPa despite the large number of windows. A 20 l/s ion pump and a Titanium sublimation pump attached to the detection region maintain these conditions (not shown in figure 3.2). See [93] for a more detailed description of the vacuum system.

The Rubidium source for the fountain was originally provided by dispensers from SAES getters [93]. Unfortunately, they were completely depleted during the middle of this

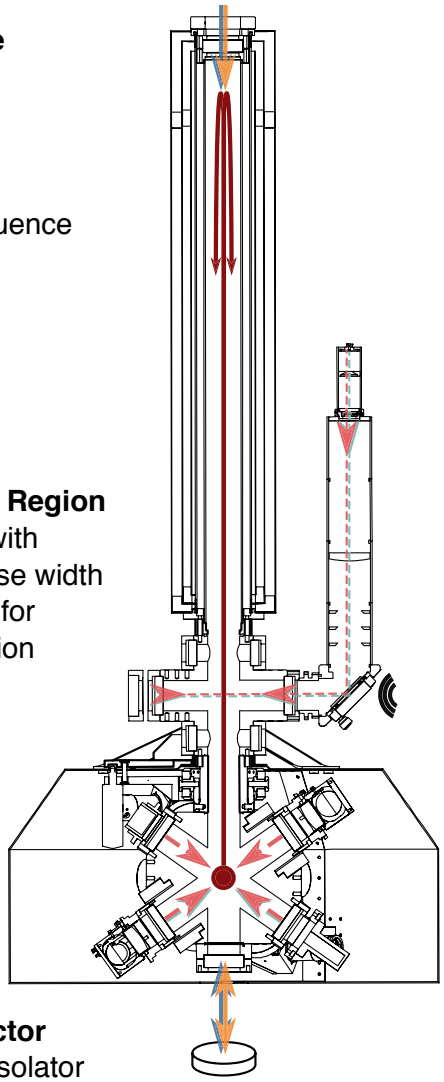

Figure 3.2: Overview of the main functional parts of the vacuum chamber and physics package. Four different functional segments are annotated top to bottom and described in the text.

work and had to be replaced in order to conduct the second mobile gravity measurement successfully. The new dispensers by the company Alvatec and have a strongly increased capacity[1] compared to the previously used models. They emit Rubidium in its natural isotopic abundances and feature significantly reduced emission of spurious elements during operation. This reduced the vacuum pressure during fountain operation by nearly one order of magnitude with respect to the previous sources to a few times 10^{-10} hPa while still providing sufficient Rb to load the MOT within 0.6 s.

A replacement of the dispenser assembly without breaking the vacuum had been anticipated during the construction of the vacuum chamber which is why it was separated using a UHV gate valve[2]. Unfortunately, the valve's Viton seal had been damaged which, according to the manufacturer, was most likely caused by accelerated aging under the constant exposure to chemically reactive Rubidium. Performing this switching operation without compromising the UHV conditions in the main chamber therefore turned out to be challenging. By working in a glove-bag filled with dry nitrogen atmosphere evaporated from a LN_2 dewar, a renewed bake-out could nevertheless be avoided.

3.1.2 MOT Chamber

The bottom section of the chamber contains a MOT which prepares the laser-cooled atoms for the fountain [81]. Six circularly polarized laser beams with a diameter of 30 mm ($1/e^2$) in a 1-1-1 configuration intersect at the MOT center. In this arrangement every beam encloses an angle of 54.7 ° to the vertical. A magnetic quadrupole field is generated by two air-cooled anti-Helmholtz coils which results in a central field gradient of approximately 0.5 mT/cm [93] at a current of 8 A. The ^{87}Rb atoms are released into the chamber through resistive heating of the Rubidium dispensers and loaded into the MOT from background gas. The Rb pressure in the vacuum system can be finely controlled through variations of the dispenser heating current, which is applied continuously during fountain operation. The MOT chamber furthermore provides a tip/tilt mechanism through a vacuum bellow which is essential for fine-tuning of the launch direction as described in [93]. In order to compensate for background magnetic fields, bias coils were implemented and fine-tuned in order to achieve the required µK temperatures during the moving molasses launch. In order to monitor the size and shape of the MOT during loading and launch, three triggered CMOS cameras are attached to the MOT chamber at different angles. The final atom number in the MOT before launch can be estimated from fluorescence captured by the cameras to around 10^9 ^{87}Rb atoms.

Magnetic Shield Implementation

During this work a magnetic shield was designed and implemented around the MOT-Chamber. It serves the two interrelated purposes of shielding the MOT from background magnetic fields and isolating the rest of the set-up from switching fields generated by the MOT-coils, which turned out to have a particularly detrimental effect on gravity observations through the vibration isolator right underneath the MOT chamber as detailed in chapter 6.5.1. Due to the comparatively small dimensions of the GAIN MOT chamber, two issues had to be overcome while designing the magnetic shield. First, the shield had to

[1] 4 dispensers containing 35 mg of Rubidium each
[2] VAT Mini UHV gate valve, Series 010

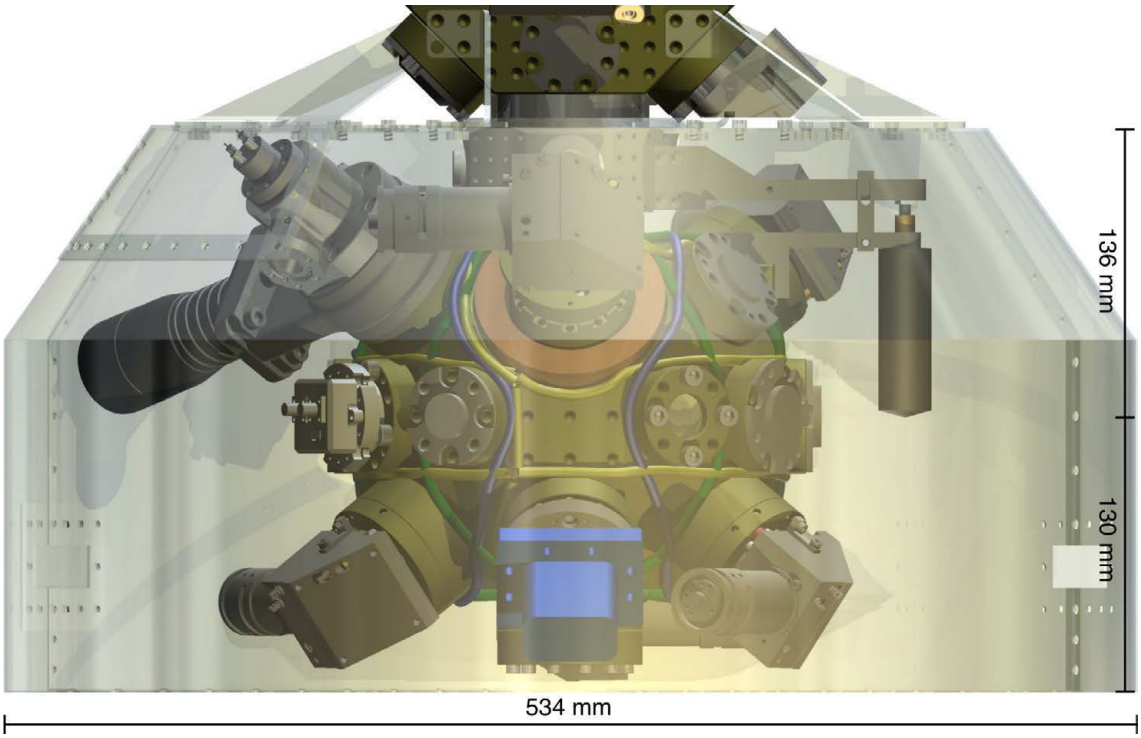

(a) CAD drawing of the MOT region with magnetic shielding (shown transparent). Several important functional elements are shown: Rubidium dispenser with gate valve (top left), vacuum bellow actor (top right), compact MOT telescopes (distributed in 1-1-1 configuration), microwave adapter (center, blue). The MOT bias field coils, wound around the chamber, are rendered as green(x), blue(y) and yellow(z) tubes.

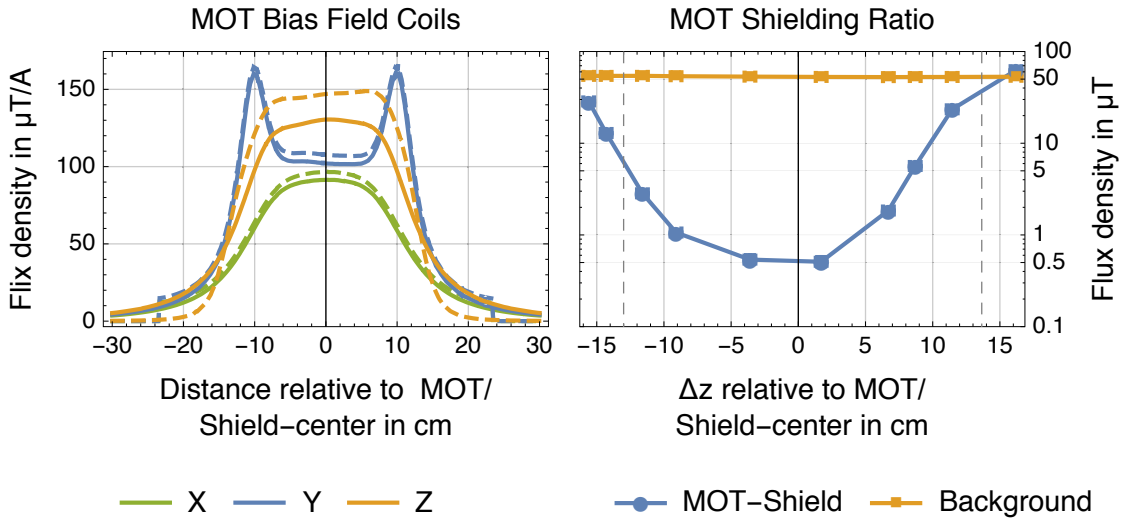

(b) Bias field simulation for the exact coil geometry shown above. Solid/dashed lines indicate the field distribution without/with MOT-shield, respectively. Spurious gradients at the center are smaller than 2 µT/(cm A).

(c) Magnetic field measurement on the central MOT shield axis, obtained with a 3D flux-meter. Background fields at the center/MOT are suppressed by a factor of 100. Dashed vertical lines indicate the upper/lower shield limits.

Figure 3.3: GAIN MOT overview. See also appendix A for a photograph of the running MOT system without magnetic shield.

be engineered tightly around the compact vacuum joint in order to provide good shielding characteristics at the MOT position without constraining the vacuum bellow. Second, the previous bias field coils used until then were far too bulky to fit into the shield and had to be redesigned completely.

The first issue was addressed with a cylindric one-layered Mu-Metal shield carefully designed to fit around the MOT section of the vacuum chamber with minimal opening at both top and bottom for the vacuum bellow and Raman beam, respectively. It is shown in the bottom of figures 3.1 and 3.2 and detailed in the CAD drawing in figure 3.3. In order to enable quick access to the MOT chamber it consists of two removable segments. One extension port close to the dispenser assembly enables future additions to the MOT chamber, such as a 2D-MOT, in order to enable faster MOT loading [95, 96]. The vacuum joint actors were furthermore adapted to allow remote motorized tip/tilt operation, which was necessary as the magnetic shield otherwise prevents access.

In order to provide a homogeneous bias field at the location of the MOT without the need for bulky Helmholtz coil pairs, the respective coils were wound directly around the MOT chamber. A preceding FEM simulation of the resulting field was used to find a configuration with 4 coils for each axis that delivers reasonable homogeneity of the bias field despite the otherwise unsuitable geometry of the MOT chamber. See figure 3.3 for a CAD drawing of the final MOT setup and the simulated magnetic field distribution.

The measured shielding behavior displayed in figure 3.3c shows a reduction of background fields of around two orders of magnitude at the location of the MOT, which agrees well with FEM simulation. This enables mG background fields without active compensation and almost supersedes the need for a homogeneous bias field altogether. This is confirmed by the atomic fountain optimization where the bias coils are now only used to separate the magnetic sub-levels during velocity selection.

3.1.3 Detection and State-Selection Chamber

The central section of the vacuum chamber consists of an octagonally shaped region, which provides twelve access ports on three horizontal(x-y) planes and four diagonal view-ports on vertical(x-z) plane. See figure 3.4 for cut-view schematics of the overall geometry. Both vacuum pumps are mounted along a horizontal axis in close proximity to the detection area. This minimizes the background gas pressure compared to other parts of the chamber which benefits the signal to background ratio during detection. To facilitate the state-selection a microwave adapter is mounted along the pumping axis which, compared to a previous configuration perpendicular to this axis, frees up one more axis for optical access. Light from an auxiliary fiber coupled to both repump- and cooling-laser enter the chamber through a diagonal view-port to implement resonant blow-away pulses for both hyperfine ground states. Three additional diagonal view-ports are available and could be used, e.g., for the implementation of advanced detection schemes or cooling methods such as Raman sideband cooling.

The fluorescence detection system consists of a resonant collimated beam which is retro-reflected in the central detection zone. The beam has a diameter of around 50 mm ($1/e^2$) and can be stopped down using a diaphragm aperture to a diameter D_{det} that can be varied between 5–30 mm. Both $F = 1$ and $F = 2$ resonant light can be coupled into this beam through independent AOMs, which allows to facilitate the state-selective detection sequence. The fluorescence light of the atoms in the detection area is imaged onto the

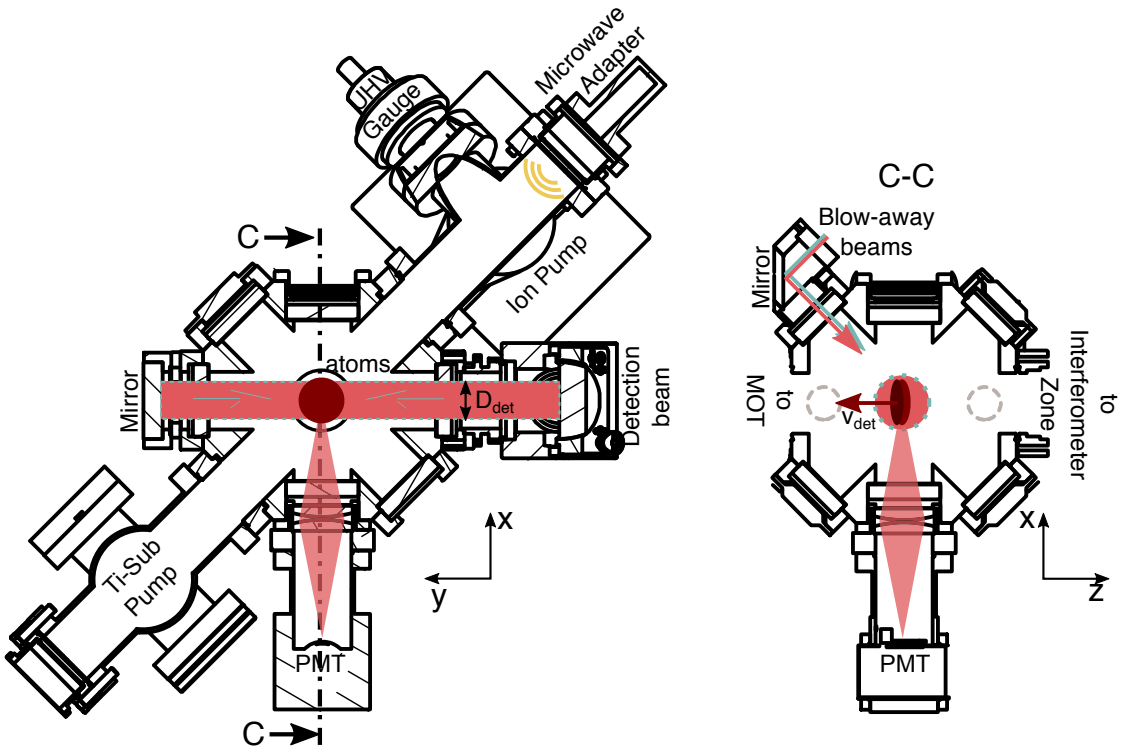

Figure 3.4: State-selection and detection region in simplified horizontal(left) and vertical(right) cut-views. The fluorescence detection system, blow-away beams and microwave adapter for state-selection and vacuum pumps are depicted schematically. Free diagonal view-ports for future modification are indicated on the vertical cut-view.

PMT by two plano-convex lenses[3] in a scale-preserving 1f-1f configuration, collecting a solid angle of around $4\pi \times 0.017\,\mathrm{sr}$. An aperture with 4 mm horizontal width in front of the PMT restricts the size of the detection region and minimizes stray light in combination with a conically-shaped beam-dump behind the opposite view-port. In order to measure the relative population of both hyperfine states, a state-selective detection sequence is used which will be detailed in chapter 4.4.

3.1.4 Interferometer Zone and Raman Beams

The section in which the atom interferometry takes place consists of a magnetically shielded, cylindrical region with a length of 0.7 m as indicated in figure 3.2. Both Raman beam frequency components enter the chamber from above through the same telescope with a beam diameter of 30 mm ($1/e^2$) in the same linear polarization. They are then retro-reflected through a quarter wave-plate in the orthogonal linear polarization on the way back to the Raman telescope (lin⊥lin configuration). Since the quantization axis provided by the vertical magnetic bias field is parallel to the Raman wave-vector $\boldsymbol{k}_{\mathrm{eff}}$, this configuration only drives $\sigma^{\pm}$ transition as indicated in figure 3.5. Counter-propagating beam pairs then drive Doppler-sensitive $\sigma^{+}\sigma^{+}$ and $\sigma^{-}\sigma^{-}$ transitions with $\Delta m = 0$ in

[3] PMT R10699, Hamamatsu; Lens: clear aperture 38 mm, focal length 70 mm

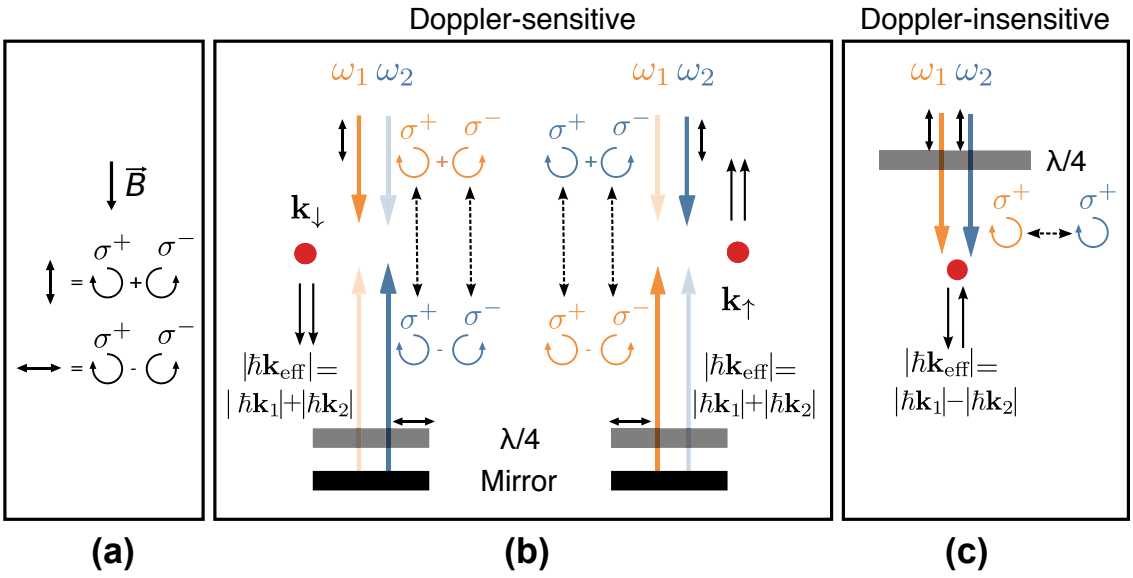

Figure 3.5: Raman polarization schemes used in GAIN. **(a)** Vertical quantization axis and the decomposition of linear into circular polarizations. **(b)** Doppler-sensitive transitions in the (lin⊥lin) scheme for both down- and upwards directed photon recoil, see text for more details. **(c)** Doppler-insensitive Raman transitions can be implemented by inserting a quarter wave-plate behind the Raman telescope and blocking the retro-reflecting mirror. Modified figure, original courtesy of V. Schkolnik.

order to couple the magnetically insensitive $|F = 1, m_F = 0\rangle \leftrightarrow |F = 2, m_F = 0\rangle$ states[4]. The effective two-photon Rabi-frequency for transitions $\Delta m \neq 0$ cancels out due to the respective Clebsch-Gordon coefficients. Doppler-insensitive transitions in the lin⊥lin configuration are suppressed by negative interference between $\sigma^+\sigma^+$ and $\sigma^-\sigma^-$ transitions and, additionally, by the detuning of the Raman frequency to account for the atomic Doppler-shift moves those transitions out of resonance during the interferometer sequence. See [97] for a quantitative description of the effective Rabi frequencies between different magnetic sub-levels.

In order to avoid level shifts due to magnetic fields, the interferometer region is carefully shielded by a three-layer Mu-metal shield which reduces stray magnetic fields by a factor of about 1000 [93]. For the Raman pulses during the interferometer sequence to work properly, it is necessary to keep the quantization axis of the atoms aligned with the propagation vector of the Raman beams. This is done using a helical coil set in a precisely wound grove which generates a highly homogeneous bias field of approximately 4 µT at a current of 9.5 mA.

3.2 Vibration Isolation System

The mirror which retro-reflects the Raman beams underneath the vacuum chamber effectively acts as the inertial reference for the gravity measurement. Any vibrations it

[4]Transitions between the $m = \pm 1$ states will also driven and can either be avoided through preselection as described in chapter 4.2, or by resolving the Zeeman splitting though a sufficient bias field.

exhibits during the interferometer therefore enter as phase noise and shift the measured gravity value. This is especially severe for low frequency vibrations below $1/T \approxeq 4\,\mathrm{Hz}$ due to the interferometer transfer function shown in figure 2.5. Moreover, with the comparatively large pulse spacing $T = 0.26\,\mathrm{s}$ used here during the gravity measurements, this phase noise easily has an amplitude of several radian which makes it difficult to assign a specific data point to the correct interferometer fringe and extract the phase information. Two established approaches exist in order to deal with this problem: isolating the mirror from external vibrations very carefully using specialized active isolation systems [98], or recording the vibrations and removing their effect using a post-correction algorithm [99]. The lowest vibration induced phase noise published [12] so far was found using the first approach whereas the second method is very attractive for mobile instruments due to the simple and compact architecture. In this work both strategies were combined by actively isolating the mirror and additionally removing remaining vibration in the feedback error signal in post-correction.

3.2.1 Active Vibration Isolator

A customized active vibration isolator was developed, built and characterized during an earlier work of the author [94, 93]. It was improved as part of this thesis by locating and centering the accelerometer axis exactly below the mirror and platform center in order to minimize cross-coupling of horizontal vibrations. Additionally, the control software was extended to allow for more general feedback filter parameters and sub-ms level synchronization with the interferometer sequence which is important for post-correction. A Tip/Tilt system for the retro-reflecting mirror was also implemented to allow for compensation of the Coriolis effect and is described in chapter 3.2.3. The rest of this chapter will briefly introduce the active system with special emphasis on the implemented improvements. For a more detailed description of the mechanical system and feedback loop parameters, refer to [94]. An illustration of the system can be found in figure 3.6. It is based on a commercial passive vibration isolation platform Minusk 50BM-10 with an effective resonance frequency of 0.5 Hz along vertical and horizontal[5] direction. In order to minimize the non-linearity of the negative-stiffness mechanism, the passive vertical resonance frequency is actually tuned slightly higher to 0.7 Hz, see [94]. Residual vibrations on the platform are measured by a low-noise seismometer Guralp CMG-3VL with a bandwidth of 0.005–100 Hz. The acceleration signal is fed into a digital feedback filter based on a NI compactRIO real-time system. A field-programmable gate array (FPGA) with a 24 bit analog-to-digital converter (ADC) and a 16 bit digital-to-analog converter (DAC) implements the digital filter with a sample rate of 1562.5 Hz, which is around two orders of magnitude higher than the achieved control bandwidth. The filtered voltage signal is then fed into a voltage-controlled current source. It sends a current to two voice-coil actuators which are built into the vertical isolation stage of the MinusK platform and exert a force between its top and bottom in order to close the feedback loop. Special care was taken to make sure that no mechanical friction is introduced by the voice coils which would otherwise drastically reduce the effectiveness of the passive isolation system.

The behavior of the active system under quiet and noisy environmental conditions is depicted in figure 3.7 which shows amplitude spectral densities, absolute transmissibility

[5] Custom-built columns from MinusK and improved leveling feet were used to achieve the 0.5 Hz horizontal resonance frequency of the inverted pendulum mechanism as described in [94]

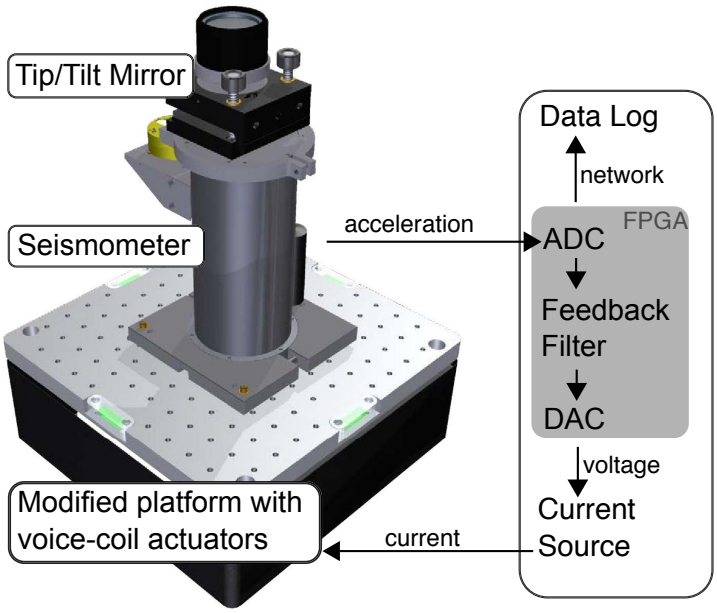

Figure 3.6: CAD drawing of active vibration isolation system with the architecture of the feedback loop. See [94] for more details.

and coherence measured using the in-loop feedback accelerometer on the platform and a second, independent sensor on the floor next to the system. The system works as expected in the relatively noisy environment shown in red, showing a strong reduction of vibrations above the effective resonance frequency of 0.05 Hz. The bandwidth of the feedback loop extends to approximately 10 Hz after which the passive mechanism of the platform works well at reducing higher frequency vibrations. In environments with low seismic excitations the transmissibility looks similar below 10 Hz but becomes approximately unity for higher frequencies. This shows that the passive mechanism of the platform is not working as expected under low noise conditions, for unclear reasons. The noise floor of the platform accelerometer is unlikely to be the problem as it is specified to below $2\times10^{-8}\,\mathrm{m/s^2/\sqrt{Hz}}$ below 20 Hz. Sensor noise should, if at all, first limit the ground accelerometer as its self-noise is substantially higher. The effective digitization noise floor of $2.3\times10^{-10}\,\mathrm{m/s^2/\sqrt{Hz}}$ is also much too small to cause this effect. Cross-coupling of high-frequency horizontal vibrations by the platform mechanics could theoretically be responsible. Since the ratio of horizontal- and vertical vibration magnitudes are roughly the same at both locations, however, this seems unlikely to cause this particular issue. Directional cross-coupling caused by the platform accelerometer is also unlikely as it should, if present, only manifest within the active feedback bandwidth which ends around 10 Hz.

This behavior was only observable during the two mobile measurement campaigns at geodetic observatories due to the quieter environmental conditions and particularly developed during the campaign in Onsala, Sweden. Extensive efforts during the campaign, which included a complete reassembly of the platform modifications, did not fix the problem. We therefore suspect that acoustics or other vibrations transmitted through air or the accelerometer cabling and/or residual friction and stick-slip movements in the platform mechanics are the cause. Although the short term sensitivity of the atom in-

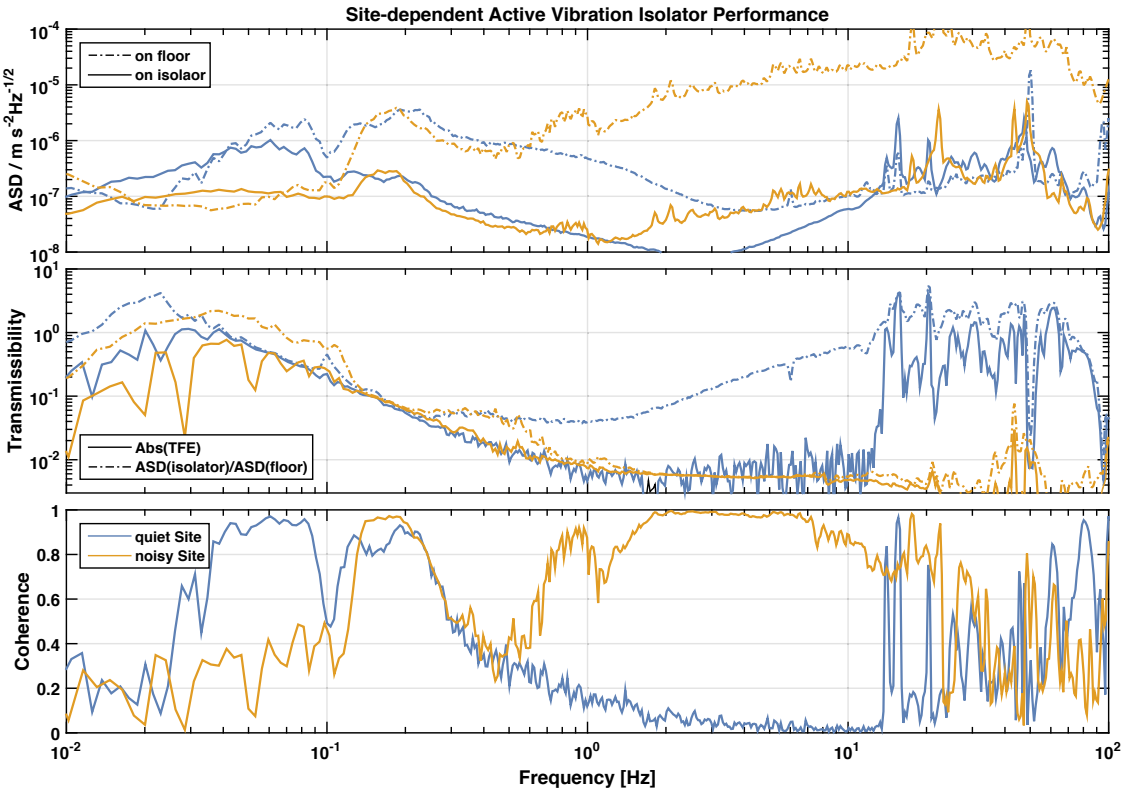

Figure 3.7: Vibration isolator performance in a noisy physics lab at HU-Berlin (yellow) and on a low-noise concrete pillar at Onsala Space Observatory, Sweden (blue). Top: amplitude spectral density (ASD) of vibrations recorded simultaneously on the platform (solid) and the ground (dashed). Middle: Transfer function estimates yielded by cross spectral density (solid) and by dividing the above ASDs (dashed). This shows coherent and incoherent contributions to the remaining noise, respectively. Bottom: Coherence between platform and floor sensors. Since sensor noise is negligible, low coherence indicates that the platform is disturbed by external, uncorrelated noise. See text for further discussion.

terferometer should currently not be compromised due to the relatively high frequency of more than 10 Hz and the interferometer transfer function, this issue should in the future be investigated further at a quiet measurement site.

Accelerometer Alignment

Since the active isolation system is only implemented along the vertical, it is crucial to avoid cross-coupling of horizontal vibrations and platform tilt modes. Our accelerometer has a particularly well-defined measurement axis with a specified directional cross-coupling of less than −65 dB which helps in minimizing this effect. In order to not be limited by misalignments of this well-defined axis it must be oriented vertically to better than 0.5 mrad. This is, unfortunately, complicated by the fact that the measurement axis is not collinear with the cylindric casing axis but is both translated from the center of the casing and tilted with respect to the cylinder axis. Some of these issues were discovered in [94] and the sensor subsequently shipped back to the manufacturer for improvement

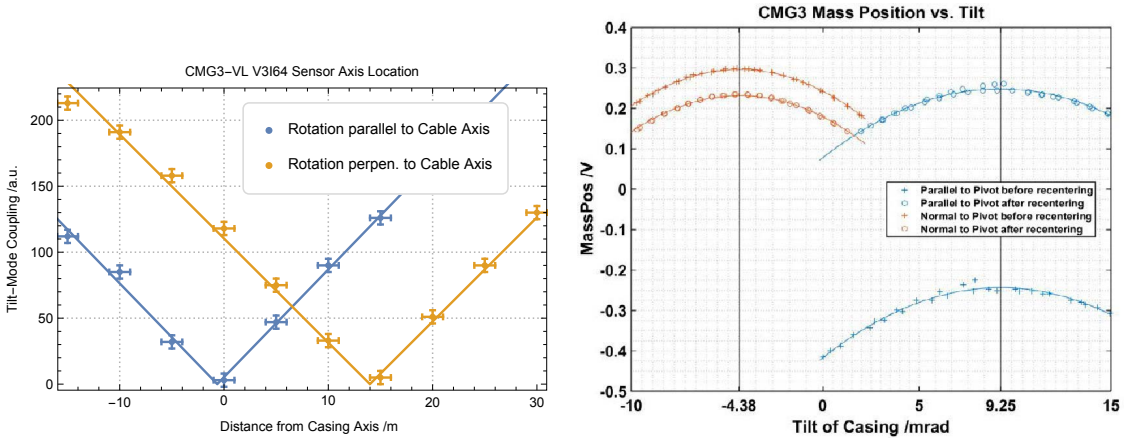

Figure 3.8: Platform accelerometer measurement axis alignment. **Left:** axis position relative to cylindric housing, measured by placing it on a rocker board and minimizing the tilt sensitivity. Note the large deviation from the center along the yellow axis. **Right:** Mass-position output as a function of the instrument tilt angle, indicating the axis alignment relative to the housing. This shows significant offsets on the 10 mrad level.

which, however, could not be accomplished within the limited amount of time between two measurement campaigns.

Both orientation and position of the measurement axis were thus measured and documented as part of this work as shown in figure 3.8 . The measurement result is a position offset of (14.0 ± 0.3) mm along one axis and respective misalignments of -4.38 mrad and 9.25 mrad with respect to the casing. An adapted mounting plate with a precision leveling stage was designed and built for the accelerometer so that the measurement axis is vertical and placed over the middle of the platform, and co-centric below the retro-reflecting mirror. This precaution should minimize the coupling of horizontal vibrations and platform tilt modes into the vertical where they may compromise the vibration isolator performance.

Group Delay

The complex transfer function of the active isolation system generally has a frequency dependent phase which potentially distorts gravity signals in frequency bands for which the group delay is not negligible. This is of relevance when comparing the signal of two different sensors with different transfer functions with signals in the relevant frequency band. In order to investigate this effect, the group delay $\tau(\omega) = -\frac{d\Phi\omega}{d\omega}$ was evaluated numerically. The result is displayed in figure 3.9 and shows that there is a delay of several seconds for signals around 10 mHz, just below the effective resonance frequency of the system. Fortunately most measured signals are either lower in frequency, e.g. tidal signals with frequencies below 3×10^{-4} Hz, or higher in frequency such as micro-seismic excitations above 0.1 Hz. Seismic excitations in the affected frequency range are usually too small in amplitude to appear in the gravity measurement but have to be considered during specific events such as earthquakes.

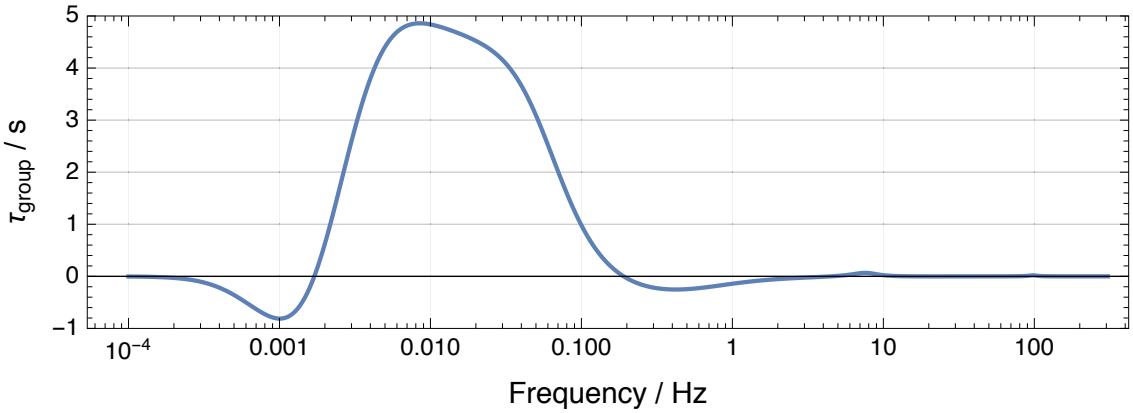

Figure 3.9: Simulated group delay of the active vibration versus frequency, based on a transfer function model which matches the transmissibility shown in figure 3.7.

3.2.2 Post-Correction

Due to the finite feedback gain and residual transmissibility of the active vibration isolation, the error signal from the CMG3 platform accelerometer still contains usable vibration signals. It can therefore be recycled to simultaneously follow the alternative approach of recording mirror vibrations and removing their detrimental effect in post-correction [99]. This is particularly useful to remove micro-seismic vibrations in the 0.1–0.3 Hz frequency band at which the gain of the feedback mechanism is often not high enough.

The phase offset caused by mirror vibrations during the interferometer sequence can be calculated using the sensitivity function approach summarized in chapter 2.4. By combing equation 2.40 with Raman phase changes caused by the mirror velocity $v(t) = \frac{1}{k_{\text{eff}}}\frac{d\phi}{dt}$, one finds

$$\Phi_{vib} = k_{\text{eff}} \int_{t_1}^{t_3} g(t)v(t)dt \tag{3.1}$$

where t_1 and t_3 are the times of first and third interferometer Raman pulses and $g(t)$ is the sensitivity function defined in equation 2.39, centered around the second pulse.

Φ_{vib} can be readily calculated from the output signal of the platform accelerometer if $v(t)$ is permanently logged to the database system (see chapter 3.4) with sub-ms jitter relative to the interferometer pulses[6]. As both functions are implemented on different hardware, a simple synchronization was first attempted in [94] using the network time protocol (NTP). Since the achieved synchronization only succeeded with a jitter of several ms, a TTL trigger was implemented later on which enables sub-ms synchronization between the acceleration data and the interferometer pulses. In order to compensate for the accelerometer‘s phase response, the recorded signal is digitally filtered in post-processing through the CMG3 transfer function on a reversed time-axis. The resulting time-series then contains the platform motion filtered twice by the CMG3 frequency response while canceling out its phase response. In addition to improving the phase matching for post-correction, this process additionally attenuates spurious signals outside the sensor band-

[6]In order to keep the post-correction phase error smaller than $\Delta\varphi = 0.1\,\text{rad}$ for $f = 50\,\text{Hz}$, the timing error should be smaller than $\sigma_t = \frac{\Delta\varphi}{2\pi f} \approx 0.24\,\text{ms}$.

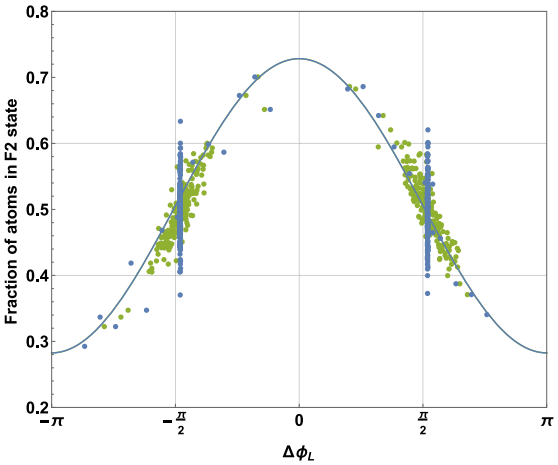

Figure 3.10: Distribution of data points on the interferometer fringe (solid line) with(green) and without(blue) vibration post-correction(blue).

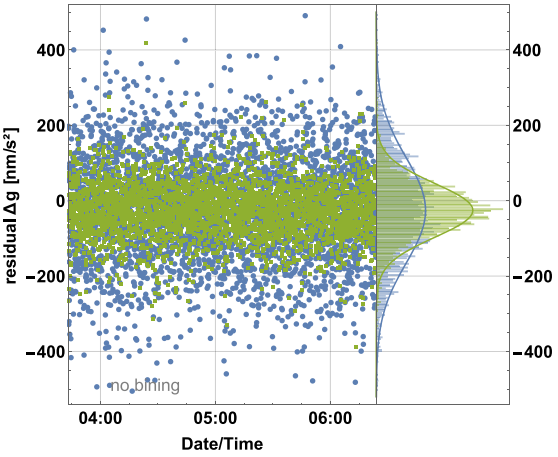

Figure 3.11: Residual noise of gravity measurements with(green) and without(blue) post-correction. The right side of the plot shows corresponding normal distributions with width σ of 71 nm/s^2 and 140 nm/s^2

width such as slow temperature drift, which may otherwise compromise the post-corrected gravity signal.

Equation 3.1 is evaluated for each individual measurement during data processing and the resulting shift Φ_{vib} is added to its effective phase value. Figure 3.10 shows the measured state population at the interferometer output port as a function of the Raman phase setting with and without post-correction. The solid line represents the expected interference fringe to which the data points adhere to much better when the additional vibration phase term is used (shown in green). This significantly reduces noise in the gravity measurement by about a factor of 2 as shown for a sample dataset in figure 3.11. The discussion of the gravity comparison campaigns will, later on in chapter 5.4, yield further insight into the efficacy of this post-correction implementation and the composition of the total gravimeter noise.

3.2.3 Tip/Tilt Mirror System

The Raman retro-reflection mirror is mounted on a Tip/Tilt stage which was designed and built during this work in order to facilitate Coriolis effect compensation following an idea from [86]. This, in combination with a motorized Raman telescope mount described in chapter 6.2.1, also allows for precise tilt alignments of the Raman beam during gravity measurements.

The system is based on a commercial, closed-loop Piezo Tip/Tilt stage, PI S-330.2SL. It has a two orthogonal axes provided by a parallel flexure mechanism with a resolution of up to 20 nrad and a dynamic range of ±1 mrad. The integrated strain-gauge sensors allow for a specified closed-loop repeatability in the 0.1 µrad range. Commercial control electronics by the same manufacturer are used to ensure the specified performance of the Piezo actors. The Raman mirror and the quarter-waveplate are encased in a tubed housing and are mounted on top of the Tip/Tilt table. Given the small size and weight of the of the mirror assembly as detailed in figure 3.12, the resonance frequency of the Tip/Tilt

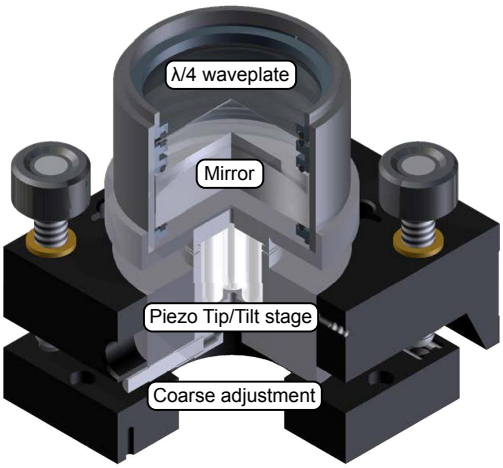

Figure 3.12: CAD drawing of the Piezo Tip/Tilt mirror system situated on the vibration isolator. The outer dimensions of the total system are $(90\times76\times94)\,\mathrm{mm}^3$. The mirror assembly on the Tip/Tilt actor has a 55 mm diameter, height of 42 mm and a weight of approximately 160 g.

system should be around 300 Hz. The total vertical distance between the pivot point and the mirror surface is 21.9 mm. Due to the limited range of the Piezo actor, the whole system is mounted on a manual mirror mount for coarse adjustment.

The Tip/Tilt system is controlled via two analog voltage outputs from the same FPGA that facilitates the digital feedback filter for the active vibration isolator. In order to synchronize the system with the interferometer sequence, a TTL trigger pulse from the timing system initiates the pre-programmed rotation sequence. The implementation details of the Tip/Tilt control system will be discussed separately in chapter 3.4.1.

3.3 Laser System

The laser system is responsible for generating all optical frequencies required in the experimental sequence as shown in figure 3.13. It must also be small and robust enough to fit into the limited available space, withstand challenging conditions during transport and it must not require frequent readjustments which would otherwise interrupt the gravity measurement. A modular system based on 780 nm diode lasers in multiple modules connected by optical fibers was chosen to meet these requirements. The first version was originally developed in [82] and used for the first gravity measurement. Due to reliability and stability issues with the first generation MOT light amplifier and distribution modules, these two components were redesigned and improved in [80, 101].

Since a detailed description of the complete laser system already exists in the above references, only a short summary of the latest version is given here, which highlights the general architecture and crucial components. The Raman laser module will receive more attention as its implementation details are important for the control of several systematic

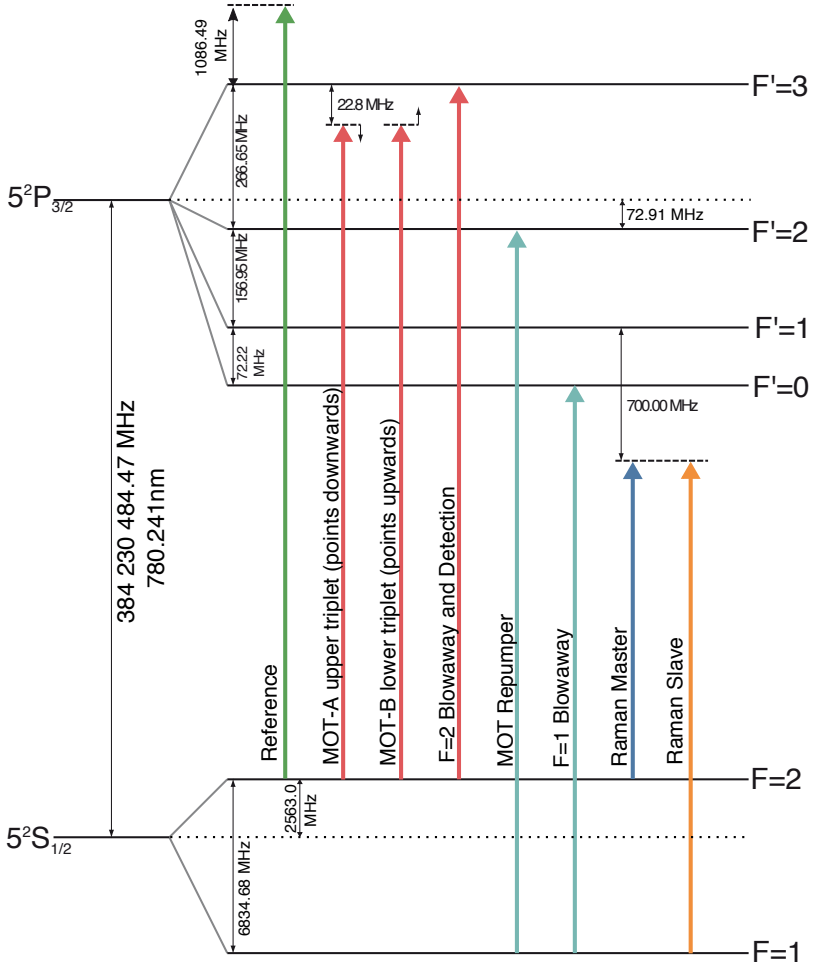

Figure 3.13: Rubidium 87 D2 line hyperfine structure with the necessary laser frequencies for laser cooling and stimulated Raman transitions for atom interferometry. Frequency values adopted from [100] and color-coded in agreement with other figures in this document

.

effects. All optical frequencies required during the experimental sequence, as depicted in figure 3.13, are generated using 5 laser sources in distinct modules connected by optical fibers as shown in figure 3.14.

Reference Laser This module provides the optical frequency reference to which all other lasers (except the Raman slave) are directly phase-locked with freely adjustable offset frequencies [82]. This architecture ensures at the same time optimal flexibility and accuracy in terms of frequency control. The spectroscopy module contains an external cavity diode laser (ECDL) and a Rb spectroscopy cell and is frequency-locked to the ^{85}Rb D2 F3 $\rightarrow$ F′4 line using modulation transfer spectroscopy (MTS) [102]. Together with a 40 MHz offset due to an internal AOM this leads to an optical frequency of 1086.69 MHz above the ^{87}Rb D2 F2 $\rightarrow$ F′3 transition.

Cooling Laser light for the MOT telescopes is generated by a distributed feedback (DFB) laser diode frequency stabilized around the $5^2S_{1/2}$ F = 2 $\rightarrow$ F′ = 3 transition.

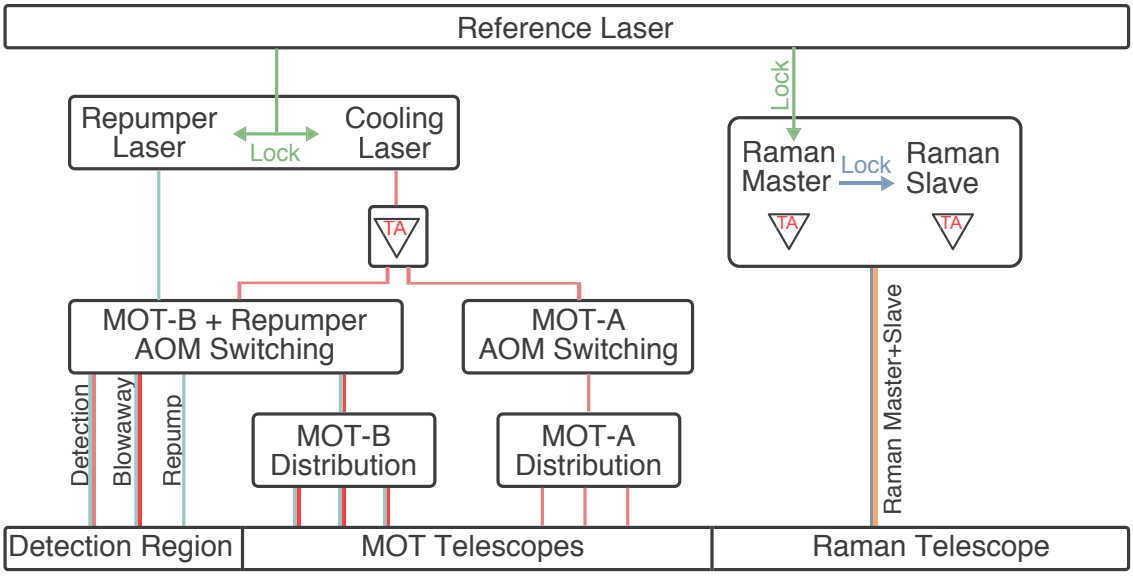

Figure 3.14: Structure of the GAIN laser system. Boxes correspond to separate laser modules connected by optical fibers with colors indicating the same optical frequencies as depicted in 3.13.

Its output is amplified by one separate 2 W tapered amplifier (TA) module which delivers a fiber-coupled output power of almost 1 W [101]. This results in a power of approximately 50 mW per beam in the vacuum chamber, which corresponds to roughly one saturation intensity for the large 30 mm $1/e^2$ MOT beam diameter. In order to facilitate the moving-molasses launch sequence, the upper(A) and lower(B) MOT beam triplets need a relative frequency shift implemented using two separate modules with single-pass AOMs used for both frequency shifting and intensity/pulse control as detailed in [80]. The MOT-B switching module also provides a repumper input and auxiliary output fibers for detection, blow-away and repump beams. Two purely passive distribution modules with one input and three outputs then deliver a total of six optical fibers to the MOT telescopes.

Repump Laser As the cooling transition of ^{87}Rb is not fully closed, atoms get lost from the cooling cycle through decay to the $F = 1$ ground state. This laser drives the $5^2S_{1/2}$ $F = 1 \rightarrow F' = 2$ transition from where the atoms can decay back to the $F = 2$ ground state which returns them to the cooling cycle. The light is generated by a DFB diode laser which delivers a approximately 10 mw each to the MOT-repump- and the detection-fiber, which is more than enough. Originally it was also coupled into the MOT-B fibers which was later removed, however, since it reduced the cooling power efficiency in the MOT-B path with the current switching module design [80]. In order to facilitate blow-away pulses for atoms in the lower hyperfine ground state the repump laser can quickly be tuned to the $F1 \rightarrow F'0$ cycling transition.

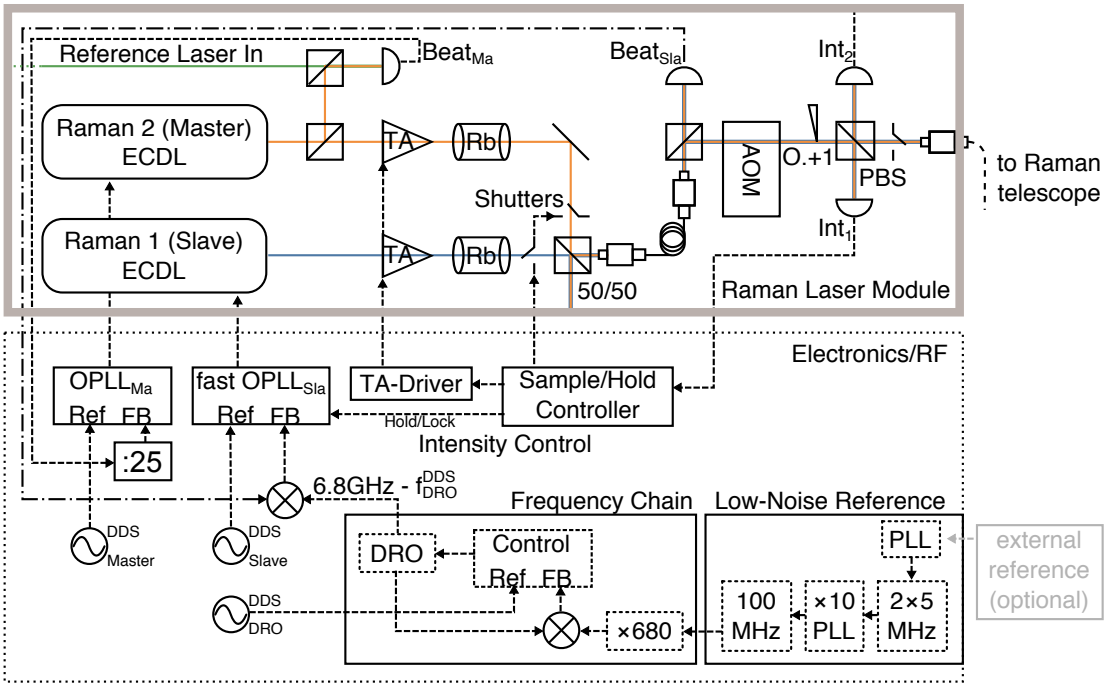

Figure 3.15: Simplified schematic of the Raman laser module with optical PLL and intensity control loops. Only crucial optical and RF components are shown for clarity. For a more detailed description refer to [82, 80].

3.3.1 Raman Laser System

Since all phase noise between the two Raman frequency components directly enter in the atom interferometer and the intensity is actively controlled to reduce light-shifts, special care was taken in the design of the module. The important aspects are summarized here for completeness, see [82, 80] for a more detailed description. Figure 3.15 shows a schematic view of the Raman laser module. Two ECDL lasers with a line-width of around 30 kHz, coined Raman master and slave, generate both frequencies required to drive stimulated Raman transitions. The Raman master is phase locked to the reference laser at a one-photon detuning of 700 MHz to the red with respect to the $5^2S_{1/2}$ $F = 2 \rightarrow F' = 1$ transition. The slave laser is phase locked to the master laser with an offset frequency equaling the hyperfine splitting of around 6.8 GHz. Both lasers are amplified by tapered amplifiers and pass through actively heated Rb cells[7] in order to minimize resonant spectral pedestals due to amplified spontaneous emission (ASE) in the amplifier chip. This serves to filter out resonant components of the pedestal which potentially cause light-shifts in the atom interferometer. The desired Raman frequency components are off-resonant enough due to their one-photon detuning of several hundred MHz with respect to the D2 line and are therefore not significantly attenuated.

The beams are then overlapped into the same polarization and coupled into an intra-module single mode PM fiber with a length of 1 m. This acts as a spatial mode filter which strongly suppresses phase instabilities due to a mode mismatch at the Raman slave

[7] During the 2nd mobile comparison campaign in Onsala, Sweden, the cells were heated to around 45 °C whereas earlier campaigns left them at room temperature.

beat-note diode behind the fiber. A single-pass AOM is used behind the fiber for flexible pulse-shaping during the experimental sequence.

An active intensity stabilization system monitors the power of both beams independently using a photo diode behind a polarizing beam splitter (PBS) in order to compensate for slow power drifts. Since both beams are already overlapped in the same spatial and polarization mode at this point, two alternating shutters in front of the beam combiner are used to measure the master and slave intensity periodically between experimental runs. A sample-and-hold controller then adjusts the TA current to stabilize the beam powers around the set-points. A second photo-diode on the other PBS side measures the power returning from the physics-package which is used for the active retro-reflection stabilization as detailed in chapter 6.2.1.

The Raman slave optical PLL is a custom design from [82] and features a HF modulation circuit to achieve a large control bandwidth of around 4 MHz to avoid phase noise in the frequency band of 0.1–60 kHz where the interferometer is most sensitive according to the transfer function shown in figure 2.4.

A schematic of the phase lock architecture is shown in figure 3.15 and explained in full detail in [82]. Since most low-noise phase-frequency detectors (PFDs) do not work at frequencies as high as 6.8 GHz, the Raman beat is first down-converted to a lower frequency using the output of a dielectric resonator oscillator (DRO) which is phase-locked to a 6.8 GHz signal with a variable offset f_{DRO}. It is part of an integrated frequency multiplication chain designed and built by the group of A. Landragin at SYRTE, Paris [99]. This results in a beat frequency between Raman master and slave given by the simple formula

$$f_{\mathrm{Sla}}^{\mathrm{Beat}} = \frac{\omega_{12}}{2\pi} = f_{\mathrm{DRO}} + f_{\mathrm{PFD}}^{\mathrm{DDS}} = 6.8\,\mathrm{GHz} - f_{\mathrm{DRO}}^{\mathrm{DDS}} + f_{\mathrm{PFD}}^{\mathrm{DDS}} \tag{3.2}$$

where f_{DRO} and f_{PFD} are created by two independent direct digital synthesizer (DDS) and can be controlled at will during the interferometer sequence as detailed in chapter 3.4.2. Note that the DRO has a limited electrical tuning range of approximately (6745±10) MHz which limits the practical values of $f_{\mathrm{DRO}}^{\mathrm{DDS}}$ at the current mechanical tuning to around (55±10) MHz. For the standard setting $f_{\mathrm{PFD}}^{\mathrm{DDS}} = 90\,\mathrm{MHz}$ the Raman resonance condition for atoms at rest is met at $f_{\mathrm{DRO}}^{\mathrm{DDS}} \approxeq 55.317\,\mathrm{MHz}$. Note that, because of the variable DRO frequency, the reference input of the Raman slave PLL can be left constant during the entire Raman frequency chirp which compensates for the atomic Doppler shift during the sequence. This circumvents problems due to potential frequency dependent PLL phase shifts which could otherwise cause systematic offsets in the gravimeter measurement.

Since DRO phase noise will directly enter in the atom interferometer phase, a low-noise frequency reference is used as an input to the multiplication chain. Due to its importance and because it also serves as a reference oscillator for all other parts of the GAIN setup this will be discussed in more detail in the next chapter.

Frequency Reference

All radio frequencies used in the experiment, including the frequency difference of the Raman lasers, are ultimately derived from the low-noise frequency reference depicted in the bottom right of figure 3.15. In order to not limit gravimeter performance by noise sources in this reference or other elements in the frequency chain great care was taken to ensure that the chosen components meet the required noise specifications [82, 93]. Since no single quartz oscillator fulfills the noise specifications at both low and high frequencies, a

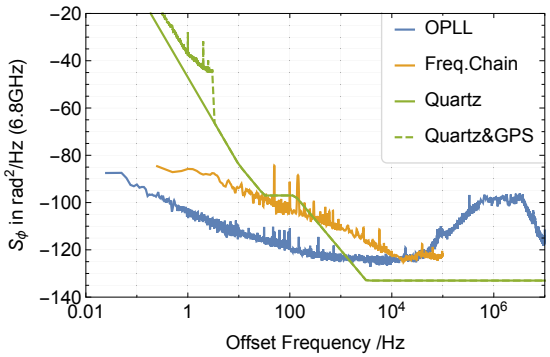

Figure 3.16: GAIN frequency chain phase noise contributions, from [82]. The green dashed line was measured separately and shows qualitatively the degrading influence of an external GPS frequency reference.

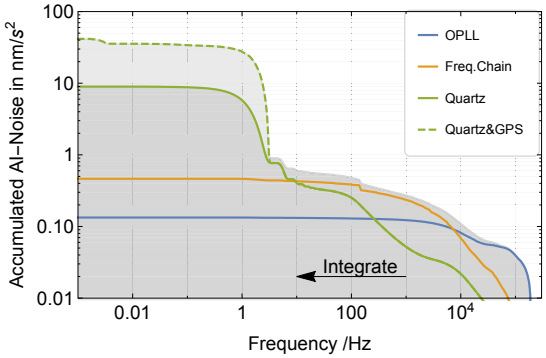

Figure 3.17: Gravimeter noise when accumulating the spectra shown on the left figure from high to low frequencies as described in the text. Quartz oscillator phase noise and/or external GPS phase noise between 1–10 Hz clearly dominate.

combination of two oscillators packaged in a Spectradynamics DLR-100 reference is used. It provides an 100 MHz ultra low-noise quartz oscillator (Wenzel ULN) phase-locked to a frequency-doubled 5 MHz quartz (Wenzel Blue Top ULN) for low phase noise both close to and far away from the carrier frequency, and has outputs at 10 MHz and 100 MHz. The 10 MHz port is used to synchronize the hardware clocks of the supplied PXI- and DAQ hardware and test equipment. In order to compensate for slow drifts of the quartz oscillators during long-term measurements, the reference can optionally be stabilized to an external 10 MHz signal with a locking bandwidth of a few Hz.

Phase Noise

The phase noise contributions of all components in the frequency generation chain directly enter in the gravimeter measurements as interferometer phase noise. This was investigated in [82] for the same Raman phase lock and will be briefly revisited here. The total resulting gravimeter noise can be calculated by integrating over the Raman phase noise PSD weighted with the squared interferometer transfer function $|H(\omega)|^2$ as detailed in chapter 2.4 and equation 2.43. When the integration is performed from the upper frequency end of the spectrum down to a certain point ω' and the resulting noise $\sigma_{g,\mathrm{Ra}}$ plotted as a function of ω', the contributions of the each frequency chain component becomes apparent. This is depicted in figure 3.17 for GAIN standard parameters of $T = 260\,\mathrm{ms}$ and $\tau = 36\,\mu\mathrm{s}$. For frequencies above 10 kHz, noise from the OPLL dominates, whereas between 10 kHz and 20 Hz the frequency multiplier chain contributes most. Phase noise below 10 Hz due to the 10 MHz GAIN reference quartz, however, dominates the overall picture leading to a best-case sensitivity of $10\,\mathrm{nm/s^2}$ for one individual measurement during regular operation without an external reference.

In order to estimate the influence of the external reference on GAIN quartz phase noise, a GPS stabilized oscillator[8] operating at HU-Berlin was characterized against a more stable

[8] Arbiter GPS

model[9] during this work. The former showed significantly more phase noise below 10 Hz than the GAIN reference quartz as indicated by the dashed green line in figure 3.16. If the GAIN quartz is stabilized to it, this noise directly enters the GAIN frequency chain within the external locking bandwidth of a few Hz and deteriorates gravimeter noise to approximately 40 nm/s^2 as calculated in figure 3.17. This value agrees well with observed interferometer phase noise in Doppler-insensitive mode where vibration induced noise is eliminated and Raman phase noise the dominates.

During the mobile gravimeter comparisons conducted in Wettzell and Onsala, locally available hydrogen maser reference signals were used instead of the tested GPS oscillator. Despite their excellent long-term stability, short-term phase noise here is still entirely determined by the employed quartz oscillator and depends on the exact model and version[10]. Unfortunately, measurements of the reference phase noise were not possible during either campaign so that we have to rely on performance specifications for this discussion. The specified Wettzell maser phase-noise is well below the specifications of the GAIN quartz and shouldn't deteriorate the Raman phase noise. This was not the case in Onsala, however, where the specifications are similar to the GPS receiver tested in Berlin.

We conclude that gravimeter noise due to Raman phase noise, depending on the external reference, had an amplitude of 10–40 nm/s^2 for the measurements presented here. This constitutes the second largest noise source in the set-up. In order to improve the gravimeter sensitivity significantly in the future, excess Raman phase noise from the external reference will have to be removed from the GAIN frequency chain. Two different approaches are available for this purpose. One can either stabilize the GAIN quartz to available references with a custom, very slow PLL. This combines the long-term stability of the reference with low phase noise of the GAIN quartz and was tested successfully using a digital PLL. The alternative approach is based on operating the GAIN quartz without external reference and monitoring the frequency drift with a counter. The associated gravity bias is detailed in chapter 6.3.2 and could simply be corrected for in post-processing with equation 6.19. This rather simple approach has already been used in other atom interferometer setups such as [99].

3.4 Timing and Control

The system responsible for controlling the data acquisition hardware and laser system electronics is crucial for creating and managing the gravimeter sequence which starts with loading the MOT and ends with the detection sequence after the interferometer pulses. The timing and jitter of the various events should be below the µs level in order to make sure that they do not cause shot-to-shot measurement fluctuations. The system also has to be able to control various types of input and output hardware simultaneously using a range of different hardware interfaces which includes the data acquisition hardware, frequency synthesizers and the Piezo tip/tilt mirror system. Furthermore, the timing and details of all events must be able to change easily and quickly, and these changes have to be automatically referenced to the obtained measurement data for subsequent analysis.

These requirements were fulfilled with an elaborate system based on a National Instruments (NI) PXI hardware and a database storage back-end described in detail in [93,

[9] Timetech GPS reference with OCXO 8607 ULN option

[10] Low frequency phase noise is not critical for many H-Maser applications, such as VLBI

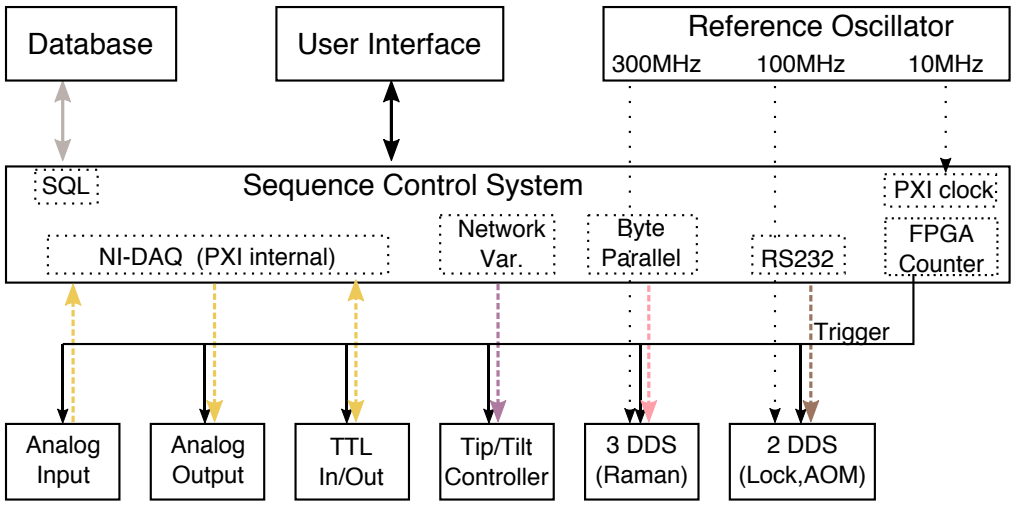

Figure 3.18: Structure of the GAIN sequence control and timing system. Various external hardware interface are shown within dashed boxes. Sub-µs timing accuracy is achieved by virtue of the common reference clock (top right) and triggering by a FPGA timer. All sequence- and measurement data are stored in an external database (top left) for secure and flexible access.

80] and are covered briefly here for completeness. During this work the system was extended to include agile and flexible frequency control of the Piezo Tip/Tilt mirror system described in chapter 3.2.3 and of the Raman laser DDS which will therefore be discussed in more detail. Several significant additions of the timing software are also mentioned.

A schematic overview of the timing system structure is shown in figure 3.18. The sequence control system is based on a NI PXI system containing several DAQ extension cards and a FPGA card NI PXI-7811R. The control software was implemented in Labview and runs on the PXI controller. The program consists of several abstraction layers from the top-level user interface down to the low-level Labview-FPGA code that governs the sequence timing. This enables high-level user control of all parameters relevant for the gravimeter and the implementation of automated measurement protocols such as the gravimeter sequence described in section 4.5. It also enabled to implement, on a yet higher abstraction layer, the automated tilting of the Raman beams during a gravimeter measurement for alignment of the measurement axis with gravity.

In order to eliminate jitter caused by indeterministic CPU execution timing, the entire sequence for one instrumental run is preloaded into internal buffers of the various input/output systems. This takes an overall time of approximately 200 ms during the MOT loading period when no other sequence events take place. The timed execution is then performed solely using trigger pulses from the deterministic FPGA counter. The triggers are delivered to the DAQ cards using TTL pulses via the PXI backplane with sub-ns jitter. From there they are relayed to multiple DDS (direct digital synthesizers) and the Tip/Tilt-Controller via the PXI-6259 card over coax cables. In order to ensure synchronization between the FPGA- and DAQ-cards, their internal oscillators are all phase-locked to the 10 MHz output of the reference oscillator through the PXI-backplane clock. All DDS are also referenced to this oscillator via 100 MHz and 300 MHz outputs derived from the Raman frequency chain system.

All voltage input and output channels are provided by two PXI-6723 and one PXI-6259 data acquisition (DAQ) cards. This results in a total of 24×16 bit input channels for timed 1 Msps data acquisition and 64×16 bit output channels with a variable range of up to ± 10 V for synchronized arbitrary waveform output during the sequence. The output channels are used to control, e.g., AOM diffraction efficiencies using voltage variable attenuators or the current drivers sourcing magnetic field coils on the physics package. Additionally, 32 external TTL signal channels are used, e.g., to control fast RF-pulse switches in the AOM signal paths and to deliver trigger pulses to the laser shutter drivers, Tip/Tilt mirror, MOT cameras, DDS and other subsystems. All channels are delivered through coax BNC- or SMA-cables via a custom-built signal breakout box which contains additional functions for some channels such as shutter drivers or active impedance converters.

Two Novatech 409b DDS[11] provide a total of 8 independent RF signals for the cooling- and repump laser PLL reference and for all AOMs in the GAIN laser system. Their internal oscillators are locked to the 100 MHz GAIN low-noise reference oscillator as shown in figure 3.18. Since the programming interface to the timing system is a comparatively slow RS232 connection, all frequency-, phase- and amplitude-values required during the sequence are preloaded into an internal 4MB "Table Mode" buffer prior to each measurement run. After optimizations of the serial communication conducted during this work, the complete programming of both DDS now takes less than 150 ms and can easily be done during the MOT loading phase without constraining the experimental cycle time.

All sequence information and recorded measurement data is simultaneously sent across the network to a MySQL database server contained in the GAIN setup as indicated in the top left corner of figure 3.18. The database layout is described in detail in [80]. This guarantees direct, convenient and secure data access with the ability to run complex data queries. To ensure data safety, the experiment data is furthermore replicated on a second, remote database server at Humboldt Universität zu Berlin.

3.4.1 Tip/Tilt Mirror Control

Sweeps of the Piezo Tip/Tilt mirror described in chapter 3.2.3 implement both the Coriolis compensation and Raman beam auto-collimation via sweeps along two perpendicular axes during both Ramam interferometer- and the auxiliary pulse-sequence as detailed in chapters 6.2.1 and 6.1.1. In order to guarantee deterministic high-level control over these sweeps, a Tip/Tilt steering system was developed during this work as described below.

Two analog voltage inputs of the closed-loop Piezo controller are used to facilitate arbitrary steering of the Tip/Tilt system. They control the internal feedback loop set-points and are thus not subjected to hysteresis, drift or other spurious Piezo effects. Due to the proximity to the vibration isolator, the simplest way to access the set-points digitally is by using two analog outputs of the existing compactRIO system which already implements the active vibration feedback filter. Since the compactRIO is clocked by its own internal oscillator, a synchronization to the rest of the timing system is necessary and performed using a TTL trigger pulse at the start of each experimental cycle. The Tip/Tilt steering is then implemented using a deterministic FPGA program running on the compactRIO which gradually changes both control voltages.

In order to facilitate a flexible but high-level control by the user, input to this program is a list of chirp segments each containing the timing and voltage and ramp values for

[11] based on Analog Devices AD9959 ICs

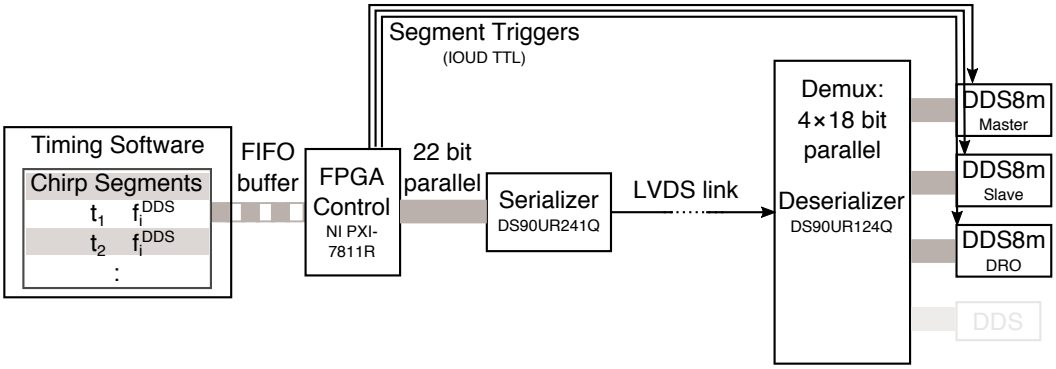

Figure 3.19: Schematic of the implemented byte-parallel Raman DDS control system. Linear chirp segments (see text) are computed by the timing software and implemented by an FPGA which controls up to four DDS8m via a fast, serial LVDS link. In order to avoid the small serialization delay, the time critical trigger signals are delivered to each DDS using standard coax connections.

both channels. The program adheres to the requested time-/voltage(s)-values and realizes a simple linear interpolation in between. Due to the comparatively high sampling rate of 20 kHz this implements a quasi-continuous Tip/Tilt sweep. Note that continuity and smoothness over the whole sequence, and not just during the interferometer pulses, is relevant here to minimize the torque on the vibration platform. Step-like mirror movements during tests, on the other hand, heavily interfered with the active feedback system and drove it beyond its dynamic range. Due to the automatic continuous sweep, however, no such interference has been observed even on the seismically quietest sites and is therefore not a problem.

The user interface provides a higher-level representation which allows to enter the orientation of the tip/tilt system relative to the geographic reference frame. Tip/tilt values and sweep rates along NS and EW axes can then be entered directly for both the Raman interferometer- and the pseudo-pulses-interval during the MOT-phase. The chirp segment list is computed from these specifications by the sequence control system and transfered to the compactRIO via Ethernet before the start of each experimental cycle.

3.4.2 Agile Raman DDS Control

The Raman laser phase locks are referenced to a total of three DDS which are labeled master, slave and DRO as shown in figure 3.15. In order to implement µHz level frequency control and fine tuning of the chirp rate, Novatech DDS408A/DDS8m synthesizers with 48 bit wide frequency control registers are used. They are clocked by 300 MHz signals directly derived from the Raman frequency generation chain for synchronization and reduced phase noise compared to internal oscillator operation.

Since these synthesizers do not have an on-board buffer for multiple output settings they need to be reprogrammed within the experimental sequence to change the Raman frequency in a flexible manner for all but the simplest tasks. For example, before the implementation of this system the Raman frequency could not be chirped during the long velocity selection pulse leading to potential smearing of the selected velocity class. As the standard RS232 interface takes at least 50 ms to transmit every command, which is

much too slow for agile frequency control, a faster interface was implemented as part of this work and depicted in figure 3.19. It is based on a 24-pin connector on the DDS PCB which allows direct access to all relevant registers inside the AD9854 synthesizer IC using only 18 pins. This enables full, real-time control over the output frequency, amplitude and phase. In order to set these registers reliably and quickly, the same FPGA board is used that implements the sequence timing. Since all three involved DDS need to be accessed only sequentially and not in parallel, multiplexer/demultiplexer boards were realized using electronic latches. They enable the addressing of up to four DDS sequentially using only one output with 18 + 4pins. In order to remove the need for long unwieldy shielded parallel signal cables between the FPGA and the DDS, which are located in different parts of the GAIN setup, a data serialization system was furthermore implemented on the Mux/Demux board together with Eugen Dischke. It is based on low voltage differential signaling (LVDS) ICs and provides a real-time and low-latency[12] compression of all signal lines onto one twisted-pair wire, such as e.g. in a standard Ethernet cable. The power usage of the serialization system is low enough that it can be sourced from the FPGA itself and it is clocked using a 10 MHz signal derived from the FPGA as well. At the current FPGA clock rate of 10 MHz and without optimization the interface is capable of writing two bytes to the DDS buffer within 6 clock cycles, or 0.6 µs. This is more than 5 orders of magnitude faster than the previous RS232 interface and enables a complete rewrite of all DDS registers (which is almost never necessary) within less than 5 µs. According to the DDS8m specifications, this could theoretically be accelerated in the future by yet another order of magnitude to less than 25 ns per byte.

The programing format used to realize the desired DDS behavior is based on the AD9854 frequency chirp mode and closely related to the tilt chirp program implemented for the Tip/Tilt mirror[13]: A list of chirp segments with time/frequency value pairs is sent to the FPGA before the beginning of the sequence. The FPGA realizes these values by programming the AD9854 using one appropriate start frequency and the sequential chirp rate values together with their respective timings during the sequence. In order to activate each chirp segment at exactly the right clock cycle, the parameters of the next segment are written to the AD9854 input buffers during the previous segment. A positive edge on the trigger input then causes the buffered values to be written to the DDS working registers immediately. To avoid potential jitters of the trigger signal due to the serialization system delay, this single line is delivered to the DDS directly through a standard coax connection (identical to the previous RS232 method). Note that this timing scheme only works if both FPGA and DDS are synchronized by the same clock as shown in figure 3.18, since cycle slips between them will otherwise lead to frequency offsets during the sequence. In order to reference the output to a fix starting point, all DDS are reset to a fixed frequency value during the MOT phase of each experimental cycle. To provide the experimenter with a more meaningful set of control parameters, an abstraction layer was implemented on which an arbitrary number of frequency ramps can be set on each DDS during the sequence. The required parameters for each ramp are frequency value, chirp rate, the exact time at which the frequency value shall be in effect and the ramp start/stop times. The time spacing between individual segments is limited only to a few µs by the time it takes to rewrite the DDS registers.

This flexible and fast Raman laser control system enables the realization of advanced

[12] The specified serialization/deserialization delay is smaller than 1 μs for a 10 MHz transmit clock

[13] In fact, both routines are implemented with the same code through a common "chirp" parent class.

AI sequences such as large-momentum beam splitters, composite pulses or multi-species experiments. It is thus a crucial addition of the setup and significantly enhances its capabilities for a broad range of future applications.

Summary

The preceding chapter gave a comprehensive overview of the experimental apparatus, with an emphasis placed on the parts on which the author contributed most during this work. This specifically includes the magnetically shielded MOT chamber, vibration isolation system and post-correction implementation, Tip/Tilt mirror system for Coriolis- and tilt-compensation which will be detailed in chapter 6, and the agile Raman frequency control system.

After this detailed hardware description, the next chapter will introduce the gravity measurement sequence with a specification of each functional segment.

Chapter 4

Gravimeter Operation

In order to perform accurate and sensitive gravity measurements with an atom interferometer, the details of the atomic source preparation, interferometry and detection sequence are essential. This chapter will therefore give a detailed description of the experimental sequence that was used for gravimeter operation. Each run of the sequence takes around 1.5 s and is repeated back-to-back continuously during the long-term gravity measurements presented in chapter 5. First, each functional element of the sequence and afterwards the measurement protocol that was used to conduct the gravity registration will be described in the following.

The sequence builds on the previous measurement protocol developed in [82, 93, 80] and was improved in order to optimize the stability, sensitivity and reliability of the gravity measurements. First, the upgraded DDS programming detailed in chapter 3.4.2 enabled to chirp the Raman laser frequency to compensate for the changing Doppler-shift during the velocity selection pulse. The gravity measurement protocol was furthermore amended with a feed-forward mechanism to operate the interferometer at exactly half-fringe even in the presence of large tidal gravity variations, which is important due to a bias in our detection system as detailed in chapter 6.6 and in [80]. Finally, a slow feedback loop was implemented to compensate for slow drifts of the total Raman power which were not accounted for using the previous intensity stabilization system described in chapter 3.3.1 and in [80].

4.1 MOT and Launch

Each experimental run starts by loading atoms from background gas into the MOT for a time of 0.6 s, which will be explained here briefly for completeness. Refer to, e.g., [103, 81] for a more through description. During the MOT phase, the cooling light is red-detuned by about 23 MHz or around 4 line-widths from the $|3^2\mathrm{S}_{1/2}\ \mathrm{F} = 2\rangle \leftrightarrow |5^2\mathrm{P}_{3/2}\ \mathrm{F} = 3\rangle$ transition. The total atom number in the MOT has been estimated to roughly 10^9 by fluorescence measurements with the cameras placed around the MOT and using a formula provided in [100]. When loading is complete, the MOT coils are switched off 5 ms before the launch in order to give eddy currents sufficient time to decay. During this time the atoms are cooled in the optical molasses. In order to accelerate the atoms upwards a relative detuning between upper and lower MOT beam triplets of $\Delta_{\mathrm{rel}} = \pm 3$ MHz is applied which transfers

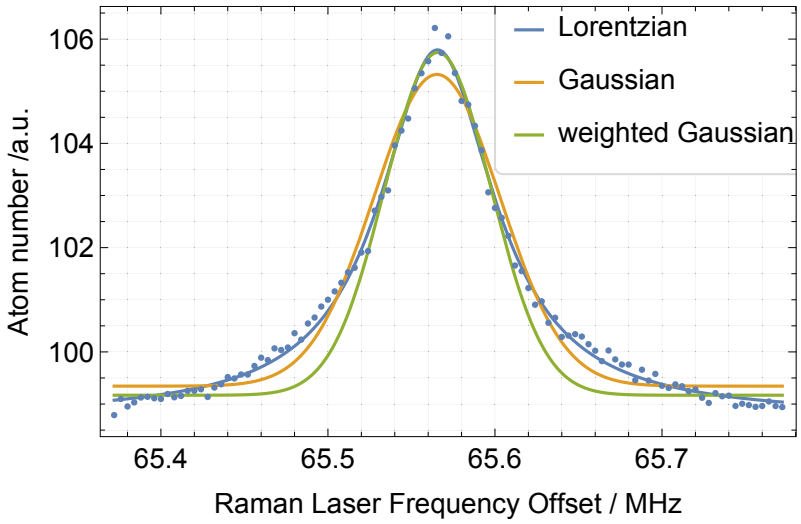

Figure 4.1: Raman frequency scan of the velocity selection pulse. The resulting momentum distribution is Lorentzian and can not strictly be assigned a temperature value [105, 106]. A regular Gaussian fit and a weighted fit which neglects the large wings of the distribution yield effective temperatures of 2.4 µK and 1.6 µK, respectively.

the cooled molasses state to a moving frame with a vertical velocity of:

$$v_{\text{launch}} = \frac{c}{\nu_0} \frac{\Delta_{\text{rel}}}{\cos\alpha} \approx 4.05\,\text{m/s} \tag{4.1}$$

where ν_0 is the optical frequency of the cooling laser and α is the angle between the cooling beam and vertical, which in 1-1-1 configuration equals $\cos\alpha = 1/\sqrt{3}$. At the end of the launch, a far-off-resonance molasses phase optimized for low final temperatures is used to minimize the expansion of the cloud during the rest of the experiment. The final temperature in this regime is proportional to the quotient of light intensity and detuning [81, 104]. During the moving molasses state we therefore increase the detuning in several steps to 144 MHz, or around 24 line-widths, and adiabatically ramp down the light intensity. The repumper light is switched off shortly after the cooling light to make sure that all atoms are in the $F = 2$ hyperfine state The achieved launch temperatures are on the order of 3 µK as detailed in the next chapter which is in agreement with the results from other ^{87}Rb fountains.

4.2 Velocity- and State Selection

After the optical molasses beams are switched off, a velocity-selection Raman pulse [7] is used to select atoms in the magnetically insensitive $m = 0$ sub-state within a narrow the vertical momentum distribution of the launched cloud. This is necessary to limit the mean Doppler-detuning of the cloud during the following interferometer pulses. The resulting low vertical velocity spread of the cloud also simplifies the identification of several systematic effects.

A bias magnetic field is applied and a Doppler-sensitive Raman π pulse with a Gaussian pulse width of $\sigma_t = 12\,\mu\text{s}\,(1/e^2)$ is employed to transfer atoms in a narrow velocity class

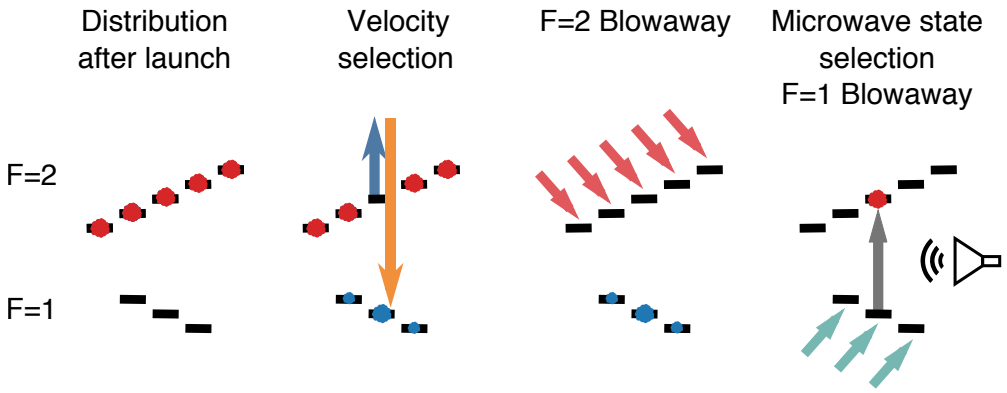

Figure 4.2: Schematic view of the state selection sequence. A Doppler-selective Raman pulse and $F = 2$ Blowaway is followed by a microwave pulse and $F = 1$ Blowaway.

from the $|F = 2, m = 0\rangle$ to the $|F = 1, m = 0\rangle$ magnetic sub-state, followed by a blow-away pulse on the $|F = 2\rangle \rightarrow |F' = 3\rangle$ cycling transition which removes all remaining atoms in the $|F = 2\rangle$ state. Due to the relatively narrow Fourier width $\sigma_\nu = 1/(2\pi\sigma_t) \approxeq 13\,\mathrm{kHz}$ of the pulse, only a about 10 % of the atoms are transferred, corresponding to a velocity spread and effective temperature of

$$\sigma_v = \frac{\sigma_\nu c}{2\nu_L} = \sigma_\nu \lambda/2 = 5.2\,\mathrm{mm/s} \qquad T_{\mathrm{vert}} = \frac{m_{\mathrm{Rb}}\sigma_v^2}{k_B} = 280\,\mathrm{nK} \tag{4.2}$$

after velocity selection. Furthermore, only atoms in the $m_F = 0$ sub-state are selected which leads to another loss factor of 1/5. The whole selection sequence thus decreases the overall atom number in the fountain by about a factor of 50.

The vertical velocity distribution can be measured by scanning the Raman laser frequency difference to measure the selected velocity class as demonstrated in figure 4.1. The shown measurement yields an effective temperature value between 1.6–2.4 µK, in agreement with the coldest reported values in the literature [107, 105]. A more precise assessment of the temperature is difficult due to the Lorentzian momentum distribution which has been reported before [105] and theoretically predicted for sub-Doppler Sisyphus cooling in optical molasses [106]. Since the Lorentzian features of the momentum distribution are most pronounced in the regime of the coldest achievable temperatures and highest densities, this indicates that our molasses launch is well optimized and further reduction of the temperature would require advanced cooling methods such as Raman sideband or evaporative cooling.

The velocity selected atoms are spin-polarized in the $|F = 1, m = 0\rangle$ state, as desired for the interferometer sequence. Due to the large, but finite 700 MHz detuning of both Raman laser frequency components from resonance, however, optical pumping due to spontaneous processes will lead to a small but still significant amount of spurious background atoms in other states. In order to remove these atoms we drive RF transition from the $|F = 1, m = 0\rangle$ to the $|F = 2, m = 0\rangle$ state with a microwave π pulse once the atoms reach the selection region of the vacuum system. A blow-away pulse resonant to the $|F = 1\rangle \rightarrow |F' = 2\rangle$ transition then removes all remaining atom in the $F = 1$ state. See figure 4.2 for a schematic overview of the full selection sequence. Afterwards the cloud consists of a clean sample of about $2{\times}10^{-7}$ atoms in the $F = 2, m = 0$ state with a well defined vertical velocity class ready for the atom interferometer sequence.

4.3 Atom Interferometry

Once the selected atoms in the $|F = 2, m_F = 0\rangle$ state reach the magnetically shielded region, a Mach-Zehnder type atom interferometer is carried out by a sequence of $\frac{\pi}{2} - \pi - \frac{\pi}{2}$ Raman pulses, spaced in time by $T = 260\,\text{ms}$ during standard gravimeter operation. During the free fall of the atoms the Raman laser frequency difference is continuously adjusted by a linear frequency chirp derived from the Raman resonance condition in equation 2.6, yielding

$$\alpha = \frac{d}{dt}\omega_{12} = \boldsymbol{k}_{\text{eff}} \cdot \boldsymbol{g} = \mp 2\pi \times 25.14\,\text{MHz/s}$$

to keep the atoms in resonance with one of the two counter-propagating pair of Raman beams due to the time varying Doppler shift. Here, minus and plus correspond to an upwards and downwards directed $\boldsymbol{k}_{\text{eff}}$, respectively[1]. Since α also changes the one-photon detuning Δ of the Raman lasers at half that rate, another, opposite chirp $\alpha_{\text{R2}} = \pm 2\pi \times 12.6\,\text{MHz}$ is applied to the Raman master laser to maintain a constant $\Delta = -700\,\text{MHz}$ with respect to the $|F' = 1\rangle$ state.

In order to make the interferometer sequence as symmetric as possible around the mean parabolic trajectory of the atoms, the second Raman pulse should in principle happen at its apex. The nearly vanishing velocity[2] at this point, however, would break the Doppler selectivity necessary to distinguish between Raman transitions with upwards and downwards directed $\boldsymbol{k}_{\text{eff}}$ in the retro-reflection scheme depicted in figure 3.5. We therefore conduct the second Raman pulse around 30 ms before the apex which provides a comfortable Doppler detuning with a velocity of around 0.3 m/s, and conduct the first and last pulse while the atoms are closer to the bottom of the interferometer zone.

Each box-shaped Raman pulse is implemented using fast RF switches to minimize transient times and associated phase shift, see also [11]. The pulse length depends on the Raman power and was, e.g., adjusted to 34 µs for a π pulse and 17 µs for a $\pi/2$ pulse during the comparison campaign in Onsala. To keep the effective Rabi frequency constant and control light shifts, the power of Raman Master and Slave laser frequencies were actively stabilized to 41 mW and 24 mW, respectively, using the intensity stabilization system described in chapter 3.3.1. Because this system does not account for slow drifts of the fiber coupling efficiency between Raman module and physics package, the total Raman power is additionally stabilized with a second, slow feedback loop. It uses the auto-collimation system detailed in chapter 6.2.1 to measure the Raman power that returns from the physics package during the central interferometer pulse which provides the largest retro-reflection signal. Since the auto-collimation efficiency is actively stabilized by the Piezo Tip/Tilt mirror, this is directly proportional to the total Raman power in the physics package. A low-pass filter is first applied to this signal to remove shot-to-shot fluctuations due to tilt noise. The RF power applied to the switching AOM depicted in figure 3.15 is then used to remove total Raman power drifts over the course of hours and days.

[1] Due to the $|F = 2\rangle$ initial state used in GAIN, upwards directed photon recoil correspond to downwards directed $\boldsymbol{k}_{\text{eff}}$, and vice versa. Here, the recoil directions are sometimes labeled $k_+ (\uparrow \boldsymbol{v}_{\text{rec}})$ and $k_- (\downarrow \boldsymbol{v}_{\text{rec}})$.

[2] The splitting of the interferometer arms leads to a residual velocity at the mean trajectory's apex of $\pm\frac{\hbar k_{\text{eff}}}{2m_{\text{Rb}}} \approxeq \pm 6\,\text{mm/s}$ for the upper and lower interferometer arm, respectively. Compare figure 2.2.

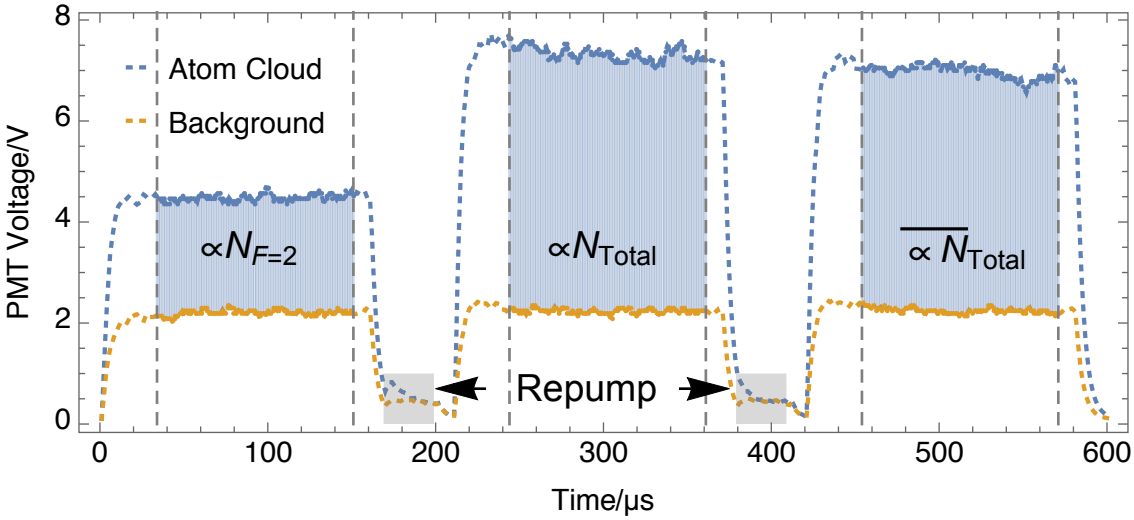

Figure 4.3: Fluorescence Detection scheme. The blue line is the signal of the atom cloud while the yellow signal was taken 40 ms afterwards and indicates fluorescence from thermal background gas. The integral for each pulse is indicated by the blue shaded areas while disregarding the slopes. Gray shaded areas show optical pumping from $|F = 1\rangle$ to $|F = 2\rangle$ with repump light.

4.4 Detection

Once the atoms reach the detection region after the end of the interferometry sequence, the internal state population is detected with a pulsed measurement using the fluorescence imaging system described in chapter 3.1.3. It consists of a sequence of three short detection beam pulses as depicted in figure 4.3, during which the laser frequency is set to a -3 MHz red-detuning relative to the $F = 2 \leftrightarrow F' = 3$ resonance. During the first pulse with a length of 400 µs only atoms in the $|F = 2\rangle$ state contribute to the fluorescence. A subsequent 10 µs pulse of repump light pumps atoms previously in $|F = 1\rangle$ into the upper $|F = 2\rangle$ state. The second detection pulse thus induces more fluorescence corresponding to the total number of atoms. The ratio of the first and second pulse signal area then yields the relative state population $P_{F2} = N_{F2}/N_{\mathrm{Total}}$, from which the interferometer phase can be deduced by inverting equation 2.41. After the second detection pulse, auxiliary repump- and detection pulses are carried out for additional time-of-flight information and to test for potential systematic effects.

Noise introduced by the detection system is an important factor and originates from a list of uncorrelated sources. Frequency and intensity fluctuations of the retro-reflected detection beam, electronic and PMT noise are potential technical noise sources which should be suppressed as much as possible. Additionally, the standard quantum limit provides a fundamental limitation to the achievable uncertainty of the detected state population $\sigma_{P2} \geq 1/\sqrt{N_{\mathrm{Total}}}$ for a given number of atoms. If a detection system achieves this limited it is said to be limited by atomic shot noise, which is optimal in the sense that the only remaining way to further decrease noise is to increase the atom number.

In order to quantify the amplitude of detection noise in the system the following terms

will be used in addition to σ_{P2}

$$SNR^{-1} = \sigma_\Phi := \frac{2\sigma_{P2}}{A} \qquad \sigma_g = \frac{\sigma_\Phi}{k_{\text{eff}} T^2} = \frac{2\sigma_{P2}}{A k_{\text{eff}} T^2} \tag{4.3}$$

when measuring on the slope of the interferometer fringe, where A is the peak-to-peak contrast ($A = 1$ for 100 % contrast). These quantities can readily be measured by replacing the interferometer pulse sequence with a simple $\pi/2$ pulse and recording the fluctuations of σ_{P2}. This was carried out during the gravity measurement campaigns and yielded values σ_{P2} of 0.005–0.009. Given the interferometer contrast of approximately $A \cong 0.55$ this results in phase noise σ_Φ of 18–32 mrad/shot or signal-to-noise ratio (SNR) of 25–52. The given range here indicates the observed performance spectrum at the conducted measurement campaign due to varying levels of fountain- and detection optimizations.

The detection volume during those campaigns had dimensions of $(4{\times}10{\times}10)\,\text{mm}^3$ and contained about 3 % of the remaining atoms due to horizontal spreading of the cloud [93]. Using the atom number estimation from chapter 4.2, this means that approximately $5{\times}10^5$ atoms contributed to the detection signal. Without any technical noise terms, atomic shot noise provides a limit of $\sigma_{P2} \geq 1.4{\times}10^{-3}$, about 4-6 times lower than observed.

The detection system is therefore probably not limited by atomic shot-noise but technical noise contributions, although a significant uncertainty in the above atom number estimation exists. The detection beam is provided by a DFB diode laser with a linewidth of about 1 MHz, which is only a factor 6 smaller than the transition linewidth, and not actively intensity-stabilized. Frequency- and intensity noise caused by the detection beam could thus easily dominate overall detection noise. Electronic noise caused by the PMT or its amplifier, or intensity noise of the Raman beams are other potential contributions to detection noise.

Since the measured detection noise had a maximum value of $\sigma_g \leq 30\,\text{nm/s}^2$, which is more than a factor two smaller than the next bigger noise terms caused by vibrations Raman phase noise, this was not of major concern for the conducted gravity measurements. If the latter are reduced significantly in the future, or for differential interferometry where vibrations and Raman laser phase noise are common-mode, improvements of the detection systems will certainly be of high interest.

4.5 Gravimeter Operation

After describing in detail the individual elements of the atomic fountain sequence in the previous chapters, we will now describe how the full interferometer phase Φ is obtained from the detected state population P_{F2}. Afterwards, the measurement protocol implemented to conduct continuous gravity registrations at the optimal phase setting will be reviewed.

4.5.1 Central Interferometer Fringe

Since the atom interferometer output is a periodic fringe signal the phase of one individual measurement can only be determined modulo 2π. Many optical interferometer setups, such as FG-5 falling corner cube gravimeters, circumvent this problem by continuously recording the output fringe over the entire course of one measurement run and counting the number of fringes. Since the detection process destroys the coherent superposition

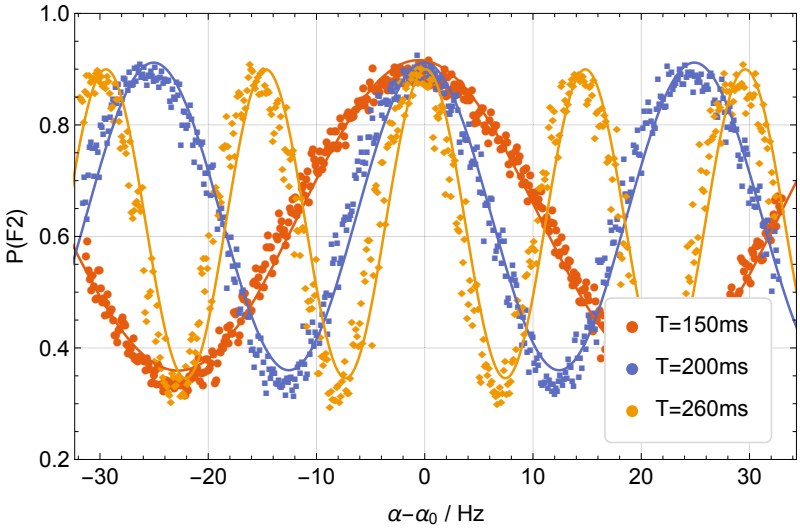

Figure 4.4: Interferometer fringes during a central chirp rate scan for different pulse separations T. At the central interferometer fringe with the correct chirp rate $\alpha_0 \approxeq 2\pi \times 25.14\,\mathrm{MHz/s}$ the measured state population is independent of T. The observed fringe contrast $A \approxeq 0.55$ also only shows a slight dependence of T.

of two states, however, this is not an option for atom interferometers. Instead, AIs are usually operated close to the central interferometer fringe by adjusting the frequency chirp α which keeps the Raman laser on resonance with the atomic transition during the atom's free fall. At the correct setting this chirp exactly compensates for the gravity induced shift so that $\alpha = \boldsymbol{k}_{\mathrm{eff}} \cdot \boldsymbol{g}$ so that the total interferometer phase in equation 2.20 vanishes.

In order to operate on the central, or dark, fringe and keep the interferometer phase Φ smaller than 2π with our standard parameters of $T = 260\,\mathrm{ms}$ and a total gravity induced phase of $\Phi = 1.07{\times}10^7\,\mathrm{rad}$, the chirp rate α has to be determined with an accuracy of $\frac{1}{T^2} = 15\,\mathrm{Hz/s}$. This corresponds to a gravity value uncertainty of $5.8{\times}10^{-6}\,\mathrm{m/s^2}$ which is non-trivial to predict at an unknown site and affords an independent measurement. This can be done in a straightforward way by altering the time T between pulses which leaves the interferometer signal constant when operating on the central fringe as shown in figure 4.4.

4.5.2 Optimized Mid-Fringe Operation

Once the interferometer operates with the correct chirp-rate it continuously measures gravity in 20 min sets using a protocol described in the following and in [80]. At the beginning of each set, a full interferometer fringe is scanned using 32 data points in order to determine the fringe contrast, amplitude and phase. Given those parameters, the measurement program then operates the interferometer within the $[-\pi, \pi]$ interval around the central fringe maximum at the most sensitive mid-fringe setting, alternating successive runs between the left and right fringe slope. This optimizes the phase sensitivity of the interferometer and enables the rejection of slow fringe amplitude- and offset drifts as well as imperfections in the detection system which lead to small distortions of the fringe signal on the flanges as detailed in chapter 6.6 of [80]. Due to tidal gravity changes, which are

on the order of $1\,\mu m/s^2$, the interferometer phase changes by about 1 rad on timescales between 6–12 h. In order to keep the interferometer operating at mid-fringe as described before the phase setting has to be corrected during these slow changes. This is done using a slow software feedback loop with a 30 s integral and weak proportional element to equalize the amplitude on the left- and right side of the fringe [93]. It proved challenging for the feedback loop, however, to keep the interferometer phase sufficiently close to the mid-fringe point during relatively quick gravity changes on spring tide slopes such as shown in figure 1.4. Since these large tidal changes can easily be predicted, an additional feed-forward path based on a simple, purely synthetic tidal model was therefore implemented during this work. The feedback loop thus only needs to compensate for small residual gravity changes not contained in this model, e.g. due to atmospheric- or loading effects. The amplitude of these residual variation is at least one order of magnitude smaller at around $100\,nm/s^2$ over several days, which can be easily handled by the feedback loop.

Interleaved into the procedure described above is a momentum recoil flip between $k_\uparrow$ and $k_\downarrow$ configuration at every second shot. This enables us to identify and cancel systematics effect such as group delays in the Raman frequency chain as detailed in chapter 6.7 with high temporal resolution as demonstrated. Since contrast and amplitude are slightly different for upwards- and downwards directed momentum recoil, separate fringes are scanned for both configurations. The final gravity value in this protocol is derived by averaging over four consecutive runs containing every possible configuration:

$$\Phi_{\text{final}} = \frac{1}{4}\left(\Phi_\uparrow^{\text{left}} + \Phi_\uparrow^{\text{right}} + \Phi_\downarrow^{\text{left}} + \Phi_\downarrow^{\text{right}}\right) \tag{4.4}$$

4.5.3 Gravity Value Extraction and Height Transfer

Running the atom interferometer in this measurement protocol for a few days yields the highly dynamic tidal gravity signal introduced in chapter 1 and shown in figure 1.4. Reducing this signal to a constant, site-dependent gravity value using an appropriate model for the observed time-dependence is a standard problem in gravimetry as described before.

Tidal models were calculated with the free software Tsoft [47] using model parameters provided by M. Schilling[3] and H. Wziontek[4]. Residual gravity signals due to atmospheric pressure changes were removed with an admittance factor of about $3\,nm/s^2/hPa$ and local pressure recordings. After subtracting the polar-motion correction and transferring the value from the effective measurement height given by equation 2.37 to a reference height, one can extract the local gravity value as the mean value of the residual dataset. Small differences due to the individual circumstances during the 4 performed gravity comparisons are described in detail in chapter 5.3.

Summary

This chapter gave a detailed account of the experimental sequence and steps taken to extract the gravity value during the mobile gravity measurements presented in chapter 6. Special attention was given to detection noise sources and a measurement scheme designed to reject systematic effects in the atom interferometer, since the accuracy and stability of the measured gravity data is a central aspect of this work. The next chapter will present

[3] Institut für Erdmessung, Leibniz Universität Hannover
[4] Federal Agency for Cartography and Geodesy, Leipzig

the result of the conducted gravity measurement and analyze the performance achieved with respect to other gravimeters during the comparison campaigns.

Chapter 5

Atomic Gravimetry at Geodetic Observatories

The goal of this work is to optimize and quantify the absolute accuracy and other key performance characteristics of GAIN during gravity measurements. Due to the dynamic nature of gravimetric signals this can best be achieved through direct comparisons with other, collocated gravimeters. A total of four gravity comparison campaigns were therefore conducted between 2012 and 2015 as part of this work and will be presented in detail below. The first two campaigns were carried out in the physics building at HUB and involved simultaneous operation over several days of GAIN and a gPhone spring-based relative gravimeter in December 2012, and of GAIN and the FG5X-220 absolute gravimeter in June 2013.

Since a university building in Berlin is a noisy, suboptimal place for state-of-the-art gravimetry and in order to demonstrate the mobility of the GAIN setup, the following two campaigns were conducted at designated geodetic reference stations in Wettzell, Bavaria in November 2013 and in Onsala, Sweden in February 2015. The superconducting relative gravimeters SG-30 and OSG-054, respectively, served as a reference for the comparison during those campaigns in combination with a previously determined absolute gravity value. All GAIN measurements were conducted in a team including my co-workers M. Hauth and, with the exception of the last campaign, V. Schkolnik. The data obtained during the first three campaigns is also presented in [80, 101] with two notable differences: First, the extensive evaluation of the systematic error budget in chapter 6 enables the specification of an absolute gravity value for the last three campaigns including the instrumental uncertainty. Second, the result of the repeated data analysis presented here includes a post-correction of vibrational noise as detailed in chapter 5. Furthermore, key characteristics such as the magnitude and origin of the observed measurement noise and time delays [80] have been revisited giving additional insight.

5.1 Initial Comparisons in Berlin

The first direct comparison between GAIN and another gravimeter was carried out in the laboratory at HUB from November to December 2012. The gPhone-98[1] relative spring-based gravimeter from Institut für Erdmessung, Leibniz Universität Hannover (IfE) oper-

[1] Microg-LaCoste

Figure 5.1: Left: GAIN and FG5X-220 during the comparison in the mechanics workshop of the physics department at HU-Berlin in June 2013. Right: The absolute gravity reference point is located under the FG5 super-spring.

ated in the same room as GAIN to provide the comparison signal. In order to permit decay of non-linear drifts and run-in effects of its precision spring after transport, the gPhone was set up several weeks prior to the comparison measurement. GAIN had been equipped and tested before the campaign with a fully functional Tip/Tilt mirror system for Coriolis compensation and automatic Raman retro-reflection. Figure 5.3 shows the recorded gravity signal from both sensors over the course of several days. In order to remove environmental gravity changes from the raw signal (shown on top), a model composed of earth tides, ocean loading, air-pressure and polar motion effects was subtracted from the data. See Appendix B.2 for the details of this model. The gPhone output signal was corrected by the same synthetic model plus additionally for a linear drift of $102\,\mathrm{nm/s^2/day}$ as determined by IfE [108]. The remaining gravity variations are within $20\,\mathrm{nm/s^2}$ which indicates good agreement between both sensors and the applied synthetic model. Differences between the GAIN and gPhone residuals on this level are apparent, however, and in this case suggests that instrumental effects in GAIN deteriorated the signal during this early campaign. A complete analysis of the GAIN long-term stability development is given in chapter 5.5.

The GAIN residual signal furthermore shows short-term RMS fluctuations of 80–$200\,\mathrm{nm/s^2/\sqrt{Hz}}$, compared to the gPhone which fluctuates between 30–$200\,\mathrm{nm/s^2/\sqrt{Hz}}$ as shown in figure 5.2. The time dependence of the RMS fluctuations over the measurement period shows an interesting difference between both sensors. Whereas the gPhone RMS is clearly correlated to daily vibration noise in the environment, such as human activity in the building or room, GAIN shows an elevated and uncorrelated noise level which could, in this instance, not be connected to a specific external disturbance. This indicates that floor vibrations, which were measured by a low-noise seismometer, are not the dominating noise term. The GAIN short-term noise behavior will be examined in detail in chapter 5.4.

The second measurement campaign carried out in Berlin took place in June 2013 and

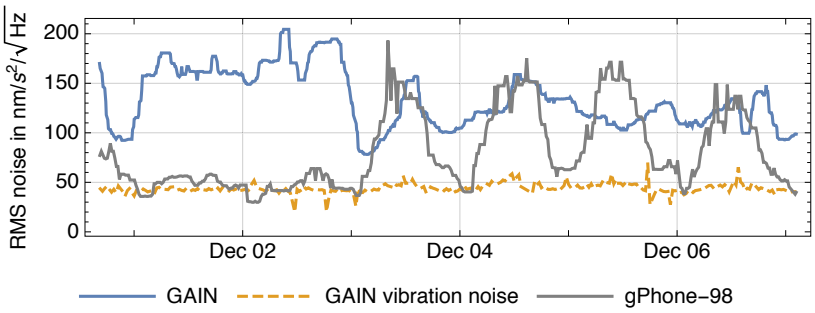

Figure 5.2: Equivalent total RMS noise for GAIN and gPhone residuals during the first comparison. The latter shows clear correlation with a weekly work schedule in the university building whereas GAIN does not. The yellow dashed line shows the GAIN vibration noise level computed from platform accelerometer data according to equation 2.39.

involved continuous GAIN measurements over approximately one week and simultaneous operation of the Microg-LaCoste FG5X-220 absolute gravimeter, which was provided by IfE and operated by O. Gitlein and M. Schilling. Successful operation of the FG5 is restricted to solid concrete surfaces[70, 14], due to floor excitations caused by its moving internal test mass. The comparison campaign therefore took place in the mechanical workshop on the ground floor of the physics department, where an absolute gravity reference point had already been established by the Federal Agency for Cartography and Geodesy (BKG) during an earlier measurement in 2010 [109]. The transport of GAIN from the laboratory on the first/second floor to the workshop environment was furthermore used to test the mobility of the setup after implementing a more robust, new amplification[101] and switching/distribution module[80] for the MOT light as described in chapter 3.3. During operation the FG5 performed 50 drops per hour with an interval of 10 s between drops in order to minimize wear and tear of the instrument. Both gravimeters were set up with a distance of approximately 2 m, with the FG5 standing on the reference point marker as shown in figure 5.1. After simultaneous operation for a few days, the position of both gravimeters was switched.

The tidal- and residual gravity data obtained during the second campaign are shown in figure 5.4. After subtracting the identical model already used in campaign 1 adapted for the measurement period, GAIN shows a very stable residual gravity level with hourly fluctuations of less than 20 nm/s^2 and without apparent long-term drift. The GAIN residual's RMS noise varies significantly between 110–280 nm/s^2/$\sqrt{\text{Hz}}$ and correlates weakly with the activity of the air conditioning in the room. This indicates that air convection or a related noise source may dominate during this campaign despite the attempts to shield the Raman mirror from these kinds of disturbances. This will be discussed in more detail in chapter 5.4. The FG5X-220 residuals show a higher equivalent RMS value of 500–3000 nm/s^2/$\sqrt{\text{Hz}}$ which follows closely the weekly schedule of human/seismic activity in the building, similar to the previously observed gPhone behavior. It should be noted that much lower FG5 noise levels have previously been reported under quiet micro-seismic conditions and with higher repetition rates [110]. The FG5 residuals furthermore show a global drift of approximately 50 nm/s^2 over the course of a few days which is not visible in the GAIN residuals and could not be explained conclusively. The comparison of the absolute gravity values of GAIN and FG5X-220 result will be carried out in chapter 5.3.

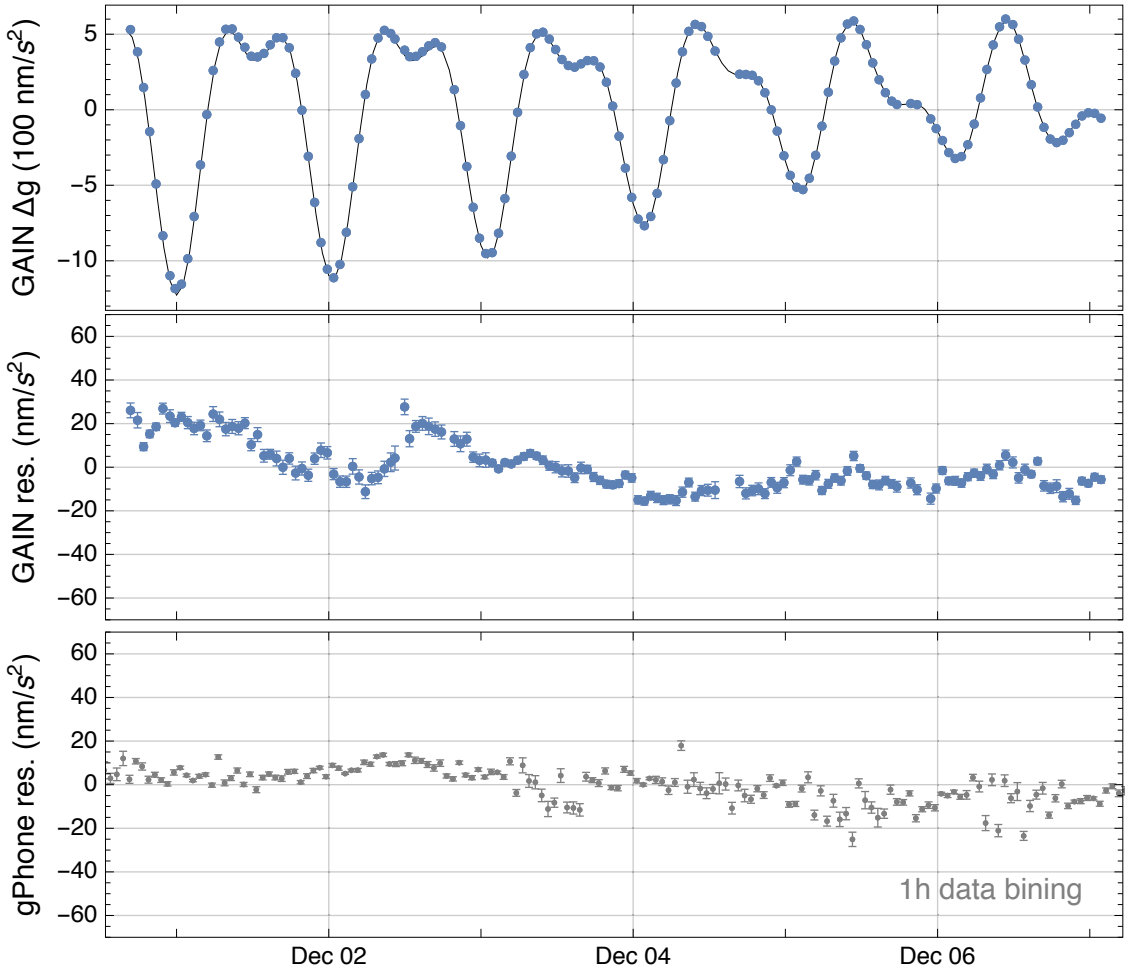

Figure 5.3: First comparison campaign in Berlin, 2012: gravity signal by GAIN and the gPhone-98. Top: GAIN tidal gravity data (blue) vs. synthetic model of gravity changes due to earth tides, ocean-loading, air-pressure and polar motion (black solid line). Middle: GAIN residual gravity signal after subtracting the above model. Bottom: gPhone residuals after subtracting the same model and a linear drift of 102 $\mathrm{nm/s^2/day}$ (see text)

.

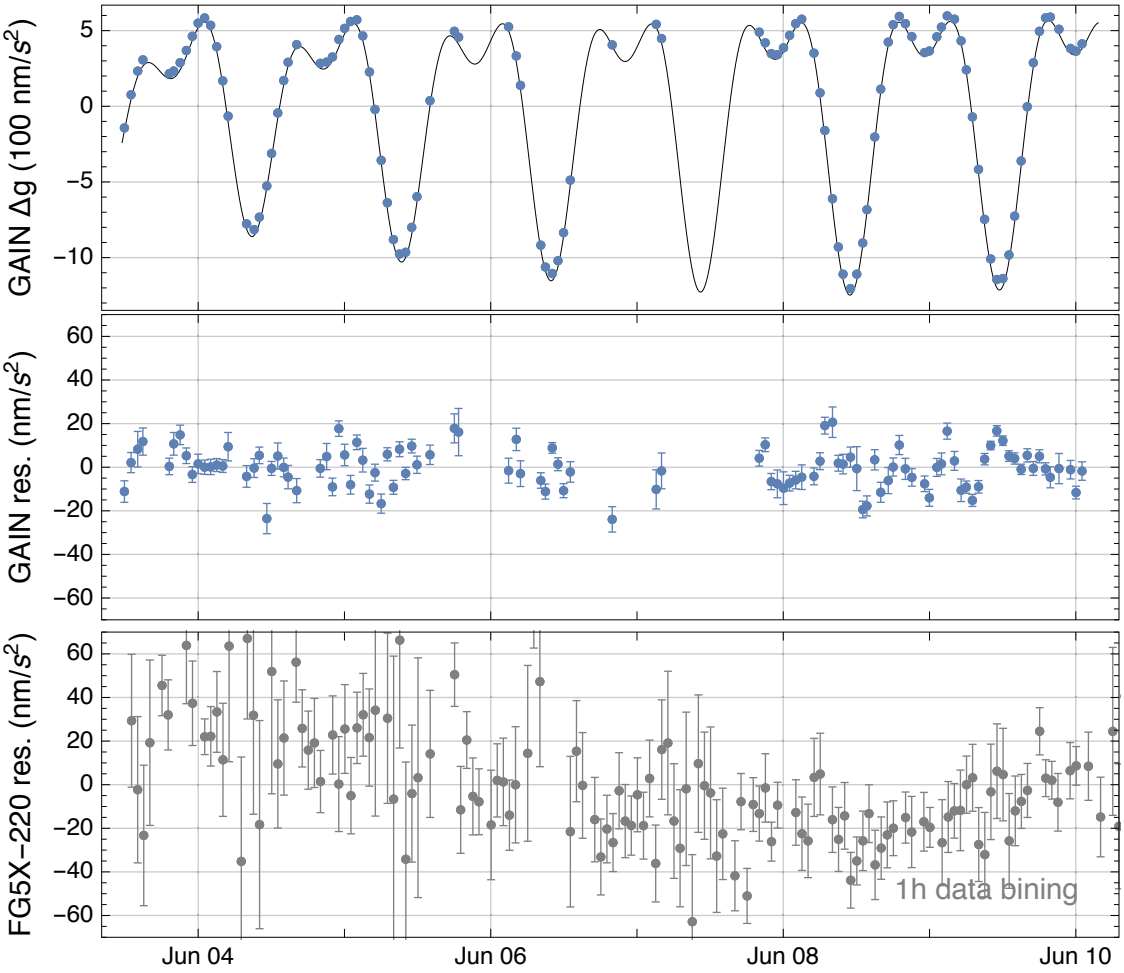

Figure 5.4: Second comparison campaign in Berlin, 2013: GAIN and the FG5X-220 gravity data comparison. Top: GAIN data (blue) vs. a synthetic model of gravity changes due to earth tides, air-pressure and polar motion (black solid line). Middle: GAIN residual gravity signal after subtracting the above model. Bottom: FG5X-220 residual gravity after subtracting the same model

.

Figure 5.5: Year and locations of the gravity measurement campaigns carried out with the GAIN atomic gravimeter as part of this work. In addition to the depicted institutions, the Institut für Erdmessung (IfE) from Leibniz University Hannover supported the comparisons in Berlin and Onsala with a gPhone and the FG5X-220 gravimeter.

5.2 Mobile Campaigns

The initial comparisons at HUB presented in the previous chapter provided a testing ground to separate instrumental effects with moderate amplitudes of more than 10 $\mathrm{nm/s^2}$ from physical gravity changes in order to identify the underlying systematic effects still present at that time in the GAIN setup. This led to the implementation of additional subsystems for, e.g., Raman intensity stabilization system and the optimization and automation of other parts of the setup such as the Tip/Tilt Raman mirror and the automated tilt alignment system. Furthermore, technical issues regarding the reliability and robustness of the mobile setup were identified and removed, specifically concerning the MOT laser system, vibration isolator and instrument control software. To demonstrate the mobility- and performance-improvements achieved through these modifications we performed two measurement campaigns at geodetic observatories in Germany and Sweden in order to compare the GAIN signal with a low-noise superconducting gravimeter. The following chapters will present the result of these campaigns and then provide a detailed analysis of the comparison between all involved gravimeters.

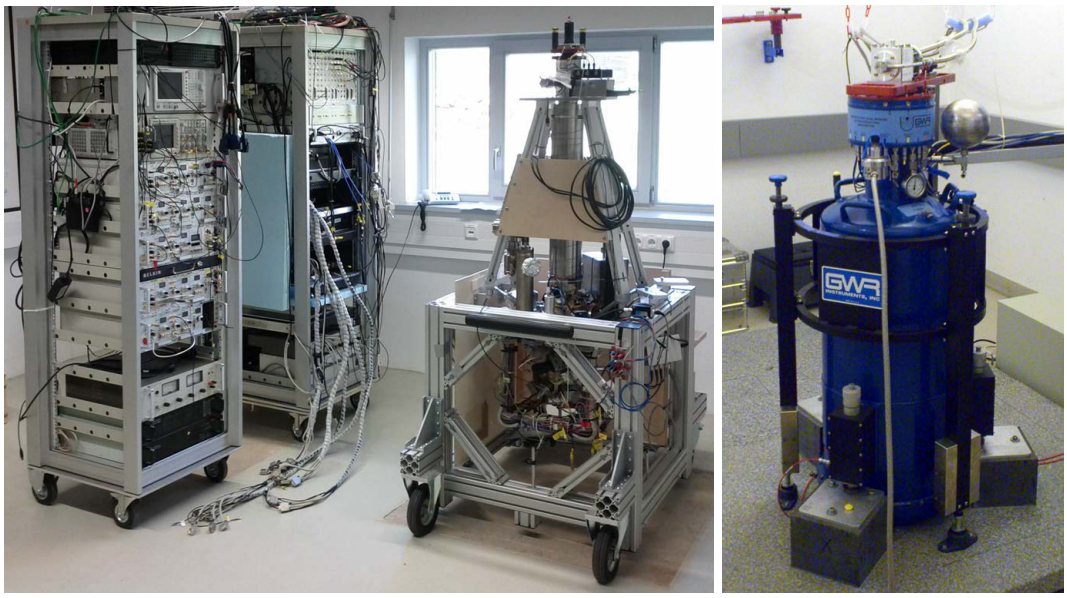

Figure 5.6: Gravimeters involved in the comparison campaign at the geodetic observatory Wettzell in November 2013. Left: Gravimetric Atom Interferometer (GAIN). Right: GWR SG-030 superconducting gravimeter. Both instruments were located in the same building at a horizontal distance of about 2 m.

5.2.1 GAIN Transport and Mobility

Since GAIN was from the beginning designed as a transportable instrument it was brought to the location of both measurement campaigns using a medium-sized truck[2]. The disassembly and transport of the physics package, laser- and electronics rack, some additional test equipment and tools was conducted within a single day by two persons. Reconnecting the three individual units, re-aligning the atomic fountain and optimizing the atom interferometer required approximately three days at the new location. This process could be significantly accelerated to only a few hours by optimizing the work-flow, software automation and some minor modifications to the physical setup. For instance, integrating the electronics- and optics rack into a single transportable unit could be done using the existing hardware and would greatly reduce the time needed for the re-establishing the numerous connections of the data-acquisition-, power- and laser systems.

In order to prevent quick temperature drops of the vacuum chamber despite cold winter temperatures during the entire transport from Berlin to Onsala, Sweden in February 2015, the physics package was surrounded with insulating Styrofoam and phase change material (PCM)[3]. The PCM successfully maintained the temperature of the vacuum system above 15 °C during the whole 20 h transport despite outside temperatures around 0 °C.

5.2.2 Wettzell campaign in November 2013

The first mobile campaign was conducted at the Geodetic Observatory Wettzell in Bavaria, Germany, which is operated by BKG and is one of the fundamental reference stations of

[2]Gross vehicle weight less than 3.5 t, no special license necessary.
[3]www.rubitherm.eu

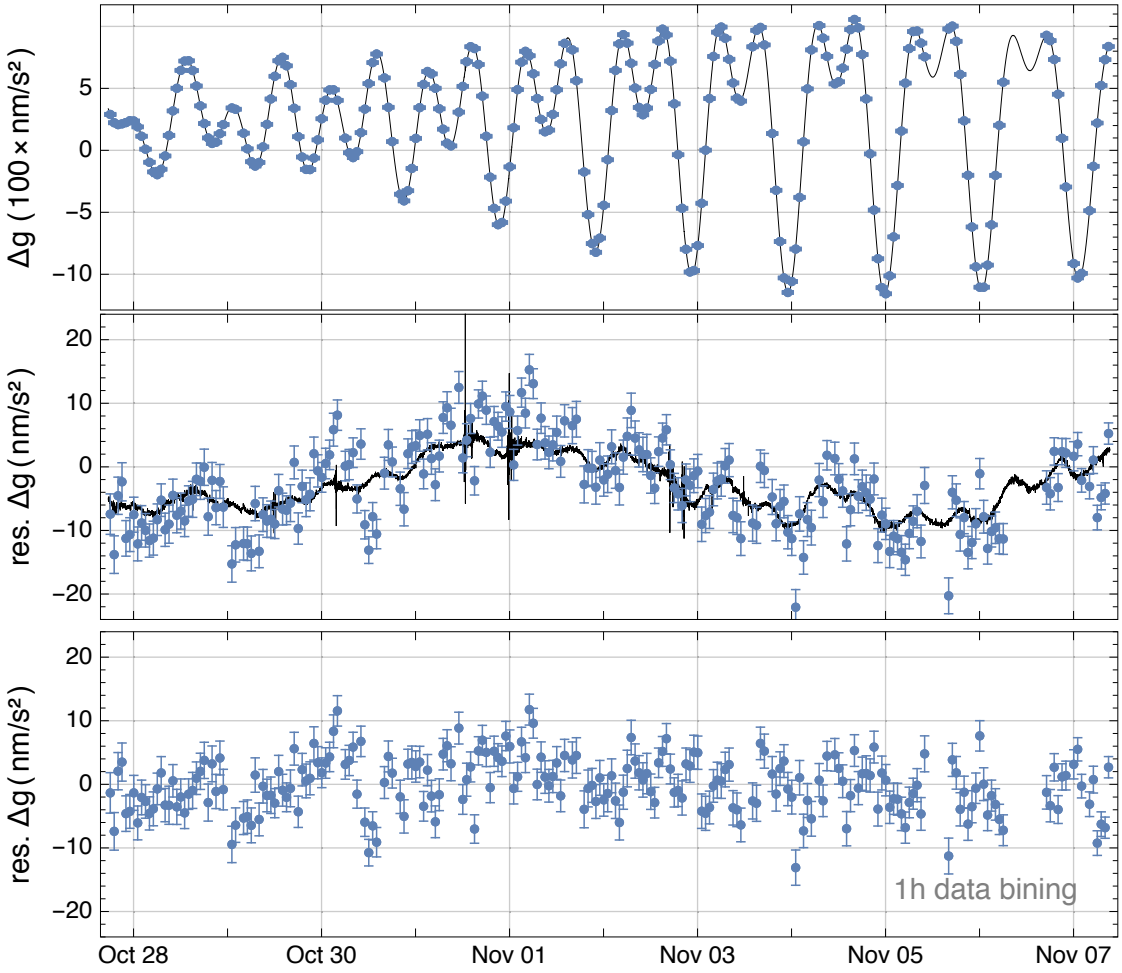

Figure 5.7: Comparison campaign in Wettzell, 2013. Top: GAIN data (blue) vs. SG-30 (black). Middle: GAIN (blue) and SCG (black) residual gravity signal after subtracting a synthetic model including earth tides, ocean loading, air-pressure and polar motion. The spikes in the black curve correspond to small earth quakes. Bottom: Difference between GAIN and SG-30 data.

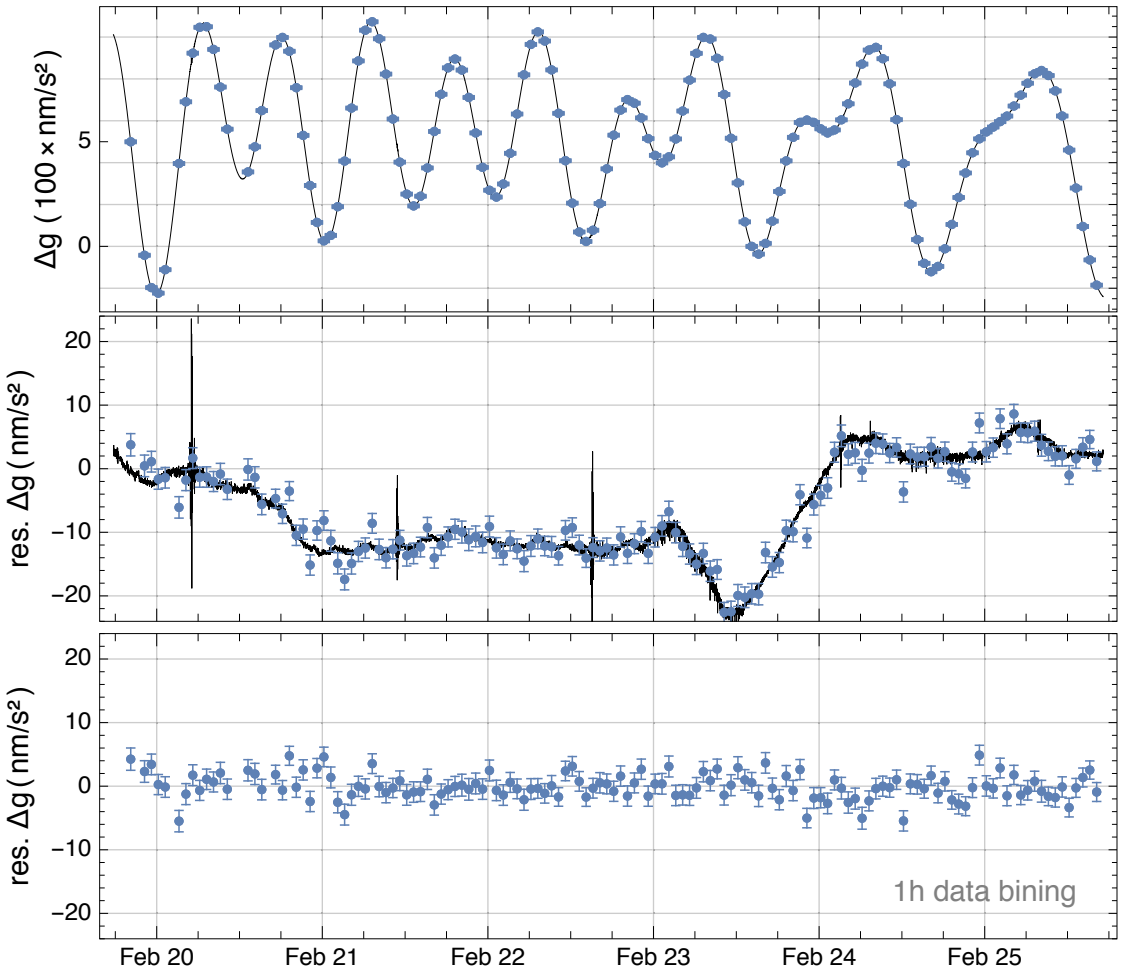

Figure 5.8: Six days of gravity data measured during the Onsala comparison campaign. GAIN data is shown in blue, SCG data in black. Top: raw tidal gravity variations without visible differences between both dataset. Middle: residual gravity after subtracting a synthetic model containing local Earth tide, loading effects, air-pressure and polar motion. Note the small earthquakes in the SCG signal. Both sensors are in excellent agreement. Bottom: Difference between GAIN and SCG datasets. No significant signal is left in the difference which indicates the absence of instrumental drifts over the measurement period.

the German Gravity Network. The local gravity value is measured regularly with state-of-the-art absolute gravimeters and monitored continuously by an on-site SCG. The GAIN campaign took place in the so-called new gravimeter building which is equipped with 5 concrete pillars which are decoupled from the building's foundation, and a separate room and pillar for the SG-30[4] instrument in order to minimize temperature fluctuations. The SG-30 is a double-sphere SCG with two independent sensor units. Its internal drift after the decay of initial run-in effects is small and linear with $(-161.84\pm0.24)\,\mathrm{nm/s^2/year}$ and $(-54.03\pm0.24)\,\mathrm{nm/s^2/year}$ for the lower and upper sphere, respectively [111]. It thus provided a precise reference for environmental gravity variations between absolute gravimeter campaigns and constituted an optimal environment to characterize the performance of the GAIN setup. Of the 5 pillars, 4 are meant for simultaneous comparison of absolute or relative gravimeters. During the campaign, GAIN was the only other instrument present and was set up on pillar FA. See appendix B.4 for further details of this campaign and a plan of the gravimeter building. After characterizations and initial tests of GAIN in October 2013, about two weeks of gravity registrations were conducted. Figure 5.7 shows the resulting gravity data of GAIN and the SCG indicating excellent agreement in the measured tidal gravity signals. Correcting for the tidal model, air-pressure, loading effects and polar-motion reveals small residual signals with a magnitude of less than $\pm10\,\mathrm{nm/s^2}$. GAIN and the SCG agree well on this residual signal, which is caused by local gravity changes not contained in the above model. The agreement of both sensors shows the absence of time dependent instrumental effects in the GAIN data and highlights the benefit of a well-characterized, stable SCG as a reference signal. This is confirmed also by the difference between SCG and GAIN which shows virtually no remaining signals, and will be analyzed more in detail in section 5.5.

5.2.3 Onsala campaign in February 2015

The second and final mobile measurement campaign took place at Onsala Space Observatory (OSO) in Onsala, Sweden in February 2015. Several improvements of GAIN were implemented leading up to this comparison campaign. The physics package was equipped with a magnetic shield around the MOT chamber which eliminates cross-coupling between the MOT coils and the vibration isolator and shortens the set-up time by eliminating the need for background magnetic fields compensation. Depleted Rubidium sources inside the vacuum chamber had been replaced with fresh ones. The vibration post-correction was furthermore used for the first time during this campaign. Finally, drawing from experiences made during the previous campaign in Wettzell, the strength of the Raman auto-collimation peak was actively stabilized and the phase control routine was improved with a feed-forward path to keep the interferometer at mid-fringe more accurately during fast tidal gravity variations.

OSO is a Swedish national facility for Radio astronomy operated by Chalmers University Gothenburg and operates several radio telescopes for astronomy and geodesy. Due to its status as a geodetic fundamental station it also operates a SCG to measure temporal gravity changes, and several absolute gravity measurements have been conducted with FG-5 gravimeters over the last decades. The GWR SG-054[5] has been in operation since June 2009. It is a single sphere instrument with a linear drift rate of $(-21.91\pm0.59)\,\mathrm{nm/s^2/year}$

[4] made by GWR instruments

[5] `http://holt.oso.chalmers.se/hgs/SCG/monitor-plot.html`

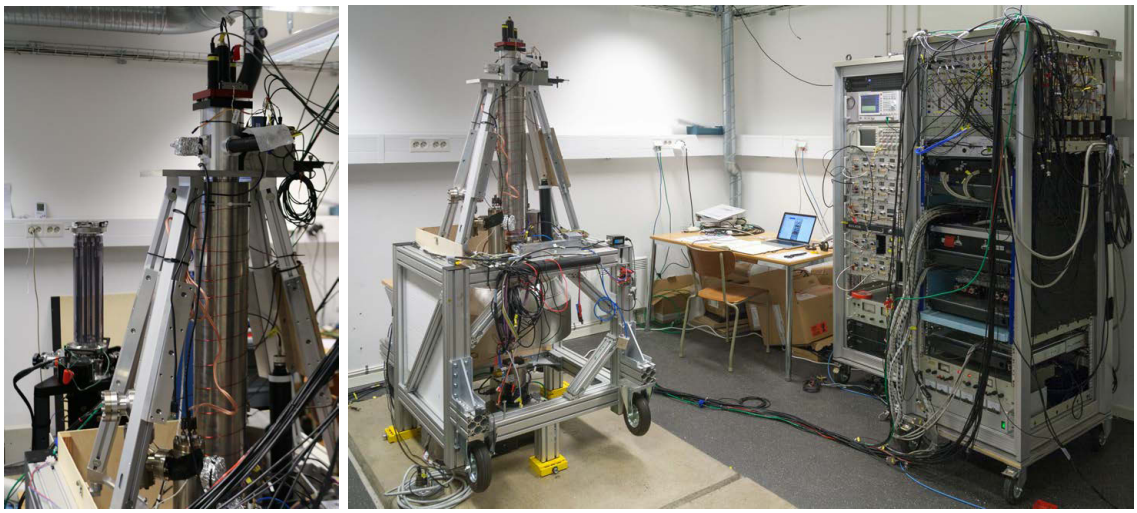

Figure 5.9: Instruments present during the comparison campaign at Onsala space observatory in February 2015. Left: GAIN physics package in front of th FG5X-220 dropping chamber. Right: Overall GAIN setup. The superconducting gravimeter GWR SG-054 was operating continuously in the same building at a horizontal distance of about 3 m

at the time of the GAIN measurement. All gravimetry experiments at OSO took place in the dedicated gravimeter building a few hundred meters away from the Kattegat coast. It was built on top of a large, sealed off rock formation in order to reduce the magnitude of hydrological gravity signals. The concrete pillars are directly connected to bedrock for optimal stability. The SCG is located in a separate room in order to reduce temperature fluctuations. Two additional pillars for visiting gravimeters are available at a horizontal distance of about 2 m as detailed in appendix B.4. The setup- and alignment preparations between transport and taking actual gravity data again took a few days. A total of 3 weeks of gravity data were collected by GAIN between February 10th to 25th. Due to the proximity of the coast and heavy weather micro-seismic noise was strongly enhanced during the measurement period. This did not compromise the GAIN performance as detailed in chapter 5.4 but lead to increased noise level in the FG5X-220 measurements. The first 10 days of gravity data were unfortunately collected with an inaccurate setting of the Coriolis compensator (see chapter 6.1.1). The Tip/Tilt rotation axis was set using a marker on the pillar which proved to be inadequate with a deviation of around 16 ° from the correct value obtained from satellite images. This part of the dataset therefore suffers from a substantial residual Coriolis shift which depends on the exact value of the atomic velocity along the South-North axis and can hardly be corrected for in post-processing. We therefore use only the last data segment with a length of 5 days, which was taken using the corrected setting, for the main part of the analysis. All further analysis regarding accuracy and stability also refers to only this part of the data. The upper graph in Figure 5.8 shows the GAIN tidal gravity data which indicates excellent agreement to the SCG signal. A first residual signal was obtained using a synthetic tidal model including ocean loading, air-pressure and polar-motion effects. It shows residual fluctuations of roughly 30 $\mathrm{nm/s^2}$ with excellent agreement between GAIN and the SCG. Subtracting both instruments' outputs yields flat white noise with very little long-term fluctuations, indicating even better agreement between GAIN and the SCG than during the first mobile campaign

in Wettzell. This confirms the effectiveness of the instrumental improvements before this campaign and shows the best performance reached by GAIN to date. In order to assess the absolute gravity value during this campaign, the FG5X-220 absolute gravimeter was also present for a direct comparison and to provide a current absolute gravity value as detailed in chapter 5.3. The instrument was operated by M. Schilling from IfE. Measurements with this instrument were conducted in North- and South-facing configuration on both pillars to rule out potential orientation dependent offsets. Each configuration was measured again after repeating the setup procedure to exclude other potential setup related error sources. Both precautions yielded no systematic offsets [70] which is an improvement over the previous generation FG5-220 and instills confidence in the obtained reference value. We therefore adopt the specified instrument uncertainty of $20\,\mathrm{nm/s^2}$ for the reference value.

Both GAIN and the FG5X-220 measured on adjacent pillars and their location was rotated after four days to compare g on both positions as well as the gravity difference between both locations. GAIN was operating continuously at its standard 0.7 Hz repetition rate with short interruptions for readjustments to the laser system and general diagnostics. The FG5X operated in its standard configuration with 50 drops separated by a 10 s interval, starting every 30 minutes. A detailed analysis of the measured absolute gravity values will be presented in the following chapter.

5.3 Absolute Gravity Value

One of the main goals of this work was to assess the accuracy of the GAIN absolute gravity value on the 10^{-9} g, or $10\,\mathrm{nm/s^2}$, level. Due to the dynamic nature of the gravity value this requires, amongst other things, a reference value with at least an equal level of accuracy. This is non-trivial even at geodetic reference stations, since even state-of-the-art absolute gravimeters are only specified to an absolute accuracy of $20\,\mathrm{nm/s^2}$ [64]. During the second Berlin and the Onsala campaign an adequate reference value was provided by the FG5X-220 gravimeter operated by IfE which measured on the same reference point within a period of a few days. During the Wettzell campaign, the gravity reference had previously been defined through multiple FG5 measurements from 82 observation epochs within 4 years and 7 different FG-5 specimen while taking into account international gravimeter comparisons [112, 111]. These measurements were transferred to the time of the GAIN measurement with high fidelity using the continuous SCG signal, resulting in an overall reference value uncertainty $18\,\mathrm{nm/s^2}$. The campaign in 2012 comparing GAIN to the gPhone does not allow an absolute value comparison on this level because of the lack of a direct absolute reference value and the early state of the GAIN setup.

In order to obtain the raw gravity value from the GAIN time-series, a model consisting of tidal gravity variations, ocean-loading, air-pressure- and polar motion effects was subtracted from the raw gravity time-series as mentioned in the previous chapters. This reduced signal is, without the mean gravity value, shown in the middle rows of figures 5.4,5.7,5.8. To guarantee an unbiased comparison between GAIN and the FG5X-220 reference values, the same synthetic tide model was used for both instrument‘s data and the air-pressure effects were calculated using equivalent pressure datasets and with identical admittance factors (see appendix B.1). The polar motion correction is crucial for the absolute gravity value as it can reach amplitudes of more than $10\,\mathrm{nm/s^2}$. Again, equivalent

Offset [nm/s^2]	**Systematic Error Budgets** Onsala 2015	Wettzell 2013	Berlin 2013
Raman Wavefronts	28 ± 22	28 ± 22	28 ± 22
RF Group delays	0 ± 10	0 ± 10	0 ± 10
Coriolis Effect	12 ± 7	0 ± 15	0 ± 15
Raman Frequency Offset	0 ± 7	0 ± 7	0 ± 7
Self Gravitation	-19 ± 5	-19 ± 5	-19 ± 5
Rb Vapor Index	-5 ± 5	-5 ± 5	-5 ± 5
Quad. Zeeman Shift	0 ± 5	0 ± 5	0 ± 5
Light Shift (1-photon)	0 ± 5	0 ± 5	0 ± 20
Light Shift (2-photon)	0 ± 5	0 ± 5	0 ± 5
Synchronous Vibrations	0 ± 5	-92 ± 50	-92 ± 50
Reference Laser Freq.	13 ± 2	10 ± 5	0 ± 20
RF Reference Offset.	0 ± 1	0 ± 1	0 ± 40
Total Offset	29 ± 29	-78 ± 59	-88 ± 77

Table 5.1: Improvement of the systematic error budget between the three absolute gravimeter comparisons. Each value is given as offset ± uncertainty. The respective total offset was added to the raw GAIN results to obtain the corrected gravity values. All uncertainties are given as 1σ standard errors (68 % confidence level)

pole coordinates were used for the reduction of both instrument's data. A detailed listing of all relevant model parameters for all four campaigns is given in appendix B.

The GAIN raw gravity value obtained from the model reduction was further corrected for the known systematic effects discussed in chapter 6 by adding the total offset from the systematic error budgets shown in table 5.1. Due to improvements of the GAIN setup the error budget was significantly reduced both in the size of the remaining offset and in the associated uncertainty between the first and the last campaign. To summarize the main improvements, the uncertainty was decreased between the Berlin and Wettzell campaign by implementing active Raman intensity stabilization, verifying the reference laser frequency using cold atom spectroscopy in the atomic fountain and phase-locking the GAIN 10 MHz reference oscillator to a low phase-noise Maser provided by the Wettzell observatory. Another significant improvement of the systematic error budget between Wettzell and Onsala was achieved by eliminating synchronous vibrations with the magnetic shield around the MOT region and by characterizing the remaining Coriolis effect uncertainty as detailed in chapter 6.1.1.

The corrected gravity value is valid at the effective measurement height of GAIN which in generally differs from the height level of the reference value. Both thus have to be transferred to a common height level while accounting for the correct vertical gravity gradient which was measured on all relevant reference points using relative gravimeters prior to the campaigns. The height levels used for the comparison were 1.2 m for the Berlin and Onsala campaign (the standard setting for FG5X gravimeters), and 1.25 m for the Wettzell campaign. The effective measurement height of the GAIN sensor was around 1.38 m and 1.42 m above ground during the Berlin/Wettzell and Onsala[6] campaigns, respectively, as detailed

[6]The 4 cm increase for Onsala is due to setup changes, namely the MOT magnetic shield after which

	Absolute Gravity [nm/s^2]		
	Onsala 2015	**Wettzell 2013**	**Berlin 2013**
GAIN Raw Value	9 817 158 325 ± 1	9 808 369 359 ± 1	9 812 641 207 ± 2
Systematic Offset	29 ± 29	-78 ± 59	-88 ± 77
Height Offset	729 ± 12	436 ± 10	412 ± 11
GAIN corrected	9 817 159 083 ± 31	9 808 369 717 ± 60	9 812 641 532 ± 66
Reference value	9 817 159 023 ± 20	9 808 369 633 ± 18	9 812 641 438 ± 23
Δg_{SCG}	-3 ± 1	-10 ± 1	0 ± 0
GAIN-(Ref.+Δg_{SCG})	**63 ± 37**	**94 ± 63**	**93 ± 81**

Table 5.2: Result of three absolute gravity comparison campaigns in Germany and Sweden, showing good agreement between GAIN and reference gravity values. GAIN raw values are obtained from the mean residual, after subtracting earth tides, air-pressure effects and polar motion. Δg_{SCG} is an offset from superconducting gravimeter residuals to correct for unmodeled environmental gravity changes between the reference- and GAIN observation periods (see text). Improvements in the GAIN setup lead to increasing agreement and substantially lower uncertainty between the first and last campaign. All uncertainties are given as 1σ standard errors (68 % confidence level).

for each campaign in appendix B. These values were obtained by measuring the height of the detection beam relative to the ground with a tape measure. The atom's height with respect to the floor during the first Raman pulse can then be extracted from the sequence data and inserted into equation 2.37 to obtain the effective measurement height. We estimate the uncertainty of the detection height measurement to 3 mm, mainly due to difficult access and the lack of precision measuring tools. This dominates the overall height transfer uncertainty due to the large vertical gradient to approximately 10 nm/s^2.

Small environmental gravity variations between observation periods which are not contained in the synthetic model can still influence the absolute gravity comparison on this level. During the campaigns in Wettzell and Onsala these variations were accounted for by transferring the measured gravity values between the different observation periods using the SCG signal. This was done by subtracting the SCG residuals' mean during both absolute gravimeter observation periods from each other, yielding:

$$\Delta g_{\mathrm{SCG}} := \overline{g_{scg}^{res}(t^{gain}))} - \overline{g_{scg}^{res}(t^{ref}))} \tag{5.1}$$

where the bar indicates the mean value. Δg_{SCG} was then subtracted from the respective reference value. Note that due to the well-characterized, linear drift and low noise of the SCG, this correction can be performed over long time periods with very low uncertainty and be used to connect several absolute gravity campaigns which was done during the Wettzell campaign [112]. Since FG5X-220 and GAIN observations on pillar AC during the Onsala campaign were only separated by a few days, this respective correction is smaller and almost negligible in comparison to other effects. The same is presumably true for the absolute gravity campaign in Berlin, however no SCG signal was available on site during this comparison.

the physics package had to be raised

The final differences between the gravity values of GAIN and the respective references, including all of the above corrections, are summarized in table 5.2. GAIN and the reference values agree on a 95 % or 2σ confidence interval, with the best agreement during the last campaign in Onsala with a gravity value difference of only $(63\pm37)\,\mathrm{nm/s^2}$. This represents an improvement of almost a factor two with respect to the Wettzell campaign and is crucial for applications of atomic gravimeters in geodesy where long-term, secular signals of a few $10\,\mathrm{nm/s^2}$ are of interest.

This level of accuracy represents the current state-of-the-art in absolute gravimetry which has, to the knowledge the author, only been demonstrated by very few other atomic gravimeters and is consistent with comparisons of several FG5 specimen [65, 113]. The first two campaigns show a slightly larger difference between GAIN and the reference value, which is consistent with the larger systematic uncertainties due to (at the time of the campaign) outstanding instrumental improvements of GAIN. It is noteworthy that during all three campaigns the GAIN result is higher than the reference values obtained by FG5 measurements, which agrees with the results of other atomic gravimeters [65, 11] and could indicate hidden systematic effects in either of the involved instruments. Future studies of all relevant systematic error budgets and comparisons to a third, independent absolute gravimeter implementation would therefore be of high interest to identify the location and source of this difference. The results shown in table 5.2 for the Onsala and Wettzell campaign differ slightly from the results published in [14], caused by a number of corrections implemented during the improved analysis during this work. For the Wettzell campaign, an inaccurate vertical gradient had been used before which was replaced with the recommended, published value for this location [114]. For the Onsala campaign analysis, the GAIN raw value increased by around $12\,\mathrm{nm/s^2}$ after accounting for the correct polar motion correction. A small additional offset caused by the Coriolis effect listed in table 5.1 was also added here. While both alterations increased the difference between GAIN and the FG5 reference values, the qualitative result of close agreement between both instruments remains.

The overall uncertainty is dominated by the GAIN and FG5 systematic error budgets as shown in table 5.2. Further improvement on this side is therefore necessary and should, on the GAIN side, be focused on reducing Raman wavefront aberration effects. In order to raise the confidence in the achieved level of accuracy and compare the GAIN sensor to many instruments at once, participation at an international or European absolute gravimeter comparison (ICAG, ECAG) seem like the natural next step. In order to accelerate the identification and study of systematics in GAIN on the low $10^{-9}\,\mathrm{g}$ level, improving the short-term sensitivity is very beneficial to shorten the required averaging times. The current status and sources of measurements noise will therefore be detailed in the following chapter.

5.4 Short-Term Stability and Noise

The residual GAIN gravity signal after correcting for tidal and other environmental effects is dominated by largely uncorrelated short-term fluctuations due to measurement noise. The total observed noise is a mixture of several contributions, the most important of which were isolated and quantified as described below. The root mean square (RMS) values of shot-to-shot fluctuations were divided by the square root of the instrumental repetition

rate f_{rep} in order to obtain all noise figures in $\mathrm{nm/s^2/\sqrt{Hz}}$, which emphasizes the effect of the measurement's cycle time on the final sensitivity and simplifies comparison to other gravimeters.

Vibration Phase Noise Any accelerations of the Raman retro-reflection mirror during the Raman pulse sequence will result in interferometer phase noise σ_{Vib} through the interferometer transfer function 2.39 as described in chapters 2.4 and 3.2. This term often represents the dominating noise source in the literature on atomic gravimetry [11, 99, 115] and other absolute gravimeters, except in very quiet environments [12, 110]. Due to the low-pass characteristics of the AI transfer function 2.48 which attenuates the effect of vibration frequencies above $1/T$, micro-seismic noise at sub-Hertz frequencies causes the biggest phase noise contribution and is generally reduced with an active isolation system (see chapter 3.2) or alternative strategies such as post-correction [99, 115]. The size of σ_{Vib} can be estimated using the accelerometer attached to the Raman mirror by multiplying the vibration spectrum $S_a(\omega)$ with the AI transfer function as shown in equation 2.48. This was carried out for all the campaigns shown here and results, despite the active vibration isolation, in a dominating contribution σ_{Vib} of 50–220 $\mathrm{nm/s^2/\sqrt{Hz}}$ depending on the level of micro-seismic vibrations, before applying the post-correction algorithm.

Raman Laser Phase Noise introduced in the locking path is another contribution which leads to interferometer phase noise through the respective transfer function shown in equation 2.43. The GAIN setup has a well characterized, low noise Raman phase lock system detailed in chapter 3.3 and in [82]. Using the combined measured noise spectra of all relevant components in the Raman PLL path, the magnitude of the associated noise term is limited by the 10 MHz RF reference on the order of $\sigma_{\mathrm{Ra}} \approx 50\,\mathrm{nm/s^2/\sqrt{Hz}}$ as described in chapter 3.3.1. This is in good agreement with the observed atom interferometer noise in the Doppler-free configuration where the sensitivity to vibration is strongly reduced and Raman phase noise becomes the dominant contribution.

Detection Noise A limited detection efficiency introduces errors in the measured atomic state population and leads to amplitude noise in the interferometer signal. The detection efficiency depends on a number of technical limitations as well as the atomic shot noise as detailed in chapter 3.1.3 and therefore varies greatly depending on the number of detected atoms. The magnitude of the associated noise term at the mid-fringe point was measured during all campaigns by observing the shot-to-shot fluctuations of the atomic signal after the complete selection sequence and after a single $\pi/2$ Raman pulse. For commonly achieved GAIN detection SNR values of 50, the equivalent interferometer noise figure at mid-fringe is around $\sigma_g^{\mathrm{Det}} \approxeq 25\,\mathrm{nm/s^2/\sqrt{Hz}}$, which is small compared to the other two contributions mentioned above. Note that this is partly due to the comparatively large interferometer pulse spacing T employed in GAIN.

The combined effect of the above, uncorrelated effects is given by the quadratic sum

$$\sigma_{\mathrm{Total}} = \sqrt{(\sigma_{\mathrm{Vib}})^2 + (\sigma_{\mathrm{Ra}})^2 + (\sigma_{\mathrm{Det}})^2} \tag{5.2}$$

assuming that other noise sources are negligible. Previous comparisons to expected noise contributions in the system [80, 101] have concluded that vibration noise of the Raman

mirror dominates overall. Due to an incorrect pre-factor of $\sqrt{2\pi}$ in the vibration phase noise computation carried out in [80], however, σ_{Vib} was actually overestimated by around a factor 2 before. Figures 5.10 to 5.13 show the observed measurement noise during all four presented campaigns with and without applied post-correction as well as the vibration induced gravity noise computed from the mirror accelerometer in a time-resolved manner. The spectrograms in figures 5.10, 5.11 clearly show the much higher vibration noise above 1 Hz frequency at the university building in Berlin with lots of human activity and a common concrete floor, compared to the data measured on decoupled concrete pillars at the remote geodetic observatories shown in figures 5.12,5.13. In the micro-seismic band from 0.1–1 Hz there is no fundamental difference between both situations, seasonal and weather changes seem to be of more importance here. Micro-seismic noise was actually lowest during the Berlin 2012 campaigns, somewhat stronger during the Berlin and Wettzell measurements in 2013 and by far the strongest in Onsala 2015 due to the proximity of the coastline and winter storms. Below 1 Hz the spectrograms of both observatory data sets show plenty of earthquakes, which are obscured in the Berlin data by human activity (steps) next to the seismometer. The AI vibration phase noise indicated by the yellow lines in figures 5.10-5.13 correlates very well with noise in the micro-seismic band as expected due to the low-pass filtering behavior of the interferometer transfer function 2.48. In order to avoid artifacts due to earthquakes and other strong, low-frequency events, a 10 sample median filter was applied to all line plots in figures 5.10-5.13. The quadratic difference

$$\Delta_{\mathrm{GAIN}} = \sqrt{(\sigma_{\mathrm{Tot}}^{\mathrm{noPC}})^2 - (\sigma_{\mathrm{Tot}}^{\mathrm{PC}})^2}$$

of the observed gravity noise with and without applied post-correction shows both in its magnitude and its time dependence excellent agreement with the computed vibration noise σ_{Vib}. This can be expected from equation 5.2 assuming that the post-correction removes virtually all of the vibration noise measured by the platform accelerometer. The agreement thus confirms the accuracy of the vibration phase-noise calculation and the effectiveness of the post-correction algorithm applied to improve the GAIN gravity signal. The noise contained in the final, post-corrected gravity signal is in fact uncorrelated with vibrations within the bandwidth of the platform accelerometer. According to the above list of expected noise sources, the signal after post-correction should thus be limited by Raman Laser phase noise $\sigma_{\mathrm{Ra}} \approx 50\,\mathrm{nm}/\sqrt{\mathrm{Hz}}$. The observed levels are, however, between 62–260 $\mathrm{nm/s^2}/\sqrt{\mathrm{Hz}}$ which is up to 5 times larger during the measurement campaigns as shown by the solid blue line in figures 5.10 to 5.13. The known noise sources alone can therefore not fully account for the observed gravity noise. A strong variation during the first three campaigns indicate that additional environmental effects dominate, however, no clear correlation with such influences was found. Some potential noise sources requiring further investigation are

- Acoustic vibration's outside the accelerometer's bandwidth, which could be reduced in the future through an acoustic isolation curtain or box.
- Air convection and related refractive index changes between the Raman mirror and the vacuum window. The GAIN physics package was only covered with a simple wooden box and insulating bubble wrap foil to suppress air movement in this region. This should in the future be improved through tubing around the Raman free-air beam path.

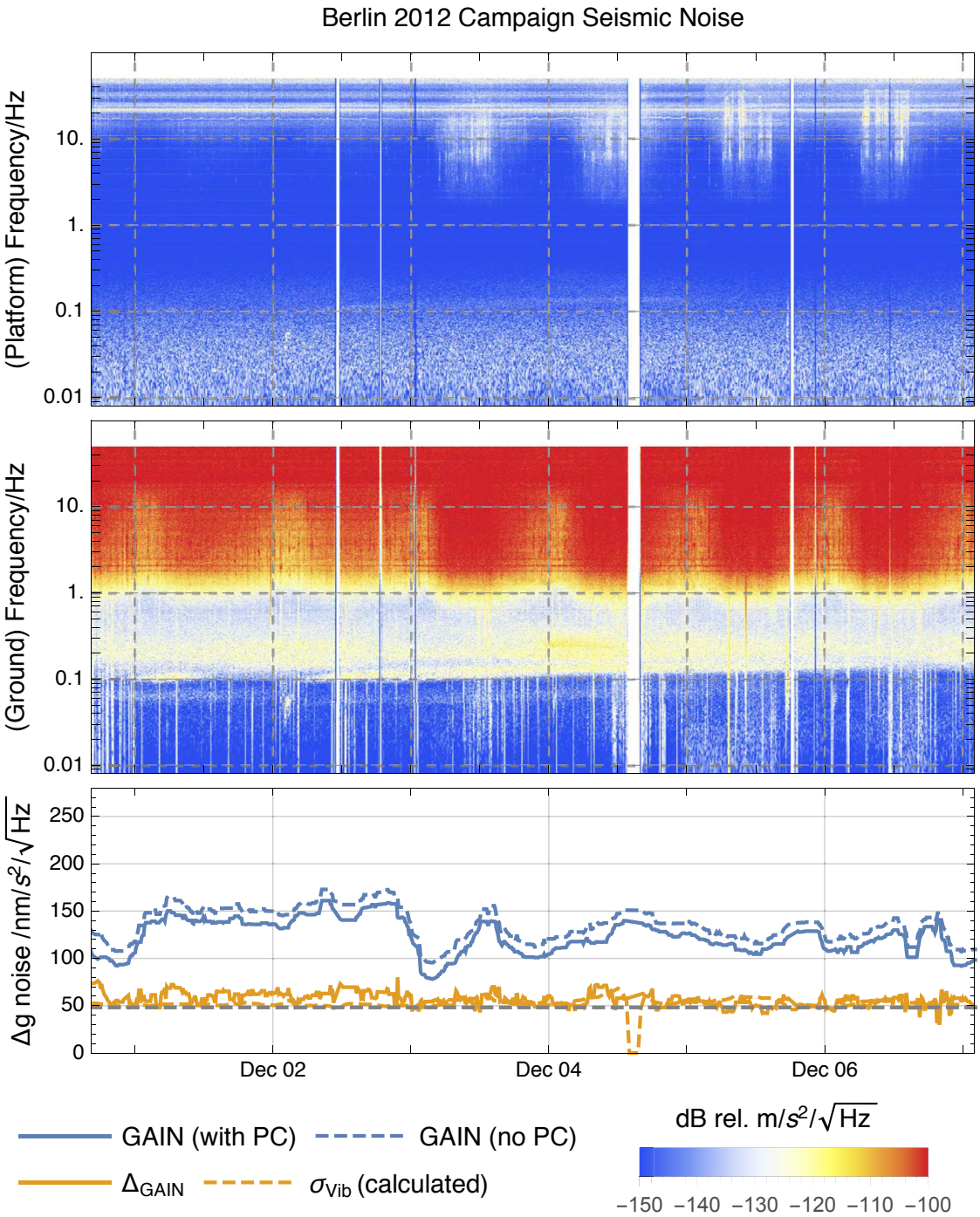

Figure 5.10: Spectrograms of vertical acceleration on the GAIN isolation platform (top) and on the ground (middle) during the gPhone comparison in Berlin in 2012, showing an intermediate micro-seismic activity and very high noise levels above 1 Hz due to daily human activity and the 2nd floor physics lab environment. Bottom: Time-dependence of observed GAIN sensitivity. The blue lines show the gravity residual RMS value over 10 min data segments with and without post-correction (PC). The yellow lines show two estimates of the expected vibration noise before PC as detailed below. Strongly time-dependent excess noise clearly exists and compromises the overall sensitivity above the Raman Laser Phase noise limit (gray dashed line). See text for further discussion.

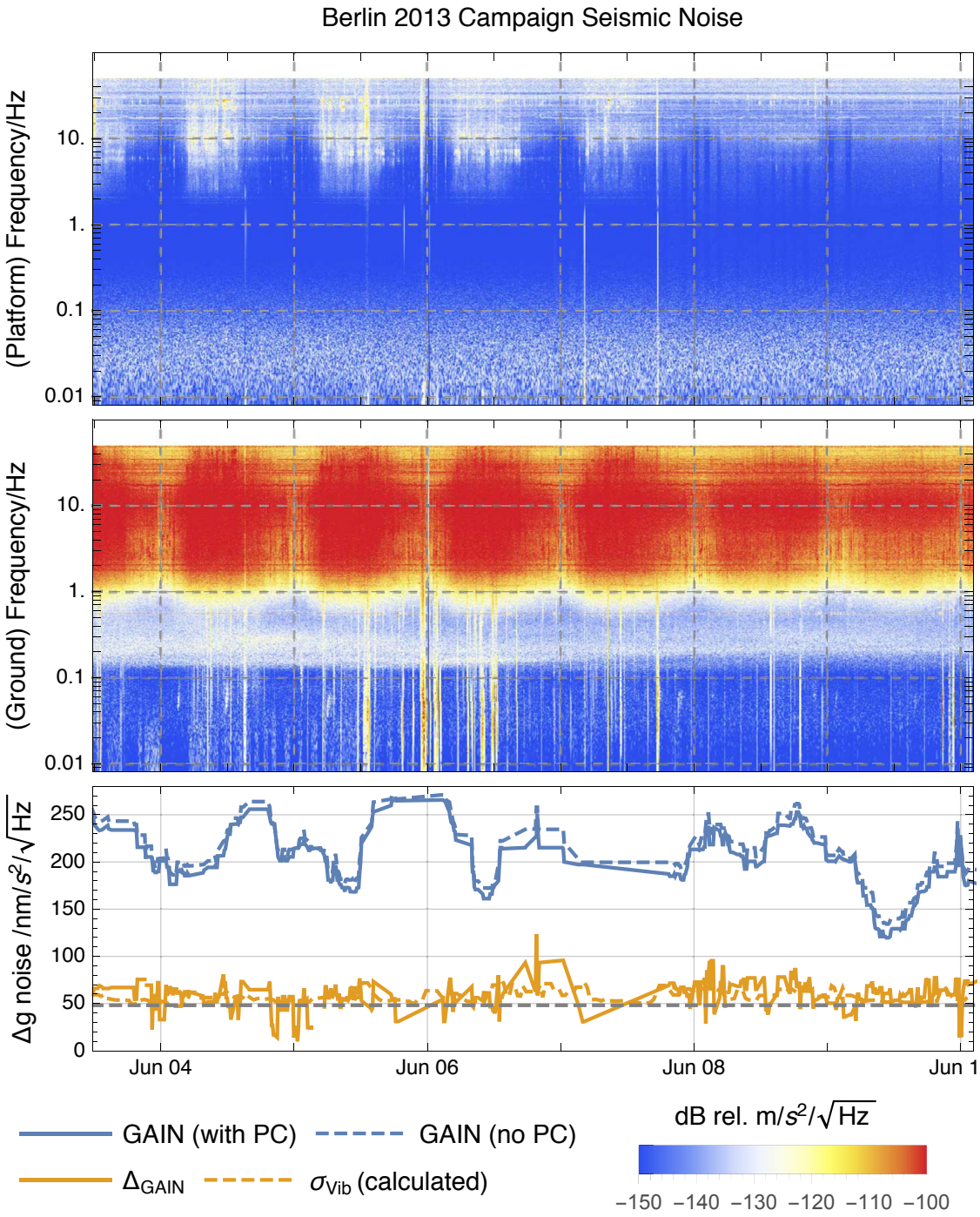

Figure 5.11: Spectrograms of vertical acceleration on the GAIN isolation platform (top) and on the ground (middle) during the comparison to the FG5X-220 in Berlin 2013. Clearly visible is a weak micro-seismic background and high noise level above 1 Hz due to human activity, particularly during the day. Bottom: Time-dependence of observed GAIN sensitivity. The blue lines show the gravity residual RMS value over 10 min data segments with and without post-correction (PC). The yellow lines show two estimates of the expected vibration noise before PC as detailed below. A time-dependent excess noise source clearly compromises the overall GAIN noise level above the Raman Laser Phase noise limit (gray dashed line). See text for further discussion.

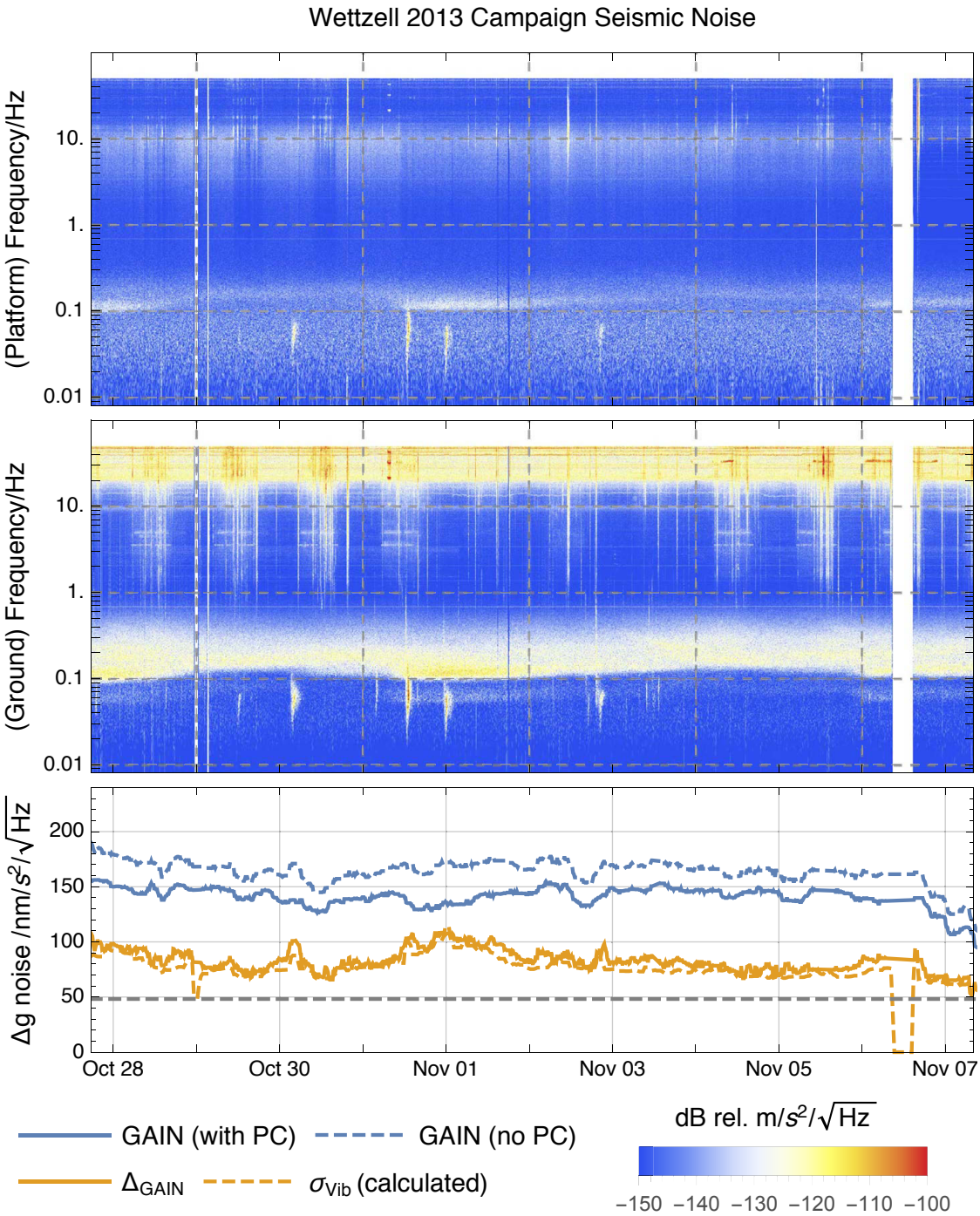

Figure 5.12: Spectrograms of vertical acceleration on the GAIN isolation platform (top) and the concrete pillar (middle) during the Wettzell 2013 measurement campaign. Visible (from low to high frequencies) are several earthquakes and the variable but moderate micro-seismic background noise. Bottom: measured GAIN sensitivity. The blue lines show the gravity residual RMS value over 10 min data segments with and without post-correction (PC). The yellow lines show two estimates of the expected vibration noise before PC as detailed below. Excess noise clearly exists with a magnitude of about $140\,\mathrm{nm/s^2/\sqrt{Hz}}$. See text for further discussion.

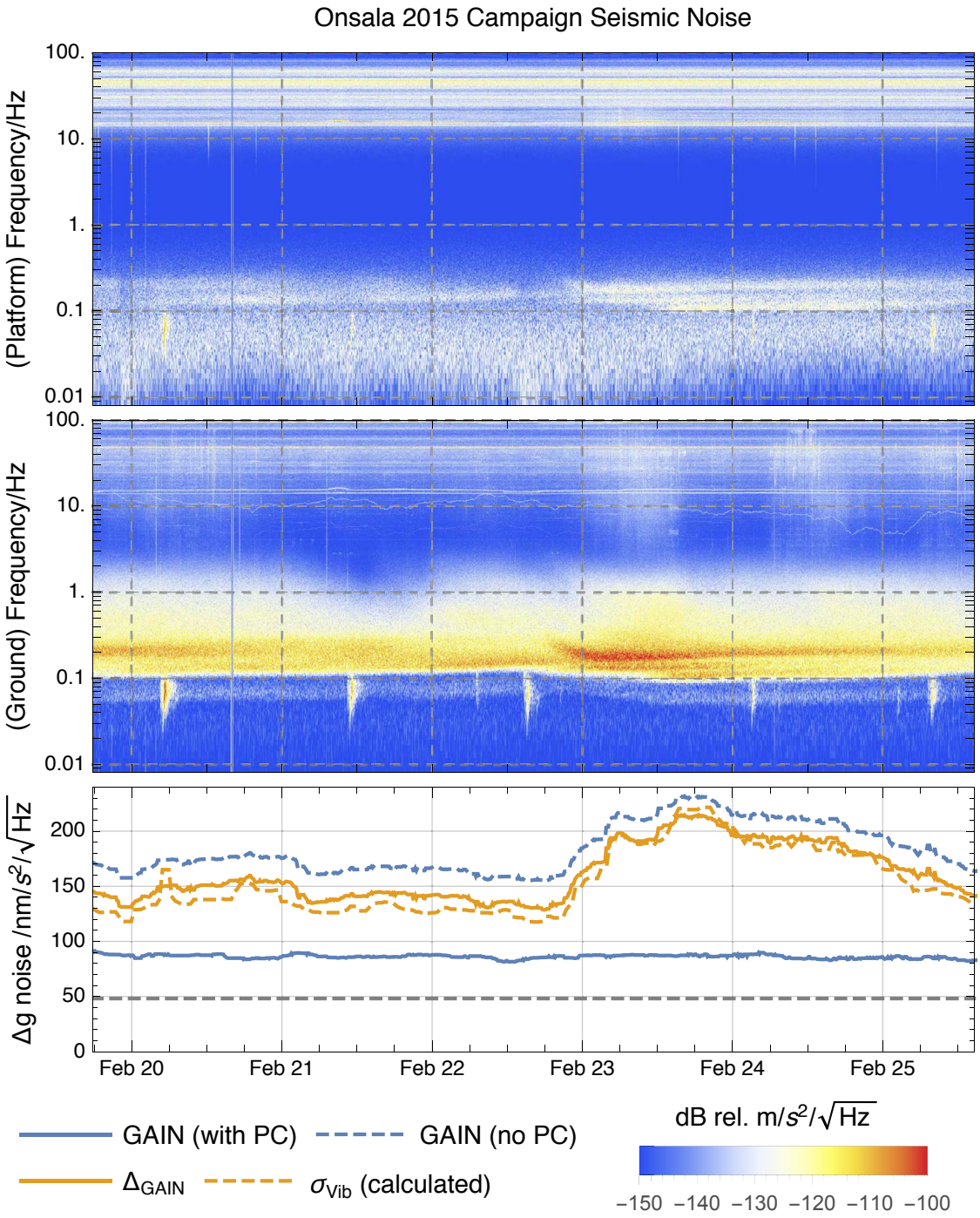

Figure 5.13: Spectrograms of vertical acceleration on the GAIN isolation platform (top) and the concrete pillar (middle) during the Onsala 2015 measurement campaign. Shown are several earthquakes, strongly elevated micro-seismic background and high frequency platform noise as discussed in chapter 3.2. Bottom: measured GAIN sensitivity. Blue lines show the gravity residual RMS value over 10 min data segments with and without post-correction (PC). Yellow lines show two estimates of the expected vibration noise before PC as detailed below. While the observed noise level is constant, excess noise still exists above Raman Laser Phase noise (gray dashed line). See text for further discussion.

- Cross-coupling of horizontal vibrations into the mirror accelerometer, as the in-loop feedback sensor is used for the post-correction signal. Note, however, that the CMG3 instrument has a high specified $-65\,\mathrm{dB}$ cross-coupling rejection and considerable effort was taken to fully exploit this as detailed in chapter 3.2.1. Starting with the Wettzell campaign, it was positioned optimally on the vibration platform with its non-central effective measurement axis located directly over the platform pivot point and under the Raman retro-reflector. At the Onsala campaign, its measurement axis further aligned with gravity with mrad accuracy. The next step to diagnose this issue is an independent 6 axis inertial measurement on the platform during gravimeter operation to fully characterize spurious modes of the isolator platform.

- Magnetic excitations of the isolator platform which are detailed in chapter 6.5.1 might also cause additional vibration noise. For the Onsala campaign, however, this can be ruled out as it was conducted with magnetic shielding around the MOT.

- The propagation delay of the retro-reflected Raman component due to the distance between atoms and mirror makes the atom interferometer sensitive to frequency noise of the Raman master laser [116]. For the narrow linewidth [82] ECDLs used here and the moderate distance between atoms and mirror of $(0.85\pm0.15)\,\mathrm{m}$, however, this effect should be around one order of magnitude smaller than the observed noise level. A future measurement of the laser frequency noise would be necessary to rule out this contribution completely.

Note that the last dataset obtained in Onsala shows a different behavior than the previous campaign, as the post-corrected signal has relatively constant noise level of around $90\,\mathrm{nm/s^2/\sqrt{Hz}}$. This supports that magnetic excitations added spurious noise before the installation of the MOT shield. The remaining noise level, however, is still too large to be consistent with Raman laser phase noise. Further investigation is therefore needed to isolate the dominating noise source.

Even with this not fully understood noise term, the sensitivity of GAIN compares well with other gravimeters. Table 5.3 shows a comprehensive list of the sensitivity to g within one second for all gravimeters that were involved in the measurement campaigns. The FG5X-220 clearly shows much higher noise than GAIN which is partly due to excess noise under the elevated micro-seismic noise levels during both the Berlin and the Onsala measurement. This is a known limitation of this instrument, numbers as low as $100\,\mathrm{nm/s^2/\sqrt{Hz}}$ have been reported under optimal micro-seismic conditions and using a higher repetition rate [110]. The GAIN data shows one of the best absolute gravimeter performances at geodetic observatories so far and outperforms the FG5 in terms of short-term measurement noise by a small amount for optimal environmental conditions and by up to an order of magnitude for a strong with an micro-seismic background. Additionally, GAIN can be operated continuously for long-term gravity registration which is not possible for the FG5 due to mechanical wear-and-tear. Together this has significant implications in geodesy and geophysics and specifically enables new ways to conduct absolute gravimetry at geodetic observatories with one single instrument.

When comparing RMS noise figures of gPhone and the SCGs to GAIN, the results depend on the chosen signal filtering as their continuous measurement principle allows control of the effective measurement bandwidth over a wide range. All relative gravimeter signals were therefore low-pass filtered with a $60\,\mathrm{mHz}$ corner frequency to remove the

Sensitivity	**Absolute**		**Relative**	
[nm/s²/√Hz]	**GAIN**	**FG5X-220**	**gPhone**	**SCG**
Berlin 2012	78–161		30–193	
Berlin 2013	120–266	183–1466		
Wettzell 2013	95–156			0.5–3
Onsala 2015	82–90	220–1786		0.3–3

Table 5.3: Sensitivity within one second for different absolute and relatives gravimeters during all 4 measurement campaigns. All values result from RMS values of residual gravity data over 10 min segments. The ranges indicate min/max noise amplitudes over several days. FG5 and gPhone noise amplitudes correlate with micro-seismic vibrations whereas GAIN shows no clear correlation to observed environmental disturbances. Relative sensor signals depend on processing parameters and were low-pass filtered to remove micro-seismic noise, the shown values agree well with results in [35].

micro-seismic frequency band. The gPhone residuals then show lower noise than GAIN for quiet vibration conditions and higher noise under noisy conditions. As environmental vibration become stronger, GAIN apparently profits more from its vibration isolation system whereas the gPhone might suffer from hysteresis or other non-linerar effects in its precision spring. Both involved SCGs show clearly superior noise levels to any other type of gravimeter. In combination with their very linear drift behavior and stable calibration, this makes them the preferred instrument for measuring very small gravity changes over long time-frames. The need for calibration and drift characterization, however, still necessitates regular comparisons with absolute gravimeters.

Other atomic gravimeters have demonstrated sensitivities as low as $42\,\mathrm{nm/s^2/\sqrt{Hz}}$ [12] and $57\,\mathrm{nm/s^2/\sqrt{Hz}}$ [117] under exceptionally quiet environmental conditions in special underground locations, which is only a factor 2 better than the results achieved here under much less ideal circumstances. The author therefore draws a positive conclusion of the achieved performance, particularly during the last campaign. For the sake of future improvement, testing the performance of GAIN at a quiet location for a period of months or longer would be of great interest.

5.5 Long-Term Stability

In addition to the absolute accuracy and short-term noise, stability over longer periods is of great importance and indicates the quality of the suppression of time-dependent systematics. This aspect has therefore been analyzed for all four presented measurement campaigns. Except for the last campaign in Onsala, similar but independent comparisons have also been carried out in [80, 101]. Note that the term long-term stability was chosen to distinguish from short-term stability/noise and extents to periods up to $10^5\,\mathrm{s}$ or about one day. This is very different from some other studies in gravimetry were time series with lengths of years or even decades exist. We use the Allan deviation, a standard tool to characterize the stability of time series in general and particulary of frequency and time measurements, to quantify the stability of the gravity signal on various time scales. It is

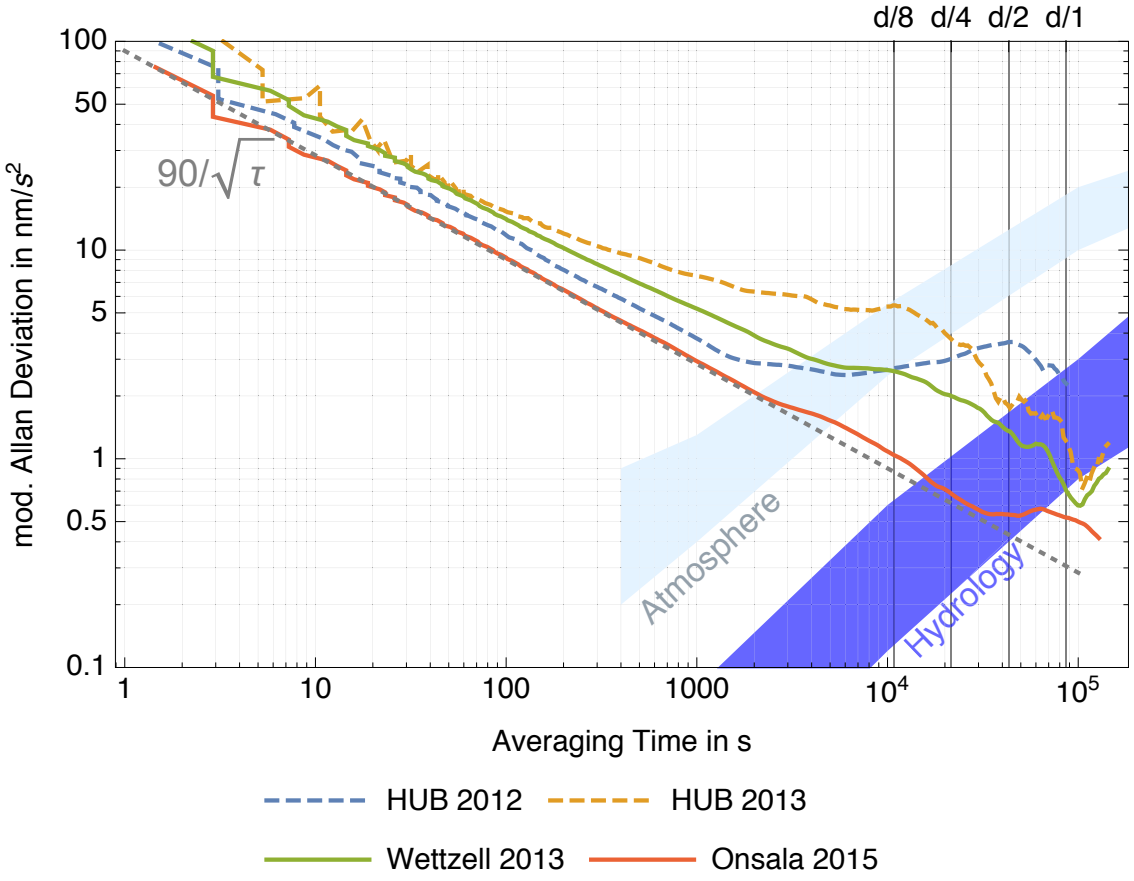

Figure 5.14: Overlapping Allan deviation for GAIN gravity residuals during all 4 campaigns. Both datasets taken at HUB in Berlin are shown dashed because the residuals were obtained by subtracting the synthetic model described in chapter 5.3. Small signal deviations below 10 nm/s^2 could thus be caused by environmental gravity changes as indicated by the blue bands which denote the timescale and magnitude of atmospheric and hydrological gravity changes [35]. The Wettzell and Onsala datasets were computed by subtracting the respective SCG signal from GAIN gravity data and only contain instrumental effects.

defined as the square root of the Allan variance [118]

$$\sigma_y^2(\tau) = \frac{1}{2\,(M-1)} \sum_{i=1}^{M-1} \left[y_{i+1} - y_i\right]^2 \tag{5.3}$$

with the dataset length M and data point means y_i obtained over the averaging time τ. Its value for a given τ indicates the stability of the dataset on the time scale of τ. In the following we will use the slightly adopted overlapping Allan deviation [119] due to its lower statistical uncertainty. All calculations were carried out using the software package Stable32 [120]. Figure 5.14 shows a summary of the residual gravity Allan deviations. Between 1–1000 s the residual gravity datasets behave mostly like uncorrelated, white noise with a stability improvement as $1/\sqrt{\tau}$. The respective short-term noise reflects in the level of the Allan deviation at 1 s where it matches the average values for the GAIN sensitivity

shown in table 5.3. Beyond 1000 s the behavior differs between campaigns and shows the progress made by the successive instrumental improvements. Note that the two dashed lines are potentially compromised by actual environmental gravity changes as a synthetic model was subtracted as detailed in chapter 5.3. The exact size of instrumental drift is therefore hard to extract from those datasets. This is not the case for the Wettzell and Onsala datasets were simultaneous SCG signals were subtracted from the GAIN gravity signal. Updated SCG calibration factors from chapter 5.5.1 were used for this purpose and no additional time-delay was applied. The Wettzell dataset shows residual instabilities on timescales of 3×10^3–10^5 s after which it falls to a minimum value of 0.6 nm/s^2. Beyond 10^5 s instabilities become apparent due to long-term drifts which lead to an increasing Allan deviation. This is mostly consistent with the analysis presented in [80, 101] with the exception that no long-term drift beyond 10^5 s was reported there. This is presumable due to the linear drift reduction carried out in that analysis.

The Onsala dataset shows clearly the best GAIN performance achieved so far, with the lowest short-term noise of around 90 nm/s$^2/\sqrt{\text{Hz}}$ averaging down consistently until 3×10^4 s. Flicker noise on semi-diurnal time scales then leads to a constant Allan deviation on the 0.5–0.6 nm/s^2 level which decreases again at diurnal periods and reaches its lowest value of 0.4 nm/s^2 just beyond 10^5 s. This is, to the knowledge of the author, the best reported stability for an atomic gravimeter so far and has been detailed in a separate publication [14]. Absolute gravimeter stabilities of below 1 nm/s^2 have, in fact, to our knowledge not been published for any other absolute gravimeter so far.

5.5.1 Scale Factor Determination

All relative gravimeters need to be calibrated to obtain the scale factor b such that the measured output voltage signals x can be related to physical gravity differences through $\Delta g = b \cdot x$. For superconducting gravimeters b is usually measured through simultaneous measurements of absolute gravimeters such as the FG5 and utilizes the time-dependence of tidal gravity variations. A scale factor estimate can be extracted from a linear regression of the SCG data points $\{x_i\}$ and the absolute gravimeter observations $\{y_i\}$ through the following formula [121]

$$\hat{b} = \frac{\sum (x_i - \bar{x})(y_i - \bar{y})}{\sum (x_i - \bar{x})^2} \qquad \sigma_b^2 = \frac{1}{n} \frac{\sum \left(y_i - \hat{a} - \hat{b}x_i\right)}{\sum (x_i - \bar{x})^2} \tag{5.4}$$

with the offset $\hat{a} = \bar{y} - \hat{b}\bar{x}$. Here, symbols with a hat denote estimated values and bars indicate the arithmetic mean. The uncertainty of the resulting estimates depends mostly on absolute gravimeter noise and the size of tidal gravity variations. This method therefore works best if the amplitude of those variations are at their monthly maximum.

The simultaneous gravity registrations of GAIN during the Wettzell and Onsala campaigns provided not only an ideal scenario to characterize the performance of GAIN but also to estimate the scale factor of the two involved SCG gravimeters and compare its value and uncertainty to previous calibration campaigns. Table 5.4 shows the summary of obtained SCG scale factors during the GAIN Wettzell and Onsala campaigns compared to previous estimates obtained from many FG5 measurements performed over several years. The estimated values of both methods agree within their error bars, however, the relative uncertainties reached with the GAIN data are much better with 0.3 ‰ and 0.4 ‰ during

Scale Factor Calibration	**Wettzell SG30**		**Onsala SG054**
[nm/s²/V]	**bottom**	**top**	
FG5 campaigns (mean)	−739.0±1.0	−678.4±1.0	−774.3±3.0
GAIN campaign	−740.25±0.23	−680.30±0.21	−773.91±0.31

Table 5.4: Comparison of SCG scale factor regressions using GAIN and previously obtained FG5 gravity data, yielding strongly reduced uncertainty. The GAIN datasets are shown in figures 5.7, 5.8 and have a length of 10 and 6 days for Wettzell and Onsala, respectively. The slightly increased uncertainty in Onsala, despite the reduced measurement noise, is due to the smaller earth tide amplitude and the shorter dataset. Uncertainties given as 1σ standard errors.

the Wettzell and Onsala campaign, respectively. This is 3-5 times better than the previous FG5 results [121] even though those represent an average over multiple campaigns over a longer period of time. Even under optimal micro-seismic noise conditions, optimized measurement schedules and when measuring only during the maximal tide amplitudes, the expected uncertainty of FG5 calibration campaigns would be 0.5 nm/s^2 after 6 days and only reaches 0.2 nm/s^2 after 60 days of registration [122].

GAIN therefore provides a quicker and significantly more precise way to determine SCG scale factors due to its high repetition rate, continuous operation and low noise under noisy environmental conditions, which is of considerable benefit in geodesy and geophysics.

5.5.2 Time Delay

When comparing the output signal of atomic- and superconducting gravimeters, the different transfer functions and the associated signal distortions have to be taken into account. Low frequency group/phase delays are particularly problematic as they subject earth tides, by far the largest gravitational effect in the above datasets, to an effective time delay.

The transfer function of SCGs is mostly determined by the analog low-pass filter, data acquisition hardware and internal feedback integrator [123]. For the two instruments in Wettzell and Onsala, which both have an analog anti-aliasing filter with a corner-frequency of around 60 s, the total time delay was measured to be on the order of 10 s as shown in table 5.5. Atom interferometers, on the other hand, effectively measure the atom‘s acceleration relative to the retro-reflection mirror during the interferometer pulse sequence. Their transfer function is therefore determined primarily by the vibration isolation system. For the GAIN active vibration isolator presented in chapter 3.2, this results in significant group delays only around the effective resonance frequency of the closed-loop system around 50 mHz. As shown in figure 3.9 the group delay essentially vanishes above and below this resonance. No observable lag should therefore be present in the GAIN gravity data, however, a significant time delay of 20 s relative to the SCG at tidal frequencies was estimated from the GAIN Wettzell data in [80]. The underlying cause for this discrepancy could not be proven conclusively and has therefore been investigated further in this work.

The analysis carried out in [80] is based on the maximization of the cross-correlation coefficient $\hat{R}_{xy}(\tau)$ between GAIN and SCG signals [124]. While this is a reliable and

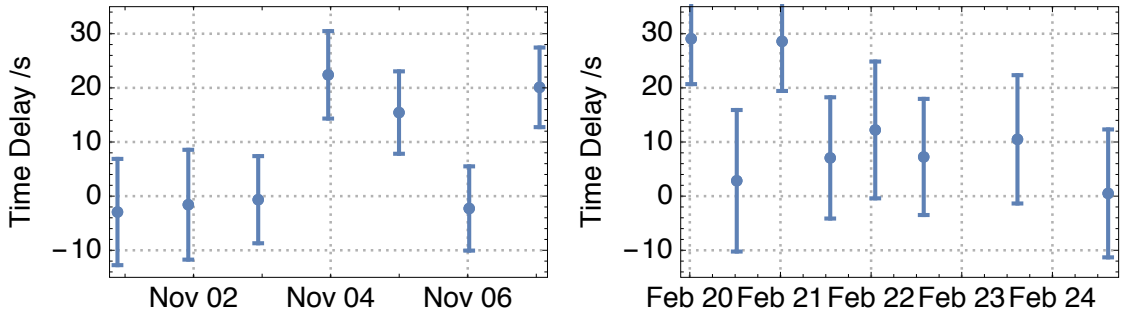

(a) Wettzell, Germany (2013) (b) Onsala, Sweden (2015)

Figure 5.15: Time delay estimates between GAIN and SCGs obtained for 24h data segments during the Wettzell and Onsala campaigns, obtained from Chi-Square minimization. Positive values indicate a time lag of GAIN. The overall time delays from weighted means are (8.6±3.1) s for Wettzell and (15.1±3.6) s.

adequate method for this purpose it unfortunately does not provide a confidence interval for the resulting delay estimates. An alternative regression method is therefore employed here which fits a time delay estimate τ_D between the two gravity time series x_i and y_i by minimizing the Chi-Square sum [125]:

$$\chi^2(\tau) = \sum_i \left(\frac{x(t_i) - \mu - y(t_i + \tau)}{\sigma} \right)^2 \tag{5.5}$$

were μ and σ are the global mean and standard deviation of the residual $x_i - y_i$. For the datasets discussed here, σ is clearly dominated by GAIN measurement noise while SCG noise is negligible. The 1σ confidence level of the time delay can then be estimated by finding the time delay value where $\Delta\chi^2 := \chi^2 - \chi^2_{min} = 1$ [125].

The analysis was furthermore conducted separately for 12 h gravity data segments around the daily tidal extrema which yields multiple estimates τ_D and shows where in the data time delays manifest. Since only tidal signals were investigated, all SCG data were passed through a non-causal low-pass filter with 5 mHz corner frequency to remove earthquakes, micro-seismic and other unwanted high frequency components while avoiding spurious phase shifts. For every data segment or data point shown in figure 5.15, time delay estimates were calculated using Chi-Square minimization as well as cross-correlation methods in order to cross-check both implementations. The resulting estimates are in very good agreement which strengthens the confidence in the following discussion.

The signature of a positive time delay around the tidal extrema is a derivative signal with a maximum on the falling slope of the tidal gravity signal, a minimum at the rising slope and a zero-crossing at the tidal extreme. The amplitude depends on the slope steepness but is generally small between 0.5–1.3 nm/s^2 for a 10 s time delay according to the measured tidal signal. Because the tidal gravity variations during the GAIN campaign were larger in Wettzell than in Onsala, the latter campaign shows a reduced sensitivity to time delay effects despite the improved GAIN sensitivity.

The result for both datasets is shown in figure 5.15. During the Wettzell campaign, the time delay estimate for 4 out of 7 segments are very close to zero wheras the values for November 4,5 and 7 indicate a significant delay of around 20 s. Correcting the GAIN

Time Delay [s]	**Wettzell**	**Onsala**
SCG vs. UTC	8.8	9.15
GAIN vs. SCG	8.6±3.1	15.1±3.6
GAIN vs. UTC	17.4	24.25

Table 5.5: Overview of time delay estimates at tidal frequencies for SCG and GAIN. GAIN estimates were obtained using the regression method described in the text. SCG values had been measured before by inserting additional signals into the internal feedback coil [126] or by calculating the DC time delay of the dominating analog low-pass filter [127]. Since no uncertainties were provided for SCG estimates, the total GAIN time delay estimates relative to UTC is also listed without errors.

data by the shown delay values of around 20 s indeed reduces the amplitude of the above mentioned time delay signature in the residual, however, with a very poor SNR. The inconsistency between the different data segments and very poor SNR suggests that the underlying process is non-stationary and might simply be caused by changing environmental perturbations or time dependent systematic effects in GAIN. Unfortunately, no correlation to environmental or systematic effects could be identified. In conclusion, we take the averaged GAIN time delay (relative to the SCG) to be the weighted average over all 7 segments resulting in $\tau_D^{WZ} = (8.6\pm3.1)\,\mathrm{s}$, significantly smaller than the result in [80]. A similar situation presents itself during the Onsala campaign as shown in figure 5.15. The first and third estimate yield a sizable delay of 30 s relative to the SCG whereas the rest agrees within their error bar on a much smaller value. This is remarkable because several systematic effects that were pointed out in [80] had been fixed before the Onsala campaign. In particular the influence of fringe deformations due to the detection system had been reduced by adding a feed-forward path to the atom interferometer phase control algorithm so that the system would maintain mid-fringe operation very precisely even during relatively fast tidal gravity changes. Persistence of the time delay after those changes indicates that the underlying cause, if existent, has not yet been identified.

Table 5.5 shows a summary of the averaged time delay estimates for both campaigns, again showing a significant time delay for GAIN. Note, however, that due to the small size of the time delay signature mention above, the above estimates were extracted from very low signal-to-noise signals and may be biased due to systematic influences on this level. In fact, the Allan deviation value for the relevant time-scale of $\tau = 3\,\mathrm{h}$ shown in figure 5.14 is $3\,\mathrm{nm/s^2}$ for Wettzell and $1\,\mathrm{nm/s^2}$ for Onsala which is similar to the respective amplitudes of a 20 s time delay signature. It is therefore still unclear whether the estimated time delay on the order of 10 s is due to unidentified parts of the GAIN transfer function or systematic effect, or simply an artifact caused by random instabilities shown in the Allan deviation. A more conclusive analysis would require a longer comparisons with SCG over several month during changing tidal periods and a further improvement in GAIN‘s sensitivity and stability on time scales of a few hours. Alternatively, a larger and more dynamic test signal than natural earth tides would increase the sensitivity of this method. This could for example be achieved by moving test masses within the vicinity of GAIN, as previously demonstrated for SCG gravimeters [128].

Summary

This chapter presented all main results of four gravity measurement campaigns which compared the atom interferometer GAIN to a gPhone spring gravimeter, two superconducting instruments and the FG5X-220 absolute gravimeter. The later two measurement campaigns were conducted at geodetic observatories in Wettzell, Germany and Onsala Sweden and demonstrate the mobility and robustness of the GAIN setup.

The measured sensitivity, long-term stability and accuracy of GAIN competes exceptionally well with current state-of-the-art gravimeters. The shown combination of long-term gravity monitoring with high stability, absolute accuracy and mobility was found to be unique to atomic gravimeters such as GAIN. Resulting application in geodesy and geophysics, such as the calibration of superconducting gravimeters were presented and discussed.

In order to deliver the stability and accuracy presented here, a range systematic effects were analysed and removed from the measurement, which will be detailed in the next chapter.

Chapter 6

Systematics

The main goal of this thesis is to exploit the potential of atom interferometers for applications in geodesy and geophysics. The absolute accuracy and stability of the measured gravity value is of fundamental importance for these tasks. The understanding and control of systematic effects is therefore of great importance for the development and application of atomic gravimeters. As a part of this work a thorough analysis of expected and observed systematics in GAIN was conducted before, during and after the implementation of the previously discussed instrumental improvements. The result is presented in the following chapter for each investigated shift.

In contrast to precision measurements of fundamental physical constants or test of the laws of physics, gravity measurements on Earth are subject to a variety of environmental influences such as tidal forces or local mass redistributions discussed in detail in chapter 1. This complicates the identification of systematic effects as a large background of real gravity signals first has to be removed before instrumental effects become visible. Because synthetic models for the prediction of tidal and other effects are limited to levels of approximately $10\,\mathrm{nm/s^2}$, the comparison to superconducting gravimeters as a reliable, low-noise reference during both mobile comparison campaigns turned out to be essential for this task. The present analysis for the GAIN setup was influenced by, but not limited to, those presented on similar experiments in [27, 83]. Whenever possible, the analysis was performed using the atomic signal in the atomic fountain itself instead of external reference signals or simulations. This enables in-situ checking of the experimental parameters, in some cases even within a measurement campaign, and makes the instrument independent of external calibrations and references and marks another advantage of atom interferometers compared to other types of gravimeters.

Due to the sheer number of relevant systematic effects a categorization into the underlying physical sources was attempted. An alternative ordering exists which orders the effects by their reaction to a flip of the momentum recoil direction $\boldsymbol{k}_{\mathrm{eff}}$. As this is of great practical importance for this experiment, a separate sub-chapter 6.7 deals with the characteristics of this rejection. Finally, a summary of all regarded systematics will be presented in table 6.3.

6.1 Fundamental Effects

This sub-chapter deals with fundamental phase shifts arising in the practical experiment that were not accounted for in the phase shift calculation in chapter 2.3. This encompasses rotations of the laboratory reference frame as well as potential higher-order phase-shifts which are listed in [85] and which are too small to play a role. A general relativistic calculation of the atom interferometer phase presented in [25, 129] has also been considered. Since the largest additional term in this calculation is smaller than $10^{-13}\,\mathrm{g}$ for the GAIN experimental parameters, however, these relativistic effects can safely be neglected here. Note, that the finite speed-of-light also manifests as a phase shift in the relativistic model. Because it can also be derived without a full GR calculation and actually needs to be considered for GAIN, it will be treated separately in chapter 6.1.3.

6.1.1 Coriolis or Sagnac Phase Shift

Due to the finite temperature and imperfect vertical alignment of the launch, the atoms in the atomic fountain will exhibit a small, residual horizontal velocity. This results in a spatial area $\mathbf{A}$ spanned by the atom interferometer which leads to a rotation dependent phase term due to the Sagnac effect [84]:

$$\Delta\Phi_{\mathrm{sag}} = \frac{2m}{\hbar}\boldsymbol{\Omega}\cdot\mathbf{A} = \frac{2m}{\hbar}\boldsymbol{\Omega}\cdot(\boldsymbol{v}_0\times\boldsymbol{v}_{\mathrm{rec}})\,T^2 = 2\boldsymbol{\Omega}\cdot(\boldsymbol{v}_0\times\boldsymbol{k}_{\mathrm{eff}}) \tag{6.1}$$

with the atomic velocity vector $\boldsymbol{v}_0$ and the coordinate frame rotation rate $\boldsymbol{\Omega}$. For a gravimeter with vertical Raman beams in a laboratory frame subject to Earth's rotation rate $\Omega_E = 2\pi/T_{\mathrm{sidereal}}$, this leads to a shift in the measured gravity value of:

$$\Delta g_{\mathrm{Cor}} = 2\left(\Omega_E\cos\bar{\theta}\right)v_{ew} = 2\tilde{\Omega}_E v_{ew} \tag{6.2}$$

where v_{ew} is the atomic velocity along the West direction, $\bar{\theta}$ is the geographical latitude and $\tilde{\Omega}_E$ the effective rotation rate at a given measurement site which is maximal at the equator and vanishes on the poles. Note that this result can alternatively be derived by inserting the vertical component of the Coriolis acceleration $\boldsymbol{a}_{\mathrm{Cor}} = -2\boldsymbol{\Omega}\times\boldsymbol{v}$ into the interferometer phase formula 2.20, hence the term Coriolis shift which will be used here from now on. Also note that v_{ew} obviously varies within the atom cloud due to the finite temperature. The experimentally relevant quantity is the mean horizontal velocity $\bar{v}_{ew}$ of the subset of atoms which arrive in the detection zone and contribute to the measured signal.

In order to keep the Coriolis shift below $10\,\mathrm{nm/s^2}$ in Berlin, Germany with $\tilde{\Omega}_E \approxeq 44.46\,\mu\mathrm{rad/s}$, the upper limit for $\bar{v}_{ew}$ given by equation 6.2 is $127\,\mu\mathrm{m/s}$. This would be difficult to ensure permanently in our current setup due to the spreading of the atomic cloud, much larger size of the detection volume and potential slow drifts of the atomic launch vector due to MOT power fluctuations.

One method to isolate Δg_{Cor} from the gravity signal is to rotate the entire apparatus by $180\,^\circ$ during a measurement which, if all other parameters remain constant, reverses $\bar{v}_{ew}$ and thus the Coriolis shift [130]. We instead employ a method first proposed in [86] which rotates the Raman laser wave vector $\boldsymbol{k}_{\mathrm{eff}}$ during the interferometer sequence by tilting the retro-reflecting mirror. The Coriolis acceleration can then be strongly suppressed by rotating the Raman beams in the opposite direction of Earth's rotation $\tilde{\Omega}_E$. Specifically,

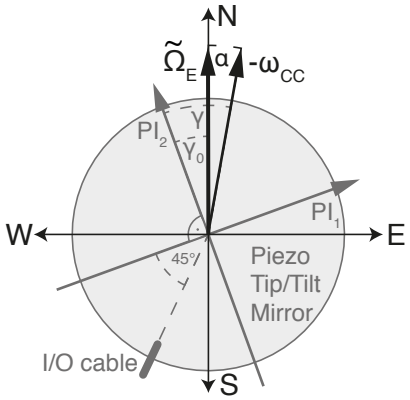

Figure 6.1: The Tip/Tilt mirror rotation axes (gray) are transformed to the geographic reference frame through the rotation matrix $\mathbf{R}_\gamma^{-1}$. The Coriolis compensator rotates around $\boldsymbol{\omega}_{\mathrm{CC}} = -\tilde{\Omega}_E \mathbf{R}_\gamma^{-1} \cdot \boldsymbol{e}_{\mathrm{PI}_2}$ and completely cancels out Earth's rotation at $\gamma = \gamma_0$ or $\alpha = 0$.

a Tip/Tilt stage rotates the retro-reflecting mirror around an axis pointing North with a rate of $-\tilde{\Omega}_E$ during the entire interferometer sequence. The corresponding Piezo Tip/Tilt actor used here was already detailed in chapter 3.2.3. Since $\tilde{\Omega}_E$ is known very accurately at a given measurement site and the well-calibrated closed-loop system allows for precise control of the rotation rate, this system allows in principle for a Coriolis rejection by more than two orders of magnitude, limited by the specified 0.5 % non-linearity of the Tip/Tilt stage. Expressed in terms of permitted horizontal velocities, this means that now up to $v_{ew} \leq 25\,\mathrm{mm/s}$ would be admissible to maintain a Coriolis shift of less than $10\,\mathrm{nm/s^2}$ which is trivial to achieve in our atomic fountain. Compared to rotating the apparatus by 180 °, this allows for automatic Coriolis compensation without interrupting the measurement and is not limited by short-term fluctuations of the atomic horizontal velocity.

Alignment with the Geographic Reference Frame

The simple calculation from above, however, does not account for the alignment uncertainty between mirror rotation axis[1] and the geographic reference system as depicted in figure 6.1. Misalignments α of a few degree have to be expected here because the accurate determination of geodetic North with respect to building walls using map services is difficult and small misalignments of the apparatus with respect to the walls may cause additional uncertainties. This introduces, to leading order, a net rotation of the Raman beam along the East-West axis which is otherwise zero. One solution to this problem would be, e.g. to use a gyro compass for improved alignment. A more elegant solution was chosen in this work instead, which uses the atomic fountain itself to measure geographic North. To clarify we first evaluate equation 6.2 with the additional mirror rotation $\boldsymbol{\omega}$, yielding:

$$\Delta g_{\mathrm{Cor}} = 2\left[v_{ew}\left(\tilde{\Omega}_E + \omega_{sn}\right) - v_{sn}\omega_{ew}\right] \tag{6.3}$$

where $\omega_{ew/sn}$ are the respective mirror rotation components in west and north direction. The second term shows that the additional rotation direction makes the Coriolis shift

[1] $\mathbf{R}_\gamma{}^1$ denotes a passive rotation, equivalent to the opposite active rotation $\mathbf{R}_\gamma$.

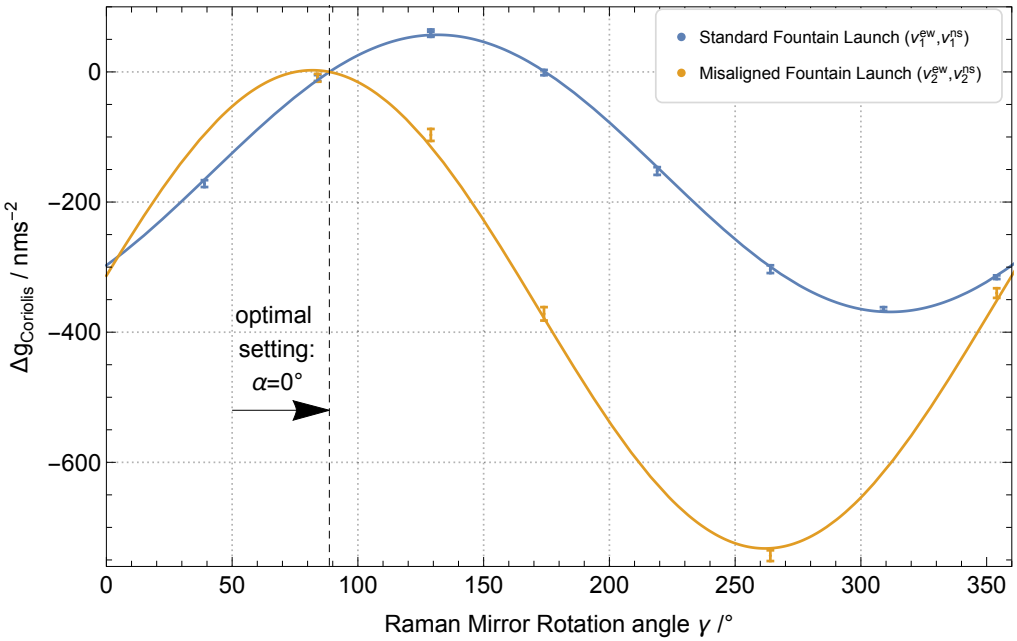

Figure 6.2: Coriolis gravity shift $\Delta g_{\mathrm{Cor}}(\gamma)$ as a function of the mirror rotation direction in internal coordinates $\gamma = \alpha + \gamma_0$. The dashed line corresponds to the optimal setting where $\alpha = 0$ and the mirror rotation is aligned with geodetic north. Blue and yellow datasets indicate two different launch vectors of the atomic fountain. Points are measured gravity shifts with respect to a superconducting gravimeter, solid lines are the result of a combined least-squares fit of both datasets yielding the parameters shown in table 6.1.

sensitive to the atom's velocity in south-north direction. Equation 6.3 can be further simplified by setting the mirror rotation rate to $|\boldsymbol{\omega}| = |\tilde{\Omega}_E|$ and using the angle α as shown in figure 6.1, resulting in

$$\Delta g_{\mathrm{Cor}} = 2\tilde{\Omega}_E \left[v_{ew} \left(1 - \cos\alpha\right) - v_{sn} \sin\alpha \right] \tag{6.4}$$

For $\alpha = 0$, we recover the previous equation 6.2. Assuming $\alpha \leq 5\,^\circ$ and a worst-case horizontal velocity $v_{sn} = 5\,\mathrm{mm/s}$ results in a residual Coriolis shift of $33\,\mathrm{nm/s^2}$ which would be significantly worse than the effect of Piezo calibration errors and dominate the remaining Coriolis shift. In order to reduce the size of this effect and extract information about all relevant parameters in this scenario, one can perform gravity measurements while changing the mirror rotation axis within $\gamma \in [0, 2\pi]$. Additionally, the horizontal velocity component of the cloud can be varied. Since the rotation axis of the GAIN Tip/Tilt mirror is freely adjustable and the horizontal velocity can be changed by moving the vacuum bellow to change the launch vector, no adjustments of the setup were needed for this measurement. The resulting datasets shown in figure 6.2 can be fitted to the Coriolis shift model in equation 6.4. The offset γ_0 between the geographic reference frame $\alpha = \gamma - \gamma_0$ and the instruments rotation axis enters the fit as one free parameter. Since the measured gravity data contain Δg_{Cor} only up to a constant offset c, one more free parameter is necessary. A joint least-squares fit of both datasets to identical γ_0 and c and individual v_{ew},v_{ns} gives all 6 parameters with the values and uncertainties shown in table 6.1. Since the shown data was taken after the gravity measurement campaign (without moving GAIN

Parameter	Fitted Value
v_1^{ew}	$(-2.00\pm0.07)\,\mathrm{mm/s}$
v_1^{sn}	$(1.85\pm0.07)\,\mathrm{mm/s}$
v_2^{ew}	$(-4.66\pm0.09)\,\mathrm{mm/s}$
v_2^{sn}	$(-0.55\pm0.09)\,\mathrm{mm/s}$
γ_0	$(88.6\pm1.6)\,^\circ$
c	$(9\pm5)\,\mathrm{nm/s^2}$

Table 6.1: Parameter values from least-squares fit of the data shown in figure 6.2. The reduced chi square value of 2.4 indicates an adequate fit. All uncertainties are given with 1σ confidence level.

in the meantime) and the previous measurements at that particular site were conducted with a slightly misaligned mirror rotation angle $\gamma = 84\,^\circ$, the fitted parameters did lead to a negative bias of the measured gravity value. Assuming that no substantial long-term drift of the atomic velocities came to play here, this bias evaluates to $(-12\pm7)\,\mathrm{nm/s^2}$ for the datasets shown in figure 6.2.

Length of Wavevector

Because only the mirror and not also the Raman telescope are rotated during the sequence, the length of $\boldsymbol{k}_{\mathrm{eff}}$ changes slightly between the three Raman pulses in the Coriolis compensation scheme. In order to investigate this effect we expand k_{eff} for a small angle β between upwards and downwards traveling Raman beam up to second order:

$$k_{\mathrm{eff}}(\beta) := |\boldsymbol{k}_1 - \boldsymbol{k}_2(\beta)| = \sqrt{k_1^2 + k_2^2 + 2k_1k_2\cos\beta} \approxeq k_{\mathrm{eff}}^0\left(1 - \frac{\beta^2}{8}\right) \tag{6.5}$$

which can be used to calculate the first order interferometer phase shift in equation 2.20 with time/phase dependent $k_{\mathrm{eff}}(\beta)$. Due to the quadratic dependence on β we can minimize this effect by choosing a symmetric tilting behavior with $\beta = 0$ during the second Raman pulse and $\beta_{\mathrm{Ra1}} = -\beta_{\mathrm{Ra3}} = \tilde{\Omega}_E T$ for the first and last pulse. This reflects very well to the situation in our setup due to the auto-collimation scheme presented in chapter 6.2.1 and results in a relative phase shift of

$$\frac{\Delta\Phi}{\Phi} = -\frac{\beta^2}{4} = -\left(\frac{\tilde{\Omega}_E T}{2}\right)^2$$

which evaluates to 2.5×10^{-11} for our typical parameters of $T = 0.26\,\mathrm{s}$ and $\tilde{\Omega}_E \approxeq 40\,\mu\mathrm{rad/s}$. This is negligible compared to other systematics and around two orders of magnitude below the targeted accuracy for the gravity measurement. It is therefore more than adequate to only rotate the mirror without the Raman telescope to compensate for the Coriolis effect.

6.1.2 Self-Gravitation of the Setup

Due to the proximity of the atoms to the walls of the vacuum chamber and rest of the physics package, the gravitational effect of the apparatus itself can cause effects on the

$10\,\mathrm{nm/s^2}$ level and has to be considered. A detailed FEM simulation of the GAIN self-gravitation was performed in [93], its main result is included here for completeness. It is based on the original CAD design of the physics package and calculates the Newtonian gravitation exerted by equivalent point masses on the atoms during their free fall. The resulting interferometer phase shift is derived by computing the perturbed trajectories and corresponding phase terms during the atom-light interaction during the Raman pulses[2]. The biggest influence was caused by the magnetic shield of the ion-pump and the solid aluminum block on top of the interferometer zone. All significant components together added up in [93] result in a net gravity bias of $19\,\mathrm{nm/s^2}$ for the usual experimental parameters $T = 0.26\,\mathrm{s}$. The high fidelity of the CAD model yields a relatively small uncertainty of only 0.5 % of this value. Due to the fact that some components of the apparatus, such as the MOT magnetic shield, were not included in this analysis, we instead assume a larger uncertainty of $5\,\mathrm{nm/s^2}$ for this effect. This effect currently does not limit the final accuracy of the instrument and can readily be improved with moderate computational cost by increasing the fidelity of the FEM model as outlined in [93].

6.1.3 Finite Speed of Light

Chirping the Raman frequencies during the interferometer may introduce a spurious phase shift if only one frequency component is chirped. For a stationary atom, the propagation delay between laser source and atom would result in an identical chirp centered around a slightly different frequency and have very little effect. Due to the constant acceleration of the atoms during their free fall, however, the propagation delay changes during the interferometer sequence which leads to a modified effective chirp-rate and an associated correction of the gravity value [11, 27, 131]

$$\Delta g_c = 2\frac{v_0}{c}\frac{\alpha_1 + \alpha_2}{\alpha_1 - \alpha_2} \tag{6.6}$$

where v_0 is the atomic velocity during the π pulse and α_i is the chirp-rate of the respective Raman frequency component so that $\alpha = \alpha_1 - \alpha_2$ compensates for the Doppler shift. This is closely related to retardation effects caused by the finite speed of light which must be corrected in falling corner-cube gravimeters[132]. Note that due to our symmetric sequence with the π pulse close to the apex this effect is quite small in comparison to other configurations which simply drop the atoms. In order to remove it completely we apply frequency chirps to both Raman frequencies $\alpha_1 = -\alpha_2 \approxeq \pm 12.58\,\mathrm{MHz/s}$ so that Δg_c vanishes. Moreover, the induced gravity bias changes sign when reversing the chirp-rate and will thus be rejected additionally by the k-reversal technique [131]. We therefore conclude that speed-of-light effects do not contribute significantly to the systematic error budget.

6.2 Raman Beam Effects

This section contains all effects which directly influence the wave-vector, wavelength or phase of the Raman beams during the interferometer sequence. $\boldsymbol{k}_{\mathrm{eff}}$, or its projection

[2] An additional path integral component also exists but is too small to be relevant here [93].

on $\boldsymbol{g}$, enters the phase directly through equation 2.20 and phase offsets $\Delta\Phi$ between interferometer pulses obviously also cause direct shifts of the measured gravity signal:

$$\frac{\Delta g}{g} = \frac{\Delta\Phi}{\Phi_g} = \frac{\Delta k_{\text{eff}}}{k_{\text{eff}}} \tag{6.7}$$

In order to obtain the absolute value of g on the 10^{-9} level, k_{eff} and differential phase shifts therefore have to be controlled or rejected on the same level.

6.2.1 Vertical Alignment

As only the projection of $\boldsymbol{g}$ onto the effective wave vector $\boldsymbol{k}_{\text{eff}} = \boldsymbol{k}_1 - \boldsymbol{k}_2$ enters in the atom interferometer phase, $\boldsymbol{k}_{\text{eff}}$ has to be well-aligned with the vertical axis. In order to quantify the related error we expand it to second order in the misalignment angle δ between $\boldsymbol{k}_{\text{eff}}$ and the plumb line $\boldsymbol{g}$.

$$\boldsymbol{k}_{\text{eff}} \cdot \boldsymbol{g} = |\boldsymbol{k}_{\text{eff}}||\boldsymbol{g}| \cos\delta \approxeq k_{\text{eff}} \cdot g(1 - \delta^2) \tag{6.8}$$

Controlling δ to less than 10 µrad would therefore results in a relative gravity shift below 10^{-10} g or 1 nm/s^2, one order of magnitude below the targeted accuracy of the gravity measurement. The situation is complicated, however, by the fact that both incident and reflected component of the Raman beam affect $\boldsymbol{k}_{\text{eff}}$ independently through relative misalignments β as given in equation 6.5. The Raman collimator and retro-reflection mirror thus both have to be controlled relative to each other *and* relative to $\boldsymbol{g}$ on this level.

Alignment of the Retro-Reflector

In order to reduce the number of degrees of freedom an auto-collimation scheme was implemented as part of this work together with M. Hauth [80]. It consists of the Piezo Tip/Tilt actor detailed in chapter 3.2.3 which is used for µrad level steering of the reflected Raman beams. After successful auto-collimation, the retro-reflected beam is coupled back into the Raman fiber and detected on a photo diode behind a polarizing beam splitter in the laser module. The auto-collimation acceptance angle of the used Raman telescope- and fiber is only about $\Delta\beta \approxeq 5\,\mu\text{rad}\left(\frac{1}{\sqrt{e}}\right)$ as shown in figure 6.3 which enables scanning of the correct retro-reflection angle to better than 1 µrad. In order to ensure persistent auto-collimation during long-term gravity measurements under the influence of slow µrad level tilt drifts of the apparatus, a tracking algorithm was implemented as part of this work which scans the auto-collimation profile during the course of each experimental run and corrects the Tip/Tilt settings for optimal retro-reflection. The angle β is scanned by approximately 40 µrad during the interferometer sequence to compensate for Earth's rotation as detailed in chapter 6.1.1, and the magnitude of the auto-collimation signal is recorded for all three Raman pulses. The signal ratio between the first and third Raman pulse is then used to generate an error signal which is low-pass filtered and fed into a feedback loop that adjusts the Tip/Tilt setting during the central Raman pulse. In order to perform the same protocol on the perpendicular tilt-axis, an equivalent mirror rotation and pulse sequence is carried out during the MOT loading phase. We did not observe any disturbances of the MOT loading, presumably due to the large one-photon detuning of the Raman laser. Likewise the auto-collimation signal was not altered or obscured by the

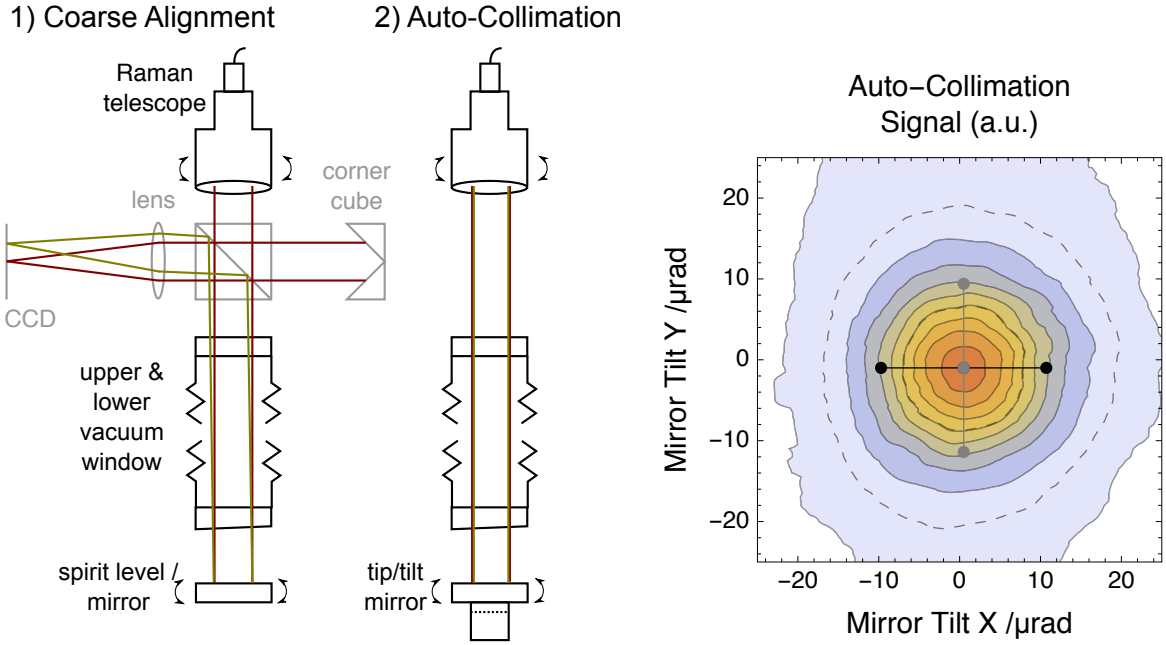

(a) 1) Coarse alignment is done using a beam splitter and a corner-cube which are temporarily inserted into the beam. The telescope is aligned with respect to a spirit level and the Raman mirror afterwards w/r to the telescope. 2) Auto-collimation into the Raman fiber can then be enabled using the Piezo tip/tilt mirror.

(b) Laser power retro-reflected into the Raman fiber as a function of mirror tip/tilt angle. Black/gray points denote the peak-sampling at three points in two axes during in-sequence tilt sweeps from which a tracking signal is derived.

Figure 6.3: GAIN Raman beam vertical alignment scheme.

MOT loading which is probably due to the extremely small solid angle collected by the Raman telescope[3].

This auto-collimation scheme competes favorably with alternate methods for aligning anti-collinear laser beams such as [133] without the need for additional elements in the beam path. This is especially advantageous for atom interferometry where wavefront aberrations caused by optical elements have to be minimized as discussed in chapter 6.2.4.

Alignment of the Raman Telescope

With the active auto-collimation system enabled, the alignment angle δ is solely dependent on the Raman telescope orientation which still has to be controlled on the 10 µrad level. For increased long-term stability the telescope was placed on a stable, adjustable mount featuring electrolytic tilt meters[4] and DC motors[5] for remote tilt control and monitoring on the µrad level. In order to find the correct tilt setting a two-step process is used as detailed in figure 6.3. First, the Raman telescope is verticalized with respect to a spirit level which is placed at the position of the retro-reflection mirror using a procedure

[3]Note that the auto-collimation peak in later measurements showed similar size but significant ellipticity. Because the semi-axes rotate with the Raman telescope, warping or misalignments are the likely cause. This did not affect operation of the auto-collimator and is therefore not discussed further here.

[4]Applied Geomechanics 755 series

[5]Newport Motorizer 860a S3820

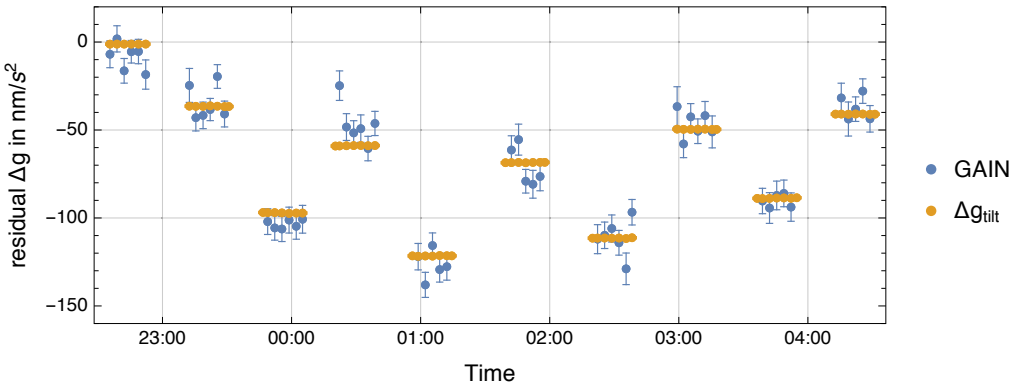

Figure 6.4: Blue: measured gravity residuals while scanning the vertical alignment δ of the Raman telescope, while maintaining retro-reflection with the auto-collimation system. Data points corresponds to 3 min of measurements. Yellow: misalignment effect as in equation 6.8, resulting in tilt values $\delta^0_{x/y}$ fitted from this dataset (fit uncertainty $\Delta\delta^0_{x/y} \leq 2\,\mu$rad).

implemented in [93]: Incident and reflected beam are aligned using an additional beam-splitter and cat-eye retro-reflector. Both beams are then focused on a CCD sensor and the collimator tilt is adjusted until the spots overlap. The liquid level is then replaced by the Raman mirror and its alignment corrected by again overlapping both spots. Afterwards the additional beam-splitter is removed from the Raman beam path. Since this method normalizes the Raman beam incident on the spirit level, as opposed to aligning it with gravity inside the vacuum chamber, the accuracy of this method is limited by the $1'$ wedge of the bottom vacuum window to around 150 µrad. Although this alone is not sufficient it provides a good starting point where the auto-collimation system is within its Tip/Tilt-limited working range of ± 1 mrad. A more accurate alignment procedure using the atomic gravity signal is then conducted as the final step. We use the motorized collimator mount to deliberately scan δ versus the measured gravity value in both x and y direction as proposed in [27]. During this scan the mirror follows automatically by virtue of the tracking algorithm and eliminates β. In order to perform this procedure routinely and efficiently it was integrated into the gravity measurement control system by the author and is performed fully automatically over the course of a few hours. The resulting gravity signal in combination with the telescope tilt meter data can then be used with equation 6.8 to find the optimal alignment angle $\delta^0_{x/y}$. Figure 6.4 shows the gravity signal during an alignment scan together with the calculated tilt-effect given the correct $\delta^0_{x/y}$. The uncertainty $\Delta\delta^0_{x/y} \leq 2\,\mu$rad corresponds to a negligible vertical alignment error of only 0.04 nm/s^2. Due to this elaborate multi-step procedure, vertical alignment is therefore not currently a problem.

6.2.2 Reference Laser Frequency Offsets

As motivated above, an absolute measurement of g at the 10^{-9} level requires knowledge of k_{eff} on the same or better level, corresponding to an absolute frequency uncertainty of well below 300 kHz. Because relative shifts of the optical frequency of the Raman beams

translate directly to k_{eff} and hence g, offsets of the laser reference frequency ν_{ref} have to be carefully controlled or characterized on the 10^{-9} level:

$$\frac{\Delta k_{\text{eff}}}{k_{\text{eff}}} = \frac{\Delta \nu_{\text{ref}}}{\nu_{\text{ref}}} \tag{6.9}$$

The literature value [100] of the ^{87}Rb D2 line was obtained through very precise spectroscopic measurements [134] with an uncertainty of 5.5 kHz or 1.4×10^{-11} which certainly fulfills this requirement. The Rubidium spectroscopy implementation in the GAIN reference laser module to which both Raman lasers are referenced, however, does not necessarily hold up to such high standards. The ^{87}Rb D2 linewidth of 6.1 MHz is about 20 times larger than the admissible frequency uncertainty which places moderate demands on the accuracy of spectroscopy setup. Potential systematic shifts on this level could originate from residual amplitude modulation or slow drifts of electronic components in the modulation transfer spectroscopy.

To avoid potential systematic frequency shift, the reference laser frequency was thus measured explicitly. Instead of comparing it to an accurate optical reference using, e.g. a frequency comb, one can again employ the cold ^{87}Rb cloud in the atomic fountain by performing D2 line spectroscopy [80] as follows: We first use the standard MOT preparation- and launch sequence and subsequent velocity- and state selection to prepare a cloud in the $F = 2$ hyperfine state in the atomic fountain. As detailed in chapter 4.2, the cloud has a very narrow vertical velocity distribution corresponding to a Doppler width of only 5 kHz which is well below the transition‘s natural linewidth. Next, the Raman slave laser is switched off with a mechanical shutter as it is not needed anymore for the rest of the sequence. We then tune the Raman Master laser close to the D2 transition frequency and probe the $|5^2S_{1/2}F = 2\rangle \rightarrow |5^2P_{3/2}F' = 1\rangle$ open transition by optically pumping a part of the atoms to the lower hyperfine state with a 80 µs resonant pulse when the atoms are on the apex of their trajectory and the mean velocity class is zero. Detecting the number of atoms in $F = 1$ as a function of the scanned frequency generates a Lorentzian signal with a FWHM width of 7.8 MHz as shown in figure 6.5. At the center of the peak we assume that the probe laser is tuned to the center of the ^{87}Rb D2 F2 $\rightarrow$ F′1 transition as depicted in figure 6.5 (left). The frequency shift of the reference laser Δf_{ref} can then be extracted in a straightforward way through

$$\Delta f_{\text{ref}} = \left(f_{\text{probe}} - f_{\text{ref}}^{\text{lit}}\right) + \Delta f_{\text{Lock}} - f_{\text{aom}} \tag{6.10}$$

where $f_{\text{probe}} - f_{\text{ref}}^{\text{lit}}$ is given by literature values and can be extracted from, e.g., figure 3.13. The lock PLL reference frequency Δf_{Lock} and Raman switching AOM frequency shift $f_{\text{aom}} = 80$ MHz are known experimental parameters.

To monitor potential drifts of the frequency offset, this measurement was repeated frequently. Before and during the last gravity comparison in Onsala, Sweden, 14 such measurements were performed over a period of one month. The mean and standard deviation of the resulting frequency offsets is $\bar{f}_{\text{ref}} = (-510\pm80)$ kHz and shows no apparent drift.

The observed frequency shift may be caused by light, magnetic or pressure shifts in the Rubidium cell investigated here [135]. Other potential error sources are the buffer gas composition and voltage offsets in the lock electronics. Since the MTS error signal has a steepness of around 0.1 mV/kHz, however, the measured shift corresponds to offsets

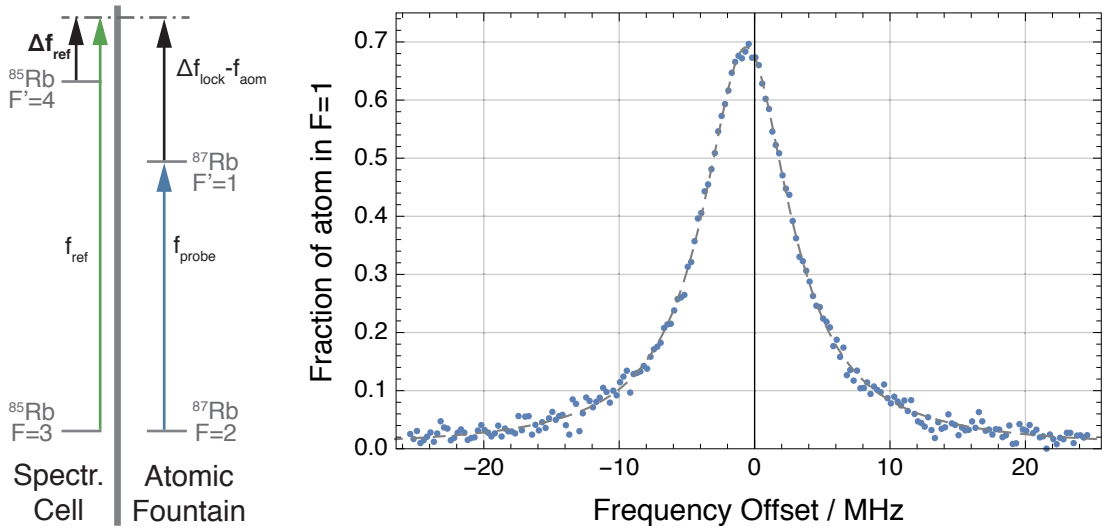

Figure 6.5: **Left:** Level scheme for probing the reference laser frequency using GAIN's atomic fountain (see text). **Right:** Spectroscopy signal and Lorentz fit of the cold atoms at the apex of the atomic fountain generated by optical pumping with the Raman Master laser. The origin indicates the center of the resonance for $\Delta f_{\mathrm{ref}} = 0$. The shown data include 200 points and yield a significant frequency offset of $\Delta f_{\mathrm{ref}} = (-616 \pm 18)\,\mathrm{kHz}$.

of several ten mV, which would be unusually large. Finally, the ^{87}Rb transition inside the fountain could be disturbed by line pulling due to light shifts. Further investigation is therefore needed to determine the predominant source of the reference laser frequency shift.

For the time being, we account for a gravity bias of $(-13 \pm 2)\,\mathrm{nm/s^2}$ during the measurement in Onsala. A similar value was measured during the comparison campaign in Wettzell.

6.2.3 Rubidium Background Vapor Pressure

The refractive index of the background gas is another potential error source for k_{eff}. Normally the low background gas pressure in a UHV system is sufficient to keep $n = 1 + \Delta n$ close enough to unity. Due to the relatively small detuning of the Raman beams from the D2 line in combination with large Rubidium partial pressure, however, there might still be a significant shift for our particular situation. Starting from the wave-number deviations $\Delta k_i = \Delta n_i k_i^0$ for each Raman frequency component i, the resulting interferometer phase shift is

$$\frac{\Delta k_{\mathrm{eff}}}{k_{\mathrm{eff}}} \approxeq \frac{1}{2}\left(\Delta n_1 + \Delta n_2\right) \tag{6.11}$$

The refractive part of the index is given by the electric susceptibility $\chi(\omega)$ to $\Delta n(\omega) := \mathrm{Re}\,(\chi(\omega))/2$ [79] . Since the two spectral components of the Raman beams are separated by the 6.8 GHz hyperfine splitting and Δn varies substantially close to atomic transitions, the refractive index has to be calculated separately for both frequency components. We use an analytic model given in [136] which considers the complete hyperfine structure and Doppler broadening at room temperature. The refractive index change for one single

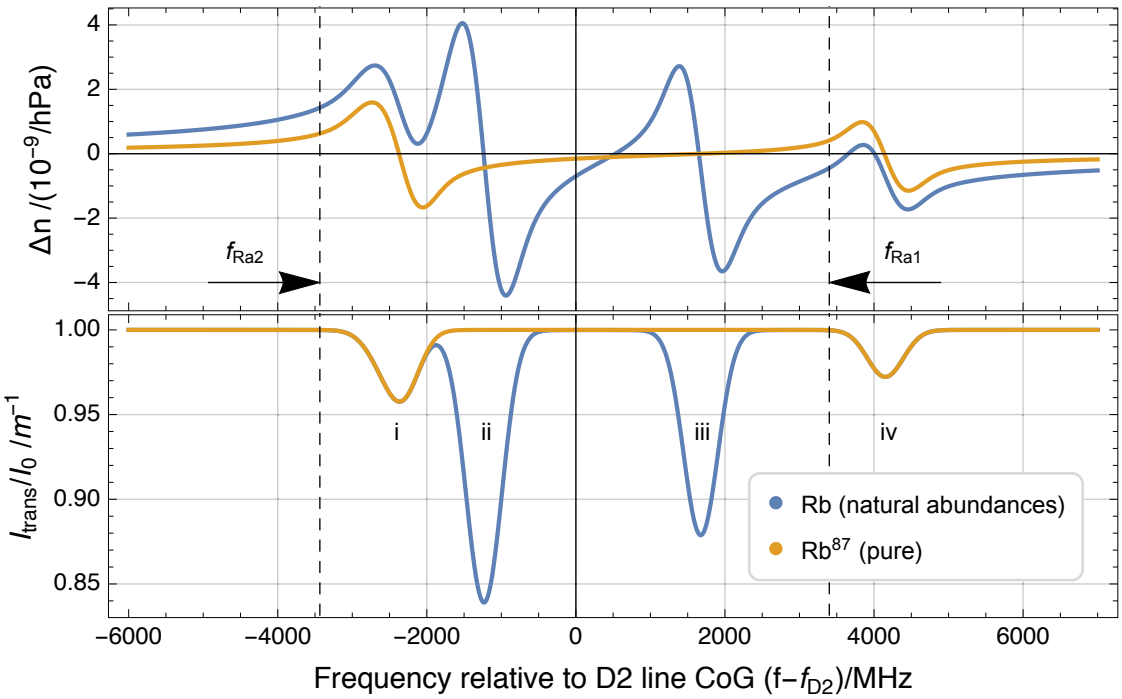

Figure 6.6: Rubidium background gas dispersion (top) and absorption (bottom) profile as a function of ^{87}Rb partial pressure, after [136]. Numerical values for room temperature, $p_{87} = 10^{-9}$ hPa and 1 m optical path length. The dashed lines show both Raman frequency components for standard GAIN settings (see figure 3.13). Annotated transitions mark i)^{87}Rb $F_2 \to F_e$, ii)^{85}Rb $F_3 \to F_e$, iii)^{85}Rb $F_2 \to F_e$ and iv)^{87}Rb $F_1 \to F_e$.

$F \to F'$ hyperfine transition is given by:

$$\Delta n(\Delta\omega) = \frac{1}{2}\mathrm{Re}\ (\chi(\Delta\omega)) = C_F^2 d^2 \frac{N}{\hbar\epsilon_0}\mathrm{Re}\ (s(\Delta\omega)) \tag{6.12}$$

here $\Delta\omega$ is the detuning relative to the center of gravity (CoG) of the D2 line, $C_F^2 d^2$ is the hyperfine transition strength, N is the number density and $s = f * g$ is a line-shape factor resulting from the convolution of the natural line-shape f and Doppler broadened profile g. One can sum up $\Delta n(\Delta\omega)$ for all hyperfine transitions and insert into equation 6.11 which gives the dispersion and absorption profiles shown in figure 6.6. Evaluating equation 6.11 for both Raman frequency components as a function of the one-photon detuning Δ (with respect to the $|F' = 1\rangle$ state, see figure 3.13) yields the behavior shown figure 6.7. The gravity shift $\Delta g_{\mathrm{index}}$ induced by ^{87}Rb partial pressure is on the order of 10 nm/s^2/hPa. For the $\Delta = -700$ MHz setting used during GAIN gravity measurements this corresponds to a shift around 5 nm/s^2 at 10^{-9} hPa for both pure ^{87}Rb and a natural isotope mixture[6]. Since the background loaded MOT in the GAIN setup operates around 10^{-9} hPa background pressures, this could results in a small but significant gravity bias. Note that, for the natural Rubidium isotope mixture, the gravity bias has an interesting a zero-crossing around a detuning of $\Delta = -1276$ MHz. This is due to the equal amplitude

[6]Both cases shown in figures 6.6 and 6.7 assume the same ^{87}Rb partial pressure in order to simulate an equal MOT loading rate. Hence, the total Rb pressure is 3.6 times larger for the natural abundance case.

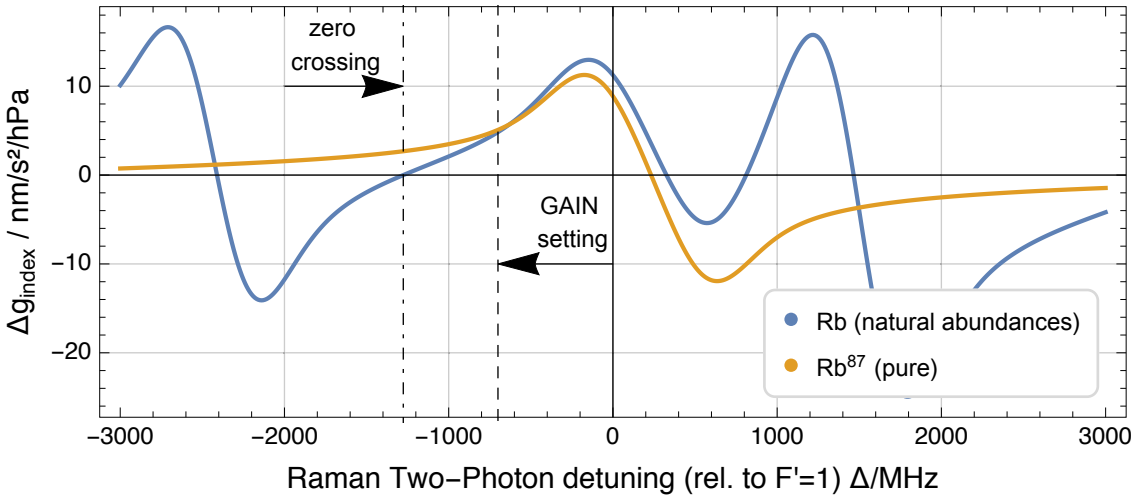

Figure 6.7: Gravity bias due to k_{eff} changes caused by the refractive index of Rubidium background gas. The dashed line shows the GAIN setting during gravity measurements presented in this work. The dot-dashed line indicates a cancellation of the effect due to an equal but opposite-sign index shift at $\Delta = -1276\,\text{MHz}$.

but opposite sign of Δn for the two frequency components and does not occur if only ^{87}Rb transitions are considered[7].

It should be noted that the used transition model has been found truly accurate only for very low intensities much below saturation, were the ground state population is undisturbed by optical pumping. Saturation line broadening is also not considered in the model [136]. Although the saturation parameter I/I_{sat} of our Raman beams is on the order of 1, the large one-photon detuning effectively means that optical pumping should not play a role and that model predictions should be accurate for frequency settings with negligible one-photon absorption.

The above treatment further assumes that the Rubidium partial pressure is constant within the interferometer zone. While pressure gradients in other parts of the chamber cancel out in the total interferometer phase, variations within the AI region would add an additional bias caused by different k_{eff} values for each Raman pulse. We therefore assume that pressure gradients in the interferometer zone are very small, which is reasonable given the geometry of the GAIN vacuum system. This assumption is also supported by optical absorption measurements of the Rubidium partial pressure which were conducted along several optical axes of the vacuum system. They yield values of below $10^{-9}\,\text{hPa}$ during operation with the dispensers switched on, which agrees well with the vacuum gauge that indicates a total pressure at the $5{\times}10^{-10}\,\text{hPa}$ level.

Based on this analysis we infer a small gravity value bias of $(5{\pm}5)\,\text{nm/s}^2$ for this effect. The large relative uncertainty accounts for remaining uncertainties in the refractive index model and the error of the exact Rubidium pressure in the interferometer zone. This small effect could in the future be eliminated under the current experimental conditions by means of further characterizations of the refractive index model and by exploiting the zero-crossing shown in figure 6.7. An alternative approach would be to reduce the Rubidium pressure in the system by more than one order of magnitude by adding a 2D-

[7] Which might be relevant to know before purchasing isotope enriched Rubidium sources.

MOT and a differential pumping stage [83].

6.2.4 Raman Wavefront Aberrations

Due to finite temperature and resulting horizontal velocity distribution within the cloud (see chapter 6.1.1) the atoms sample different parts of the Raman beam wavefront during each of the three interferometer pulses according to their respective horizontal positions within the beam. In a realistic scenario with wavefronts that are curved and locally distorted due to imperfect optical elements, this leads to a phase shift for a given atomic trajectory $x(t)$ of:

$$\Phi_{\mathrm{wf}} = \phi^{\mathrm{eff}}(x(t_1)) - 2\phi^{\mathrm{eff}}(x(t_2)) + \phi^{\mathrm{eff}}(x(t_3)) \tag{6.13}$$

where $\phi^{\mathrm{eff}}(x)$ is the effective wavefront phase given by the difference of up- and downwards traveling Raman beam wavefronts [137]. Since only the difference between up- and downwards traveling wavefront plays a role, the only optical elements that have to be regarded in the GAIN setup are the lower vacuum window, the quarter wave plate and the retro-reflecting mirror. One approach to minimize this effect is to reduce the number of critical optical elements by putting the retro-reflecting mirror into the vacuum chamber as shown elsewhere [130]. A different approach was chosen here which is compatible with the GAIN active vibration isolation and retro-reflector Tip/Tilt stage. It relies on accurate characterization of the optical wavefronts and a model to calculate the resulting interferometer phase shift which can then be removed in post processing. This was carried out by Vladimir Schkolnik and Bastian Leykauf [138, 137] and is summarized here for completeness. Wavefront distortions of the above-mentioned optical elements were mea-

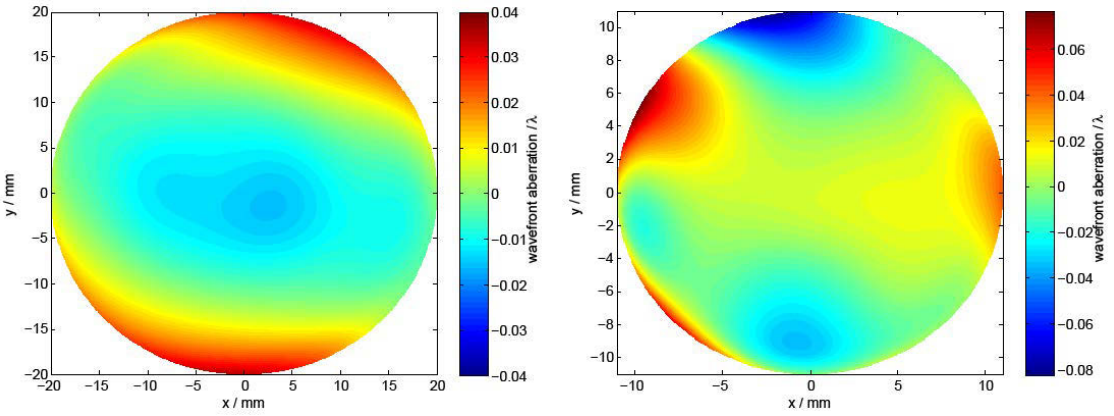

Figure 6.8: Measured wavefronts of critical optical components in the Raman beam path (2" diameter). Left: retro-reflection mirror, measured by FBH using a Zygo interferometer. Right: zero-order $\lambda/4$ wave-plate, measured using a Shack-Hartman sensor.

sured using a Shack-Hartmann sensor. Since an in-situ measurement of the lower vacuum window is not possible without opening the UHV chamber, a set of 5 vacuum windows with identical dimensions and optical quality were instead used as surrogates. The retro-reflecting mirror was characterized using a Zygo interferometer equipped with a $\lambda/100$ reference flat by courtesy of Ferdinand-Braun Institut für Höchstfrequenztechnik (FBH). In order to calculate the resulting phase shift of a given wave-front, both the spatial profile and velocity distributions of the atom cloud are approximated to be Gaussian with widths

Optical Element	dg_{wf} [nm/s^2]	Δdg_{wf} [nm/s^2]
Lower vacuum window	$2 \times (-5*)$	$2 \times 11*$
$\frac{\lambda}{4}$ waveplate	$2 \times (-11)$	2×2
Retro-reflection mirror	4	2
Total	**-28**	**22**

Table 6.2: Gravity value biases dg_{wf} induced by wavefront aberrations of optical elements in the Raman beam-path, as determined in [137]. The factors of two indicate that the bias has to be applied for each pass of the beam through an element. Asterisk indicate that values were estimated by averaging over surrogate optics as explained in the text.

corresponding to the measured cloud's size and temperature. The phase shift according to equation 6.13 is then integrated only over the part of the distribution which reaches the detection zone and contributes to the signal. The calculation was tested and confirmed by entering an additional window into the beam path and comparing the predicted phase shift to the measured gravity bias [138]. The model shows that the phase approaches zero as the temperature of the atomic cloud is reduced, which is expected and has also been shown in [130]. Temperatures lower than 2 µK are unfortunately inaccessible with the molasses cooling technique used in GAIN. Reducing the size of this effect therefore encourages the use of advanced cooling techniques like Raman sideband cooling or evaporative cooling in a magnetic or optical trap.

In order to give an estimate of the effect in the current setup, biases for all significant optical elements were calculated for the given temperature and detection parameters. For the inaccessible vacuum window the mean bias values for all 5 windows from the surrogate batch was defined as an estimate. Its significant deviation from zero indicates characteristic wavefront features stemming from the production process resulting in a negative bias. The largest measured bias value of all surrogate windows was defined as the estimate uncertainty in order to give a bound, conservative value [139]. The resulting phase shifts are listed in table 6.2. A total bias of $(-28 \pm 22)\,\mathrm{nm/s^2}$ was removed from all gravity values measured during this work as a result of this analysis.

6.2.5 Gouy Phase

With the standard GAIN Raman telescope, the Raman beam inside the vacuum chamber is in good approximation Gaussian with a $\frac{1}{e^2}$ beam waist radius of $w_0 \cong 15\,\mathrm{mm}$ and a Rayleigh length of $z_R = w_o^2\pi/\lambda \cong 876\,\mathrm{m}$. Due to the retro-reflection scheme the atoms interact with both incident and the retro-reflected part at different longitudinal positions of the Gaussian beam. An additional Gouy phase term therefore has to be considered. Note that this is fundamentally different from the wavefront aberrations discussed in chapter 6.2.4 because the Gouy phase is a consequence of the longitudinal Gaussian mode and would persists even at arbitrarily low atomic temperatures. For a Gaussian beam propagating along the z-direction with its waist centered[8] at the retro-reflecting mirror at $z = 0$ it generally results in a phase shift of $\zeta(z) = \arctan(z/z_R)$. The differential phase

[8]The beam waist position is located at the coordinate origin which can be chosen at will here as no symmetries of the atomic trajectory were used for this analysis.

term imprinted on the atoms during the i-th Raman pulse is therefore given to first order by:

$$\phi_i^{\mathrm{Go}} = -\arctan(\frac{z_i}{z_R}) + \arctan(\frac{z_i + \Delta z_i}{z_R}) \cong \frac{\Delta z_i}{z_R} + O(\Delta z_i^3) \tag{6.14}$$

were z_i is the atom's position relative to the beam waist and Δz_i is twice the distance between atom and retro-reflector. Equation 6.14 is valid for an upward directed photon recoil and changes sign for k_{eff} pointing downwards. Since the Rayleigh range is usually chosen to be on the order of hundreds of meters it is safe to perform the first order expansion as in equation 6.14. Note also that this actually corresponds to a worst-case estimation because the arctan slope has its maximum at zero and the Gouy phase therefore monotonically decreased the further away the atoms are from the beam waist. By combining the parabolic atomic trajectories with equation 6.14 we can calculate the total phase shift in the atom interferometer, yielding:

$$\Delta\Phi^{\mathrm{Go}} = \phi_1^{\mathrm{Go}} - 2\phi_2^{\mathrm{Go}} + \phi_3^{\mathrm{Go}} \cong \frac{2gT^2}{z_R} \tag{6.15}$$

For k_{eff} pointing upwards, the above-mentioned Rayleigh length and $T = 0.26\,\mathrm{s}$ this results in a phase shift of $\Delta\Phi^{\mathrm{Go}} = 1.5\,\mathrm{mrad}$ which is negligible compared to other systematic effects and its value is in good agreement with the analysis performed in [93]. The size of this systematic effect changes quickly, however, if the Raman beam is expanded to smaller waist diameters. In order to estimate the maximum acceptable waist size for gravimetry applications we substitute the beam waist into equation 6.15 which yields a relative phase offset of

$$\frac{\Delta\Phi^{\mathrm{Go}}}{\Phi_0} = \frac{\Delta g^{\mathrm{Go}}}{g} = \left(\frac{\lambda}{\pi w_0}\right)^2 \tag{6.16}$$

with $k_{\mathrm{eff}} \cong 4\pi/\lambda$. Interestingly the effect depends only on the wavelength of the Raman beams and the chosen waist radius. The quadratic relation is displayed in figure 6.9 for $n = 2$, $\lambda = 780\,\mathrm{nm}$ and shows that in order to keep the associated gravity bias well below $10\,\mathrm{nm/s^2}$, the beam waist diameter should be larger than 1 cm.

6.2.6 Raman Beam Diffraction

The above chapter concluded that a large Raman beam diameter is advantageous in order to minimize the Gouy phase. This large beam, however, also has to be accommodated by the aperture of the vacuum window in the Raman axis. If that aperture is too small, significant diffraction ripples occur which can lead to substantial amplitude fluctuations along the beam profile.

In order to limit intensity ripples of a Gaussian beam with radius w_0 $\left(1/e^2\right)$ through a circular aperture with radius a to less than 1 %, the beam radius should be smaller than

$$w_0 \leq \sqrt{2}\frac{2a}{4.6} \tag{6.17}$$

as shown in [140, 141]. For the GAIN Raman beam aperture with $a = 20\,\mathrm{mm}$, this criterion leads to a maximal beam radius of $w_0^{\max} = 12.3\,\mathrm{mm}$. The Raman telescope used during the gravity comparison campaigns, however, was slightly bigger than this with $w_0 = 15\,\mathrm{mm}$. A certain amount of diffraction was therefore certainly present during the measurements. Due to the comparatively large horizontal velocity and small vertical splitting of the atoms

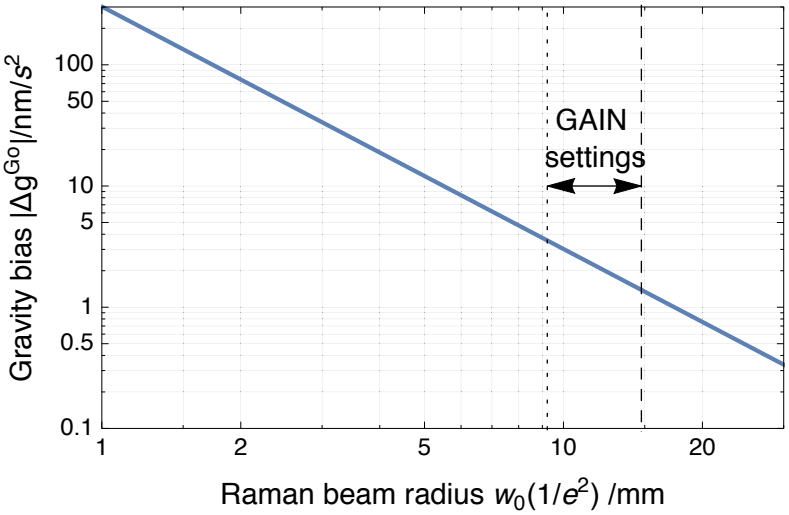

Figure 6.9: Gravity bias induced by the Gouy phase vs. Raman beam waist size. Plotted is the worst-case estimate for atoms close to the beam waist from equation 6.16. Dashed and dotted vertical lines show settings used for GAIN gravimetry campaigns and test measurements, respectively.

during the interferometer sequence, potential position dependent light shift or other effects are likely to average out between the different parts of the atom cloud. A systematic bias of the gravity value is therefore improbable here but can not be completely ruled out. In order to adhere to the 1 % criterion more strictly in the future, a new Raman telescope with beam radius $w_0^{\max}$ was purchased and will be used for future gravity measurements.

6.3 Raman RF Control

This section contains several systematics which originate from the frequency control, chirping and switching of the Raman beams during and in between the interferometer pulses. Not mentioned explicitly here are effects due to pulse-length and -intensity or incorrect chirp rates because they were already found to be negligible in [11].

6.3.1 Raman Chirp Group Delays

The linear frequency chirp of the Raman lasers during the interferometer sequence compensates for the atomic Doppler-shift and is essential for operating the atom interferometer. It also, however, makes the interferometer sensitive to phase shifts $\phi_{\mathrm{RF}}(f)$ introduced by elements of the Raman frequency chain.

Assuming a non-linear frequency dependence $\phi_{\mathrm{RF}}(f) \propto \eta f^2$, which is equivalent to a first order group delay effect parametrized by η, leads to a spurious atom interferometer phase shift:

$$\Phi_{\mathrm{RF}} = \phi_{\mathrm{RF}}(f_0) - 2\phi_{\mathrm{RF}}(f_0 + \alpha T) + \phi_{\mathrm{RF}}(f_0 + 2\alpha T) = 2\eta(\alpha T)^2 \tag{6.18}$$

where α is the slope of the frequency ramp. Group delays such as this can be introduced by all RF components in the Raman frequency chain which facilitate the frequency chirp,

including the DDS, mixers, amplifiers, AOMs. An explicit measurement of $\phi_{\mathrm{RF}}(f)$ is possible and was demonstrated in [11]. Instead of repeating this intricate but not fully conclusive measurement with the GAIN setup, we instead rely on the suppression of this effect by reversing the momentum recoil direction and k_{eff} in the interferometer which enables a cancellation of this effect by averaging over the two different configurations.

Residual effects due to the local group delay structure and the small offset in chirp center frequencies between up-/downwards recoil still exist, however. In order to estimate their size we refer to the half-sum between up- and downward directed recoil which shows a total effect of around $40\,\mathrm{nm/s^2}$ as shown in figure 6.16. Averaging over both configurations certainly provides a significant rejection, but a small residual contribution can not be excluded based on this short analysis. We therefore attribute a common mode rejection by a factor of 4, and a remaining uncertainty of $10\,\mathrm{nm/s^2}$ to this effect.

6.3.2 RF Reference Oscillator Offset

All frequencies in the experiment, including the Raman frequency offset, are referenced to a 10 MHz quartz oscillator as detailed in chapter 3.4. The accuracy of this frequency is crucial, since the gravity value is directly referenced to it through the chirp-rate in equation 2.20. Because the frequency synthesizer derives both its output frequency and its frequency increment interval from the reference, the chirp-rate actually depends on it quadratically, or $\alpha \propto f_{\mathrm{ref}}^2$. More precisely, small offsets of the reference oscillator shift the chirp-rate and cause a systematic shift in the gravity value due to $\boldsymbol{k}_{\mathrm{eff}} \cdot \boldsymbol{g} = \alpha$, yielding

$$\frac{\Delta g}{g} = -\frac{\Delta \alpha}{\alpha} = -2\frac{\Delta f_{\mathrm{ref}}}{f_{\mathrm{ref}}} \tag{6.19}$$

where the factor two is caused by the two-fold effect of the reference oscillator on both the chirp-rate step-size and -frequency. Figure 6.10 shows measured gravity changes versus frequency offsets and confirms the expected behavior.

This result also agrees with [142] and could in the future be used to implement a post-correction of the measured gravity value to account for slow oscillator drifts. Note, however, that for relative frequency shifts of 10^{-7} or larger, several secondary effects such as changes of the selected velocity class or shifts of the Raman resonance frequency become relevant which are not contained in equation 6.19 and are in their combination hard to predict. In order to keep the reference oscillator as stable as possible during gravity measurements, we stabilized its frequency to an external reference with a bandwidth of around 0.5 Hz. This was the case during both external measurement campaigns conducted with GAIN where 10 MHz reference signals from Hydrogen-Masers were used. Due to their excellent accuracy and stabilities of better than 10^{-14} on time scale of those campaigns, this effectively eliminates this effect in the gravity measurement. During the previous measurement at Humboldt Universität zu Berlin, however, no stable reference oscillator was available and f_{RF} was manually adjusted by mechanical tuning of the oscillator with a resolution of 20 mHz. This leads to a sizable uncertainty of $40\,\mathrm{nm/s^2}$ during the both campaigns conducted in Berlin.

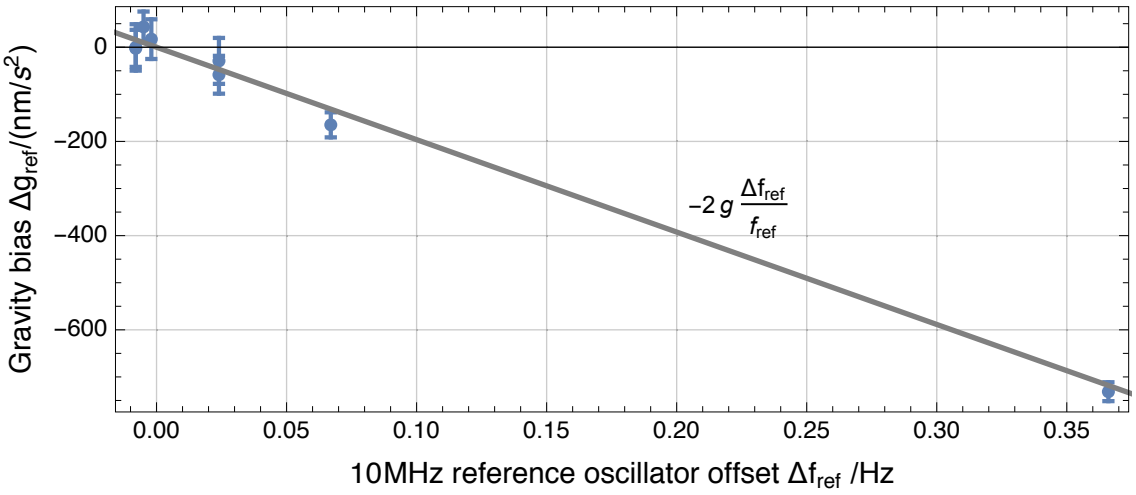

Figure 6.10: Measured gravity bias due to frequency offsets Δf_{ref} of the 10 MHz reference oscillator. The data points are in good agreement with the expected behavior given by equation 6.19.

6.4 Atomic Frequency shifts

The ^{87}Rb hyperfine structure is subject to well-known systematic shifts in the presence of light fields and magnetic fields which are inevitable and indispensable during the interferometry sequence. This section contains the size and influence of these shifts on the gravity measurement, which are dominated by one-photon light shifts and quadratic Zeeman shifts as shown below. Light shifts due to off-resonant Raman transitions and frequency offsets and DC-Stark shifts are smaller but have been considered nevertheless.

6.4.1 One-Photon Light Shift

The coupling of hyperfine levels during the Raman pulses causes shifts of both hyperfine ground states due to the AC-Stark effect, which can be divided into average and differential components as detailed in chapter 2.2.1 and defined in equations 2.13 and 2.12, respectively. Under the assumption that both interferometer paths see the same light intensity, which is very reasonable given their small splitting, the average level shift cancels in the interferometer phase due to the symmetry of the sequence. The differential shift $\delta_{\mathrm{AC}} = \Omega_e^{\mathrm{AC}} - \Omega_g^{\mathrm{AC}}$, on the other hand, leads to an additional phase for a Mach-Zehnder interferometry sequence [23] which is given by:

$$\Delta\Phi_{\mathrm{AC}} = \frac{\delta_{\mathrm{AC}}^1}{\Omega_{\mathrm{eff}}} - \frac{\delta_{\mathrm{AC}}^3}{\Omega_{\mathrm{eff}}} \tag{6.20}$$

where the upper index denotes the 1st and 3rd Raman pulse and Ω_{eff} is the effective two-photon Rabi frequency. This shows that the effect cancels out if the light shift is equal for the first and third pulse. This suppression is limited, however, by the fact that the cloud expands during the sequence due to its finite temperature. The atoms thus move within the transverse profile of the Raman beams and generally experience unequal light shifts during the first and last Raman pulse. The remaining effect can be mitigated by

controlling the intensity ratio of the Raman beams because the individual light shifts of the upper and lower hyperfine ground state are dominated by the separate resonant Raman frequency components as expressed by equation 2.24. By choosing the correct ratio the differential shift δ_{AC} can thus in principle be eliminated.

The intensity ratios predicted by equation 2.25 were verified with the GAIN setup by Matthias Hauth [80] using an additional Raman pulse during the interferometer sequence. This non-resonant pulse does not drive two-photon transitions and thus leaves the three pulse interferometer intact, but inflicts the same light-shift as a resonant Raman pulse due to its very similar one-photon detuning Δ. The resulting level shifts were observed for different Δ and Raman intensity ratios I_2/I_1 and were found to confirm the predicted behavior. At the $\Delta = -700\,\mathrm{MHz}$ setting selected during all GAIN gravity measurement campaigns the required intensity ratio is $\frac{I_2}{I_1} = 1.72$. In order to operate the atom interferometer at this ratio as precisely as possible, an active control system described in chapter 3.3.1 was implemented by Matthias Hauth. It uses a slow feedback system to remove slow drifts of the Raman power in front of the last fiber coupler. The standard deviation of residual power fluctuations is on the 1 mW level which induces small phase shift of several 10 mrad for one pulse [80] which is then further suppressed by the symmetry of the sequence. Since $\Delta\Phi_{\mathrm{AC}}$ does not depend on the photon recoil direction, residual interferometer phase shifts will additionally be suppressed by the k-reversal technique detailed in chapter 6.7.

The remaining systematic bias on the measured gravity value is therefore very small and hard to quantify. A small error margin of $5\,\mathrm{nm/s^2}$ has been applied in order to account for this effect.

6.4.2 Two-Photon Light Shift

In addition to the one-photon light shift discussed in chapter 6.4.1, off-resonant Raman transitions cause an additional light shift. As detailed in chapter 3.1.4, the direction of the momentum recoil in the atom interferometer is selected by adhering to the resonance condition in equation 2.6 for driving Doppler-sensitive two-photon transitions. For Raman lasers on resonance with $|g, \boldsymbol{p}\rangle \rightarrow |e, \boldsymbol{p} + \hbar\boldsymbol{k}_{\mathrm{eff}}\rangle$ this leads to a detuning $-2\omega_D = -2k_{\mathrm{eff}}v_a$ of the opposite momentum state for a given vertical atomic velocity v_a. This leads to

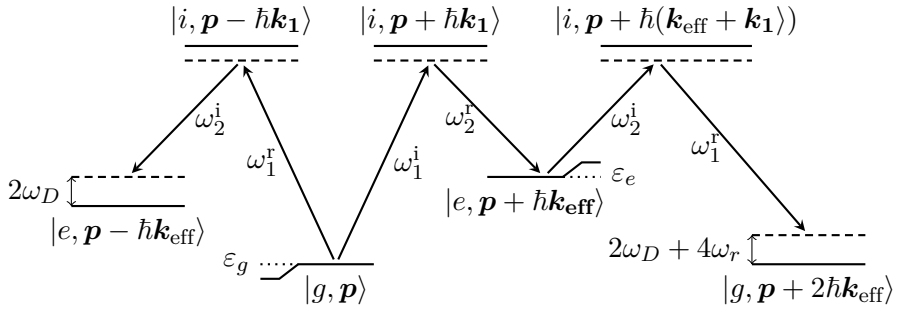

Figure 6.11: Coupling and detuning of momentum states by off-resonant Raman transitions as discussed in the text. $\omega^{\mathrm{i/r}}$ denote the incident/reflected Raman beams. ε_e and ε_g show the level shifts of the two populated states involved in the interferometry sequence.

residual couplings with these detuned states $|g, \boldsymbol{p}\rangle \leftrightarrow |e, \boldsymbol{p} - \hbar\boldsymbol{k}_{\mathrm{eff}}\rangle$ and $|e, \boldsymbol{p} + \hbar\boldsymbol{k}_{\mathrm{eff}}\rangle \leftrightarrow$

$|g, \boldsymbol{p} + 2\hbar\boldsymbol{k}_{\text{eff}}\rangle$ as depicted in figure 6.11 which in turn results in an additional differential level shift [143] of:

$$\delta\omega_{\text{TPLS}} = \frac{1}{\hbar}\left(\varepsilon_e - \varepsilon_g\right) = \frac{\Omega_{\text{eff}}^2}{4}\left(\frac{1}{\pm 2\omega_D} + \frac{1}{\pm 2\omega_D + 4\omega_r}\right) =: \pm\frac{\Omega_{\text{eff}}^2}{4\delta_D} \tag{6.21}$$

where Ω_{eff} is the effective Rabi frequency of the Raman transition, $\omega_r = \hbar k_{\text{eff}}^2/2m$ is the recoil frequency and δ_D abbreviates the effective Doppler shift. Note that $\delta\omega_{\text{TPLS}}$ changes sign when flipping the momentum vector which means that, in contrast to the one-photon light shift, the k-reversal technique does not reject this effect. The resulting interferometer phase shift can be calculated using the sensitivity function in equation 2.38 and further simplified by assuming fix pulse areas of $\pi/2$ and π for the Raman pulses which leads to an interferometer phase shift of [143]

$$\Phi_{\text{TPLS}} = \frac{1}{4}\left(\frac{\Omega_{\text{eff}}^{(1)}}{\delta_D^{(1)}} - \frac{\Omega_{\text{eff}}^{(3)}}{\delta_D^{(3)}}\right) \tag{6.22}$$

where $\Omega_{\text{eff}}^{(i)}$,$\delta_D^{(1)}$ denote parameters for the i-th Raman pulse. Since the interferometer sequence in the GAIN atomic fountain is arranged almost symmetrically on the parabolic trajectory of the atoms, the Doppler shift during both the 1st and 3rd pulse is relatively large. This strongly suppresses Φ_{TPLS} compared to a configuration where the atoms are simply dropped and the velocity during the first pulse is thus small. For the standard GAIN parameters with $T = 0.26\,\text{s}$ this leads to a substantial Doppler detuning of 5.8 MHz which, in combination with the effective Rabi frequency of 15 kHz, leads to a very small phase shift of 1.3 mrad corresponding to $1.3\,\text{nm/s}^2$. This is about one order of magnitude smaller than the targeted accuracy and currently not an issue. For less symmetric configurations of GAIN, however, where the atomic velocity during the 1st pulse is small this effect can be much larger and has to be accounted for. Further phase shifts due to couplings from Doppler-insensitive Raman transitions due to polarization errors might also arise [143] and should be characterized in the future by looking at the Raman spectrum. In order to account for these potential effects, we assume a total uncertainty of $5\,\text{nm/s}^2$ caused by two-photon light shifts.

6.4.3 Light shifts due to Raman Frequency Offsets

Interferometer phase shifts can occur if the Raman resonance condition in equation 2.6 is not met precisely during the atom interferometer sequence. The resulting asymmetry leads to a sensitivity to non-inertial effects as first reported in [11] and described theoretically in [144]. The reported phase shifts due to offsets from the correct Raman frequency for similar experimental parameters have a magnitude of roughly $14\,\text{nm/s}^2/\text{kHz}$.

The importance of this effect for GAIN parameters will briefly be discussed here. After the GAIN velocity selection, which is performed with a Gaussian pulse envelope, the atomic velocity distribution of the remaining atoms is to a very good approximation represented by a narrow Gaussian which corresponds to a Doppler width of 10 kHz as detailed in chapter 4.2. Scans of the Raman resonance condition yields the required settings with an uncertainty of approximately 500 Hz which results in a gravity value uncertainty of $7\,\text{nm/s}^2$.

6.4.4 Quadratic Zeeman Shift

Level shifts caused by magnetic fields are an important error source and have been carefully considered already during the design of the GAIN setup [93, 11]. They are, as a first step, reduced by only allowing atoms in the magnetically insensitive $m_F = 0$ sub-state to participate in the atom interferometer by virtue of the selection sequence described in chapter 4.2. The dominant level shift is then caused by the second order Zeeman shift modeled by the Breit-Rabi formula [100]. This results in an equal and opposite shift of the upper and lower hyperfine ground state leading to a "clock transition" frequency shift of

$$K := \frac{\Delta\omega_{\mathrm{clk}}}{B^2} = \frac{(g_j - g_i)^2 \mu_B^2}{2\hbar\Delta E_{\mathrm{clk}}} = 2\pi \cdot 57.5 \, \frac{\mathrm{kHz}}{\mathrm{mT}^2} \tag{6.23}$$

where ΔE_{clk} is the energy splitting between both states, μ_B is the Bohr magneton and g_j and g_i are the fine-structure Landé and nuclear g-factors.

Since the atoms in both arms of the Raman interferometer are in opposite internal states this causes a differential level shift which can be calculated by evaluating the path integral along the unperturbed trajectories in both interferometer arms. In order to find a simple expression that includes the effect of magnetic field gradients across the small splitting between both interferometer paths we expand the squared magnetic field to second order around the classical, mean parabolic trajectory $\bar{z}(t)$, yielding:

$$B^2(\bar{z} + \Delta z) \approxeq B^2(\bar{z}) + 2\gamma(\bar{z})B(\bar{z})\Delta z + \left(\gamma^2(\bar{z}) + \kappa(\bar{z})B^2(\bar{z})\right)\Delta z^2 + ... \tag{6.24}$$

where $\gamma := \partial_z B$ and $\kappa := \partial_z^2 B$ are the vertical gradient and curvature of the magnetic field, respectively, and $\Delta z(t) = \pm v_{\mathrm{rec}} \left(T - |t - t_{\mathrm{Ra2}}|\right)/2$ parametrizes the distance of both interferometer paths from the mean parabolic trajectory $\bar{z}(t)$. By evaluating the phase shift along both paths and using the sensitivity function $g_s(t)$ introduced in chapter 2.4 the resulting phase shift can be written as an integral along the classical, mean trajectory:

$$\Delta\Phi_{\mathrm{B}^2} = K \int g_s(t) \left(B^2(t) + \left(\gamma^2(t) + B(t)\kappa(t)\right)\Delta z^2(t)\right) dt \tag{6.25}$$

$$=: \Delta\Phi_{\mathrm{B}^2}^{\mathrm{mean}} + \Delta\Phi_{\mathrm{B}^2}^{\mathrm{split}} \tag{6.26}$$

with, e.g., $B(t) := B(\bar{z}(t))$. The first term shows the dominating effect of magnetic field fluctuations along the mean trajectory and the second term a higher order effect due to the small interferometer path splitting. Note that the first order term in γ is equal in both interferometer arms due to the antisymmetry of the (differential) level shift, and therefore cancels out in the measured phase difference.

We will first estimate a worst-case value for the leading order $\Delta\Phi_{\mathrm{B}^2}^{\mathrm{mean}}$. External background magnetic fields are strongly reduces in the interferometer region due to the 3-layer Mu-Metal shield described in chapter 3.1. A constant bias field of approximately $B_0 \approxeq 5\,\mu\mathrm{T}$ is applied to provide a well-defined quantization axis and avoid spin-flips during the interferometer sequence. Measurements performed in [93] show that spatial field fluctuations due to external background fields have a magnitude of approximately $\Delta B \approxeq 100\,\mathrm{nT}$ which was confirmed by Zeeman spectroscopy in the fountain as shown in figure 6.12. In order to give a worst-case estimate of the differential level shift, we assume that the first half of the atom interferometer is subjected to a constant field $B_0 + \Delta B$ and the second half subjected only to B_0.

$$\Delta\Phi_{\mathrm{B}^2}^{\mathrm{mean}} < TK\left((B_0 + \Delta B)^2 - B_0^2\right) \approxeq 2TKB_0\Delta B \tag{6.27}$$

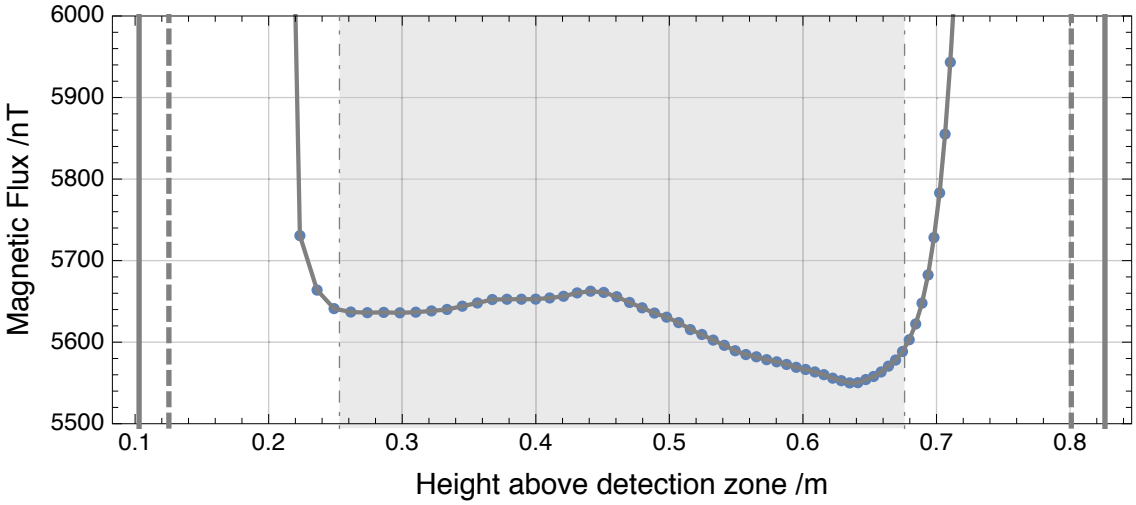

Figure 6.12: Magnetic field measurement in the interferometer zone, conducted by scanning the linear Zeeman shift of the $m = \pm 1$ sub-states versus cloud position using a single, Doppler-insensitive Raman pulse. Gray solid and dashed lines show the border of the inner and outer layers of the magnetic shield. The shaded area indicates the region in which the interferometer sequence takes place. Measurement and data courtesy of Qing-Qing Hu.

For the usual interferometer time $T = 0.26\,\mathrm{s}$ this results in a significant shift of 75 mrad equivalent to a gravity bias of $\Delta g = 70\,\mathrm{nm/s^2}$. Note, however, that this scenario is impossible for the symmetric fountain configuration employed in GAIN where the second Raman pulse happens close to the apex of the trajectory. Instead, this effect should largely cancel out due to the almost symmetric trajectory and the real shift will be much smaller. The sign of the phase-shift furthermore does not depend on the direction of the momentum recoil so that the effect is rejected by the k_{eff}-reversal technique detailed in chapter 6.7. This is also consistent with the result of gravimeter measurements using different T but symmetric trajectories, which faithfully reproduce the expected linear vertical gravity gradient. We therefore attribute only a small residual uncertainty of $5\,\mathrm{nm/s^2}$ to quadratic Zeeman shifts $\Delta\Phi_{\mathrm{B^2}}^{\mathrm{mean}}$.

In order to evaluate the additional phase due to the interferometer path splitting, which has a maximum value of 3 mm for the usual GAIN parameters, we estimate the maximum size of the second term $\Delta\Phi_{\mathrm{B^2}}^{\mathrm{split}}$ in equation 6.25. As a worst-case scenario we assume again that gradient and curvature only influence the first half of the interferometer sequence and therefore neglect the common-mode suppression due to the symmetric fountain trajectory. By reusing the values for $T, B_0, \Delta z$ from above and assuming constant values $\gamma = 100\,\mathrm{nT}/0.01\,\mathrm{m}$, $\kappa = 100\,\mathrm{nT}/(0.01\,\mathrm{m})^2$ we find:

$$\Delta\Phi_{\mathrm{B^2}}^{\mathrm{split}} < K(\gamma^2 + B_0\kappa)\frac{v_{\mathrm{rec}}^2 T^3}{12} \approx 0.3\,\mathrm{mrad} \tag{6.28}$$

which corresponds to a very small gravity bias of $\Delta g \approxeq 0.3\,\mathrm{nm/s^2}$. Since the real gradient and curvature will on average be much smaller and additionally rejected by the symmetry of the trajectory, this effect is negligible and currently not a problem. This assessment agrees with a similar path integral calculation carried out in [83].

Note that the overall magnitude of the main quadratic Zeeman shift $\Delta\Phi_{\mathrm{B^2}}^{\mathrm{mean}}$ is among

the largest remaining unknowns in GAIN and only not a problem because of the two-fold cancellation described above. To be even safer in the future, both effects should be further reduced from the onset simply by lowering the background magnetic field by a factor of 5-10 which would still be well above residual field fluctuations and thus provide a clean enough quantization axis. Finally, on-site magnetic flux measurements inside the interferometer zone as shown in figure 6.12 could be conducted automatically and used to post-correct the gravity value. Advanced techniques [145, 146] would enable an even more precise mapping of the field or its gradients if necessary.

6.4.5 DC Stark Effect

Metal surfaces show stray potential differences over centimeter-sized areas due to different exposed crystalline facets and surface contaminations [147]. These potentials typically have a size of 1–10 mV over length scales of centimeters and have to be considered in, e.g., precision force measurements between two conducting surfaces [148] or inhomogeneous broadening of Rydberg energy levels close to surfaces [149]. Because of the atom‘s vicinity to the metal vacuum chamber wall, this potentially leads to a phase shift in atom interferometers through the DC-Stark effect as considered in [11] and will be discussed here briefly for GAIN.

The magnitude of the associated level shift is given by

$$\Delta\omega = \frac{\alpha_0}{2\hbar} E_z^2 \qquad \alpha_0 = -h \cdot 8{\times}10^{-6}\,\frac{\mathrm{Hz}}{(\mathrm{Vm})^2} \tag{6.29}$$

where α_0 is the ground-state polarizability of Rubidium[100] and E_z is the magnitude of the electrostatic field. Since α_0 is identical for both hyperfine ground states this effect is common mode in the interferometer and cancels out to first order. The vertical splitting of both interferometer arms, however, leads to a remaining effect in case of electric field gradients. In order to estimate its size in a worst-case scenario we calculate the force exerted by the gradient on the induced electric dipoles

$$\Delta g = \frac{\alpha_0}{m_{\mathrm{Rb}}} E_z \partial_z E_z \approx \frac{\alpha_0}{m_{\mathrm{Rb}}} \frac{E_z^2}{l} \tag{6.30}$$

where l is the length scale of the electric gradient. For a gravity effect of $\Delta g = 10^{-9}$ g and $l \approx 10$ cm similar to the size of the interaction region, an electric field of 1.65 V/cm would be required. This is about two orders of magnitude larger than observed values [147] on other metal surfaces under similar conditions. Given the small, cm length scale of reported surface potentials and the large dimensions of the interferometer zone, an averaging effect furthermore applies for larger pulse spacing T. For instance, in GAIN with $T = 0.26$ s and a symmetric trajectory the free fall distance between first/last and center Raman interferometer pulse is about 30 cm.

Surface charges are therefore not currently a problem for GAIN. In order ensure this fact for measurements below the 10^{-10} g level, reductions of patch potentials[9] or a measurement of surface potentials in the interferometer zone would be required.

[9] Graphite spray has been reported to reduce patch charges while preserving UHV compatibility

6.4.6 Cold Collision Shift

Collision in clouds of cold or ultra-cold atomic gases cause frequency shifts which depend on the effective density. During the 1990s, the differential shift of the hyperfine clock transition was a dominating systematic effect in Cesium atomic fountain clocks and one of the main reasons of interest in the development of Rubidium fountains. For thermal clouds such as the ones used in GAIN, this shift has been carefully characterized during the work on Cesium and Rubidium atomic fountains in [150, 107, 105]. The differential frequency shift of ^{87}Rb atoms in the magnetically insensitive $m = 0$ sub-states was measured in [107] to

$$\Delta\omega_{\text{coll}} = \kappa\rho \qquad \text{with} \qquad \kappa = 2\pi \cdot \frac{-0.38\,\text{mHz}}{10^9\,\text{cm}^{-3}} \tag{6.31}$$

where ρ denotes the atom density in the cloud. In order to estimate the resulting interferometer phase shift we again follow the sensitivity function approach introduced in chapter 2.4. For a time-dependent atomic density $\rho(t)$, which reflects well the situation in an atomic fountain with an expanding thermal cloud, one gets

$$\Delta\Phi_{\text{coll}} = \kappa \int_{-T}^{T} g(t)\rho(t)dt = \kappa T\,(\bar{\rho}_2 - \bar{\rho}_1) \tag{6.32}$$

Here, $\bar{\rho}_1$ and $\bar{\rho}_2$ denote the mean densities during the first and second half of the interferometer sequence, respectively. If the mean density was constant during the sequence, no phase shift would occur. This is, however, not the case for GAIN, due to the significant horizontal expansion at a temperature of around 2 µK. After velocity and state selection, the cloud that participates in the interferometer sequence consist of up to $N = 2{\times}10^7$ atoms as detailed in chapter 4.2. One can estimate the mean density evolution by assuming a three dimensional Gaussian cloud shape originating in a point source, with widths $\sigma(t) = \sigma_v \cdot (t - t_{\text{Launch}})$, yielding

$$\rho(t) = \frac{N}{(2\pi)^{3/2}(\sigma_v^{xy})^2\sigma_v^z\,(t - t_{\text{Launch}})^3} \tag{6.33}$$

For the above atom number, $T = 0.26\,\text{s}$, horizontal spread velocity of $\sigma_v^{xy} \approxeq 14\,\text{mm/s}$ and vertical spread velocity of $\sigma_v^z \approxeq 5.2\,\text{mm/s}$, this leads to mean densities during the interferometer sequence of $\bar{\rho}_1 \approxeq 1.1{\times}10^8\,\text{cm}^{-3}$ and $\bar{\rho}_2 \approxeq 1{\times}10^7\,\text{cm}^{-3}$.

Combined with equation 6.32 this results in a total interferometer phase shift of around $\Delta\Phi_{\text{coll}} = 60\,\mu\text{rad}$. This is equivalent to a gravity bias of only $6{\times}10^{-12}$ g which can be safely neglected in the gravimeter at the current level of accuracy. Note that the associated shifts would increase by around a factor of 50 without pre-selection. They are also intrinsically 30 times larger when using an atomic fountain with Cesium instead of ^{87}Rb, for which they are estimated in [27].

6.5 Synchronous Noise

6.5.1 Vibration Isolator Excitations

Accelerations of the Raman mirror during the atom interferometer sequence directly shift the measured phase as described in detail in chapter 3.2. If they are uncorrelated to the interferometer sequence, as usually the case for environmental vibration, these shifts

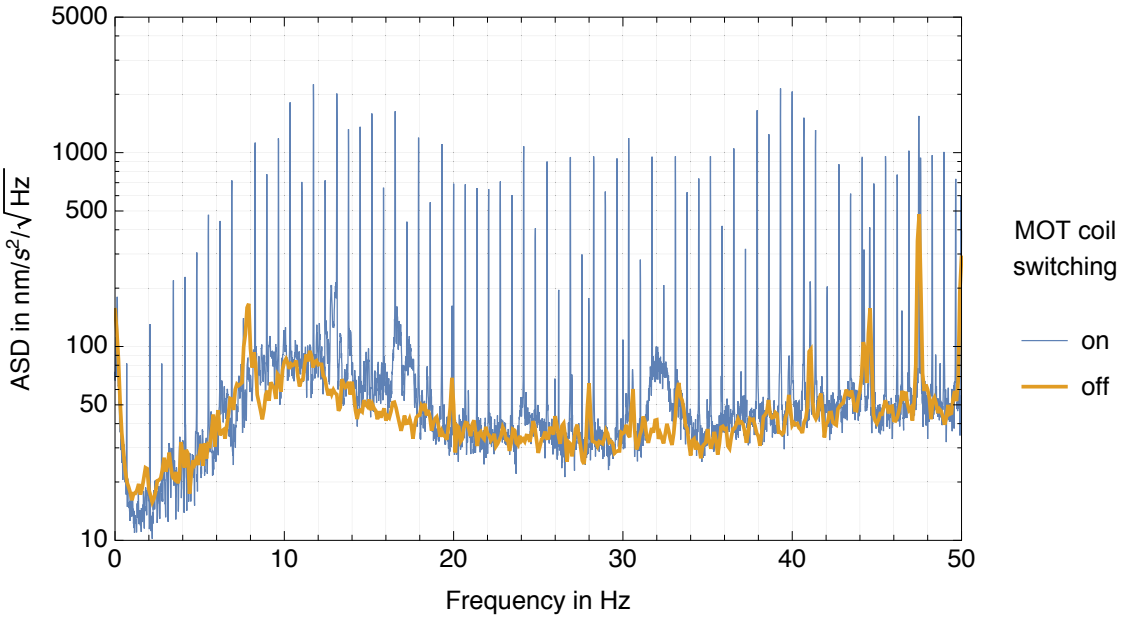

Figure 6.13: Platform accelerometer spectrum during running(blue) and stopped(yellow) GAIN gravimeter operation in Wettzell before integrating the MOT magnetic shielding. Spikes in the blue spectrum show synchronous excitations of the vibration isolator through magnetic coupling (see text). The frequency spacing between spikes is identical to the GAIN sequence repetition rate of 0.67 Hz.

will increase the interferometer phase noise and reduce the sensitivity to g, but not cause systematic shifts. This is different for excitations that originate from the instrumental sequence itself and are therefore synchronized with the measurement cycle. This effect is well known for falling corner-cube absolute gravimeters where floor excitations caused by the falling test-mass hitting the bottom of the chamber can induce synchronous vibrations of the floor. When operated at sufficient repetition rates on oscillatory foundations this can cause a significant gravity bias.

Although the atomic cloud's mass is much too small to cause such an effect in an atom interferometer, a similar issue can arise from the magnetic fields of the MOT field coils which are switched on and off during the MOT loading and launch-sequence. This switching causes problematic, synchronous vibration isolation excitations through two different coupling paths. The first path is a direct magnetic attraction of the mild steel casing of the platform accelerometer and other ferro-magnetic components on the isolator platform due to the magnetic field gradient caused by the MOT coils. Additional coupling is introduced by the intrinsic sensitivity of the feedback sensor in the accelerometer to the field itself, which was measured to approximately $5\times10^{-8}\,\mathrm{m/s^2/mT}$. Which of those routes contributed more to the coupling depends on the platform properties along with field amplitude- and gradient and is ultimately unclear for our scenario. The significance of the total cross-coupling, however, was evident from artifacts in the accelerometer output spectrum when the experimental sequence was active as shown in figure 6.13. In order to investigate the effect on previous gravity measurements, an additional break between instrumental runs was introduced into the measurement sequence. This changes the phase

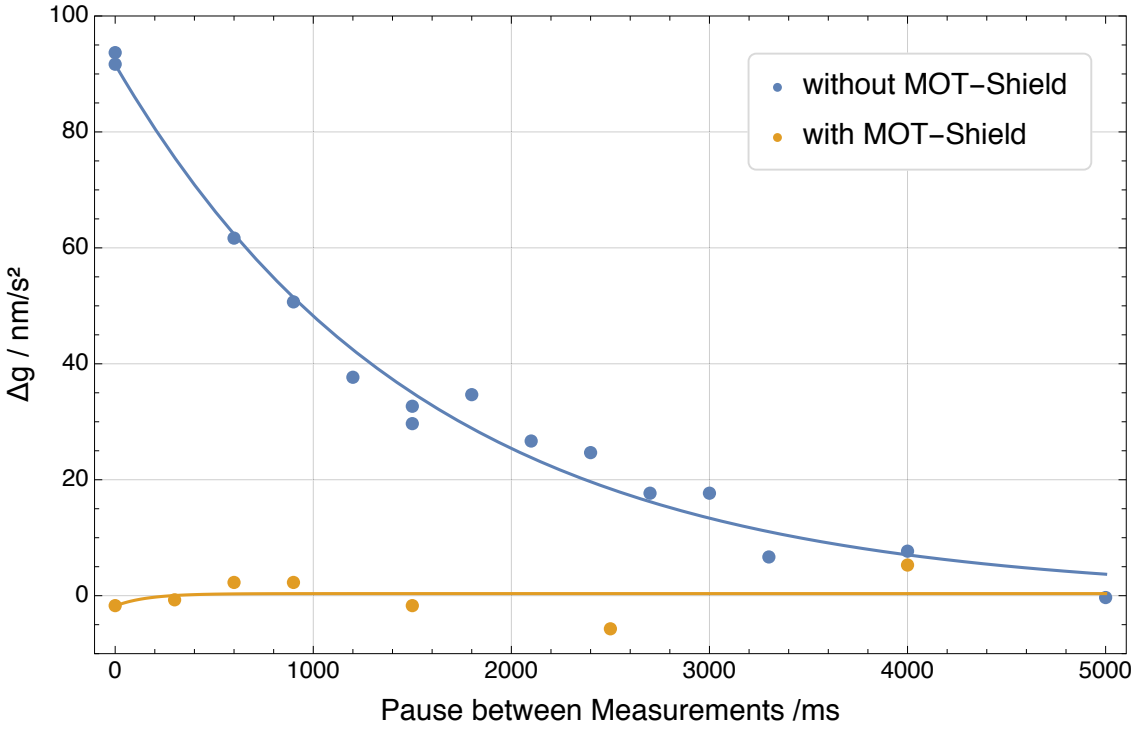

Figure 6.14: Measured gravity shift versus the length of breaks between interferometer cycles, before and after installation of a magnetic shield around the MOT region.

between magnetically induced platform excitations and the interferometer pulse sequence. The measured gravity value versus length of the break is shown in figure 6.14 and discloses a substantial effect. Fitting an over-damped oscillator model to the plotted dataset yields a bias of $(91\pm4)\,\mathrm{nm/s^2}$ for the standard gravity measurement. It is unclear, however, how constant and thus applicable this bias is to other measurement campaigns, as varying placement, environmental conditions or parameters of the mechanical isolator platform could change the response magnitude. We therefore assign a large uncertainty of $50\,\mathrm{nm/s^2}$ to this effect for all campaigns in question. In order to remove this effect conclusively a Mu metal magnetic shield around the MOT region of the physics package was therefore implemented during this work. As shown in chapter 3.1.2 it reduces the magnetic field coupling between MOT and the environment by about a factor of 50–100, which was sufficient to all but eliminated visibility of the cycling MOT field in the accelerometer spectrum. The second dataset in figure 6.14 shows again gravity data versus pauses of varying length between instrumental runs, demonstrating that there is no remaining gravity bias due to synchronous vibrations after installation of the MOT shield.

6.5.2 50Hz Line Noise

Periodic disturbances of various components of the experimental setup due to 50 Hz line noise are very common and could potentially introduce interferometer phase shifts, particularly if the experiment is line triggered. If it is not line triggered, this would simply be another measurement noise contribution. In order to investigate this effect a line-phase detector was implemented after the Wettzell campaign which measures the time between

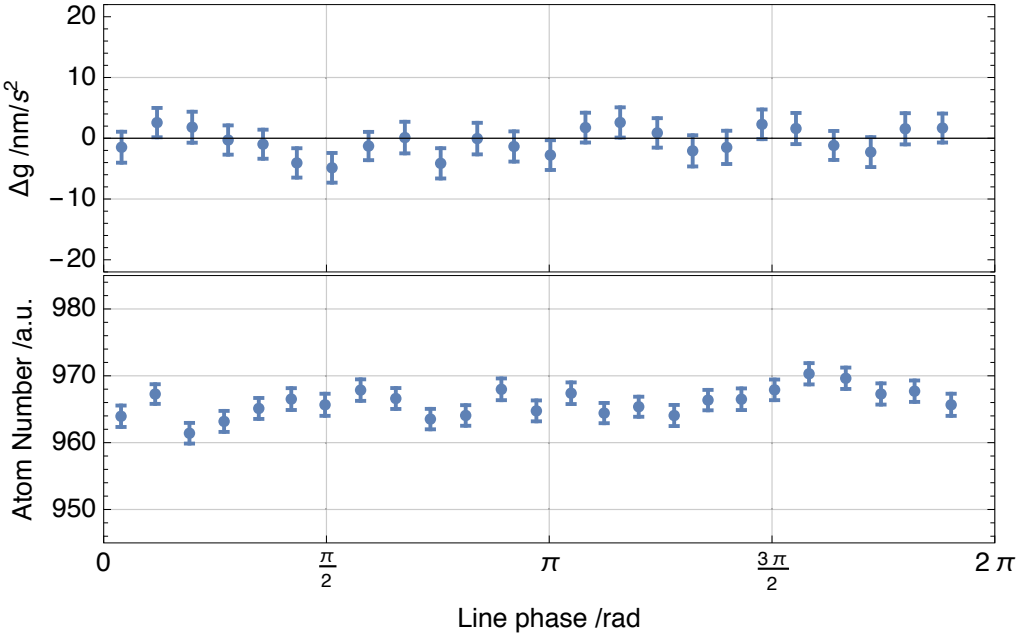

Figure 6.15: Residual gravity value and the number of detected atoms versus 50Hz line phase relative to the interferometer sequence. The shown dataset was obtained after the implementation of the MOT-shield during the campaign in Onsala, Sweden. Each data point represents an average value over 1000 instrument cycles.

the 1st Raman pulse and a positive zero-crossing of the line voltage. Figure 6.15 shows residual gravity values and detected atom number versus the measured 50 Hz line phase. Both quantities show a small dependence on the line phase which is only visible with substantial averaging. The residual gravity changes are on the order of $\pm 5\,\mathrm{nm/s^2}$ and atom number fluctuations have a magnitude of around $\pm 0.5\,\%$. The measurement also confirms that no accidental line-triggering occurs during gravity measurements as all phase values occur with equal probability. The small observed gravity changes therefore average out during gravimeter measurements and therefore do not lead to significant systematic shifts.

Note that during the first three comparison campaigns before the installation of the MOT shield, stronger atom number correlations to the line-phase of up to $\pm 5\,\%$ were observed[93] due to external magnetic disturbances during the moving molasses launch. By virtue of the normalized detection scheme, however, this did not affect the gravity signal and thus did not increase the size of this effect during those campaigns.

6.6 Detection System Bias

Distortions of the interferometer fringe due to systematic effects in the detection system can lead to significant shifts of the measured gravity value. Such a fringe deformation was observed and described in detail for GAIN in [80]. The effect is summarized here for completeness even though it does not lead to a significant correction of the measured gravity value. The GAIN detection system is based on the successive florescence detection as detailed in chapter 4.4. At the time of detection, the clouds at both interferometer

output ports have a position offset of 0.4 mm due to the $\hbar k_{\text{eff}}$ momentum difference after the last interferometer pulse. This is smaller than the vertical size of each cloud and leads to a large overlap which means that the second pulse yields roughly the total atom number[10]. The detection pulses for both output ports are separated by 400 µs which corresponds to a free fall distance of 1.4 mm. Due to the Gaussian-shaped excitation beam and inhomogeneous imaging onto the PMT aperture this results in unequal detection efficiencies for both clouds which slightly distorts the interferometer fringe output. This distortion is maximal on the flanks of the fringe pattern and leaves the maximum/minimum untouched. When operating at mid-fringe for optimal phase sensitivity, [80] predicted resulting gravity shifts as large as $\pm 70\,\text{nm/s}^2$. Fortunately this shift is rejected when averaging over the left and right flank with respect to the fringe maximum, and in this case enters merely as a noise term which can be easily identified in the spectral density of the gravity time series. All gravity measurements during this work were performed using symmetric operation on both sides of the interferometer fringe and should therefore not be affected.

Residual effects might occur, however, during relatively fast tidal gravity changes which temporarily offset the operating point from mid-fringe due to interferometer phase control lag. This could mimic effective time delays as observed in [80] and discussed in detail in chapter 5.5.2. In order to eliminate this issue before the last measurement campaign an additional feed-forward path was implemented. It uses a tidal gravity model[11] to keep the interferometer operating exactly at mid-fringe even during relatively rapid tidal gravity changes. The feedback path therefore only has to compensate slow gravity variations due to environmental effects not contained in the model.

Due to the symmetric mid-fringe operation, detection system biases should therefore not be a problem.

6.7 Momentum Recoil Reversal Technique

As mentioned throughout the discussion some of the above systematics change their sign with the overall interferometer phase when the direction of the momentum recoil is reversed, and others do not. In order to formalize this we categorized all systematic contributions into Φ_- and Φ_+. The overall atom interferometer phase including those effects is then given by [80]

$$\Phi_{\text{total}}^{\uparrow/\downarrow} = \pm \left(k_{\text{eff}} \cdot gT^2 \pm \Phi_{\text{rec}} + \Phi_- \right) + \Phi_+ \tag{6.34}$$

Here, $\Phi_{\text{rec}} = \gamma v_{\text{rec}} T/2$ denotes an additional phase shift due to the slightly different atomic trajectories for both configurations which for GAIN parameters translates to a difference of nearly 5 mrad. Additional path integral terms of the interferometer phase shift were neglected here due to their small size. Most of the systematic effects discussed in the above chapters depend on the recoil direction and contribute to Φ_-. Φ_+ consists most notably of RF group delay, one-photon light shift and quadratic Zeeman shifts which can thus be separated from the gravity induced phase shift by regarding the half-difference

[10] Specifically, the second detection pulse takes place symmetrically between both clouds, around which the first and last pulse are spaced by the cloud distance.

[11] This does not restrict the choice of potential measurement sites as simple synthetic models suffice which can be generated automatically for most locations without prior gravity registrations.

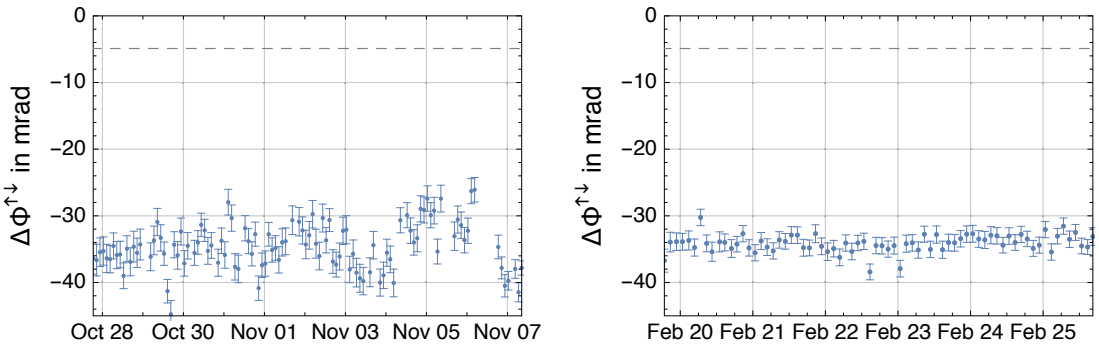

(a) Wettzell, Germany (2013) (b) Onsala, Sweden (2015)

Figure 6.16: Time dependence of Φ_{indep} systematics as indicated by the half-sum $\Delta\Phi^{\uparrow/\downarrow}$ for two gravity measurement campaigns, showing similar magnitude. The stability improvements in the second campaign is presumably caused by improved Raman intensity stabilization and other improvements of the setup. The dashed line shows the expected phase shift Φ_{rec} due to small atomic trajectories differences between up/downwards directed recoil.

and half-sum of the total phase shifts in both configurations:

$$\bar{\Phi} := \frac{\Phi^{\uparrow}_{\text{total}} - \Phi^{\downarrow}_{\text{total}}}{2} = k_{\text{eff}} \cdot gT^2 + \Phi_- \tag{6.35}$$

$$\Delta\Phi^{\uparrow/\downarrow} := \frac{\Phi^{\uparrow}_{\text{total}} + \Phi^{\downarrow}_{\text{total}}}{2} = \Phi_{\text{rec}} + \Phi_+ \tag{6.36}$$

The half-difference $\bar{\Phi}$ is the final phase shift used to obtain the gravity value. The half-sum $\Delta\Phi^{\uparrow/\downarrow}$ embodies the above-mentioned $\boldsymbol{k}_{\text{eff}}$-independent shifts and is therefore useful to study their size and time-dependence.

Figure 6.16 shows the respective dataset for the two last mobile measurement campaigns. The magnitude of Φ_+ is below $-40\,\text{mrad}$ which corresponds to a gravity bias of less than $-40\,\text{nm/s}^2$.

The cancellation of the systematics contained in Φ_+ is limited by the slightly different atomic trajectories and Raman chirp center frequency in both configurations. Residual uncertainties therefore persist for each effect and are specified in the respective sub-chapter or in the summary in table 6.3. Note that, except if the majority Φ_+ effects cancel each other, even a moderate cancellation by a factor of 4 leads to a residual uncertainty of less than $10\,\text{nm/s}^2$ which is significantly smaller than other dominating effects such as Raman wavefront aberrations. In the future this could be improved by shifting the pulse sequence around the apex of the atomic trajectories to match the center frequency of the Raman chirp. The selected velocity class could furthermore be adjusted between both configurations by $\pm\frac{\hbar k_{\text{eff}}}{2m}$ to cancel the effect of Φ_{rec} and yield identical mean atomic trajectories.

6.8 Systematic Error Budget

The above-mentioned systematics effects were identified, analyzed and removed before and in between the four gravimeter comparison campaigns presented in the next chapter.

The final error budget discussed in this chapter and summarized in table 6.3 represents the state during the campaign in Onsala, Sweden in February 2015. Not all comparison campaigns presented in the following chapter therefore reflect the current state of GAIN setup and level of accuracy or stability which is clearly marked in the next chapter.

Note the sign difference between bias values listed here and offsets in the next chapter. By convention, in this work, biases indicate the effect of a certain systematic on the measured g value and thus should be subtracted. Offsets, on the other hand, give the correction and thus have to be added to the raw g value to obtain the corrected result.

Note that table 6.3 without the Raman wave-front systematic indicates a systematic uncertainty of less than $20\,\mathrm{nm/s^2}$. This would surpass the accuracy of current state-of-the-art absolute gravimeters and shows again the potential of atom interferometers for gravimetry.

Systematic effect	**Bias (nm/s^2)**	**Error (nm/s^2)**	**Applied Mitigation Strategy**	$\boldsymbol{k}_{\mathrm{eff}}^{\uparrow/\downarrow}$
Raman Wavefronts	-28	±22	Wavefront Characterization	-
RF Group Delays	0	±10	k_{eff}-Reversal	+
Coriolis Effect	-12	±7	Tip/Tilt Mirror	-
Raman Frequency Offset	0	±7	Gaussian Velocity Selection	-
Self Gravitation	19	±5	FEM Modeling, Post-Correction	-
Rb Background Vapor	5	±5	Refractive Index Modeling	-
Quad. Zeeman Shift	0	±5	k_{eff}-Reversal, Magnetic Shielding	+
Light Shift (1-photon)	0	±5	k_{eff}-Reversal, Intensity Stabilization	+
Light Shift (2-photon)	0	±5	Symmetric Launch Sequence	-
Synchronous Vibrations	0	±5	Magnetic Shielding of MOT	-
Reference Laser Freq.	-13	±2	Spectroscopy in Atomic Fountain	-
Total	**-29**	**±29**		

Table 6.3: Systematic error budget for the mobile campaign in Onsala, Sweden, effects ordered by size. Systematics smaller than $1\,\mathrm{nm/s^2}$ are not listed, namely: vertical alignment, speed-of-light effects, detection system bias, synchronous line noise, RF frequency offsets and Gouy Phase. The last columns indicates the behavior under a flip of the momentum recoil direction (+:constant, -:opposite sign)

Summary

This section gave an exhaustive description of all systematics effects that were considered and rejected during the preparation, measurement and analysis of the mobile gravity comparisons. The final systematic error budget was found to be $29\,\mathrm{nm/s^2}$ which makes this experiment one of the most accurate atomic gravimeters world wide. The excellent long-term stability and accuracy would not have been possible without these considerations which justifies the considerable time effort invested into this analysis. They form an integral part of this work and will be essential for gravimetric and other applications in geodesy and geophysics.

Chapter 7

Conclusion and Outlook

The main objective of this thesis was to improve the performance characteristics of the GAIN setup for mobile applications in geodesy and gravimetry, and to increase the absolute accuracy of the measured gravity value to the 10^{-9} g level. To this end, several instrumental improvements were carried out by the author and described in this thesis.

The Raman retro-reflector was equipped with a Piezo Tip/Tilt mirror system which was then used to compensate the Coriolis effect and to perform automatic auto-collimation of the reflected beam back into the Raman fiber. This enabled, in combination with the implementation of a motorized Raman beam steering system, the automatic alignment of the GAIN measurement axis with gravity. Other major improvements of the setup were the integration of a cleaner, larger Rubidium source and new programming hardware for the Raman DDS frequency synthesizers, which now use fast FPGA processing to enable arbitrary frequency and phase control during the sequence. A magnetic shield around the MOT zone of the physics package was also implemented to remove magnetic excitation of the vibration isolation system which had previously caused major systematic and random perturbations. Finally, a post-correction algorithm for residual vibrations was implemented and applied subsequently to all conducted measurement campaigns. This significantly increased the sensitivity to g and lead to major new insights into the observed GAIN measurement noise.

During and after the implementation of these instrumental improvements, four comparison campaigns between GAIN and different state-of-the-art relative and absolute gravimeters were conducted. This included comparisons to relative spring-based and superconducting gravimeters as well as the state-of-the-art falling corner-cube gravimeter FG5X-220. The last two comparisons took place at remote locations in Wettzell, Germany and Onsala, Sweden to verify the mobility of the GAIN setup. The presented analysis of all four measurement campaigns shows the improvement in long-term stability and accuracy over time as systematic effects were increasingly suppressed or compensated in post-processing. The best performance was reached in the last campaign with an absolute accuracy due to the systematic error budget of $37\,\mathrm{nm/s^2}$, sensitivity of $85\,\mathrm{nm/s^2/\sqrt{Hz}}$ and current world-record long-term stability of $0.4\,\mathrm{nm/s^2}$, or $4{\times}10^{-11}$ g, after one day of integration time. These numbers compare very well with other mobile state-of-the-art atomic gravimeters [65] and make GAIN one of the most advanced devices of this kind to date.

The comparisons between GAIN and the FG5X-220 furthermore unveiled interesting differences in the general characteristics of atomic and falling corner-cube gravimeters. Despite the good agreement in the measured gravity values, the repeatedly larger result

from GAIN in combination with slightly elevated values also measured by other atomic gravimeters [65, 13] indicates that hidden systematic offsets in at least one class of instruments might still exist today. Further investigations are needed here, but this point also illustrates that the comparison of different absolute gravimeter implementations is not only interesting in its own right, but essential to find and remove these hidden systematics. Since, until recently, falling corner-cube gravimeters such as the Microg-LaCoste FG5 completely dominated this field, the advent of atomic gravimeters in geodesy will certainly lead to a strongly increased confidence in the accuracy of future gravity networks.

Another characteristic difference is the resilience against environmental noise. Because of the increased micro-seismic noise level during the campaigns in Onsala and Berlin, measurement noise of the FG5X was strongly increased due to technical limitations of the FG5(X) super-spring [110] which decouples its inertial reference mirror from the environment. GAIN was, due to its higher repetition rate and more efficacious vibration isolation system, not affected by elevated micro-seismic noise and showed much lower measurement noise than the FG5 under those conditions. In contrast to GAIN or other atomic gravimeters, falling corner-cube instruments also require a solid concrete foundation to achieve adequate performance as the lifting and falling of the corner-cube induces vibrations. GAIN does not possess this restriction as no moving parts exist in the physics package. Both advantages apply to atomic gravimeters in general and provide access to a much larger set of potential measurement sites for state-of-the-art absolute gravimetry. The ability of atomic gravimeters to perform continuous gravity registrations over long periods of time in combination with reduced measurement noise furthermore enables applications which were before restricted to relative gravimeters, such as tidal model characterizations or the investigation of ground water induced gravity effects. Falling corner-cube instruments practically never operate continuously over extended periods of time to prevent wear and tear of the complicated mechanical dropping system. Although GAIN can not yet reach the excellent short-term sensitivity of superconducting gravimeters it has already provided unique sets of continuous absolute gravity data over weeks with a noise level similar to relative spring-based gravimeters without the long-term drift. Future improvements of GAIN‘s short- and long-term stability as well as its accuracy and mobility will make it even more attractive for the above applications in geodesy. These improvements should first focus on reducing the excess noise contribution described in this work and a further reduction of Raman wavefront aberrations as well as other remaining systematics. Advanced concepts to improve the sensitivity such as interleaved interferometry [151] and dead-time free measurements with two atomic species or isotopes [152] have been demonstrated and might provide a further quantum leap in sensitivity. In order to exploit this potential for geodesy on a larger scale, commercialized atomic gravimeters [75, 76, 77] are starting to appear on the market [153]. The robust and scalable architecture of atom interferometers further enables applications under harsh environments where spring-based relative gravimeters reach fundamental limitations, which has spurred the development of specialized atomic sensors for airborne, shipborne [152, 154] or borehole gravimeters. As the broader potential of inertial sensor and specifically gravimeters based on atom interferometry is completely open, the future will show plenty of interesting new applications of this versatile concept.

Appendices

Appendix A

MOT Photograph

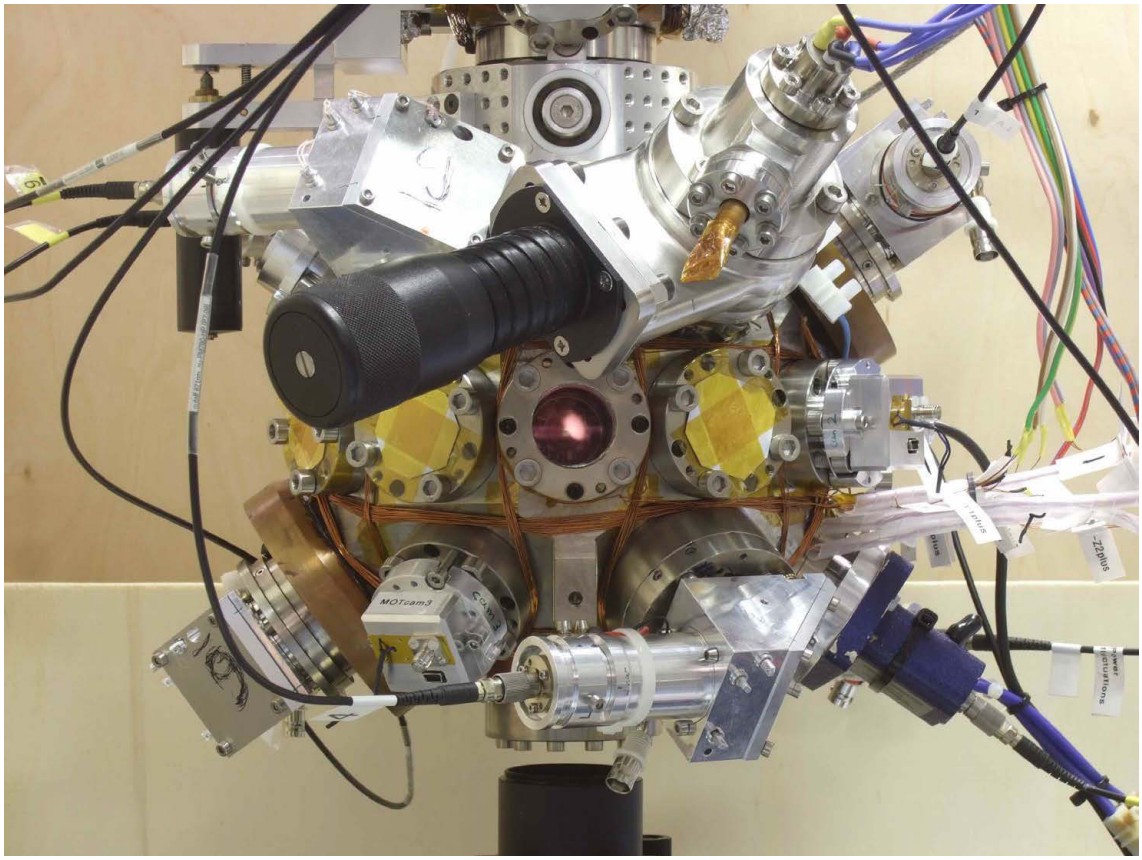

Figure A.1: Photograph of the MOT system just before installation of the MOT shield. The atomic fountain system is fully connected and in operation with optimized launch temperature using the compensation coils wound around the MOT chamber as specified in figure 3.3. Fluorescence light from the ^{87}Rb MOT is visible through the central viewport.

Appendix B

Measurement Campaigns

This chapter lists all parameters required to reproduced the results of the gravity comparison campaigns. This includes, for every campaign, the used tidal parameters, source and admittance factor used for air-pressure correction, the height of GAIN detection zone and GAIN effective measurement height, and the vertical gravity gradient at this height. All tidal model and polar motion correction calculation have been performed with Tsoft [47]. The polar motion correction was also computed with the same software using pole coordinates from IERS at `http://hpiers.obspm.fr/iers/eop/eopc04_14/`.

B.1 Air-Pressure Correction

During each campaign the atmospheric loading effect was calculated from local air pressure records using an admittance factor a_p which leads to a simple gravity correction of $\Delta g_{air}(t) = a_p \left(p(t) - p^{std}\right)$, where p^{std} is the base pressure at a given altitude according to the standard barometric formula:

$$p(h) = 1013.24\,\mathrm{hPa} \exp\left(1 - \frac{0.0065h}{288.15\,\mathrm{m}}\right)^{5.255} \tag{B.1}$$

Since the admittance factor a_p changes slightly for different stations it is given for each of the four measurement campaigns.

If air pressure data from a nearby weather station at different altitude was used for air pressure correction, an offset $\Delta p = p(h_{gravi}) - p(h_{station})$ was added to the respective records to account for the different base pressure level at the campaign measurement site.

B.2 Campaign 1: GAIN and gPhone (Berlin, 2012)

Location

s The measurement was performed at Humboldt Universität zu Berlin in Lise-Meitner Building, Newtonstr. 15, D-12489 Berlin in room 1‘601.

latitude [°N]	longitude [°E]	altitude [m]	GAIN detection height [m]	GAIN effective meas. height [m]
52.43337	13.53062	39.65	0.812±0.003	1.398±0.003

Tidal Model

The earth tide parameters for Berlin were provided by IfE [108]. The listed parameters include the effect of ocean loading, e.g. no additional loading correction was performed.

Frequency min. [cyc/d]	**Frequency max. [cyc/d]**	**Amplitude**	**Phase [°]**	**Tide Symbol**
0.0	0.000001	1.0	0.0	DC
0.0001	0.249951	1.1792	-0.0222	Long
0.721500	0.906315	1.14970	-0.1150	Q1
0.921941	0.974188	1.14870	0.1114	O1
0.989049	0.998028	1.14800	0.1711	P1
0.999853	1.216397	1.13360	0.1122	K1
1.719381	1.906462	1.17420	1.6708	N2
1.923766	1.976926	1.18320	1.3700	M2
1.991787	2.002885	1.18300	0.4141	S2
2.004710	2.182843	1.17780	0.2538	K2
2.753244	3.081254	1.06900	0.0000	M3

Air Pressure

Air pressure data was obtained from the nearby Berlin Schönefeld airport weather station on `werdis.dwd.de` (product: de.dwd.nkdz.req.HV) yielding hourly pressure records on station level. A small offset of 0.76 hPa was added to the data to account for the slightly lower altitude of the campaign measurement site as detailed in B.1.

- Admittance Factor: $a_p = -3.0\,\mathrm{nm/s^2/hPa}$

Gravity Gradient

The vertical gravity gradient in room 1‘601 was measured by BKG in 2010 using relative gravimeters [109]. The local value is given by $(-3010\pm40)\,\mathrm{nm/s^2/m}$.

B.3 Campaign 2: GAIN and FG5X-220 (Berlin, 2013)

Location

The measurement was performed at Humboldt Universität zu Berlin in Lise-Meitner Building, Newtonstr. 15, D-12489 Berlin in room 0‘701. See table 5.2 for absolute gravity data.

latitude [°N]	longitude [°E]	altitude [m]	GAIN detection height [m]	GAIN effective meas. height [m]	comparison height [m]
52.43337	13.53062	35.27	0.813±0.003	1.384±0.003	1.2

Tidal Model

The earth tide parameters for Berlin were provided by IfE [108]. The listed parameters include the effect of ocean loading, e.g. no additional loading correction was performed.

Frequency min. [cyc/d]	**Frequency max. [cyc/d]**	**Amplitude**	**Phase [°]**	**Tide Symbol**
0.0	0.000001	1.0	0.0	DC
0.0001	0.249951	1.1792	-0.0222	Long
0.721500	0.906315	1.14970	-0.1150	Q1
0.921941	0.974188	1.14870	0.1114	O1
0.989049	0.998028	1.14800	0.1711	P1
0.999853	1.216397	1.13360	0.1122	K1
1.719381	1.906462	1.17420	1.6708	N2
1.923766	1.976926	1.18320	1.3700	M2
1.991787	2.002885	1.18300	0.4141	S2
2.004710	2.182843	1.17780	0.2538	K2
2.753244	3.081254	1.06900	0.0000	M3

Air Pressure

Air pressure data was obtained from the nearby Berlin Schönefeld airport weather station on `werdis.dwd.de` (product: de.dwd.nkdz.req.HV) yielding hourly pressure records on station level. A small offset of 1.28 hPa was added to the data to account for the slightly lower altitude of the campaign measurement site as detailed in B.1.

- Admittance Factor: $a_p = -3.0\,\mathrm{nm/s^2/hPa}$

Gravity Gradient

The vertical gravity gradient in room 0‘701 was measured by BKG in 2010 using relative gravimeters [109]. The local value is given by $(-3080\pm50)\,\mathrm{nm/s^2/m}$.

B.4 Campaign 3: GAIN and SG-30 (Wettzell, 2013)

Location

The measurement was performed at the geodetic observatory in Wettzell, Germany. See table 5.2 for absolute gravity data.

latitude [°N]	longitude [°E]	altitude DHHN92 [m]	GAIN detection height [m]	GAIN effective meas. height [m]	comparison height [m]
49.14483	12.87631	606.58	0.815±0.003	1.386±0.003	1.25

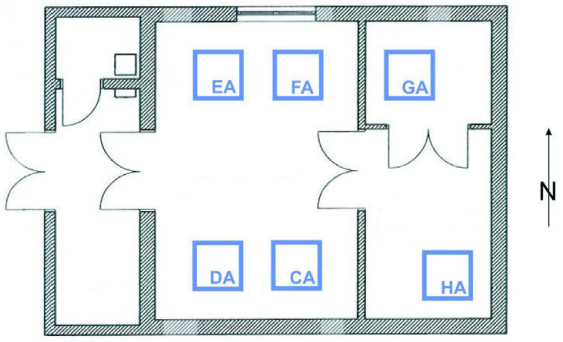

Figure B.1: Floor plan of the new gravimeter house at Wettzell observatory by [111]. The SG-30 superconducting gravimeter was installed on pillar GA and GAIN was installed on pillar FA

.

Tidal Model

The earth tide parameters for Wettzell listed below were provided by H. Wziontek [111]. They include the effect of ocean loading, no additional loading correction was performed.

Frequency min. [cyc/d]	**Frequency max. [cyc/d]**	**Amplitude**	**Phase [°]**	**Tide Symbol**
0.	0.00001	1.	0.	long
0.000011	0.003426	1.16	0.	SA
0.004709	0.010952	1.16	0.	SSA
0.025811	0.031745	1.16	0.	MSM
0.033406	0.044653	1.16413	-0.2564	MM
0.060131	0.06864	1.13394	-2.634	MSF
0.069845	0.080798	1.14618	0.5581	MF
0.096422	0.104932	1.0572	-2.7465	MSTM
0.106136	0.115412	1.15201	0.4617	MTM
0.130192	0.143814	1.07174	1.4338	MSQM
0.145166	0.249952	1.07405	2.762	MQM

continued on next page

Frequency min. [cyc/d]	Frequency max. [cyc/d]	Amplitude	Phase [°]	Tide Symbol
0.721499	0.833113	1.15321	-0.5698	SGQ1
0.851181	0.859691	1.15099	-0.6368	2Q1
0.860895	0.892332	1.14803	-0.5287	SGM1
0.892639	0.892951	1.09091	1.0752	3MK1
0.893096	0.89613	1.14598	-0.1533	Q1
0.897806	0.906316	1.14643	-0.0698	RO1
0.92194	0.93045	1.14852	0.1212	O1
0.931963	0.940488	1.15457	0.3437	TAU1
0.958085	0.963857	1.14417	0.3892	NTAU
0.965532	0.965828	1.14991	0.3143	LK1
0.965842	0.966285	1.08257	0.5669	M1
0.966298	0.966757	1.15184	0.1653	NO1
0.968564	0.974189	1.15037	0.165	CHI1
0.989048	0.995144	1.14713	0.3049	PI1
0.996967	0.998029	1.14896	0.1671	P1
0.999852	1.00015	1.12173	3.001	S1
1.00182	1.00365	1.1356	0.223	K1
1.00533	1.00562	1.24923	0.8594	PSI1
1.00759	1.01369	1.16486	-0.1826	PHI1
1.02855	1.03447	1.15449	0.0787	TET1
1.03629	1.03919	1.15557	0.1071	J1
1.03932	1.03965	1.08156	0.3972	3MO1
1.0398	1.07108	1.15508	0.1947	SO1
1.07258	1.08095	1.15285	0.1639	OO1
1.09916	1.2164	1.15369	0.379	NU1
1.71938	1.8234	1.13564	1.7441	3N2
1.82552	1.85695	1.1492	1.5689	EPS2
1.85878	1.85938	1.06597	0.0086	3MJ2
1.85954	1.86243	1.16147	2.3841	2N2
1.86363	1.89507	1.1615	2.1001	MU2
1.89536	1.89569	1.07294	0.0679	3MK2
1.89583	1.89675	1.17662	1.9754	N2
1.89795	1.90646	1.17787	1.9107	NU2
1.92377	1.92742	1.18174	1.8966	GAM2
1.92939	1.93016	1.22538	-0.4048	ALF2
1.93136	1.93319	1.18426	1.4344	M2
1.93439	1.93532	1.22596	1.0342	BET2
1.93698	1.94275	1.16266	-0.1161	DEL2
1.95823	1.96371	1.18772	0.8189	LAM2
1.96583	1.96857	1.18615	1.0721	L2
1.96873	1.96917	1.06721	-0.1797	3MO2
1.96918	1.97693	1.18773	1.0716	KNO2
1.99179	1.99829	1.18409	0.4838	T2

continued on next page

Frequency min. [cyc/d]	Frequency max. [cyc/d]	Amplitude	Phase [°]	Tide Symbol
1.99971	2.00077	1.18393	0.34	S2
2.00259	2.00303	1.20345	1.0792	R2
2.00471	2.00517	0.98011	-1.0829	3MQ2
2.00531	2.01369	1.18461	0.5371	K2
2.03129	2.04739	1.18205	0.1235	ETA2
2.06758	2.07366	1.16462	-0.6703	2S2
2.07594	2.18284	1.16938	-0.3883	2K2
2.75324	2.86971	1.07009	0.5366	MN3
2.89264	2.90389	1.06944	0.3803	M3
2.92711	2.94033	1.08194	0.109	ML3
2.96599	3.08126	1.05853	0.2767	MK3
3.79196	3.83311	0.52662	-81.2471	N4
3.8644	3.90146	0.31428	61.6901	M4
3.93775	3.9379	1.05822	37.2413	K4
3.93775	3.9379	1.05822	37.2413	K4

Table B.3: Solid earth tidal model parameters in Tsoft format for Wettzell, Germany.

Air Pressure

Air pressure data was obtained from the collocated SG-30 air pressure sensor, yielding a high-resolution time-series with 1 s sample rate.

- Admittance Factor: $a_p = -3.0\,\mathrm{nm/s^2/hPa}$

Gravity Gradient

The vertical gravity gradient on pillar FA was measured by BKG using relative gravimeters. The local value is given by $(-3200 \pm 30)\,\mathrm{nm/s^2/m}$ at a height of 0.25–1.25 m above the pillar [114].

B.5 Campaign 4: GAIN, OSG-054, FG5X-220 (Onsala, 2015)

Location

The measurement was performed in the gravimeter house at Onsala Space Observatory in Onsala, Sweden in February 2015. GAIN was located on pillar AA from February 3-8 and on pillar AC from February 8-26. The superconducting gravimeter OSG-054 was located about 3 m away on a separate pillar. The FG5X-220 was located on pillar AC from February 3-8 and on pillar AA from February 8-12. The absolute gravity comparison between GAIN and the FG5X-220 was performed only for the pillar AC. See table 5.2 for absolute gravity data.

latitude [°N]	longitude [°E]	altitude [m]	GAIN detection height [m]	GAIN effective meas. height [m]	comparison height [m]
57.396490	11.925821	8	0.853±0.003	1.423±0.003	1.2

Tidal Model

The earth tide parameters for Onsala listed below were provided by M. Schilling [70]. No additional loading correction was performed.

Frequency min. [cyc/d]	**Frequency max. [cyc/d]**	**Amplitude**	**Phase [°]**	**Tide Symbol**
0.	0.000001	1.	0.	M0S0
0.000001	0.0024	1.16	0.	LONG
0.002401	0.00345	2.9101	-24.89	SA
0.003451	0.005918	1.11735	-3.54	SSA
0.005919	0.00851	1.58376	-9.71	STA
0.008511	0.01096	1.77749	22.93	SQA
0.010961	0.04466	1.08405	1.17	MM
0.044661	0.0808	1.14242	0.01	MF
0.080801	0.11542	1.14761	-0.42	MTM
0.115421	0.25	1.15726	-6.31	MSQM
0.250001	0.870024	1.15095	-0.48	SIG1
0.870025	0.90632	1.14498	-0.34	Q1
0.906321	0.94049	1.14826	0.12	O1
0.940491	0.97419	1.15235	0.22	M1
0.974191	0.99803	1.15482	0.15	P1
0.998031	1.00015	1.10669	-2.33	S1
1.00015	1.00365	1.14098	0.14	K1
1.00365	1.00563	1.26419	1.04	PSI1
1.00563	1.01369	1.17893	-0.27	PHI1
1.01369	1.04481	1.16117	-0.1	J1
1.04481	1.2164	1.15611	0.01	OO1
1.2164	1.83797	1.13158	-0.15	3N2

continued on next page

Frequency min. [cyc/d]	**Frequency max. [cyc/d]**	**Amplitude**	**Phase [°]**	**Tide Symbol**
1.83797	1.87215	1.14168	1.54	2N2
1.87215	1.90647	1.18469	2.1	N2
1.90647	1.94276	1.19367	1.27	M2
1.94276	1.97693	1.1896	-0.49	L2
1.97693	2.00304	1.18677	0.34	S2
2.00304	2.18285	1.19937	0.26	K2
2.18285	3.33333	1.08563	1.04	M3
3.33333	4.	5.5586	-164.08	M4

Table B.4: Solid earth tidal model parameters in Tsoft format for Onsala, Sweden.

Air Pressure

Air pressure data was obtained from the collocated OSG-054 instrument sensor, yielding a high resolution time series with a 1 s sample rate.

- Admittance Factor: $a_p = -3.5\,\mathrm{nm/s^2/hPa}$

Gravity Gradient

The vertical gravity gradient on pillar AA and AC was measured by IfE and H.G Scherneck using relative gravimeters. The local value is given by $(-3000\pm30)\,\mathrm{nm/s^2/m}$ on pillar AA and $(-3260\pm30)\,\mathrm{nm/s^2/m}$ on pillar AC at a height of 1.3 m above the floor [70, 127].

Bibliography

[1] Terry Quinn. "Fundamental Constants: Measuring Big G". In: *Nature* 408.6815 (Dec. 21, 2000), pp. 919–921. DOI: 10.1038/35050187.

[2] C. Lämmerzahl. "The Search for Quantum Gravity Effects I". In: *Applied Physics B* 84.4 (Sept. 2006), pp. 551–562. DOI: 10.1007/s00340-006-2374-z.

[3] Clifford M. Will. "The Confrontation between General Relativity and Experiment". In: *Living Reviews in Relativity* 17 (2014). DOI: 10.12942/lrr-2014-4.

[4] O. Carnal and J. Mlynek. "Young's Double-Slit Experiment with Atoms: A Simple Atom Interferometer". In: *Physical Review Letters* 66.21 (May 27, 1991), pp. 2689–2692. DOI: 10.1103/PhysRevLett.66.2689.

[5] David W. Keith et al. "An Interferometer for Atoms". In: *Physical Review Letters* 66.21 (May 27, 1991), pp. 2693–2696. DOI: 10.1103/PhysRevLett.66.2693.

[6] F. Riehle et al. "Optical Ramsey Spectroscopy in a Rotating Frame: Sagnac Effect in a Matter-Wave Interferometer". In: *Physical Review Letters* 67.2 (1991), p. 177. DOI: 10.1103/PhysRevLett.67.177.

[7] Mark Kasevich and Steven Chu. "Atomic Interferometry Using Stimulated Raman Transitions". In: *Phys. Rev. Lett.* 67.2 (July 8, 1991), pp. 181–184. DOI: 10.1103/PhysRevLett.67.181.

[8] M. Kasevich and S. Chu. "Measurement of the Gravitational Acceleration of an Atom with a Light-Pulse Atom Interferometer". In: *Applied Physics B Photophysics and Laser Chemistry* 54.5 (May 1992), pp. 321–332. DOI: 10.1007/BF00325375.

[9] Mark A. Kasevich et al. "Atomic Velocity Selection Using Stimulated Raman Transitions". In: *Physical Review Letters* 66.18 (1991), pp. 2297–2300. DOI: 10.1103/PhysRevLett.66.2297.

[10] M. A. Kasevich. "Atom Interferometry in an Atomic Fountain". PhD. Stanford: Stanford University, June 1992. 140 pp.

[11] Achim Peters. "High Precision Gravity Measurements Using Atom Interferometry". PhD. Stanford University, 1998.

[12] Zhong-Kun Hu et al. "Demonstration of an Ultrahigh-Sensitivity Atom-Interferometry Absolute Gravimeter". In: *Physical Review A* 88.4 (Oct. 2013), p. 043610. DOI: 10.1103/PhysRevA.88.043610.

[13] Olivier Francis et al. "The European Comparison of Absolute Gravimeters 2011 (ECAG-2011) in Walferdange, Luxembourg: Results and Recommendations". In: *Metrologia* 50.3 (June 1, 2013), pp. 257–268. DOI: 10.1088/0026-1394/50/3/257.

[14] C Freier et al. “Mobile Quantum Gravity Sensor with Unprecedented Stability”. In: *Journal of Physics: Conference Series* 723 (June 2016), p. 012050. DOI: 10.1088/1742-6596/723/1/012050.

[15] Alexandre Gauguet. “Gyromètre à Atomes Froids: Etude de La Stabilité Limite et Des Effets Systématiques Liés Aux Séparatrices Lasers.” Université Pierre et Marie Curie-Paris VI, 2008. URL: https://hal.archives-ouvertes.fr/tel-00322150/.

[16] J. K. Stockton, K. Takase, and M. A. Kasevich. “Absolute Geodetic Rotation Measurement Using Atom Interferometry”. In: *Physical Review Letters* 107 (Sept. 22, 2011), p. 133001. DOI: 10.1103/PhysRevLett.107.133001.

[17] G Tackmann et al. “Self-Alignment of a Compact Large-Area Atomic Sagnac Interferometer”. In: *New Journal of Physics* 14.1 (Jan. 20, 2012), p. 015002. DOI: 10.1088/1367-2630/14/1/015002.

[18] J. M. McGuirk et al. “Sensitive Absolute-Gravity Gradiometry Using Atom Interferometry”. In: *Physical Review A* 65.3 (Feb. 8, 2002). DOI: 10.1103/PhysRevA.65.033608.

[19] Grant Biedermann. “Gravity Tests, Differential Accelerometry and Interleaved Clocks with Cold Atom Interferometers”. Stanford University, 2007. URL: http://www.stanford.edu/group/kasevich/cgi-bin/wordpress/wp-content/uploads/2012/09/Gb-thesis.pdf.

[20] K. S. Hardman et al. “Simultaneous Precision Gravimetry and Magnetic Gradiometry with a Bose-Einstein Condensate: A High Precision, Quantum Sensor”. In: *Physical Review Letters* 117.13 (Sept. 21, 2016). DOI: 10.1103/PhysRevLett.117.138501.

[21] J. B. Fixler et al. “Atom Interferometer Measurement of the Newtonian Constant of Gravity”. In: *Science* 315.5808 (Jan. 5, 2007), pp. 74–77. DOI: 10.1126/science.1135459.

[22] Gabriele Rosi. “Precision Gravity Measurements with Atom Interferometry”. PhD. University of Pisa, 2012.

[23] David S. Weiss, Brenton C. Young, and Steven Chu. “Precision Measurement of Hbar/m Cs Based on Photon Recoil Using Laser-Cooled Atoms and Atomic Interferometry”. In: *Applied physics B* 59.3 (1994), pp. 217–256. DOI: 10.1007/BF01081393.

[24] G. W. Biedermann et al. “Testing Gravity with Cold-Atom Interferometers”. In: *Physical Review A* 91.3 (Mar. 24, 2015). DOI: 10.1103/PhysRevA.91.033629.

[25] Savas Dimopoulos et al. “Testing General Relativity with Atom Interferometry”. In: *Physical Review Letters* 98 (Mar. 15, 2007), p. 111102. DOI: 10.1103/PhysRevLett.98.111102.

[26] D. Schlippert et al. “Quantum Test of the Universality of Free Fall”. In: *Physical Review Letters* 112 (May 22, 2014), p. 203002. DOI: 10.1103/PhysRevLett.112.203002.

[27] Achim Peters, Keng Yeow Chung, and Steven Chu. "High-Precision Gravity Measurements Using Atom Interferometry". In: *Metrologia* 38.1 (2001), p. 25. DOI: 10.1088/0026-1394/38/1/4.

[28] E G Adelberger. "New Tests of Einstein's Equivalence Principle and Newton's Inverse-Square Law". In: *Classical and Quantum Gravity* 18.13 (July 7, 2001), pp. 2397–2405. DOI: 10.1088/0264-9381/18/13/302.

[29] T. Kovachy et al. "Quantum Superposition at the Half-Metre Scale". In: *Nature* 528.7583 (Dec. 23, 2015), pp. 530–533. DOI: 10.1038/nature16155.

[30] Savas Dimopoulos et al. "Gravitational Wave Detection with Atom Interferometry". In: *Physics Letters B* 678.1 (July 2009), pp. 37–40. DOI: 10.1016/j.physletb.2009.06.011.

[31] Remi Geiger et al. "Matter-Wave Laser Interferometric Gravitation Antenna (MIGA): New Perspectives for Fundamental Physics and Geosciences". In: *arXiv:1505.07137 [physics.atom-ph]* (May 2015). URL: arxiv.org/abs/1505.07137.

[32] Justin Khoury and Amanda Weltman. "Chameleon Fields: Awaiting Surprises for Tests of Gravity in Space". In: *Physical Review Letters* 93.17 (2004), p. 171104. DOI: 10.1103/PhysRevLett.93.171104.

[33] Paul Hamilton et al. "Atom-Interferometry Constraints on Dark Energy". In: *Science* 349.6250 (2015), pp. 849–851. DOI: 10.1126/science.aaa8883.

[34] Wolfgang Torge and Jürgen Müller. *Geodesy*. 4th ed. De Gruyter textbook. Berlin ; Boston: De Gruyter, 2012. 433 pp. ISBN: 978-3-11-020718-7 978-3-11-025000-8.

[35] David Crossley, Jacques Hinderer, and Umberto Riccardi. "The Measurement of Surface Gravity". In: *Reports on Progress in Physics* 76.4 (Apr. 1, 2013), p. 046101. DOI: 10.1088/0034-4885/76/4/046101.

[36] Friedrich Robert Helmert. *Die Mathematischen Und Physikalischen Theorien Der Höheren Geodäsie*. Vol. 1. 2 vols. Leipzig: Teubner, 1880.

[37] Nikolaos K. Pavlis et al. "The Development and Evaluation of the Earth Gravitational Model 2008 (EGM2008): THE EGM2008 EARTH GRAVITATIONAL MODEL". In: *Journal of Geophysical Research: Solid Earth* 117 (B4 Apr. 2012). DOI: 10.1029/2011JB008916.

[38] Torsten Mayer-Gürr et al. "ITG-GRACE: Global Static and Temporal Gravity Field Models from GRACE Data". In: *System Earth via Geodetic-Geophysical Space Techniques*. Ed. by Frank M. Flechtner et al. Berlin, Heidelberg: Springer Berlin Heidelberg, 2010, pp. 159–168. ISBN: 978-3-642-10228-8. URL: http://dx.doi.org/10.1007/978-3-642-10228-8_13.

[39] *Earth Gravitational Model 2008*. 2013. URL: http://earth-info.nga.mil/GandG/wgs84/gravitymod/egm2008/.

[40] A. T. Doodson. "The Harmonic Development of the Tide-Generating Potential". In: *Proceedings of the Royal Society A: Mathematical, Physical and Engineering Sciences* 100.704 (Dec. 1, 1921), pp. 305–329. DOI: 10.1098/rspa.1921.0088.

[41] Yoshiaki Tamura. "A Harmonic Development of the Tide-Generating Potential". In: *Bull. Inf. Marées Terrestres* 99 (1987), pp. 6813–6855.

[42] Torsten Hartmann and Hans-Georg Wenzel. "The HW95 Tidal Potential Catalogue". In: *Geophysical Research Letters* 22.24 (Dec. 15, 1995), pp. 3553–3556. DOI: 10.1029/95GL03324.

[43] A. E. H Love. *Some Problems of Geodynamics.* OCLC: 920849484. Place of publication not identified: Cambridge Univ Press, 1911. ISBN: 978-1-107-53647-0.

[44] Ernst W. Schwiderski. "On Charting Global Ocean Tides". In: *Reviews of Geophysics* 18.1 (1980), p. 243. DOI: 10.1029/RG018i001p00243.

[45] John M. Wahr. "Body Tides on an Elliptical, Rotating, Elastic and Oceanless Earth". In: *Geophysical Journal of the Royal Astronomical Society* 64.3 (Mar. 1981), pp. 677–703. DOI: 10.1111/j.1365-246X.1981.tb02690.x.

[46] L. Timmen and H.-G. Wenzel. "Worldwide Synthetic Gravity Tide Parameters". In: *Gravity and Geoid: Joint Symposium of the International Gravity Commission and the International Geoid Commission.* Ed. by Hans Sünkel and Iginio Marson. Berlin, Heidelberg: Springer Berlin Heidelberg, 1995, pp. 92–101. ISBN: 978-3-642-79721-7. URL: http://dx.doi.org/10.1007/978-3-642-79721-7_11.

[47] Michel Van Camp and Paul Vauterin. "Tsoft: Graphical and Interactive Software for the Analysis of Time Series and Earth Tides". In: *Computers & Geosciences* 31.5 (2005), pp. 631–640. DOI: http://dx.doi.org/10.1016/j.cageo.2004.11.015.

[48] T. M. Niebauer. "Correcting Gravity Measurements for the Effects of Local Air Pressure". In: *Journal of Geophysical Research* 93 (B7 1988), p. 7989. DOI: 10.1029/JB093iB07p07989.

[49] *IAG Resolution No. 9.* 1983. URL: http://iag.dgfi.tum.de/index.php.

[50] G Bödecker. *International Absolute Gravity Basestation Network (IAGBN) – Absolute Gravity Observations Data Processing Standards & Station Documentation.* Bulletin d'Information No 63. Contributing Paper. Bureau Gravimétrique International (BGI), Dec. 1988, pp. 51–57. URL: http://bgi.omp.obs-mip.fr/publications/bgi_bulletin.

[51] T. Klügel and H. Wziontek. "Correcting Gravimeters and Tiltmeters for Atmospheric Mass Attraction Using Operational Weather Models". In: *Journal of Geodynamics* 48 (3-5 Dec. 2009), pp. 204–210. DOI: 10.1016/j.jog.2009.09.010.

[52] *Atmospheric Attraction Computation Service.* 2016. URL: http://atmacs.bkg.bund.de.

[53] Ludger Timmen. "Absolute and Relative Gravimetry". In: *Sciences of Geodesy - I.* Ed. by Guochang Xu. Berlin, Heidelberg: Springer Berlin Heidelberg, 2010, pp. 1–48. ISBN: 978-3-642-11740-4 978-3-642-11741-1. URL: http://link.springer.com/10.1007/978-3-642-11741-1_1.

[54] *IERS EOP Parameters.* URL: ftp://hpiers.obspm.fr/iers/eop/.

[55] Martina Harnisch and Günter Harnisch. "Study of Long-Term Gravity Variations, Based on Data of the GGP Co-Operation". In: *Journal of Geodynamics* 41 (1-3 Jan. 2006), pp. 318–325. DOI: 10.1016/j.jog.2005.08.006.

[56] M. Hauth et al. “Atom Interferometry for Absolute Measurements of Local Gravity”. In: *Proc. of the Int. School of Physics ”Enrico Fermi”, Course 188, Edited by Tino G. M. and Kasevich M. A.* SIF, Bologna and IOS Press, Amsterdam, May 2014, pp. 557–586. DOI: 10.3254/978-1-61499-448-0-557.

[57] L. A. Krieg and Ohio State University. Department of Geodetic Science. *Mathematical Modelling of the Behaviour of the Lacoste and Romberg ”G” Gravity Meter for Use in Gravity Network Adjustments and Data Analyses*. Columbus: [s.n.], 1981.

[58] Manuel Schilling and Olga Gitlein. “Accuracy Estimation of the IfE Gravimeters Micro-g LaCoste gPhone-98 and ZLS Burris Gravity Meter B-64”. In: Berlin, Heidelberg: Springer Berlin Heidelberg, 2015. URL: http://link.springer.com/10.1007/1345_2015_29.

[59] J. Hinderer, D. Crossley, and R.J. Warburton. “Superconducting Gravimetry”. In: *Treatise on Geophysics*. Elsevier, 2015, pp. 59–115. ISBN: 978-0-444-53803-1. URL: http://dx.doi.org/10.1016/B978-0-444-53802-4.00062-2.

[60] John M. Goodkind. “The Superconducting Gravimeter”. In: *Review of Scientific Instruments* 70.11 (1999), p. 4131. DOI: 10.1063/1.1150092.

[61] *GWR Instruments*. 2015. URL: http://www.gwrinstruments.com.

[62] William M. Telford, Lloyd P. Geldart, and Robert E. Sheriff. *Applied Geophysics*. 2. ed., transferred to digital printing. OCLC: 552143005. Cambridge: Cambridge Univ. Press, 2004. 770 pp. ISBN: 978-0-521-33938-4 978-0-521-32693-3.

[63] J E Faller and I Marson. “Ballistic Methods of Measuring g - the Direct Free-Fall and Symmetrical Rise-and-Fall Methods Compared”. In: *Metrologia* 25.1 (Jan. 1, 1988), pp. 49–55. DOI: 10.1088/0026-1394/25/1/008.

[64] T. M. Niebauer et al. “A New Generation of Absolute Gravimeters”. In: *Metrologia* 32.3 (1995), p. 159. DOI: 10.1088/0026-1394/32/3/004.

[65] Olivier Francis et al. “CCM.G-K2 Key Comparison”. In: *Metrologia* 52 (1A Jan. 1, 2015), p. 07009. DOI: 10.1088/0026-1394/52/1A/07009.

[66] T M Niebauer et al. “The Self-Attraction Correction for the FG5X Absolute Gravity Meter”. In: *Metrologia* 50.1 (Feb. 1, 2013), pp. 1–8. DOI: 10.1088/0026-1394/50/1/1.

[67] James E. Faller. “Super Spring”. In: *The Journal of the Acoustical Society of America* 68.6 (1980), p. 1900. DOI: 10.1121/1.385186.

[68] Robert Lee. Rinker. “Super Spring : A New Type of Low-Frequency Vibration Isolator”. PhD. University of Colorado, 1983.

[69] Manuel Schilling and Ludger Timmen. “Traceability of the Hannover FG5X-220 to the SI Units”. In: Berlin, Heidelberg: Springer Berlin Heidelberg, 2016. URL: http://link.springer.com/10.1007/1345_2016_226.

[70] Manuel Schilling. Private communication. 2015.

[71] Jürgen Müller et al. “A Land Uplift Model in Fennoscandia Combining GRACE and Absolute Gravimetry Data”. In: *Physics and Chemistry of the Earth, Parts A/B/C* 53-54 (Jan. 2012), pp. 54–60. DOI: 10.1016/j.pce.2010.12.006.

[72] Jeffrey Kennedy et al. "Gravity-Measured Water Storage Change and Subsurface Hydraulic Properties at a Managed Recharge Facility in Tucson, USA". In: Environment and Engineering Geophysical Society, Jan. 2012, pp. 58–58. DOI: 10.4133/1.4721694.

[73] Andreas Guntner et al. "Monitoring Water Storage Variations with a Superconducting Gravimeter in a Field Enclosure". In: *EGU General Assembly 2016*. Vienna, Apr. 2016, p. 5173.

[74] Patrick Cheinet. "Conception et Réalisation d'un Gravimètre à Atomes Froids". Université Pierre et Marie Curie-Paris VI, 2006. URL: http://hal.upmc.fr/tel-00070861/.

[75] *MuQuans*. 2014. URL: http://www.muquans.com/.

[76] *AoSense*. 2016. URL: http://aosense.com.

[77] *AtomSensors*. 2016. URL: http://www.atomsensors.com/.

[78] Paul R. Berman, ed. *Atom Interferometry*. San Diego: Academic Press, 1997. 478 pp. ISBN: 978-0-12-092460-8.

[79] Daniel A. Steck. *Quantum and Atom Optics*. revision 0.5.12. Eugene, Oregon, 2011. URL: http://steck.us/teaching.

[80] Matthias Hauth. "A Mobile, High-Precision Atom-Interferometer and Its Application to Gravity Observations". PhD. Berlin: Humboldt Universität zu Berlin, 2015.

[81] Harold J. Metcalf and Peter Van der Straten. *Laser Cooling and Trapping*. Graduate texts in contemporary physics. New York: Springer, 1999. 323 pp. ISBN: 0-387-98747-9 0-387-98728-2.

[82] Malte Schmidt. "A Mobile High-Precision Gravimeter Based on Atom Interferometry". PhD. Berlin: Humboldt Universität zu Berlin, 2011. URL: http://edoc.hu-berlin.de/dissertationen/schmidt-malte-2011-11-02.

[83] J. Le Gouët. "Etude Des Performances d'un Gravimetre Atomique Absolu : Sensibilite Limite et Exactitude Preliminaire". PhD. University Paris-Sud 11, 2008. URL: https://tel.archives-ouvertes.fr/tel-00311422v4.

[84] Pippa Storey and Claude Cohen-Tannoudji. "The Feynman Path Integral Approach to Atomic Interferometry. A Tutorial". In: *J. Phys. II France* 4.11 (1994), pp. 1999–2027. DOI: 10.1051/jp2:1994103.

[85] Kai Bongs, R. Launay, and Mark A Kasevich. "High-Order Inertial Phase Shifts for Time-Domain Atom Interferometers". In: *Applied Physics B* 84.4 (Aug. 2006), pp. 599–602. DOI: 10.1007/s00340-006-2397-5.

[86] Jason M. Hogan, David M S Johnson, and Mark A Kasevich. "Light-Pulse Atom Interferometry". In: *Proceedings of the International School of Physics Enrico Fermi Course CLXVIII on Atom Optics and Space Physics*. Ed. by E. Arimondo et al. Oxford: IOS Press, June 2007, pp. 411–447. DOI: 10.3254/978-1-58603-990-5-411.

[87] Ch J. Bordé. "Atomic Clocks and Inertial Sensors". In: *Metrologia* 39.5 (2002), p. 435. DOI: 10.1088/0026-1394/39/5/5.

[88] Ch. J. Bordé. "5D Optics for Atomic Clocks and Gravito-Inertial Sensors". In: *The European Physical Journal Special Topics* 163.1 (Oct. 2008), pp. 315–332. DOI: 10.1140/epjst/e2008-00827-3.

[89] Wolfgang P Schleich, Daniel M Greenberger, and Ernst M Rasel. "A Representation-Free Description of the Kasevich–Chu Interferometer: A Resolution of the Redshift Controversy". In: *New Journal of Physics* 15.1 (Jan. 7, 2013), p. 013007. DOI: 10.1088/1367-2630/15/1/013007.

[90] Stephan Kleinert et al. "Representation-Free Description of Light-Pulse Atom Interferometry Including Non-Inertial Effects". In: *Physics Reports* 605 (Dec. 2015), pp. 1–50. DOI: 10.1016/j.physrep.2015.09.004.

[91] P. Cheinet et al. "Measurement of the Sensitivity Function in a Time-Domain Atomic Interferometer". In: *IEEE Transactions on Instrumentation and Measurement* 57.6 (June 2008), pp. 1141–1148. DOI: 10.1109/TIM.2007.915148.

[92] C. Antoine. "Matter Wave Beam Splitters in Gravito-Inertial and Trapping Potentials: Generalized Ttt Scheme for Atom Interferometry". In: *Applied Physics B* 84.4 (Sept. 2006), pp. 585–597. DOI: 10.1007/s00340-006-2378-8.

[93] Alexander Senger. "A Mobile Atom Interferometer for High-Precision Measurements of Local Gravity". Mathematisch-Naturwissenschaftliche Fakultät I, 2012. URL: http://edoc.hu-berlin.de/dissertationen/senger-alexander-2011-11-22.

[94] Christian Freier. "Measurement of Local Gravity Using Atom Interferometry". Diplomarbeit. Technische Universitaet Berlin, 2010. 95 pp. URL: http://www.physik.hu-berlin.de/qom/publications/pdfs/freier2010a.pdf.

[95] Jia-Qiang Huang et al. "Intense Source of Cold Cesium Atoms Based on a Two-Dimensional Magneto–optical Trap with Independent Axial Cooling and Pushing". In: *Chinese Physics B* 25.6 (June 2016), p. 063701. DOI: 10.1088/1674-1056/25/6/063701.

[96] N. Castagna et al. "A Novel Simplified Two-Dimensional Magneto-Optical Trap as an Intense Source of Slow Cesium Atoms". In: *The European Physical Journal Applied Physics* 34.1 (May 4, 2006), pp. 21–30. DOI: 10.1051/epjap:2006037.

[97] T. Petelski. "Atom Interferometers for Precision Gravity Measurements". PhD. Firenze: European PhD School, Feb. 4, 2005. 209 pp. URL: http://www.fi.infn.it/sezione/esperimenti/MAGIA/PhDTorstenPetelski.pdf.

[98] Joel M. Hensley, Achim Peters, and Steven Chu. "Active Low Frequency Vertical Vibration Isolation". In: *Review of Scientific Instruments* 70.6 (1999), pp. 2735–2741. DOI: 10.1063/1.1149838.

[99] J. Le Gouët et al. "Limits to the Sensitivity of a Low Noise Compact Atomic Gravimeter". In: *Applied Physics B* 92.2 (June 27, 2008), pp. 133–144. DOI: 10.1007/s00340-008-3088-1.

[100] Daniel A. Steck. *Rubidium 87 D Line Data*. 2.1.4. 2001. URL: http://www.steck.us/alkalidata/rubidium87numbers.pdf.

[101] Vladimir Schkolnik. "Probing Gravity with Quantum Sensors". PhD. Berlin: Humboldt Universität zu Berlin, 2016.

[102] D J McCarron, S A King, and S L Cornish. "Modulation Transfer Spectroscopy in Atomic Rubidium". In: *Measurement Science and Technology* 19.10 (Oct. 1, 2008), p. 105601. DOI: 10.1088/0957-0233/19/10/105601.

[103] E L Raab et al. "Trapping of Neutral Sodium Atoms with Radiation Pressure". In: *Physical Review Letters* 59.23 (Dec. 7, 1987), pp. 2631–2634. DOI: 10.1103/PhysRevLett.59.2631.

[104] Ch Salomon et al. "Laser Cooling of Cesium Atoms below 3 K". In: *EPL (Europhysics Letters)* 12.8 (1990), p. 683. URL: http://iopscience.iop.org/article/10.1209/0295-5075/12/8/003/meta.

[105] Y. Sortais et al. "Cold Collision Frequency Shifts in a 87 Rb Atomic Fountain". In: *Physical Review Letters* 85.15 (2000), p. 3117. DOI: 10.1103/PhysRevLett.85.3117.

[106] Y. Castin, J. Dallbard, and C. Cohen-Tannoudji. "The Limits of Sisyphus Cooling". In: *Light Induced Kinetic Effects on Atoms, Ions and Molecules*. Pisa, 1991. URL: http://www.phys.ens.fr/~dalibard/publications/Elba1990.pdf.

[107] Chad Fertig and Kurt Gibble. "Measurement and Cancellation of the Cold Collision Frequency Shift in an 87 Rb Fountain Clock". In: *Physical review letters* 85.8 (2000), p. 1622. DOI: 10.1103/PhysRevLett.85.1622.

[108] Manuel Schilling. Private communication. 2013.

[109] Reinhold Hoppe and Reinhard Falk. *Absolute Und Relative Schweremessungen in Der Humboldt-Universität Zu Berlin (Campus Adlershof) Messungen Im Lise-Meitner-Bau*. Technischer Bericht G4-2010-5. Bundesamt für Kartographie und Geodäsie (BKG), 2010, p. 12.

[110] Michel Van Camp. "Uncertainty of Absolute Gravity Measurements". In: *Journal of Geophysical Research* 110 (2005), B05406. DOI: 10.1029/2004JB003497.

[111] Hartmut Wziontek. Private communication. 2014.

[112] Hartmut Wziontek. "Integration of Regional Absolute Gravimeter Comparisons into the Framework of the International Comparisons". Strasbourg, France, Nov. 17, 2014.

[113] Z Jiang et al. "The 8th International Comparison of Absolute Gravimeters 2009: The First Key Comparison (CCM.G-K1) in the Field of Absolute Gravimetry". In: *Metrologia* 49.6 (Dec. 1, 2012), pp. 666–684. DOI: 10.1088/0026-1394/49/6/666.

[114] Reinhard Falk. Private communication. 2016.

[115] J. Lautier et al. "Hybridizing Matter-Wave and Classical Accelerometers". In: *Applied Physics Letters* 105.14 (Oct. 6, 2014), p. 144102. DOI: 10.1063/1.4897358.

[116] J. Le Gouët et al. "Influence of Lasers Propagation Delay on the Sensitivity of Atom Interferometers". In: *The European Physical Journal D* 44.3 (Sept. 2007), pp. 419–425. DOI: 10.1140/epjd/e2007-00218-2.

[117] P Gillot et al. "Stability Comparison of Two Absolute Gravimeters: Optical versus Atomic Interferometers". In: *Metrologia* 51.5 (Oct. 1, 2014), p. L15. DOI: 10.1088/0026-1394/51/5/L15.

[118] David W. Allan. "Should the Classical Variance Be Used as a Basic Measure in Standards Metrology?" In: *IEEE Transactions on instrumentation and measurement* 1001.2 (1987), pp. 646–654. DOI: 10.1109/TIM.1987.6312761.

[119] William J. Riley. *Handbook of Frequency Stability Analysis*. US Department of Commerce, National Institute of Standards and Technology Gaithersburg, MD, 2008. URL: tf.nist.gov/timefreq/general/pdf/2220.pdf.

[120] William J. Riley. *Stable32 Software Package for Frequency Stability Analysis*. Version 1.43. S. Hamilton, MA 01982 USA, 2004.

[121] Olivier Francis and Tonie van Dam. "Evaluation of the Precision of Using Absolute Gravimeters to Calibrate Superconducting Gravimeters". In: *Metrologia* 39.5 (2002), p. 485. DOI: 10.1088/0026-1394/39/5/9.

[122] Michel Van Camp et al. "Optimized Strategy for the Calibration of Superconducting Gravimeters at the One per Mille Level". In: *Journal of Geodesy* 90.1 (Sept. 25, 2015), pp. 91–99. DOI: 10.1007/s00190-015-0856-7.

[123] Michel Van Camp et al. "Accurate Transfer Function Determination for Superconducting Gravimeters". In: *Geophysical Research Letters* 27.1 (Jan. 1, 2000), pp. 37–40. DOI: 10.1029/1999GL010495.

[124] Julius S. Bendat and Allan G. Piersol. *Random Data: Analysis and Measurement Procedures*. 4th ed. Wiley series in probability and statistics. Hoboken, N.J: Wiley, 2010. 604 pp. ISBN: 978-0-470-24877-5.

[125] William H. Press. *Numerical Recipes in C*. 2nd ed. Cambridge ; New York: Cambridge University Press, 1992. 994 pp. ISBN: 0-521-43108-5.

[126] Hartmut Wziontek. Private communication. 2016.

[127] Hans-Georg Scherneck. Private communication. 2015.

[128] B Richter, H Wilmes, and I Nowak. "The Frankfurt Calibration System for Relative Gravimeters". In: *Metrologia* 32.3 (Jan. 1, 1995), pp. 217–223. DOI: 10.1088/0026-1394/32/3/010.

[129] Jason Hogan. "Towards Precision Tests of General Relativity Using an Atom Interferometer". Stanford University, 2010.

[130] Anne Louchet-Chauvet et al. "The Influence of Transverse Motion within an Atomic Gravimeter". In: *New Journal of Physics* 13.6 (June 28, 2011), p. 065025. DOI: 10.1088/1367-2630/13/6/065025.

[131] B. Cheng et al. "Influence of Chirping the Raman Lasers in an Atom Gravimeter: Phase Shifts Due to the Raman Light Shift and to the Finite Speed of Light". In: *Physical Review A* 92.6 (Dec. 9, 2015). DOI: 10.1103/PhysRevA.92.063617.

[132] H Baumann et al. "Experimental Assessment of the Speed of Light Perturbation in Free-Fall Absolute Gravimeters". In: *Metrologia* 52.5 (Oct. 1, 2015), pp. 635–645. DOI: 10.1088/0026-1394/52/5/635.

[133] Holger Müller et al. "Active Sub-Rayleigh Alignment of Parallel or Antiparallel Laser Beams". In: *Optics Letters* 30.24 (Dec. 15, 2005), p. 3323. DOI: 10.1364/OL.30.003323.

[134] Jun Ye et al. “Hyperfine Structure and Absolute Frequency of the 87 Rb 5P 3/2 State”. In: *Optics letters* 21.16 (1996), pp. 1280–1282. DOI: 10.1364/OL.21.001280.

[135] Qi Xiang-Hui et al. “Ultra-Stable Rubidium-Stabilized External-Cavity Diode Laser Based on the Modulation Transfer Spectroscopy Technique”. In: *Chinese Physics Letters* 26.4 (2009), p. 044205. DOI: 10.1088/0256-307X/26/4/044205.

[136] Paul Siddons et al. “Absolute Absorption on Rubidium D Lines: Comparison between Theory and Experiment”. In: *Journal of Physics B: Atomic, Molecular and Optical Physics* 41.15 (Aug. 14, 2008), p. 155004. DOI: 10.1088/0953-4075/41/15/155004.

[137] Bastian Leykauf. “The Effect of Wavefront Aberrations in Light-Pulse Atom Interferometry”. Bachelorarbeit. Humboldt Universität zu Berlin, July 2, 2014. 52 pp.

[138] V. Schkolnik et al. “The Effect of Wavefront Aberrations in Atom Interferometry”. In: *Applied Physics B* 120 (June 2, 2015), pp. 311–316. DOI: 10.1007/s00340-015-6138-5.

[139] Vladimir Schkolnik. Private communication. 2015.

[140] A. E. Siegman. *Lasers*. 1st ed. Mill Valley, California: University Science Books, 1986. ISBN: 0-935702-11-5.

[141] Alex Sugarbaker. “Atom Interferometry in a 10m Fountain”. PhD. Stanford: Stanford University, Aug. 2014. 162 pp. URL: http://purl.stanford.edu/kd753jv6128.

[142] Sébastien Merlet. “Détermination Absolue de g Dans Le Cadre de l’expérience de La Balance Du Watt”. Observatoire de Paris, 2010. URL: http://hal.upmc.fr/tel-00517127/.

[143] A. Gauguet et al. “Off-Resonant Raman Transition Impact in an Atom Interferometer”. In: *Physical Review A* 78.4 (Oct. 2008), p. 043615. DOI: 10.1103/PhysRevA.78.043615.

[144] P. Gillot et al. “Limits to the Symmetry of a Mach-Zehnder-Type Atom Interferometer”. In: *Physical Review A* 93.1 (Jan. 12, 2016), p. 013609. DOI: 10.1103/PhysRevA.93.013609.

[145] B Wu et al. “Accurate Measurement of the Quadratic Zeeman Coefficient of 87Rb Clock Transition Based on the Ramsey Atom Interferometer”. In: *Journal of Physics B: Atomic, Molecular and Optical Physics* 47.1 (Jan. 14, 2013), p. 015001. DOI: 10.1088/0953-4075/47/1/015001.

[146] Zhong-Kun Hu et al. “Simultaneous Differential Measurement of a Magnetic-Field Gradient by Atom Interferometry Using Double Fountains”. In: *Physical Review A* 84.1 (July 27, 2011). DOI: 10.1103/PhysRevA.84.013620.

[147] J. B. Camp, T. W. Darling, and Ronald E. Brown. “Macroscopic Variations of Surface Potentials of Conductors”. In: *Journal of Applied Physics* 69.10 (1991), p. 7126. DOI: 10.1063/1.347601.

[148] F. Antonucci et al. “Interaction between Stray Electrostatic Fields and a Charged Free-Falling Test Mass”. In: *Physical Review Letters* 108.18 (Apr. 30, 2012). DOI: 10.1103/PhysRevLett.108.181101.

[149] J. D. Carter and J. D. D. Martin. "Energy Shifts of Rydberg Atoms Due to Patch Fields near Metal Surfaces". In: *Physical Review A* 83.3 (Mar. 7, 2011). DOI: 10.1103/PhysRevA.83.032902.

[150] Kurt Gibble and Steven Chu. "Laser-Cooled Cs Frequency Standard and a Measurement of the Frequency Shift Due to Ultracold Collisions". In: *Physical Review Letters* 70.12 (Mar. 22, 1993), pp. 1771–1774. DOI: 10.1103/PhysRevLett.70.1771.

[151] I. Dutta et al. "Continuous Cold-Atom Inertial Sensor with 1 Nrad / Sec Rotation Stability". In: *Physical Review Letters* 116.18 (May 6, 2016). DOI: 10.1103/PhysRevLett.116.183003.

[152] Nassim Zahzam et al. "New Advances in the Field of Cold Atom Interferometers for Onboard Gravimetry". Presentation. St. Petersburg, 2016. URL: http://www.elektropribor.spb.ru/tgsmm2016/eginf.

[153] V. Menoret et al. "Quantitative Analysis of a Transportable Matter-Wave Gravimeter". Presentation. St. Petersburg, 2016.

[154] Alexis Bonnin. "Simultaneous Interferometry with Two Atomic Species 87Rb/85Rb and Applications to Inertial Measurements". PhD. Université Paris-Saclay, Nov. 2015. URL: https://tel.archives-ouvertes.fr/tel-01272542.

List of Figures

List of Tables

Acronyms

ADC analog-to-digital converter. 45

AG absolute gravimeter. 9, 19

ASD amplitude spectral density. 47

ASE amplified spontaneous emission. 55

BKG Federal Agency for Cartography and Geodesy. 75, 79, 142, 143, 146

DAC digital-to-analog converter. 45

DDS direct digital synthesizer. 55

DFB distributed feedback. 53

DRO dielectric resonator oscillator. 55

ECDL external cavity diode laser. 53

EEP Einstein's equivalence principle. 7, 9

FBH Ferdinand-Braun Institut für Höchstfrequenztechnik. 116

FCCG falling corner-cube gravimeter. 9, 19, 21

FPGA field-programmable gate array. 45, 58

GAIN gravimetric atom interferometer. 22, 41, 73, 74, 94, 162

HUB Humboldt Universität zu Berlin. 22, 73, 96

IfE Institut für Erdmessung, Leibniz Universität Hannover. 73, 74, 84, 142, 143, 148

LCR LaCoste-Romberg. 17

LLI local Lorentz invariance. 7

LPI local position invariance. 7

LVDS low voltage differential signaling. 61

MOT magneto-optical trap. 8, 40, 41, 53, 63

MTS modulation transfer spectroscopy. 53

NTP network time protocol. 49, 58

OSO Onsala Space Observatory. 82

PBS polarizing beam splitter. 55

PCM phase change material. 79

PFD phase-frequency detector. 55

PLL phase-locked loop. 34, 53–55

PSD power spectral density. 33, 56

RF radio frequency. 23

RMS root mean square. 94

RWA rotating wave approximation. 25

SCG superconducting gravimeter. 18, 79, 86, 94, 95, 97, 98

SNR signal-to-noise ratio. 99

TA tapered amplifier. 53

UFF universality of free fall. 7, 9

UHV ultra-high vacuum. 8, 38

WEP weak equivalence principle. 7

Publications

Print

- **Mobile Quantum Gravity Sensor with Unprecedented Stability**
  C Freier, M Hauth, V Schkolnik, B Leykauf, M Schilling, H Wziontek, H-G Scherneck, J Müller, and A Peters. (June 2016) *Journal of Physics: Conference Series* 723 12050

- **The Effect of Wavefront Aberrations in Atom Interferometry**
  V Schkolnik, B Leykauf, M Hauth, **C Freier**, and A Peters. *Applied Physics B* 120, 311–316 (2015).

- **Atom Interferometry for Absolute Measurements of Local Gravity**
  M Hauth, **C Freier**, V Schkolnik, A Peters, H Wziontek, and M Schilling. *Proceedings of the International School of Physics 'Enrico Fermi'*, Course 188, 557–586 (2014).

- **First Gravity Measurements using the Mobile Atom Interferometer GAIN**
  M Hauth, **C Freier**, V Schkolnik, A Senger, M Schmidt, and A Peters. *Applied Physics B* 113, 49–55 (2013).

- **A Mobile High-Precision Absolute Gravimeter based on Atom Interferometry**
  M Schmidt, A Senger, M Hauth, **C Freier**, V Schkolnik, and A Peters. *Gyroscopy and Navigation* 2, 170–177 (2011).

Oral Presentations

Only those presentations are listed where the thesis author is first author and presenter.

- *Colloquium Talk*, Séminaire Temps/Fréquence du SYRTE, Paris, France (2016)

- *Invited Talk*, École de Physique des Houches "Advanced atomic sources and extreme cooling of atoms and molecules: techniques and applications", Les Houches, France (2016)

- *Colloquium Talk*, Nanyang Technical University, Singapore (2015)

- *Colloquium Talk*, National University of Singapore, Singapore (2015)

- *Contributed Talk*, Deutsche Physikalische Gesellschaft (DPG) Annual Meeting, Heidelberg, Germany (2015)
- *Colloquium Talk*, Chalmers University, Gothenburg, Sweden (2015)
- *Contributed Talk*, "Geodätische Woche" during the Intergeo Conference, Berlin, Germany (2014)
- *Contributed Talk*, Deutsche Physikalische Gesellschaft (DPG) Annual Meeting, Berlin, Germany (2014)
- *Contributed Talk*, International Association of Geodesy (IAG) Scientific Assembly, Potsdam, Germany (2013)
- *Contributed Talk*, Deutsche Physikalische Gesellschaft (DPG) Annual Meeting, Stuttgart, Germany (2012)

Poster Presentations

Only those presentations are listed where the thesis author is first author and presenter.

- International Conference on Laser Spectroscopy (ICOLS), Singapore (2015)
- Deutsche Physikalische Gesellschaft (DPG) Annual Meeting, Hannover, Germany (2013)
- Young Atom Opticians Conference (YAO), Hannover, Germany, (2011)
- Deutsche Physikalische Gesellschaft (DPG) Annual Meeting, Dresden, Germany (2011)

Student Supervision

Master Student

- Bastian Leykauf
  Gradiometric Measurements with a Juggling Atomic Fountain
  (working title, in preparation)

Bachelor Students

- Linos Hecht
  Implementation of Components for Raman Sideband Cooling (2015)
- Marek Mandel
  Implementierung des Versuchs "Magneto-optische Falle" für das Fortgeschrittenenpraktikum (2014)

Acknowledgments

This work would not have been possible without the assistance and support of numerous people to whom I want to express my gratitude and best wished for the future.

First of all, I would like to thank my supervisor Achim Peters for the opportunity to be a part of his research group during my time as a PhD student. His experience with the subject matter and his profound knowledge in the lab, paired with the readiness to share his insight and long term commitment to the project, was crucial in realizing the results presented in this work.

I also want to thank my fellow GAIN campaigners Matthias Hauth and Vladimir Schkolnik. Pushing all aspects of the experiments forward at the same time and conducting the measurement campaigns afterwards would not have been possible without the shared work and commitment of the whole team. Thanks also to both of them for proof-reading this work and their constructive, important suggestions on the manuscript.

A warm "thank you" also goes out to Manuel Schilling, Hartmut Wziontek and Hans-Georg Scherneck for being so supportive and enthusiastic about GAIN and the conducted measurement campaigns. They also always provided the optimal gravimetric tide models and reliable reference measurements using their own gravimeters. Special thanks to Manuel for proof-reading the introduction of this work and sharing some of his insight into geodesy and geophysics.

Matthias Schoch, Eugen Dischke and Klaus Palis for help in designing and building electronics and to Thorsten Rausche for giving important feedback on my mechanical designs and for realizing them swiftly and well. All colleagues of the QOM and NANO group for providing a productive, creative and fun work environment.

My biggest thanks go out to Trista for accompanying me during my entire PhD period and being there for me through all its ups and downs. It would not have been the same without you. Further thanks to her and Emily for correcting the language and making my writing more English than "Denglish". Finally, thanks to my family and all my friends for your advice, support and all the good times.

Selbstständigkeitserklärung

Hiermit erkläre ich, die vorliegende Arbeit selbstständig und nur unter Verwendung der angegebenen Quellen und Hilfsmittel angefertigt zu haben. Ich habe mich anderweitig nicht um einen Doktorgrad beworben und besitze einen solchen auch nicht. Die dem Verfahren zugrundeliegende Promotionsordnung der Mathematisch-Naturwissenschaftlichen Fakultät der Humboldt Universität zu Berlin habe ich zur Kenntnis genommen.

Berlin, den May 30, 2017 Christian Freier